Neutron Spectroscopy in Proton Therapy

Khalid Aloufi

Thesis submitted for the Degree of Doctor of Philosophy

Department of Medical Physics and Biomedical Engineering

Faculty of Engineering Sciences

University College London

February 2016

Declaration

I, Khalid Aloufi, confirm that the work presented in this thesis is my own. Where information has been derived from other sources, I confirm that this has been indicated in the thesis.

Signature

.....

Abstract

Aim: During proton therapy, neutrons are generated through the interactions of a proton beam with the treatment head and the patient's body. A minor neutron dose to healthy tissues could be significant because of the high radiation weighting factor of neutrons. The aim of this research was to conduct a Monte Carlo (MC) simulation assessment of the relative neutron dose (neutron equivalent dose/prescribed proton therapy dose) and dose distribution during the proton irradiation at Clatterbridge Hospital.

Materials and methods: Due to the required criteria for a neutron detector in a proton therapy room, a prototype neutron detector based on EJ-331 (gadolinium-loaded liquid scintillator) was simulated using Geant4 and GAMOS.4.0.0 MC simulation codes. Then, the detector was constructed, calibrated and tested. Four pulse shape discrimination (PSD) methods were obtained and evaluated: charges ratio, charge to amplitude ratio, amplitude-fall time and fall time-amplitude.

The proton beam line at Clatterbridge Hospital was simulated using Geant4 and GAMOS.4.0.0 MC simulation codes. Neutrons and gamma rays were tracked during the proton irradiation and their deposited energies (DEs) were scored in a voxelised water phantom (50 x 100 x 50cm^3). The simulated prototype neutron detector was located 15cm in front of and 30cm below the final collimator of the simulated proton therapy beam line.

In addition, measurement was taken using the prototype neutron detector during the proton irradiation at Clatterbridge Hospital. The measurement geometry was adjusted so that it was the same as the MC simulation geometry to allow a comparison with the MC simulation results and to validate the MC results.

Results: The measured prototype neutron detector energy resolution was the same as the simulated detector, which was 17% at 477keV (Cs^{137} Compton edge). Using a Figure of Merit to evaluate the obtained PSD methods, the best PSD method performance was found to be the charges ratio. Thus, the charges ratio PSD method was applied to the collected data from the measurements at the proton therapy room in Clatterbridge Hospital.

A good agreement was found (within 80%) between the measured and the MC results. Hence, the MC simulation of the relative DE distributions from the neutrons and the gamma rays in the voxelised water phantom were validated.

The MC simulation results showed that the contribution of gamma rays to the integral equivalent radiation dose was 5.1%. In addition, the contributions of internal and thermal neutrons to the integral equivalent neutron dose were 4.1% and 1.2% respectively. Thus, fast external neutrons are the main source (89.6%) of the secondary radiation dose during proton irradiation at Clatterbridge Hospital.

Most of the neutron DE was distributed in and around the target voxel. In contrast, the gamma-ray DE was widely distributed. The relative integral neutron equivalent dose, which was 1.48mSv/Gy, and its distribution, in the patient's body (i.e. the voxelised water phantom), can be generalised for any prescribed proton therapy dose during proton therapy at Clatterbridge Hospital.

Conclusion: Fast external neutrons are the main concern in terms of the additional unwanted secondary radiation dose during proton therapy at the Clatterbridge proton beam. Although the neutron dose was small compared to the prescribed proton therapy dose, it is not negligible and the dose distribution can be used as the basis of the risk estimation from radiation induced secondary cancers.

Table of Contents

List of Figures

List of Tables

Acknowledgments

I am grateful to my supervisor, **Prof. Gary Royle**, for his support and encouragement. My gratefulness is extended to **Prof. Robert Speller** for his support and encouragement. I would like to show my appreciation to **Dr Andrzej Kacperek** and the **staff** at the proton therapy unit at Clatterbridge Hospital for their cooperation and assistance. I would like to thank **my family** for their unlimited support. Lastly, I would like to thank the Royal Embassy of Saudi Arabia and the Ministry of Health in Saudi Arabia for their funding and support.

Chapter 1. Introduction

1.1 Aim and objectives

A minor neutron dose to healthy tissues could be significant because of the high radiation weighting factor of neutrons. The final goals of this research are to assess the integral relative neutron dose and the relative neutron dose distribution during the proton therapy at Clatterbridge Hospital. The relative neutron dose is the neutron dose per prescribed proton therapy dose. Therefore, the main research question is whether the neutron dose during proton therapy is significant or negligible.

Using Monte Carlo (MC) simulation, the distribution of the neutron dose within a voxelised water phantom was obtained during simulated proton irradiation at Clatterbridge Hospital. In addition, several experiments, measurements and MC simulations were conducted, and several objectives were achieved.

a. MC simulation objectives:

1. MC simulation of a neutron detector (i.e. the fourth prototype neutron detector design).
2. MC simulation of the proton therapy beam line at Clatterbridge Hospital.
3. MC simulation of the relative deposited energy (DE) distributions and the relative integral DEs from neutrons and gamma rays in a voxelised water phantom during proton irradiation.
4. MC simulation of the measurements' setup, which was done in the proton therapy room at Clatterbridge Hospital to identify the scintillation spectra of neutrons and gamma rays during proton irradiation.

b. Experiment and measurement objectives:

1. Building four prototype neutron detectors.

The physical and clinical criteria for a neutron detector in a proton therapy room were considered. The physical criteria are the required neutron detector properties

related to the detection material and devices, while the clinical criteria are the required neutron detector properties related to the proton therapy facility. In addition, the MC simulation was used as the guideline to validate the fourth prototype neutron detector design for use in a proton therapy room.

The experimental objectives of the first, second and third prototype neutron detectors were the following:

- To confirm that the neutron detector was working appropriately, a Cs^{137} spectrum was obtained, to be compared with a typical Cs^{137} spectrum from the literature. In addition, to evaluate the improvement to the prototype neutron detectors, energy resolutions of the prototype neutron detectors were compared.
- Results were compared from an oscilloscope and a multichannel analyser (MCA). This was done to confirm that the results from the oscilloscope and the MCA were the same. Based on this, the procedures followed when using the oscilloscope were confirmed as being performed correctly. Therefore, the secondary neutron spectrum, during the proton irradiation at Clatterbridge Hospital, can be obtained using the neutron detector and the oscilloscope.

The experimental objectives of the fourth prototype neutron detector were the following:

- Obtaining pulse shape discrimination (PSD) methods.

A neutron detector in a proton therapy room should be able to show the full neutron energy spectrum details in the mixed radiation field. Therefore, four PSD methods were used to distinguish between different radiation particles. The best-performing PSD method was applied to the collected data during the proton irradiation at Clatterbridge Hospital.

- Taking measurements during the proton irradiation at Clatterbridge Hospital.

The aim of taking measurements in the proton therapy room at Clatterbridge hospital was to validate the MC simulation results of the neutron scintillation spectrum and its relative DE (or its absorbed dose). Hence, the MC simulation of the relative DE

distributions from the neutrons and gamma rays in the voxelised water phantom can be validated.

1.2 Novelty of the research

Firstly, an assessment of the relative neutron dose and its distribution during the proton therapy at Clatterbridge Hospital was not fulfilled. In this research, the relative neutron dose and its distribution were obtained using an MC simulation program. In addition, the following radiation dose quantities and radiation spectra were obtained:

- The relative integral gamma-ray dose and its distribution.
- The relative integral internal neutron dose.
- The relative integral thermal neutron dose.
- The relative integral thermalised neutron dose.
- Neutron and gamma-ray spectra.

Secondly, the gadolinium-loaded liquid scintillator (EJ-331) had not been used in this application before (i.e. neutron spectroscopy in proton therapy). In this research, a neutron detector based on EJ-331 was simulated, constructed and calibrated (i.e. the fourth prototype neutron detector). Using the fourth prototype neutron detector, the neutron and gamma-ray spectra were obtained during the proton irradiation at Clatterbridge Hospital.

Thirdly, four PSD methods were obtained and evaluated: charges ratio, charge to amplitude ratio, amplitude-fall time and fall time-amplitude. The fall time-amplitude PSD method was novel in utilising the relation between the pulse fall time and its relevant amplitude.

1.3 Clinical impact of neutrons in proton therapy

Regarding the high radiation weighting factor of neutrons, a minor neutron dose could be significant. During scattering proton therapy, the neutron dose could be ten to several ten times more than during spot-scanning proton therapy [1] [2]. However, the dose distribution (dose location) is the basis of the risk estimation from radiation induced secondary cancers [3].

The estimation of secondary cancers risk involves converting the neutron dose to risk. Several studies estimated the cancers risk related to the radiation dose in healthy tissue during radiotherapy, and showed comparisons between proton therapy delivery techniques, treatment procedures, and patient conditions (e.g. age and gender) [4] [5] [6].

- **System comparisons**

The secondary cancer lifetime attributable risks (LARs) was estimated according to simulated doses of organs, absolute risk models and excess relative risk (ERR). Monte Carlo simulation was used to estimate the dose during scattering and spot-scanning proton therapy, and 6MV Intensity-Modulated Radiation Therapy (IMRT). The organs doses were estimated during radiotherapy at spine and head locations. The treated patients were simulated to be voxelised phantoms of different genders and ages. The risk for patients was proportional to the patient body size because small patients mean fewer interactions incurred by the proton beam, resulting in lower neutron dose. Most of the LARs' estimated values for different body organs were found to be less than 0.1%, but a few were found to have a value of slightly more than 1%. For example, thyroid cancers the LAR from 54Gy scattering proton therapy for a brain tumour of a four-year-old patient was found to be 1.1% [4]. However, the spot scanning presented the lowest risk and there was a lower risk associated with IMRT than with scattering proton therapy for organs close to the treatment area. Infrequently, studies have reported that photon therapy has an advantage over scattering proton therapy regarding the secondary cancers risk. For example, a comparison between scattering proton therapy and IMRT showed that the secondary equivalent dose at 20cm from the field edge of the scattering proton therapy beam was several times greater than that found using IMRT [2]. It was however reported nine years later in 2015 that this study was

"wrongly dose quantified'' and that the comparison must be done under the same conditions. Therefore, it was reported that the secondary dose during scattering proton therapy was significantly lower than IMRT [3].

In addition, Monte Carlo simulations confirmed that the secondary cancers risk from secondary neutrons produced during proton therapy, was low but not negligible. In contrast, the secondary cancers risk when using scattering proton therapy was 6 and 11 times less than modulated and conventional photon therapy respectively. In addition, the secondary cancers risk when using scanning proton therapy was approximately half of those related to scattering proton therapy (i.e. 0.8% and 1.5% respectively) [5] [6]. The secondary cancers risk from scattering proton therapy was 80% dominated by the external neutron source. The estimated risk from a 70Gy brain tumour treatment was found to be small but not negligible (i.e. <1%). Moreover, the risk was of more concern regarding young females and children. There are also concerns regarding the risks of breast cancer. In addition, leukaemia was reported as being the highest risk for adults [7].

- **Estimation of secondary cancers risk from neutrons during proton therapy**

The secondary cancer risk is widely calculated using results found in the BEIR VII report introduced by the National Academy of Science Committee. This report reviewed the data from the after effects of the Japanese-atomic-bomb, laboratory studies, patients treated with radiation and populations living in high radiation background areas. Therefore, the excess relative risks (ERR) of several cancer types were estimated. The ERR is defined as [8]:

$$\mathbf{ERR = (A/B) -1\ (Sv^{-1})}$$

Where, A is exposed population cancer occurrence and B is unexposed population cancer occurrence.

Example of ERR for liver cancer, thyroid cancer and leukaemia are 0.32/Sv, 0.53/Sv and 1.1/Sv. The probability of cancers causation (PCC) is then defined as [8]:

$$\mathbf{PCC = (ERR \times dose)/ (1+ (dose \times ERR))\ (\%)}$$

An MC simulation study showed the risk of developing secondary cancers to be within 2% of delivering a 76Gy therapeutic proton dose during scattering proton therapy treatment of prostate cancer. The highest secondary neutron dose was found to be located near the treatment target [9]. In another study, the risk was estimated for a 10-year-old boy to be 3.4% during the scattering proton therapy treatment of a cranial tumour [10]. Furthermore, it was reported that the secondary cancers risk during a scattering proton therapy treatment of a cranial-spinal tumour was1.2% higher than that of spot scanning. In addition, the risk of developing secondary cancers during the proton treatment of a spinal tumour in an eight-year-old female was 0.71%, 1.05% and 0.6% for the breast, lung and rectum respectively. Moreover, the risk of developing secondary cancers in the lung and rectum was lower for an 11-year-old boy, at 0.32% and 0.43% respectively [6]. The overall risk of producing secondary cancers from the lung treatment using the scattering proton therapy system was found to be 11.1% and 4.7% for a 15 year-old female and male respectively [11]. However, the overall higher rate of secondary cancers risk for females was significantly related to the risk of breast and lung secondary cancers. In addition, the neutron dose assessment of different body organs was significantly affected by patient size and organ location (e.g. the distance from the treated target).

Thus, commonly, the risk of secondary cancers during proton therapy has been highlighted with the scattering proton therapy delivery technique. In addition, the risk of secondary cancers related to photon therapy was rarely reported to be less than that related to proton therapy. For example, it was reported that the secondary neutron dose from passive proton therapy at 20cm from the treated target was found to be several times higher than with IMRT [2].

To conclude, the risk of secondary cancers in proton therapy is low and uncertain because it is related to a low neutron dose. However, the probability of developing secondary cancers increases as the neutron dose increases. Regarding the risk of secondary cancers, there are arguments in favour of scattering proton therapy over photon radiotherapy. However, spot-scanning proton therapy treatment has the lowest risk of secondary cancers compared to both scattering proton radiotherapy and photon (IMRT and conventional) radiotherapy. In addition, the estimation of secondary cancers risk involves converting neutron dose to risk. Moreover, the dose distribution is the basis of the secondary cancers risk estimation.

1.4 Proton interactions with matter

- Ionisation and excitation

A proton's interactions with electrons result in either the direct ionisation of the material atoms (ejection of the orbital electrons) or excitation (rising energy of the orbital electrons). In this kind of interaction, the path of the proton (i.e. heavy charged particle) through the matter remains straight, even though it interacts with electrons, because of the large mass difference between the two particles. The masses of a proton and an electron are 1.6726×10^{-27}kg and 9.1085×10^{-31}kg respectively [8]. Therefore, the maximum transferred energy to a single electron is about 0.00218 of the proton's energy ($4Em_e/m_p$), where E is the proton energy and m_e and m_p are the respective electron and proton masses [12].

Thereby, the proton is slowed down along its path, and a small fraction of its energy is deposited in the matter. The proton's specific ionisation increases along its path. The specific ionisation is the amount of ion pairs produced along the path of the ionisation radiation particles over the unit distance of the path [13]. The ionisation density increases as the proton is slowed down (i.e. there is more proton energy loss per matter thickness) until the maximum is reached at the end of the path, which is called the Bragg peak, where a significant amount of proton energy lost [8]. The significance of proton therapy treatment is the high proton energy deposition at the path end (i.e. the target volume of the proton therapy treatment). Figure 1 shows a Geant4 Monte Carlo simulation of the energy deposition of 60MeV proton particles in water as a function of their depth.

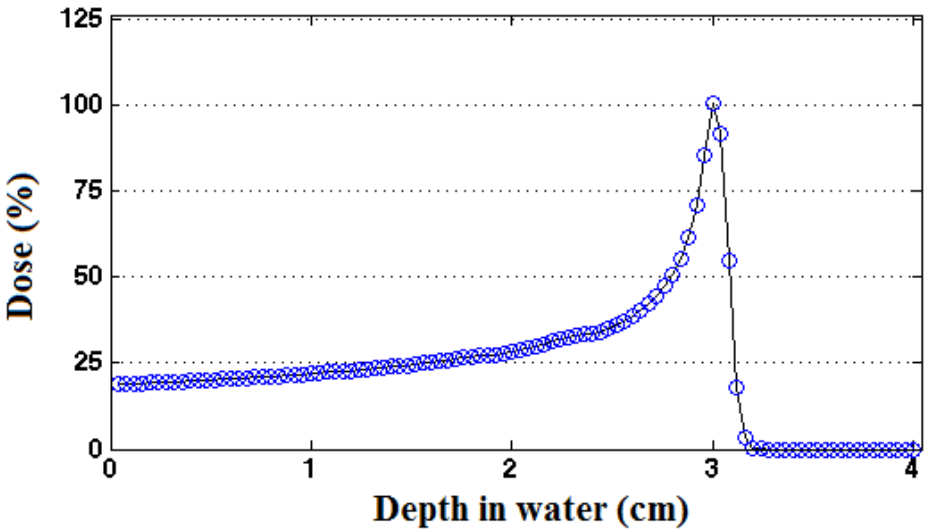

Figure 1: Monte Carlo simulation of the energy deposition of 60MeV proton particles in water as a function of their depth.

- Elastic scattering

The elastic scattering of protons occurs when protons pass near the atomic nuclei of the matter (both the protons and atomic nuclei have positive charges). This type of interaction has been utilised in designing proton therapy scattering delivery systems. Scattering foils are placed on the path of the narrow pencil proton beam to produce a wider field size proton beam [14]. Thus, by inserting a thin slab of material with a high atomic number, the protons are deflected from their initial straight path with a negligible energy loss [15] [14].

The energy loss of protons per material thickness ($-\frac{dE}{dx}$), or material stopping power, is related to the material's atomic number; for example, the proton $-\frac{dE}{dx}$ in water is lower than in lead. The energy loss is expressed by the Bethe-Bloch formula [12]:

$$-\frac{dE}{dx} = \frac{4\pi z^2 e^4}{m_0 v^2} NB$$

$$B = Z\left[\ln\frac{2m_0v^2}{J} - \ln\left(1-\frac{v^2}{c^2}\right) - \frac{v^2}{c^2}\right]$$

Where, v, ze and m_0 are the velocity, charge of the charged particle and the rest mass of electron respectively. Z, N, J and C are the atomic number, the number of density,

the average ionisation and excitation of the absorber and the speed of light respectively.

However, there is a wider proton scattering angle from the scattering of protons on materials with a high atomic number [16]. Figure 2 shows energy loss (MeV) and scattering angle (mRad) of 160MeV protons crossing 1g/cm^2 of different elements as a function of material radiation length[16].

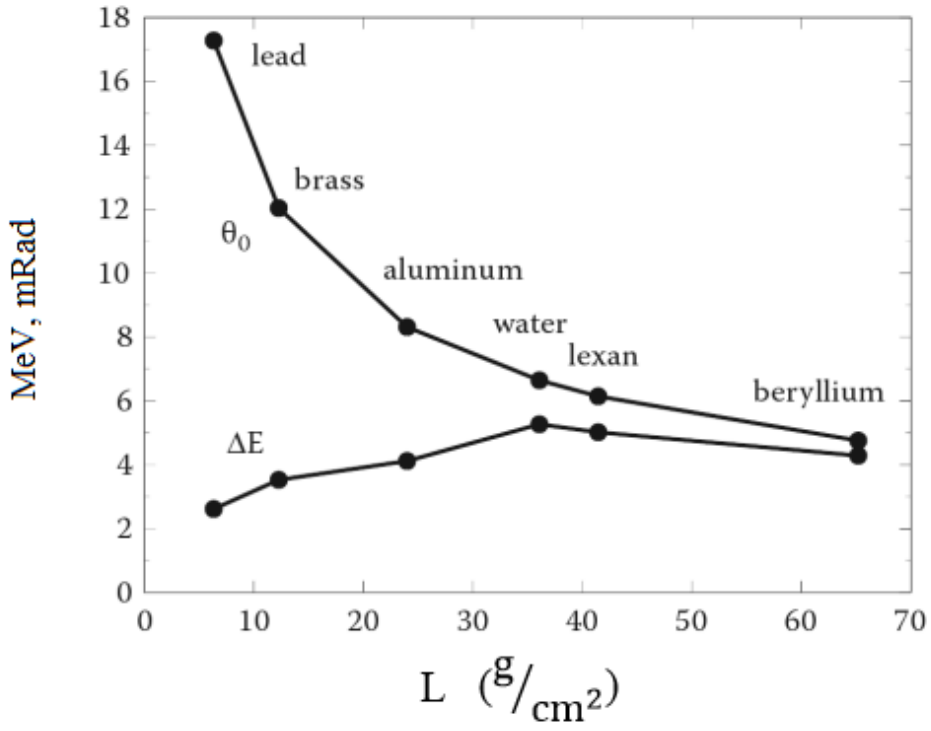

Figure 2: Energy loss (MeV) and scattering angle (mRad) of 160MeV protons crossing 1g/cm^2 of different elements, where L is the radiation length [16]**.**

- Nuclear reactions

Nuclear reactions occur less frequently than ionisation and excitation. In these reactions, the original protons are absorbed by the atomic nuclei of the matter, and secondary particles, such as neutrons and gamma rays, are created [14]. The production of secondary radiation particles (mainly neutrons) could be one of the most highlighted disadvantages of using proton therapy treatment (mainly in scattering proton therapy delivery systems), in addition to the high cost of the construction of the

proton therapy facility and the uncertainties regarding treatment and the proton range [14] [17] [18].

1.5 Neutron interactions with matter

In general, neutrons interact with matter through scattering and nuclear reactions. Neutrons are neutral-charge, indirect-ionisation radiation particles. Usually, neutrons interact with materials' nuclei and the probability of these interactions is called the interaction cross section—for example, the neutron absorption and scattering cross section [19]. The probability of the interaction per nucleus is called the neutron microscopic cross section. The unit of cross section is barn, which equals $10^{-28}\mathrm{m}^2$ (area unit). Moreover, the cross section of all matter nuclei is called the macroscopic cross section, which is the product of the microscopic cross section multiplied by the number of material atoms. Furthermore, the total macroscopic cross section can be obtained by summation of all the macroscopic cross sections, such as the absorption and scattering macroscopic cross section of the material [12]. The following equations show the relation between the macroscopic and microscopic cross sections and the neutron mean free path [12]:

$$\boldsymbol{\Sigma = \sigma \text{ x } n}$$

$$\boldsymbol{\Sigma = \Sigma_{Scattering} + \Sigma_{Apsorbtion} + \cdots}$$

$$\textbf{Neutron mean free path} = \boldsymbol{1/\Sigma}$$

Where Σ, σ and n are total macroscopic cross section, microscopic cross section and number of atoms of the absorber respectively. $\Sigma_{\mathrm{Scattering}}$ and $\Sigma_{\mathrm{Apsorbtion}}$ are the scattering and absorption macroscopic cross sections respectively.

Secondary charged particles, such as electrons, protons and alphas, could be produced from the interactions of neutrons with the nuclei; secondary neutrons could also be produced.

Usually, neutrons are classified with regard to their energies. Several terms have been used to classify neutrons into energy groups. For example, the terms 'intermediate', 'resonance' and 'slow' are used to define neutrons' energy ranges between thermal

and fast [8]. Examples of some of the terms used to classify neutrons into energy groups between thermal and fast energy ranges are shown in Table 1.

Table 1: Examples of terms used to classify neutrons into energy groups between thermal and fast neutron energy ranges.

Classification	Energy range
Thermal	0.025eV [20]
Epithermal	0.5eV to 100keV [20]
Slow	0.025eV to 1eV [21]
Resonance	1eV to 100eV [21]
Intermediate	1eV to 1MeV [21]
Fast	>1MeV [21]

However, the energy ranges of some groups are intersected. In addition, the energy ranges of the same group (i.e. thermal or slow neutrons) are sometimes determined differently. For example, the neutron energy range below 0.5eV was introduced as a slow neutron energy range [12]. In another case, the slow neutron energy range was considered to be below 1eV [21]. Moreover, terms were introduced to define neutron subgroups within the slow energy range (i.e. under 1eV) as 'epithermal', 'cold', 'very cold' and 'ultra-cold'. In contrast, a neutron with an energy range from 0.5eV to 100keV was considered to be epithermal [20]. However, it is difficult to recognise neutron energies below 100keV; hence, they can be considered to be thermal neutrons [22].

The neutron interactions with matter are divided into three categories: thermal, slow and fast.

1.5.1 Thermal and slow neutron interactions

A nuclear reaction occurs when neutrons are captured (absorbed) by the atomic nuclei, and secondary particles, such as protons, electrons and alphas, are released. A high reaction Q value (i.e. in MeV) is produced compared to the initial thermal neutron low kinetic energy (0.025eV).

The scattering of slow neutrons with atomic nuclei transfers insignificant kinetic energy, which is difficult to measure. However, slow neutrons can be captured by the nuclei after they are moderated by scattering. Table 2 shows the most used materials to detect thermal neutrons and their properties [22] [12].

Table 2: The most used materials to detect thermal neutrons and their properties [22] [12].

Isotope	Natural abundance (%)	Reaction	Cross section (barns)	Detectable radiation
$^{155}_{64}$Gd	14.7	n ($^{155}_{64}$Gd, gamma) $^{156}_{64}$Gd	6.1 x 10^4	Gamma-ray spectrum up to 8MeV
$^{157}_{64}$Gd	15.7	n ($^{157}_{64}$Gd, gamma) $^{158}_{64}$Gd	2.6 x 10^5	Gamma-ray spectrum up to 8MeV
$^{10}_{5}$B	19.6	6% n ($^{10}_{5}$B, alpha) $^{7}_{3}$Li (ground state) 94% n ($^{10}_{5}$B, alpha) $^{7}_{3}$Li (excited state)	3.8 x 10^3	Alpha 1.78MeV Alpha (1.47MeV) and gamma rays (478keV)
$^{3}_{2}$He	100	n ($^{3}_{2}$H, proton) $^{3}_{1}$H	5,330	Proton (0.573MeV) $^{3}_{1}$H (0.191MeV)
$^{6}_{3}$Li	7.4	n ($^{6}_{3}$Li, alpha) $^{3}_{1}$H	940	Alpha (2.05MeV) $^{3}_{1}$H (2.73MeV)

1.5.2 Fast neutron interactions

Neutrons captured by atomic nuclei significantly decrease with neutron energy. More significantly, a scattering of fast neutrons by the atomic nuclei occurs where recoil nuclei are produced and neutron energy is moderated (i.e. to be thermal). The scattering of fast neutrons with the atomic nuclei transfers significant kinetic energy, particularly through collision with light nuclei, such as hydrogen and helium, where recoil protons are the significant secondary radiation particles produced [12]. A single neutron collision with hydrogen ($^{1}_{1}$H) can transfer the entire energy of the fast neutron to the recoil proton. The neutron energy transfer is related inversely with the nucleus mass number (collision with heavy nuclei transfers a low neutron energy). The following equation shows the maximum neutron kinetic energy that can be transferred to the target nuclei [12]:

$$\frac{\textbf{Kinetic energy of recoil nucleus}}{\textbf{Kinetic energy of neutron}} = \frac{\mathbf{2A}}{\mathbf{(1+A)^2}}(\mathbf{1} - \mathbf{cos}\,\theta)$$

Where A is target nucleus mass / neutron mass and ɵ is the neutron scattering angle. The equation shows the maximum neutron energy that can be transferred at a scattering angle of 180^0 to the proton target (i.e. hydrogen). Table 3 shows the maximum neutron energy that can be transferred by a single collision with some materials' nuclei [12].

Table 3: The maximum neutron energy that can be transferred by a single collision with materials' nuclei [12].

Isotope	Maximum energy transfer
$^{1}_{1}H$	1
$^{2}_{1}H$	0.889
$^{3}_{2}He$	0.75
$^{4}_{2}H$	0.64
$^{12}_{6}C$	0.284

1.6 Neutron detection and spectroscopy

In general, the required neutron spectrometer has the following properties [23]:

- Low background sensitivity.
- Good energy resolution.
- Wide neutron range response and high efficiency.

Regarding the application in which neutron energy spectrum or neutron counts are needed, neutron detectors are categorised as counters and spectrometers. In general, neutron detectors are based on scattering (recoil nucleus) and neutron-induced nuclear reactions (neutron absorption). Based on neutrons' interactions with matter, several neutron detectors have been designed.

1.6.1 Thermal neutron detectors

Thermal neutron detectors are based on neutron-induced nuclear reactions. The detection materials used always have a high thermal neutron capture cross section, as demonstrated previously in Table 2.

For example, thermal neutrons captured by gadolinium result in gamma rays up to 8MeV and internal conversion (IC) electrons with a discrete electron energy spectrum [24]. The discrete IC electron spectrum is shown in Figure 3.

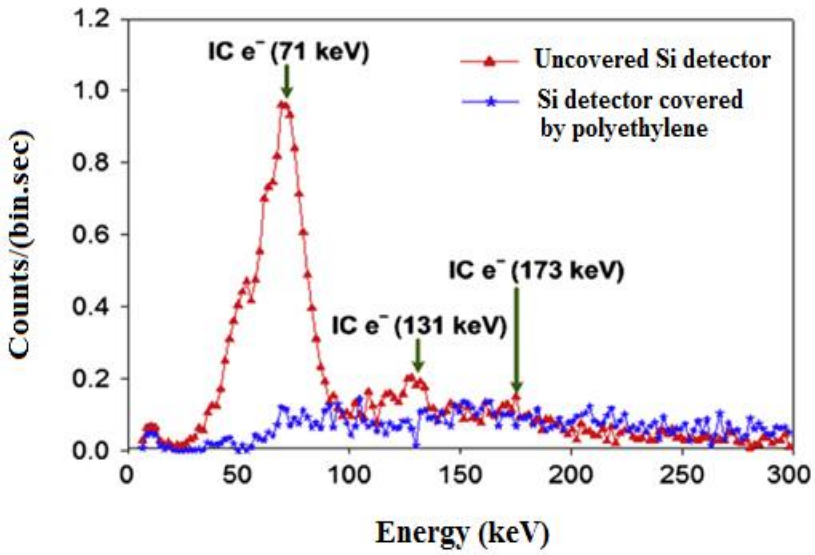

Figure 3: IC electron spectrum from the gadolinium thermal neutron capture reaction [24].

Theoretically, the energy range of the IC is a discrete energy spectrum from 29keV to 246KeV, however, experimentally some of the IC energy peaks cannot be recognised clearly (e.g. IC of 173keV). The IC electrons with 71keV in Figure 3 are the most important product of the gadolinium thermal neutron capture reaction because they are produced at the highest percentage (39%) of the total emitted IC electrons [12] [24]. Thus, the number of detected IC electrons can be utilised to determine the amount of thermal neutrons being captured.

In addition, the designing of thermal neutron counters involves covering the high thermal neutron capture cross-section materials with an efficient fast neutron moderator, such as paraffin, wax or polyethylene.

1.6.2 Fast neutron detection and spectroscopy

Fast neutron counters and spectrometers are based on moderation and neutron-induced nuclear reactions. Fast neutron counters are always based on the moderation of fast neutrons (using fast neutron moderators) to thermal neutrons and a detection material of a high thermal neutron capture cross section.

Fast neutron spectrometers are based on the following methods:

- Non-elastic scattering.
- Moderation.
- Neutron-induced nuclear reactions.

1. Detectors based on non-elastic scattering

Neutron spectrometers are widely based on a neutron non-elastic scattering reaction [25]. Fast neutrons with an energy range from keV to MeV can be recognised through non-elastic scattering (primary neutron energy and direction are changed) using low atomic number materials—for example, organic scintillators (liquid and plastic) and recoil proton telescope neutron spectrometers [26] [27]. The non-elastic scattering of neutrons produces detectable recoil charged nuclei. Then, fast neutrons' energies can be detected through measuring the energies of the recoil charged nuclei. The most commonly used detection material is hydrogen ($^{1}_{1}$H). As shown in Table 3, neutrons can transfer their entire energy to $^{1}_{1}$H nuclei in one collision, regarding their near-equivalency in neutron and $^{1}_{1}$H masses.

2. Detectors based on fast neutron moderation

A fast neutron moderating material can be utilised around the thermal neutron detector to make a fast neutron detector. For example, surrounding a lithium iodide (LiI) thermal neutron detector with different neutron moderator thicknesses is called the Bonner sphere spectrometer (multi-sphere) [12]. The Bonner sphere spectrometer has wide neutron energy response with constant efficiency. It is the only available spectrometer that covers a neutron energy range from thermal to GeV. However, the poor energy resolution and the requirement for complex spectrum unfolding codes are the disadvantages of this kind of spectrometer [28].

3. Detectors based on neutron-induced nuclear reactions

Fast neutron spectroscopy is based on determining the energy of the secondary charged particles that result from fast-neutron and detection-material reactions. The main reactions used for fast neutron spectroscopy are n ($^{3}_{2}$He, p) $^{3}_{1}$H and n ($^{6}_{3}$Li, alpha) $^{3}_{1}$H [23] [12]. The response function of these detectors is a peak equal to the Q value of the reactions plus the incident neutron energy. However, less commonly,

other neutron spectrometers based on a nuclear reaction have been used, such as diamond detectors and threshold activation detectors [29] [30].

The n ($^{3}_{2}$He, p) $^{3}_{1}$H reaction is used for neutron spectrometry with a neutron energy range below 5MeV—for example, $^{3}_{2}$He-proportional counters [31]. In contrast, the n ($^{6}_{3}$Li, alpha) $^{3}_{1}$H reaction is limited in neutron spectroscopy to several keV.

4. Comparisons

Table 4 shows some commercially available neutron detectors based on the previous three neutron detection methods.

Table 4: Examples of available neutron detectors based on scattering, moderation and nuclear reaction methods.

Method	Detector type	Detector Dimension	Response (MeV)	Energy resolution (%)	Detection efficiency (%)	Reference
Non-elastic scattering	Organic scintillator (BC501A)	5inch×5inch	Up to 135	8.5 at 2MeV	64 at 2MeV	[32] [33] [34]
Non-elastic scattering	Gas-recoil proportional counter	–	keV–1MeV	–	<1	[12]
Moderation	Bonner sphere systems (LiI)	–	Thermal to GeV	Poor	Constant	[28] [12]
Nuclear reaction	$^{3}_{2}$He-gridded ionisation chamber	–	0.05–10	2 at 1MeV	0.3 at 1MeV	[25]
Nuclear reaction	Diamond detectors	–	Up to 20	–	–	[29]

Thus, it can be concluded that the optimum neutron detector for detecting secondary neutrons during proton irradiation is an organic scintillator detector. The reason for this is that it has a wide neutron energy range and a low neutron intensity. In addition, $^{3}_{2}$He-proportional counters are preferable for neutron spectroscopy with a neutron energy range below 5MeV, as they have a high energy resolution and a low sensitivity to gamma rays [35].

1.7 Radiation dosimetry

1.7.1 Absorbed dose

Absorbed dose is defined as the amount of radiation energy transferred per unit mass of material. Two units have been introduced, the rad and the gray, to quantify the absorbed dose. 1 gray equals 100 rad (rad is the old absorbed dose unit), and is equal to 1 joule/kg. The absorbed dose can be measured directly by calorimeters; however, indirect absorbed dose detectors are commonly used, such as ionisation chambers and scintillation detectors [12].

1.7.2 Equivalent dose

The term 'dose equivalent' in International Commission on Radiological Protection (ICRP) Publication 26 (1977) was changed to 'equivalent dose' in ICRP Publication 60 (1990). Equivalent dose describes the effectiveness of the absorbed dose on living tissue. Therefore, an equivalent dose (or dose equivalent) is the product of the absorbed dose and the radiation weighting or quality factors, as shown in the following relations [8]:

- Dose equivalent (rem) = absorbed dose (rad) × radiation quality factor.
- Equivalent dose (sievert) = absorbed dose (gray) × radiation weighting factor.

The quality factor is a value introduced by the Nuclear Regulatory Commission (NRC) to describe the ratio of the biological damage from different radiation types to the biological damage from gamma rays. This quality factor was renamed by the ICRP as the 'weighting factor' [8]. ICRP Publication 60 introduced the weighting factor as a function of the energy transfer per unit length in water. Some quality factor values given by the NRC were different from those given by the ICRP. The NRC mentioned the quality factor values of neutrons only up to 0.5MeV, whereas the ICRP mentioned the weighting factor values for a wider neutron energy range. Table 5 shows the radiation weighting and quality factors introduced by the ICRP (Publication 92) and

the NRC (10 CFR Part 20). In addition, radiation weighting factors of neutrons, as reported in ICRP Publication 92, are shown in detail in Table 6 [8].

Table 5: Radiation weighting factors of different radiation types as reported by the ICRP and NRC [8]**.**

Radiation type	Radiation weighting factor (ICRP)	Radiation quality factor (NRC)
Gamma ray	1	1
Proton	5	10
Alpha	20	20
Neutron	5–20	2–11

Table 6: Radiation weighting factors of neutrons reported in ICRP Publication 92 [8]**.**

Energy	Radiation weighting factor
Thermal	5
0.01MeV	10
0.1MeV	10
0.1–2MeV	20
2–20MeV	10
>20MeV	5

However, the continuous neutron energy function, which was proposed by ICRP Publication 92 and endorsed by the ICRP publication 103, was excepted as a better representation of the neutron weighting factors than the previously used step function [36] [37]. The main difference between the two functions was the values of the weighting factor for low neutron energies. Figure 4 shows the continuous and step neutron energy functions, introduced by ICRP (1991, 1992).

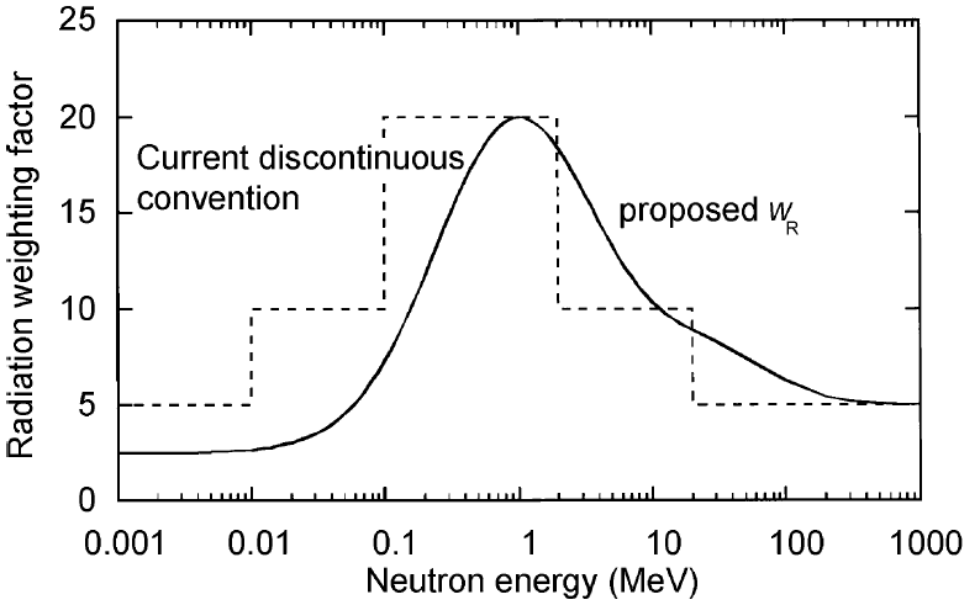

Figure 4: the continuous (i.e. proposed W_R) and step (i.e. Current discontinuous) neutron energy functions, introduced by ICRP (1991, 1992) [37].

Two units have been introduced, rem and sievert (Sv), to quantify the equivalent dose (1Sv equals 100rem, which is the old unit for the equivalent dose). It was reported that the higher the linear energy transfer (LET) radiation, the greater the radiobiological effectiveness [8]. Therefore, the radiation weighting factor was considered to be more for high linear energy transfer (HLET) radiation. For example, the weighting or quality factors of gamma-ray and alpha particles are 1 and 20 respectively. Table 7 shows the radiation quality factor values as a function of the radiation LET [12].

Table 7: Radiation weighting factors as a function of the LET (T) as reported in ICRP Publication 60 [12].

T (keV/μm)	Radiation weighting factor
<10	1
10–100	0.32T – 2.2
>100	$300/\sqrt{T}$

In addition, a quantity called the 'tissue weighting factor' was introduced by the ICRP to describe the sensitivity of different human organs to radiation. This quantity serves to recognise the individual organic radiation dose. The product of the equivalent doses multiplied by the tissue weighting factors (in different organs) is called the effective dose. The summation of all organ tissue weighting factors is 1, where the most

radiation-sensitive organ was given the higher fraction. Table 8 shows examples of tissue weighting factors for different organs reported in ICRP Publications 60 and 26.

Table 8: Examples of tissue weighting factors for different organs as reported in ICRP Publications 60 and 26 [8]**.**

Organ	Tissue weighting factor (ICRP Publication 60)	Tissue weighting factor (ICRP Publication 26)
Gonad	0.20	0.25
Lung	0.12	0.12
Red bone marrow	0.12	0.12
Breast	0.05	0.15
Thyroid	0.05	0.03

1.8 Proton therapy delivery techniques

Radiotherapy treatment was proposed to the medical field in 1946, involving high proton energy deposition at the target volume (i.e. the tumour) compared to low proton energy deposition at the entrance [13]. The first proton therapy treatment was conducted at Lawrence Berkeley National Laboratory, California, USA, in 1954 [38]. The lateral and depth distribution of the proton beam over the target volume is determined by the proton therapy delivery technique. Passive (scattering) and active or dynamic (scanning) are two methods used to deliver the proton dose to the entirety of the target volume [16].

1.8.1 Proton therapy delivery technique using scatterers

Generally, proton beam delivery systems using scatterers (scattering proton therapy systems) have the same components, but the arrangement may be different [39]. Depending on whether one or two scatterers are used, the scattering proton therapy is called either a single- or double-scattering system. The proton beam generated from the accelerator and entering the proton therapy room is usually a narrow pencil beam with a particular energy value. The proton beam, travelling through the scattering beam line components, is undergoing two stages. The first stage is the spreading and flattening of the initial narrow pencil proton beam; the second is the modulating or shaping of the beam to cover the target volume (lateral, distal and deep proton beam

distribution) [40] [15]. For example, figure 5 shows a schematic of the double-scattering proton therapy beam line geometry at Clatterbridge Hospital [41].

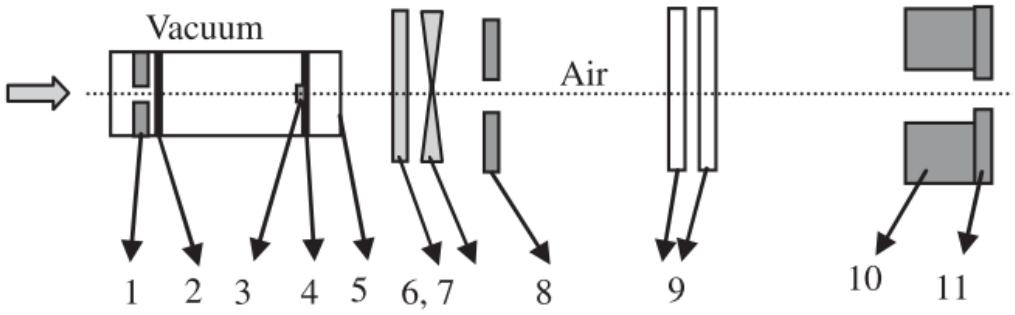

Figure 5: The schematic of the double-scattering beam line geometry at Clatterbridge Hospital. collimators (1, 8 and 11), central stopper (3), scattering foils (2 and 4), range shifter (6), modulator wheel (7), monitor chambers (9) and nozzle (10) [41].

Proton beam shaping

a. Proton beam spreading and flattening

- Scatterers

A scatterer, or scattering foil, is a disc of metal that can have different thicknesses (i.e. straight or step thickness) and is usually made of a high atomic number material such as tantalum, lead or tungsten. In addition, it can be made of a combination of two materials, usually with one material having a high atomic number [40]. Scatterers are used to spread the initial narrow field size proton beam to a useful wide field size [15]. Regarding the required beam field size, double scatterers are used. The first scatterer (straight disc) provides a Gaussian-shape proton beam distribution, whereas the second scatterer (step-thickness disc) provides a flat, uniform proton beam distribution [42] [15].

b. Proton beam modulation

- Modulator wheel

The modulation of the intensity and range of the Bragg peak is called the 'spread-out Bragg peak' (SOBP). The modulation can be done by using a rotating step-thickness absorber wheel, which is the modulator wheel. Usually, a modulator wheel is made of a low atomic number material, such as poly(methyl methacrylate) (PMMA), polycarbonate, or aluminium [43]. Figure 6 shows examples of the modulator wheel designs, whereas Figure 7 shows the SOBP.

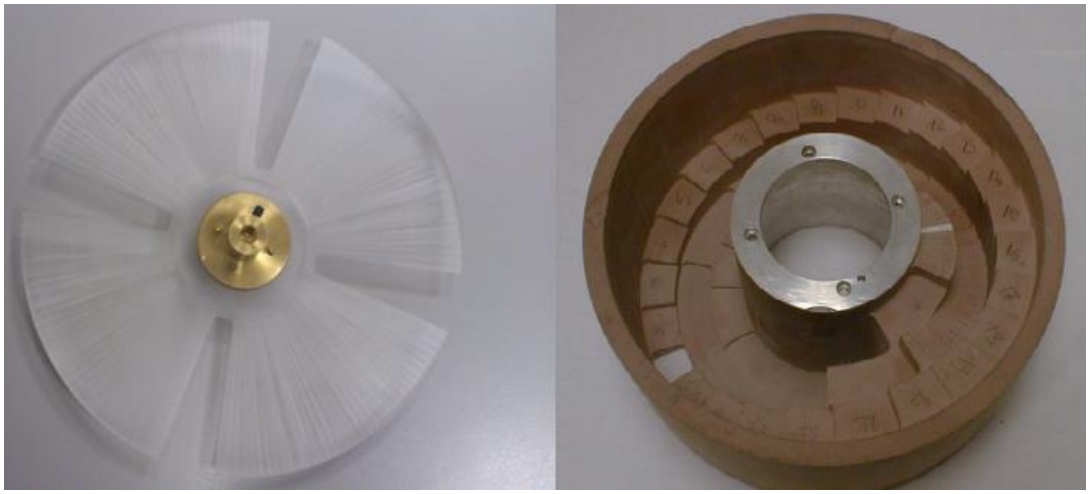

Figure 6: Examples of modulator wheel designs [43] [44]**.**

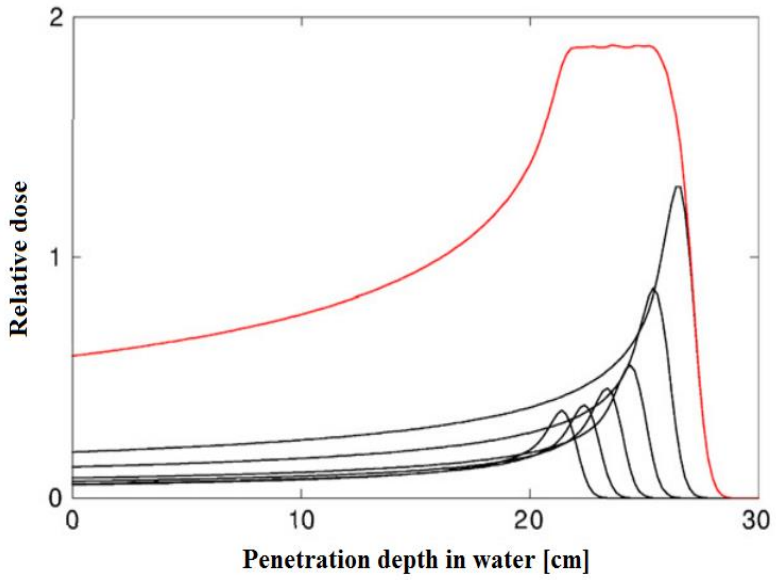

Figure 7: SOBP [45].

A modulator is used to distribute the proton beam deeply and to cover the target volume. Alternatively, the SOBP can be achieved using a ridge filter or variable proton beam energies with different intensities extracted from a cyclotron [45]. However, usually the proton beam is extracted with a fixed proton beam energy and intensity from the cyclotron [46] [43]. The SOBP peaks shown in figure 7 was a "cumulative total of six beam pulses''. The proton energy (i.e. monoenergetic proton) was modulated (e.g. using modulator wheel) in depth to produce variable energies (i.e. multiple energies) across the entire treated target [47] .

- Range compensators

Range compensators are usually made of low atomic number and high-density materials to increase the ratio of proton beam absorption to scattering, such as Lucite [48]. Range compensators are used to shape the distal proton beam fall-off to be similar to the target distal surface. The shape of the compensator is specifically made for the particular patient being treated in terms of the treatment target's distal shape [49].

- Apertures

Usually, alloys or single materials are used to make the apertures—for example, lead, brass or Cerrobend. The aperture is used to determine the lateral profile of the proton beam. Therefore, it blocks the proton beam laterally, which is similar to the purpose of the collimator [50]. However, the shape of the aperture is patient-specific in terms of the treatment target's lateral shape [49]. Figure 8 shows an example of aperture and range compensator designs.

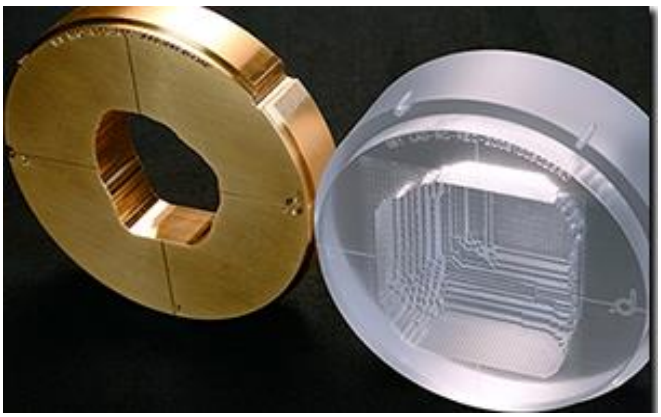

Figure 8: Example of aperture and range compensator designs [51].

1.8.2 Proton therapy delivery techniques using a magnet

- **Pencil proton therapy delivery technique**

In the pencil or the spot-scanning beam delivery technique, the initial extracted narrow proton beam is distributed over the entirety of the target using magnets. The magnets direct the proton beam from one position to another throughout the target volume. The shaping devices, such as scatterers, collimators and range compensators, are not used in spot-scanning delivery systems [52]. For, example figure 9 shows a schematic of the spot-scanning beam line geometry at the MD Anderson proton therapy centre [53].

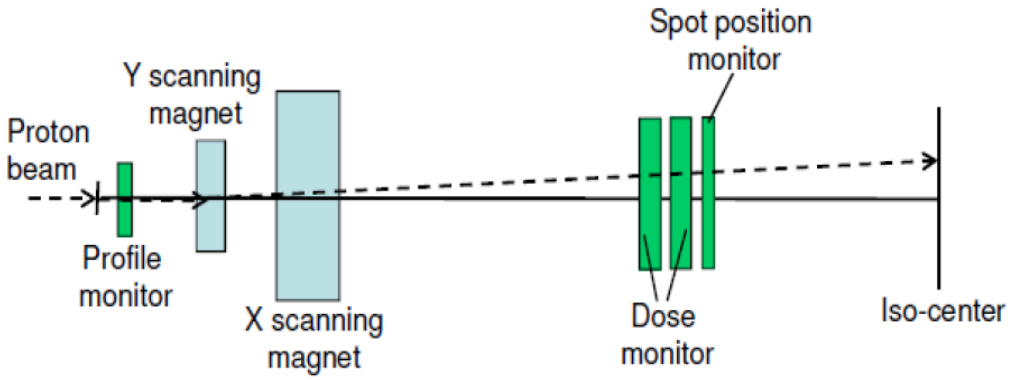

Figure 9: A schematic of the spot-scanning proton beam line geometry at the MD Anderson proton therapy centre [53]**.**

- **Wobbling proton therapy delivery technique**

In contrast to the scattering proton therapy system, the initial narrow pencil proton beam can be widened using wobble magnets. The scattering materials on the proton beam track are eliminated, unlike with the scattering proton therapy system [54]. Instead, compensators and collimators are used in the wobbling proton therapy delivery technique [55] [56]. Figure 10 shows a diagram of a wobbling proton delivery system.

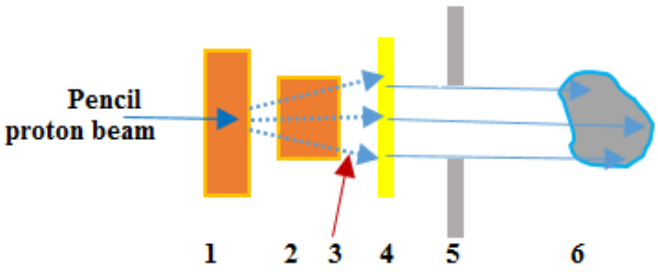

Figure 10: Diagram of a wobbling proton delivery system. Wobble magnets (1 and 2), deflected proton beam (3), modulator wheel (4), collimator (5), and irregular target (6).

1.9 Neutron dose assessment during proton therapy

1.9.1 Neutron production

- Scattering delivery technique

During the delivery of scattering proton therapy, in order to deliver a useful, uniform, flat proton beam to the target volume, the initial narrow pencil proton beam needs to be converted to a wide, flat and uniform proton beam profile, which is the beam-spreading process. This is done by using high atomic number materials (scatterers). In addition, the proton beam needs to be modulated to cover the whole target volume. During proton beam spreading and modulating, the proton particles interact with the beam treatment head materials located in the proton beam path. Thereby, secondary neutrons are generated from these interactions (external neutron source). In addition, the interaction of the proton particles with the target volume is another source of secondary neutrons (internal neutron source) [57].

The energy range of the neutrons produced was reported to be from thermal to fast, with a maximum energy equal to the proton therapy energy [58]. Although it has been agreed that the external neutron production is dominant in terms of the neutron dose, the dominant component (i.e. scatterer, modulation wheel, or final collimator) was debated [1] [6] [59]. For example, Table 9 shows an example of studies reporting the dominant component for the secondary neutron dose during scattering proton therapy treatment.

Table 9: Dominant component for the neutron dose during scattering proton therapy treatment.

Location	Dominant external neutron dose	Method (MC or measured)
Midwest Proton Radiotherapy Institute [60]	Scatterers and range modulator	Measured
Massachusetts General Hospital [61]	Final collimator	MC simulation
MD Anderson Proton Therapy Center [50]	Modulation wheel and final collimator	MC simulation
MD Anderson Proton Therapy Center [62]	Increased with modulation, snout size, proton energy, and aperture closure	Measured
Massachusetts General Hospital [63]	Aperture and modulation wheel	MC simulation

It can be concluded from Table 9 that the dominant component for the neutron dose during proton therapy treatment has three overall specifications, which are the following:

1. The highest (or high) atomic number.
2. The nearest (or near) to the patient's location.
3. The highest (or high) interception with the proton beam; for example, the neutron dose increased significantly (four times) from 2mSv/Gy to 8mSv/Gy without and with a modulator (15cm thickness) respectively [58]. In addition, the neutron dose increased significantly (three times) from 0.6mSv/Gy to 1.8mSv/Gy without and with an aperture (13cm thickness) respectively [64].

- Spot-scanning delivery technique

The neutron production during the spot-scanning delivery technique was reported to be significantly low compared to the scattering delivery technique, because of the absence of proton beam shaping devices such as scatterers, collimators and compensators [52]. Therefore, the dominant neutron source was the internal neutrons generated inside the target volume. During spot scanning, neutrons are generated in the target volume, from thermal to the maximum proton energy [65].

In contrast, compensators and collimators are used in wobbling proton therapy systems. Therefore, the neutron production from the wobbling proton therapy system is higher compared to that of the spot-scanning proton therapy system [66] [56]. The neutron dose from the wobbling proton therapy system, using a multileaf collimator (MLC), compensator, and aperture, was reported to be four times higher than that of the spot-scanning proton therapy system [66].

Thus, the neutron dose assessment during proton therapy depends strongly on the proton therapy delivery technique (scattering, wobbling or scanning) and the proton beam line configurations, as does the measurement geometry, such as the neutron dose measurement as a function of distance and angle [67]. Furthermore, the method used, such as MC simulations or a clinical neutron dose assessment, makes a difference [68] [69] [70].

1.9.2 Comparisons and discussion of the neutron dose assessment

Table 10 shows the neutron equivalent dose (location1 and location2) and the effective dose or integral equivalent dose (if mentioned) during the use of the proton therapy scattering system. Two locations were chosen because most of the MC simulation and measured neutron dose results were obtained as a function of the distance (e.g. location1 and location2) from the proton therapy beam axis. In addition, other parameters, such as the angle to the proton beam axis, could be changed.

Table 10: Neutron equivalent doses at location1 and location2 (i.e. distance from the proton therapy beam axis) and the effective neutron or integral equivalent dose (mSv/Gy) during scattering proton therapy.

Institute	Proton energy (MeV)	Neutron dose (mSv/Gy) at location1	Neutron dose(mSv/Gy) at location2	Effective dose (mSv/Gy) and target	Method (MC or measured)
Massachusetts General Hospital [1]	177	2–3 at 10cm	0.02 at 50cm	0.48mSv/Gy in Alderson–Rando phantom	Measured (PADC or CR-39)
MD Proton Treatment and Research Center [64]	225	3.9 at 2.5cm	0.18 at 60cm	– Anthropomorphic phantom	Measured (SOI)
Proton Therapy Center, National Cancer Center, Republic of Korea [71]	–	0.17 at 20cm	0.086 at 50 cm	– Solid phantom	Measured (CR-39)
MD Anderson Proton Therapy Center [9]	250	12 at a few cm	1.9 at several cm	5.5mSv/Gy in simulated Anthropomorphic phantom	MC simulation (MCNPX)
Harvard Cyclotron Laboratory [58]	158	6.3 at 50cm and 90°	2.3 50cm and 0°	– Simulated Lucite phantom	MC simulation (MCNPX)

It can be noted from Table 10 that, in general, the MC simulation results were higher than the measured results. However, the limitations of the measurements, such as using a realistic human-body phantom and the difficulty of measuring the neutron dose, could be the reasons behind the underestimation of the measurement results.

Thereby, it was found that the amount of MC simulation studies to assess neutron dose during proton therapy was higher than that of practical measurements. The reasons for this are likely to be the following:

- The difficulty of neutron detection in a high gamma-ray background.

- The difficulty and complexity of constructing realistic human-body phantoms [72].
- Most of the measured neutron doses were obtained in terms of the distance from the proton therapy beam axis. The MC simulations give better neutron dose distribution results for body organs [72].
- The dose distribution, or localised dose, is the basis of the risk estimation from radiation induced secondary cancers [72].

In addition, the neutron dose strongly depends on the proton therapy beam configurations, and the distance from, and angle to, the proton beam target or proton beam axis. Neutron dose assessment during scattering proton therapy is at the maximum in these conditions:

- At the closest points to the primary proton beam.
- With more blocked proton therapy beam configurations.
- With more proton therapy energy.

For example, the neutron dose was assessed for paediatric and adult patients during brain tumour proton therapy. It was found that the neutron doses to the different body organs strongly depended on the patient's age and organ location (body size and distance from the central proton beam), and the proton beam configurations (field size, proton energy and beam modulation). The neutron dose increased with proton energy and range modulation. In contrast, it decreased with distance and field size [72].

It has been reported that proton therapy delivers a smaller secondary radiation dose compared to photon therapy [73] [71]. In addition, the neutron dose during spot-scanning proton therapy is significantly smaller than that during scattering proton therapy (i.e. less than a tenth at 10cm from the spot-scanning proton therapy beam axis [52]) [16] [1] [74] [75] [2]. This is a result of the elimination of the proton beam blocking devices (i.e. scatterers, the modulation wheel, and compensators).

Therefore, the distance from the proton beam axis and the proton energy are the only factors that affect the neutron dose assessment during spot-scanning proton therapy. Table 11 shows the neutron doses (location1 and location2) and the effective dose or equivalent dose (if mentioned) during the spot-scanning proton therapy treatment.

Table 11: Neutron equivalent dose (location1), neutron dose (location2), and the effective neutron or equivalent dose (mSv/Gy) during spot-scanning proton therapy treatment.

Institute	Proton energy (MeV)	Neutron dose (mSv/Gy) at location1	Neutron dose (mSv/Gy) at location2	Effective dose or integral equivalent dose(mSv/Gy) and the target	Method (MC or measured)
Paul Scherrer Institut (PSI) [1]	177	2–3 (below 10cm)	>0.001 (over 50cm)	Effective dose was 0.35mSv/Gy in Alderson–Rando phantom	Measured (PADC)
Westdeutsches Protonentherapiezentrum Essen [76]	226	–	–	Equivalent dose was 0.38mSv/Gy at polystyrene phantom surface	Measured (TLD-700 and TLD-500)
Paul Scherrer Institut [52]	177	3.6 (10cm at 120˚)	0.9 (10cm at 0˚)	Equivalent dose was 2mSv/Gy in water phantom	MC simulation (FLUKA)
Samsung Medical Center, Korea [66]	230	• SSPT • SSPT* • WPT	–	Equivalent doses were • 0.492mSv/Gy • 0.351mSv/Gy • 3.13mSv/Gy In water phantom	MC simulation (MCNPX)

- SSPT is spot-scanning proton therapy without MLC and aperture.
- SSPT* is spot-scanning proton therapy with MLC and aperture.
- WPT is wobbling proton therapy with MLC, compensator, and aperture.

It can be recognised from Tables 10 and 11 that, in general, the integral neutron dose during proton therapy was reported to be below 1% of the prescribed proton dose (below 10mS/Gy). In addition, the neutron dose during spot-scanning proton therapy is significantly lower than that during scattering proton therapy.

In addition, the amount of measurements and MC simulations performed to assess the neutron dose during spot-scanning proton therapy was significantly smaller than the results obtained from scattering proton therapy. The reasons for this could be the following:

- The difference in the start time and the widespread usage between the scattering and spot-scanning proton therapy systems.
- The current MC simulation and measured results show that the internal neutron dose is significantly lower than the external neutron dose during proton therapy. Therefore, the neutron dose from spot-scanning proton therapy (internal neutron dose only) is significantly smaller than that from scattering proton therapy (both external and internal neutron doses) [52]. Thereby, the

neutron dose was considered to be negligible during spot-scanning proton therapy [1] [6] [59] [77] [78].

- The difficultly of in vivo measurements (i.e. the absence of more realistic human-body phantoms). In addition, the difficulty in neutron dose measurement in a mixed neutron-gamma radiation field.

However, the neutron dose to healthy tissue near the target could be the same for both spot-scanning and scattering proton therapy. The neutron dose at a few centimetres (<5cm) from the target during spot-scanning proton therapy was reported to be comparable to the dose from scattering proton therapy [1]. The reason for this was that, near the treatment target, the dominant source of neutrons was the internal neutrons generated inside the target volume. However, it was reported that 92.3% of the absorbed dose—at 2.5cm from the target of the pencil beam during scanning proton therapy—was due to scattered protons, and using patient-specific apertures reduced the dose to a tenth [79]. In addition, it was reported that the contribution of the internal neutrons was more than 40%, near to the treatment target [9]. Figure 11 shows the measured results of the neutron dose per proton treatment dose from spot-scanning proton therapy, scattering proton therapy, and IMRT as a function of the distance from the proton therapy and the photon therapy beam axes[1].

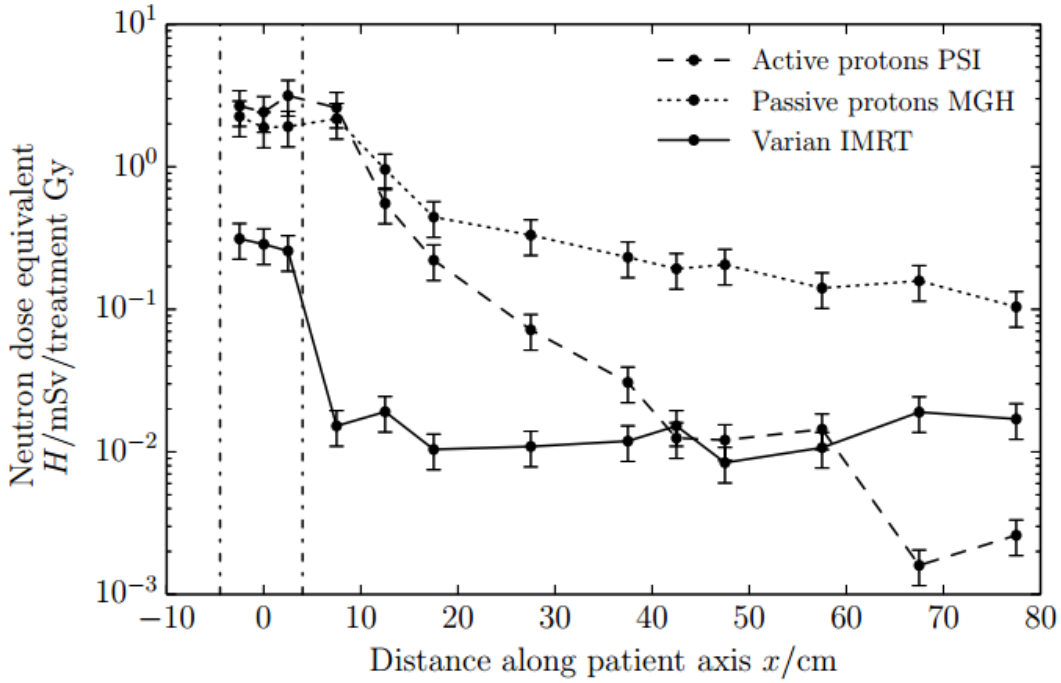

Figure 11: Neutron dose per treatment dose from active and passive proton therapy and photon IMRT as a function of the distance from the proton therapy and the photon therapy beam axes The two vertical dotted lines indicate the target borders [1].

Figure 11 confirms that the neutron dose at a few centimetres (<5cm) from the treatment target for both spot-scanning and scattering proton therapy is approximately the same. In addition, the neuron dose from Varian IMRT was low compared to that produced by the proton therapy delivery systems (i.e. PSI and MGH). The IMRT neutron dose decreased exponentially from 0.2mSv/Gy (i.e. 200µSv/Gy) to 0.01mSv/Gy (i.e. 10µSv/Gy), which corresponded to the attenuation at 20cm from the target border at the detector. Then it appeared to be steady. The reason for this is due to the neutron dosimeter used, which was PADC (allyl diglycol carbonate). Using a PADC dosimeter and Cf^{252} neutron source, the lowest detectable neutron dose was reported to be 153µSv. Therefore, it cannot reliably measure dose lower than this value [80].

The internal neutron dose is unavoidable, whereas the external neutron dose can be minimised—for example, through using an effective neutron moderator (shield) around the dominant component of neutron production in the proton therapy treatment head (i.e. around the brass collimator [81]).

Chapter 2. Prototype neutron detector designs

2.1 Introduction and overview

Based on neutron energy and its interactions with matter, several detectors have been designed. Thermal neutron detectors are designed to detect the charged particles produced by thermal neutron capture reactions [82]. Fast neutron counters are based on fast neutron moderation and detecting the charged particles produced by thermal neutron capture reactions. Fast neutron spectrometers are designed to detect the charged particles produced by nuclear reactions and fast neutron scattering, such as H-3 filled proportional counters and organic liquid scintillator (OLS) detectors respectively [35] [83]. Therefore, in order to design a neutron detector, the main questions are:

1. What is the required energy response of the neutron detector?
2. What is the required neutron detector efficiency and energy resolution?
3. What is the ability of the detection material to distinguish between different radiation types?

Regarding the first and second questions, during proton therapy, the neutron energy spectrum was found to be within an energy range of thermal to the maximum proton therapy energy possible [84]. Therefore, the required detector energy response varied according to different proton therapy facilities. The estimated secondary neutron spectrum energy range in the proton therapy room at Clatterbridge Hospital is from thermal to 60MeV. The detector efficiency and energy resolution are determined by the detection material, the type and energy range of radiation, and the detector design [12].

Regarding the third question, the proton therapy environment was found to be a mixed radiation field that contained significant amounts of neutrons and gamma rays [64] [85]. Therefore, the detection material should have an excellent ability to distinguish between these radiation types. Thus, the neutron detector in a proton therapy room should have the ability to show details of a full neutron energy spectrum in a mixed radiation field.

In order to design a neutron detector that is efficient enough to detect secondary neutrons and to show the secondary neutron energy spectrum during the mixed radiation field of the proton therapy environment, the following aspects were considered.

Firstly, the physical and clinical criteria for a neutron detector in a proton therapy room were noted. The physical criteria are the required neutron detector properties that relate to the detection material and devices, whereas the clinical criteria are the required neutron detector properties relating to the proton therapy facility.

Physically, organic scintillators can be liquid or plastic (pure or loaded). The ability to distinguish between different radiation particles with an OLS is superior as compared to an organic plastic scintillator [86]. Moreover, loading the OLS with high cross sections of thermal neutron capture material allows the detection of thermal neutrons [87]. Thus, one of the commercially available loaded OLSs will be selected to be the detection material for this study. The prototype neutron detector design was examined through four stages, which were the first, second, third and fourth designs.

The first, second and third prototype detector designs were constructed based on a gadolinium-loaded OLS (EJ-331) and a 9939B EMI photomultiplier tube (PMT). In the first, second and third designs, only the cell of the detection material was changed (Teflon 9cm x 20cm, glass 5.3cm x 5cm, and white plastic 5.3cm x 5cm respectively), while the instruments—oscilloscope, MCA, shaping amplifier, cables and PMT—remained the same.

Secondly, in order to validate the fourth prototype detector design, an MC simulation was used as a guideline when constructing the neutron detector. The MC simulation was used to validate the design of the radiation detector, to plan experiments and to analyse the simulated data [88] [89] [90] [91].

Thirdly, the fourth prototype detector design was constructed based on EJ-331 and a 9305KB PMT. The liquid container was cylindrical, measuring 10cm x 10cm in diameter and length, and the inside walls were painted with an adhesive light reflector (EJ-520). Then, the detector was tested and calibrated.

Finally, the design of the fourth prototype detector was judged to have met the physical and clinical criteria, and was considered to be efficient in detecting neutrons and

gamma rays in the proton therapy room. In addition, it can be used in other mixed neutron and gamma radiation fields.

2.2 Aim and objectives

The neutron detector was designed taking into account the physical and clinical criteria for a neutron detector to be used in a proton therapy room. Even though, commercially, an adequate neutron detector could be found, the selection of detector size and specific detection material, in addition to keeping the cost low, would be difficult. Moreover, the preparation of the detection material, in terms of dissolved oxygen elimination, and the specific selection of a scintillation light reflector would need to be done carefully. The aim was to build an efficient neutron detector to be used in a proton therapy room, particularly to be used in in the proton therapy room at Clatterbridge Hospital.

The objectives of building four prototype neutron detectors will be discussed under the following subject's titles:

- First prototype neutron detector design.
- Second prototype neutron detector design.
- Third prototype neutron detector design.
- Fourth prototype neutron detector design.

2.3 Criteria for a neutron detector in a proton therapy room

2.3.1 Physical requirements

1. Detection material and scintillation efficiency

Neutron detectors that are to be used in a proton therapy room are designed taking into account their ability to distinguish secondary neutrons from gamma rays, and to detect neutrons with an energy range from thermal to the maximum proton therapy energy. In general, OLS detectors are the most popular detection materials used for neutron detection and spectroscopy [34]. An OLS can detect neutrons with a wide energy range (from keV to MeV) without surrounding the detector with neutron-moderating materials, such as paraffin or polyethylene [25]. It is superior in PSD (i.e. neutron and gamma pulses can be easily differentiated) [92]. In addition to fast neutron detection, thermal neutron detection can be provided by loading the OLS (up to 1.5% by weight) with materials of a high thermal neutron capture cross section, such as gadolinium, lithium and boron. This type of OLS is called a loaded OLS, such as the EJ-331, NE-323 and BC-521 [12].

The properties required by a loaded OLS to perform as an optimum neutron detection material are [12]:

- Must have adequate neutron detection efficiency with a wide energy range response (from thermal to fast neutrons).
- Must have excellent light transparency and fast scintillation light lifetime. This is to prevent self-absorption of light and delay in the output signals.
- Must have a refractive index that is near to the refractive index of the glass, which is 1.5. This is important to prevent loss of scintillation light due to the different refractive indexes of the materials.
- Must have adequate scintillation efficiency (>50% of anthracene light output) with high linearity (light photons/MeV).

A. OLS scintillation efficiency

Most of the deposited radiation energy in organic scintillators is converted into non-radioactive forms, mainly into heat and lattice vibrations. The amount of light photons produced per unit of deposited radiation energy is called the scintillation efficiency (light photons/MeV). The amount of light photons produced is based on the type and energy of the incident radiation particles [12]. For example, the number of scintillation photons produced from neutron interaction (i.e. recoil protons) is several times lower than that produced by gamma-ray interaction (i.e. recoil electrons) [12]. OLS scintillation efficiency is commonly described as a fraction of anthracene scintillation efficiency (~15,200 light photons/deposited MeV [93]), which has the highest scintillation light yield among all organic scintillator detectors [12].

Thus, the detection material used as the active volume of the neutron detector should produce sufficient scintillation light to recognise the incident radiation particles (i.e. by using a PMT. Table 12 shows the scintillation efficiencies of some commercially available loaded OLS detection materials, which are commonly within the range of 65 to 68% of anthracene scintillation efficiency.

Table 12: Scintillation efficiencies of some commercially available loaded OLS detectors.

Loaded OLS	Scintillation efficiency
Gadolinium-loaded OLS (EJ-331, BC-512 and NE-323)	68% of anthracene
Boron-loaded OLS (EJ-339, BC-523A and NE-321A)	65% of anthracene

B. Detection efficiency

Detection efficiency is classified into two categories: absolute and intrinsic. The absolute detection efficiency is the number of recorded radiation particles over the total number of source-emitted radiation particles, whereas intrinsic detection efficiency is defined as the number of recorded radiation particles over the number of incident particles on the detector.

Intrinsic detection efficiency is much more suitable to be measured, as it does not depend on measurement geometry. The intrinsic detection efficiency of the neutron

detector was determined by the type and energy of the incident radiation particles, and by the detection material's type and volume [12].

In a proton therapy room, thermal neutrons, fast neutrons, gamma rays and heavy charged particles are produced from interactions between the primary protons and heavy materials within the treatment head (scattering proton therapy systems) [94]. Thermal neutrons, fast neutrons and gamma rays are significant types of radiation that could reach the detector's active volume. However, the contribution of fast neutrons to the total secondary radiation dose was found to be approximately 90% [95]. A secondary neutron dose during proton therapy is the only concern in terms of the additional, unwanted radiation to healthy tissue [2] [72]. Therefore, fast neutron detection efficiency is an important criterion for a neutron detector.

Detection materials with low mass are the most convenient materials to use as neutron detection materials, such as OLS detectors. These materials have excellent neutron detection efficiency, as well as low gamma-ray detection efficiency.

In a proton therapy room, the secondary neutron energy spectrum is different for different proton beam facilities with regard to the maximum proton therapy energy [58] [96]. Thus, the selected OLS volume should be able to detect the maximum secondary neutron energy. However, larger OLS dimensions would significantly increase detection efficiency. For example, the calculated detection efficiency of EJ-331 exposed to 60MeV neutron energy improved from (18±1) % to (33±1.4) % by increasing the OLS length from 5cm to 10cm. Figure 12 shows neutron detection efficiency as a function of detection material thickness for 60MeV neutrons. In addition, figure 13 shows hydrogen and carbon total neutron cross sections, up to 20MeV (i.e. ENDF data) [97].

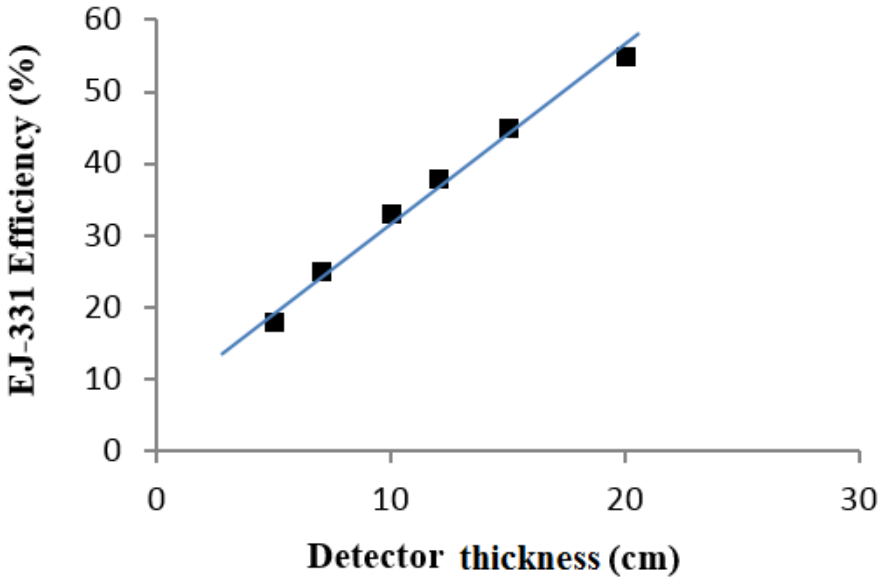

Figure 12: Calculated neutron detection efficiency as a function of detector thickness for 60MeV neutrons.

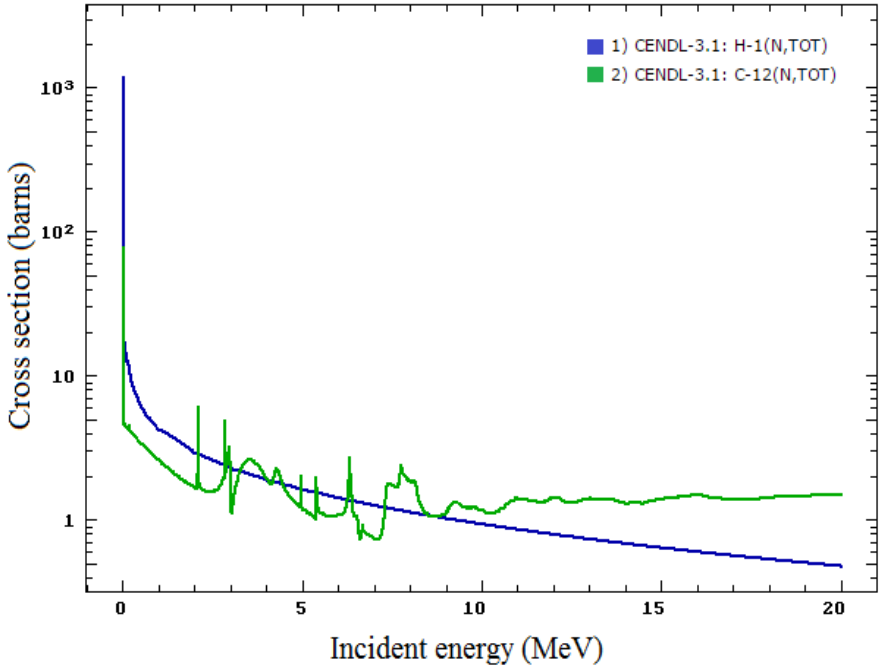

Figure 13: Hydrogen and carbon total neutron cross sections, up to 20MeV (ENDF data) [97].

C. Detector energy resolution

Energy resolution is defined as the full width at half maximum (FWHM) over the centre value of the energy peak (peak centroid). It reflects the ability of radiation detectors to separate close energy peaks.

The energy resolution of the scintillation detectors (i.e. pulse height resolution) is a result of the fluctuation of the scintillation photons over the radiation energy peak. This fluctuation is determined by three parameters related to the detector's design and detection material. The first parameter is the variation in the scintillation photon production per deposited radiation energy (photons/MeV). The second parameter is the probability that the scintillation photons reach the light-to-electron convertors (i.e. the photocathode of the PMTs or the silicon diodes). The third parameter is the variation in the amount of photoelectrons emitted from the light-to-electron convertor (i.e. the photocathode of the PMT) [53]. The first parameter is based on the natural characteristics of the detection material, while the second and third parameters are related to detector design (i.e. light reflector) and the light-to-electron convertor's properties respectively. Thus, the energy resolution of the scintillation detector is a result of the overall specifications of the detection system.

The energy resolution of inorganic scintillators, for instance caesium iodide (CsI) and sodium iodide (NaI), was found to be within 3% to 10% at Cs^{137} photopeak energy (i.e. 662keV), while it was 16% to 20% for organic scintillators at Cs^{137} Compton edge energy (i.e. 477keV) [99] [12] [100] [101] [33].

D. OLS pulse shape discrimination

According to the mixed radiation field of proton therapy, the neutron detector should have the ability to distinguish between radiation particles. The difference between neutron and gamma-ray pulse shapes produced by the OLS can be analysed by an efficient PSD method. PSD was applied extensively using two popular methods: the charge comparison PSD method and the rise time PSD method. The PSD methods using the OLS will be covered in detail in Chapter 3.

E. Dissolved oxygen elimination

The reported experimental and theoretical results showed that dissolved oxygen in the OLS increased light absorption (by decreasing light attenuation length), and decreased the scintillation light yield by approximately 30% and altered the scintillation signal's shape [102] [103] [104]. This makes the PSD inefficient for discriminating gamma rays from neutrons [105] [106]. Thus, releasing dissolved oxygen from the OLS is an important requirement for a neutron detector. Figure 14 shows the oxygen releasing factor (f_Q), which is the ratio of the light yield from an OLS containing oxygen to an OLS oxygen-free sample as a function of the nitrogen gas bubbling time of the OLS containing oxygen [107].

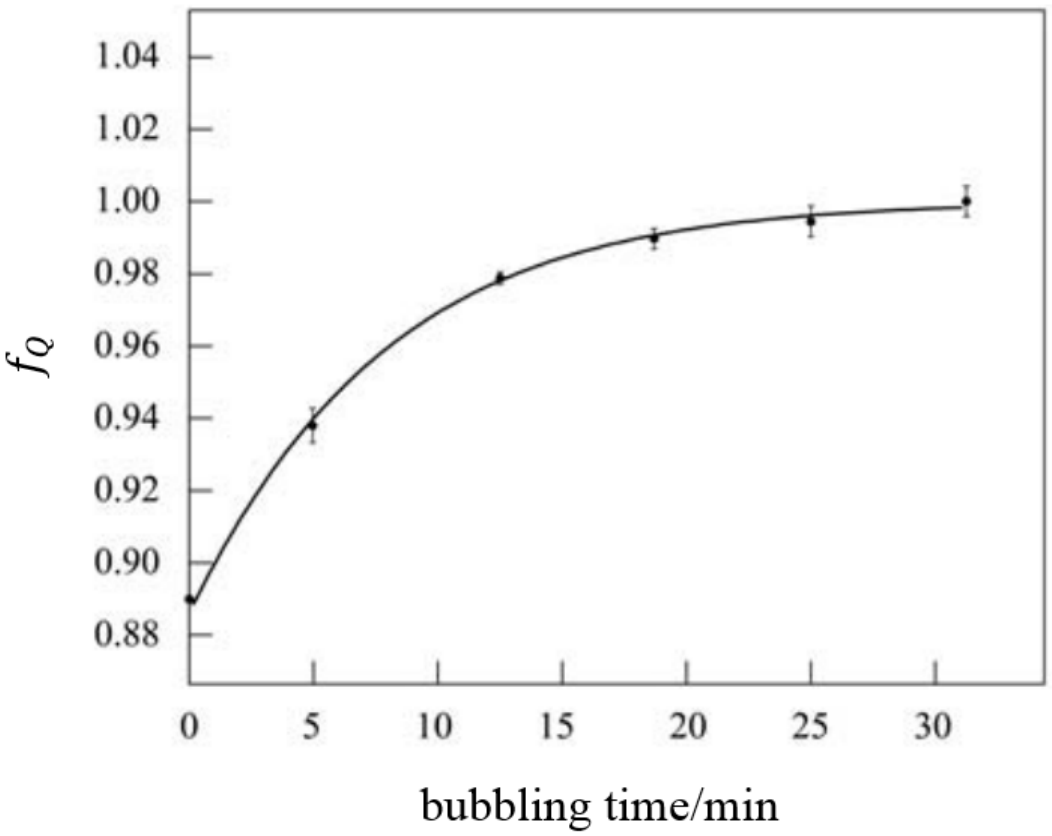

Figure 14: f_Q as a function of nitrogen gas bubbling time of an OLS containing oxygen [107]**.**

2. The detector's container and light reflector

The volume of the detection material required to detect the secondary neutron range, varying from thermal to maximum energy, depends on the proton therapy's maximum energy. For example, 5cm for a liquid scintillator (NE-213) is the minimum detection length required to detect neutron energy up to 60MeV and gamma-ray energy up to 10MeV [100].

The light reflector could be a diffuse light reflector or a specular light reflector. Diffuse light reflectors are preferable, as the light reflection angle is nearly independent of the light incident angle. Therefore, there is a higher probability that the light will reach the PMT surface as compared to specular light reflectors [12].

3. Photomultiplier tube

A PMT is a device that converts light (i.e. visible, infrared and ultraviolet) into electrical signals. It is part of the neutron detector and has to be chosen carefully. With regard to a neutron detector in a proton therapy room, the selected PMT should have the following properties:

1. The photocathode's maximum quantum efficiency—which is the amount of electrons produced from the photocathode per incident scintillation photon—should approximately match the maximum wavelength emission of the scintillation material.
2. The secondary neutron dose during proton therapy is expected to be significantly low, based on the researchers' reports. The neutron dose was found to be less than 0.05% of the prescribed proton therapy dose [64] [71] [108]. Therefore, good photocathode sensitivity would be suitable for this application. However, high photocathode sensitivity should not lead to a high dark current (thermionic noise) [109]. Thermionic noise is the electrical signals produced by electrons ejected from the photocathode of the PMT in the absence of scintillation light [110]. In addition, high dark current is a significant problem when it occurs alongside low radiation intensity, such as secondary neutron intensity during proton therapy. Therefore, high dark current PMTs are clearly unsuitable to be used with neutron detectors in a proton therapy room.

3. The diameters of the PMT and the detection material container should be approximately the same. This is to increase the probability of the scintillation light being incident on the PMT glass window.

2.3.2 Clinical requirements

1. Radiation environment of a proton therapy room

The proton therapy room has a mixed radiation environment. It contains scattered protons, secondary neutrons, gamma rays, electrons and heavy ions. However, neutrons and gamma rays are the significant secondary radiation that reaches a neutron detector. Thus, the neutron detector should have the ability to recognise the difference between these two radiation types.

2. Neutron production and energy

Neutron production during proton therapy is the number of neutrons produced per prescribed protons (i.e. prescribed therapy dose). During the proton therapy, the secondary neutron sources were classified into external and internal sources. The external neutron source is the neutron generator outside the patient's body, while the internal source is the opposite (i.e. the neutrons generated inside the treated target). There are two proton therapy treatment methods. Scattering and spot-scanning were the two methods used to deliver the proton dose to the entirety of the target volume.

In the spot-scanning method, the internal secondary neutron production is dominant, whereas, in the scattering method, the external neutron source is the dominant.

In the scattering proton therapy system, the measured neutron dose was found to be significantly varied at different proton therapy facilities and with different measurement conditions [11]. This was due to:

- The proton beam energy.
- The prescribed proton therapy dose.
- The treatment field size.
- The treatment head geometry.
- The measurement geometry.

The neutron production was found to decrease as the treatment field size increased, where more primary protons were blocked by the beam line aperture [111]. Furthermore, it was confirmed, experimentally and using the MC simulation method,

that the secondary neutron dose decreases with increased distance from the proton therapy beam axis [64] [112].

Thus, the estimated secondary neutron energy range in the proton therapy room at Clatterbridge Hospital is from thermal to 60MeV. In addition, the measurement conditions, such as the treatment field size and the prescribed proton therapy dose, should be considered.

3. Accessibility and movability

The ability to locate and move the neutron detector within the proton therapy treatment room, especially to be by the patient's side, is a significant advantage of the neutron detector design. Moreover, it is more practical to use a compact and lightweight neutron detector that has fewer supporting devices.

4. MC simulation and measurement validation

Comparison of the in-field measurements with the MC simulations was mainly made to validate the obtained neutron spectrum (or dose) [58] [66]. In addition, the validation of the in-field measured neutron dose can be done by comparing the results from two neutron detectors [113].

2.3.3 Summary

Table 13 shows a summary of the required criteria for a neutron detector in a proton therapy room.

Table 13: Summary of the required criteria for a neutron detector in a proton therapy room.

Criteria	Requirements
Optimum detection material	Loaded OLS.
Loaded OLS scintillation efficiency	65–68% of anthracene.
Detector's detection efficiency	Efficient at detecting neutrons from thermal to 60MeV.
Typical detector's energy resolution	16–20% at the Cs^{137} Compton edge position.
PSD	Loaded OLS has an excellent ability to distinguish between different radiation particles.
Light reflector	A loaded OLS container should be provided with a specular or adhesive light reflector.
Releasing dissolved oxygen	Purging the loaded OLS with inert gas.
PMT	To be matched with the loaded OLS scintillation light wavelength at high PMT quantum efficiency and low dark current.
Accessibility and movability	Compact, lightweight and as few supporting devices as possible.
Results validation	MC simulation and measurement comparisons.

2.4 Neutron detectors based on an OLS

An OLS is a hydrocarbon (hydrogen and carbon) compound [114]. Interactions between neutrons and the OLS molecules are through scattering and nuclear reactions [115]. In addition, Compton electrons are produced by interactions between gamma rays and OLS molecules. However, due to the low atomic numbers of hydrocarbons, photoelectric absorption is insignificant [116]. An OLS yields a different scintillation signal shape for gamma rays and neutrons. OLS detectors are extensively used in both neutron and gamma-ray detection and spectroscopy; however, the neutron detection efficiency is significantly higher than the gamma-ray detection efficiency [117] [118].

Neutron (indirect ionisation radiation particle) spectroscopy can be achieved through the detection of secondary charged particles produced from the interactions between neutrons and OLS molecules. Firstly, recoil nuclei (charged particles) result from the scattering of fast neutrons on hydrogen and carbon nuclei. Scattering on hydrogen nuclei potentially transfers full neutron energy, while scattering on carbon nuclei transfers 28.4% of the neutron energy at the maximum [12]. Therefore, materials that contain a high percentage of light nuclei, such as hydrogen and deuterium, are the most efficient fast neutron detection materials [12] [119]. Secondly, charged particles are released from the nuclear reactions of fast neutrons and carbon nuclei. In addition, gamma rays are produced from hydrogen thermal neutron capture, which has a cross section of 0.329 barns [120] [121].

Thermal neutron detection using OLS detectors is often based on fast neutron moderation thermal neutron capture. The detection of thermal neutrons can be performed through the detection of secondary charged particles released from the thermal neutron capture reaction (i.e. conversion electrons and alpha particles). In addition, hydrogen thermal neutron capture significantly produces gamma rays with an average energy of 2.223MeV [122]. Loaded OLS detectors are used widely in neutrino detection, in addition to neutron and gamma-ray detection and spectroscopy [123] [124].

Fast neutron spectroscopy using an OLS is based on scattering and nuclear interactions. Neutron detectors based on scattering are widely used and are the most popular approach. Using an OLS, fast neutrons are detected through collisions of the neutrons with hydrogen and carbon nuclei. This produces recoil nuclei that can be

detected directly [125]. In addition, the interactions of fast neutrons of energy (more than 8MeV) with carbon nuclei produce charged particles, which can be detected [25].

The majority of the detectors used for both thermal and fast neutron detection and spectroscopy are boron-loaded OLS, lithium-loaded OLS and gadolinium-loaded OLS detectors. On the one hand, these detectors can be compared with regard to fast neutron detection efficiency; the only difference is the effectiveness of the applied PSD method, which can separate neutrons from gamma rays. On the other hand, thermal neutron detection efficiency varies according to boron, lithium and gadolinium properties. Thermal neutrons are detected through the secondary charged particles released from boron, lithium and gadolinium thermal neutron capture reactions. These reactions are shown at the following [12] [126] [24]:

$$\text{Thermal neutron} + {}^{10}_{5}\text{B} \rightarrow \begin{cases} \text{ground } {}^{7}_{3}\text{Li} + \text{alpha Qvalue (2.792MeV)} \\ \text{excited } {}^{7}_{3}\text{Li} + \text{alpha Qvalue (2.31MeV)} \end{cases}$$

The percentages of the ${}^{10}_{5}\text{B}$ thermal neutron capture reaction are 94% and 6% of the excited and ground states respectively. In addition, excited ${}^{7}_{3}\text{Li}$ emits 478keV gamma rays. The boron thermal neutron capture cross section is 3,840 barns. The abundance of the ${}^{10}_{5}\text{B}$ isotope in natural boron is 19.8%.

$$\text{Thermal neutron} + {}^{6}_{3}\text{Li} \rightarrow {}^{3}_{1}\text{H} + \text{alpha Qvalue (4.78MeV)}$$

The cross section of the ${}^{6}_{3}\text{Li}$ thermal neutron capture is 940 barns. The abundance of the ${}^{6}_{3}\text{Li}$ isotope in natural lithium is 7.4%.

Loading the OLS with gadolinium, which has the highest thermal neutron capture cross-section isotope (${}^{157}_{64}\text{Gd}$), offers the detection of thermal neutrons through secondary charged particles that result from the interaction. Natural gadolinium, which is used in loading the scintillator material, has seven isotopes: ${}^{152}_{64}\text{Gd}$ (0.2%), ${}^{154}_{64}\text{Gd}$ (2.15%), ${}^{155}_{64}\text{Gd}$ (14.73%), ${}^{156}_{64}\text{Gd}$ (20.4%), ${}^{157}_{64}\text{Gd}$ (15.6%), ${}^{158}_{64}\text{Gd}$ (24.8%) and ${}^{160}_{64}\text{Gd}$ (21.90%) [127]. ${}^{157}_{64}\text{Gd}$ is the highest thermal neutron capture cross section (255,000 barns) and the ${}^{156}_{64}\text{Gd}$ thermal neutron capture cross section is 60,800 barns. The thermal neutron cross sections of other isotopes are insignificant [128]. Electrons (conversion electrons) and gamma rays are produced from the following interactions [24]:

Thermal neutron + $^{157}_{64}\mathrm{Gd} \rightarrow {}^{158}_{64}\mathrm{Gd}$ + conversion electrons + gamma rays Qvalue (7.9MeV)

Thermal neutron + $^{155}_{64}\mathrm{Gd} \rightarrow {}^{156}_{64}\mathrm{Gd}$ + conversion electrons + gamma rays Qvalue (8.5MeV)

Gadolinium-loaded OLSs have been developed for neutron spectrometry. They have the ability to distinguish between different radiation types, have excellent detection characteristics and have wide neutron energy range responses [129] [130]. The de-excitation of excited $^{158}_{64}\mathrm{Gd}$ produces 3.288 gamma rays with an average energy of 2.394MeV and a discrete electron spectrum (from 29keV to 246keV), with the highest yield of 26.8% at 71keV [131] [24]. Thus, counting gamma rays or electrons at the previous energies can be utilised to estimate the counts of thermal neutrons captured [132].

To conclude, a gadolinium-loaded OLS was selected to be the detection material. This selection was due to its high neutron detection efficiency with wide range energy response, and the ability to distinguish between neutrons and gamma rays.

2.5 Materials and methods

2.5.1 EJ-331 gadolinium-loaded OLS

The detection material used in all the experiments was the gadolinium-loaded OLS (EJ-331), which is produced by Eljen Technology. EJ-331 produces a flash of light in the wavelength of visible light (424nm) when exposed to radiation. The scintillation efficiency (light output/DE) of the gadolinium-loaded OLS is 68% of anthracene. This material is equivalent to NE-323 and BC-521 detection materials. The properties of EJ-331 and BC-521 are shown in Table 14.

Table 14: The properties of EJ-331 and BC-521 [130] [133]**.**

Properties	EJ-331	BC-521
Gadolinium content	0.5%, w/w	0.5%, w/w
Specific gravity (g/cc)	0.90	0.89
Light output of anthracene	68%	68%
Wavelength of maximum emission	424nm	424nm
Bulk light attenuation length	>4m	>4m
Refractive index	1.50	1.50
Flash point	44°C (111°F)	44°C (111°F)
No of H atoms per cm^3	$5.27x10^{22}$	$5.25x10^{22}$
No of C atoms per cm^3	$4x10^{22}$	$4x10^{22}$
H:C ratio	1.32	1.314

The table shows the properties of two commercially available gadolinium-loaded liquid scintillators. The properties are similar, while the differences (for example, the H:C ratio and specific gravity) are insignificant.

The EJ-331 was considered to be convenient for neutron spectroscopy in the mixed radiation field of the proton therapy room for the following reasons:

1. It has good scintillation efficiency, which is 10,400 (photons/MeV).
2. It has good detection efficiency for a wide neutron energy range (from thermal to fast neutrons).
3. It has an excellent ability to distinguish between different radiation particles.

2.5.2 Radiation sources

Gamma-ray sources were used:

a. To test the performance of the four prototype neutron detectors.
b. To compare the obtained spectra using an MCA and an oscilloscope.
c. To compare the obtained Cs^{137} spectrum with extracted data from the Cs^{137} spectrum provided by Eljen Technology (i.e. the reference Cs^{137} spectrum). Eljen Technology obtained the reference Cs^{137} spectrum

using an EJ-301 liquid scintillator, which has equivalent properties to the NE-213 liquid scintillator [134].

d. To calibrate the energy range of the fourth prototype neutron detector and to define its energy resolution.

Table 15 shows the gamma-ray sources that were used in the experiments.

Table 15: Gamma-ray sources used in the experiments.

Source	Type	Half-life	Energy peak (MeV)	Compton edge (MeV)	Activity (kBq)
Cs^{137}	Gamma emitter	30 years	0.662	0.477	180
Co^{60}	Gamma emitter	5.27 years	1.17 and 1.33	0.96 and 1.12	6.22

2.5.3 OLS detectors' energy range calibration using gamma-ray sources

The interactions of the gamma rays with matter are via:

- Photoelectric absorption.
- Pair production.
- Compton scattering.

Compton scattering is the dominant interaction, while photoelectric absorption and pair production (i.e. with gamma-ray energy >10MeV) are insignificant in terms of low atomic number materials, such as the OLS [135]. Figure 15 shows gamma-ray cross sections of OLS (e.g. EJ-331).

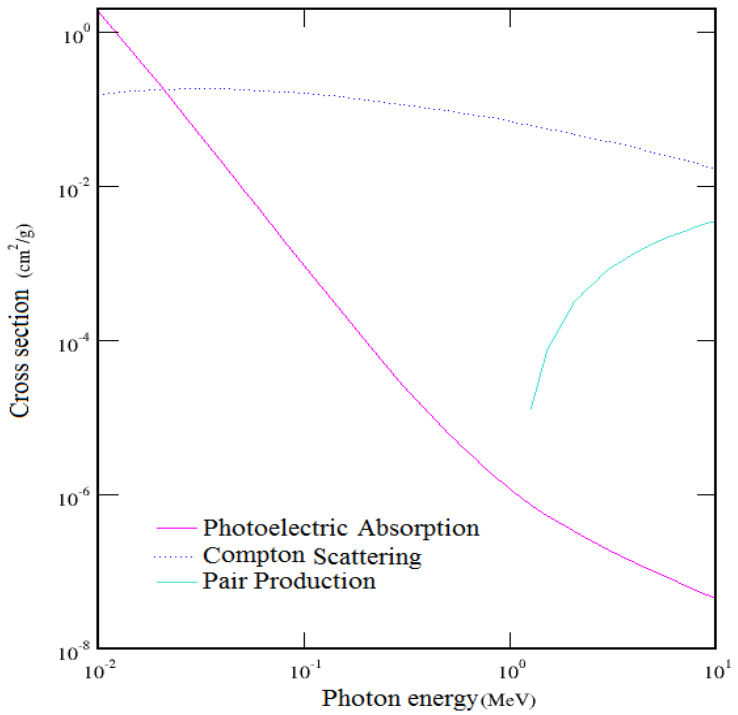

Figure 15: Photon cross sections of C_9H_{12} (i.e. EJ-331) [136].

Figure 15 was obtained using data from the National Institute of Standards and Technology (NIST) website [136] . The plot shows that the Compton scattering cross section of EJ-331 detection material at 0.662keV (i.e. Cs^{137} full energy peak) is approximately 1.5×10^4 more than the photoelectric absorption cross section.

Compton scattering electrons are produced in an energy range of zero to Compton edge energy, based on the scattering angle of the incident gamma ray, which is from 0º to 180°. The maximum gamma-ray energy transfer occurs at a 180° gamma-ray scattering angle (backscattering gamma rays) in terms of the following equation [12]:

$$\mathbf{Gamma_E{}'} = \frac{\mathbf{Gamma_E}}{\mathbf{1} + \frac{\mathbf{Gamma_E}}{\mathbf{0.511}}(\mathbf{1} - \mathbf{\cos\theta})}$$

Here, $Gamma_E$ is the energy of the incident gamma ray, $Gamma_E{}'$ is the energy of the scattered gamma ray, and θ is the gamma-ray scattering angle.

The energy calibration of the OLS detectors using the gamma-ray source is done using the Compton edge of the gamma-ray spectrum. The Compton edge energy can be calculated with the following equation [116]:

$$\textbf{Compton edge (MeV)} = 2 \times (\textbf{Gamma}_{\textbf{E}})^2 / (0.511 + (2 \times \textbf{Gamma}_{\textbf{E}}))$$

However, when using the gamma-ray source to calibrate OLS detectors, the Compton edge cannot be observed directly in the gamma-ray spectrum shape. In general, the Compton edge is located between the position of the spectrum peak and the position of the half peak height [138]. Figure 16 shows an OLS detector's typical gamma-ray spectrum (i.e. DE spectrum) and a sketch of the ideal gamma-ray spectrum [138].

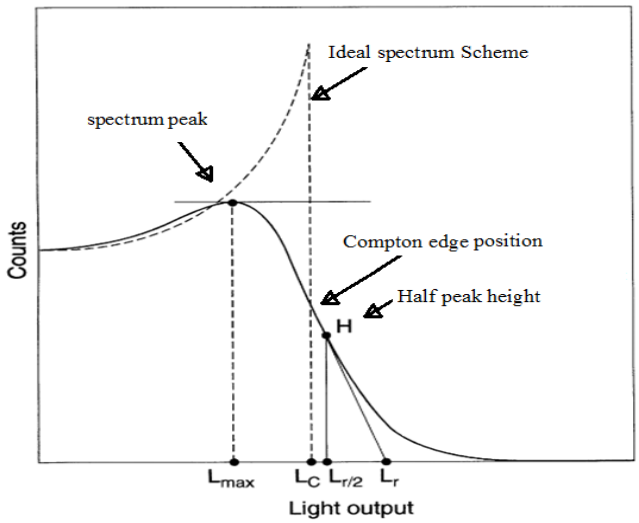

Figure 16: Typical gamma-ray spectrum of an OLS detector and sketch of the ideal gamma-ray spectrum [138].

Practically, the Compton edge position on the gamma-ray spectrum is recognised using two methods [101]. The first is the MC simulations and the second is the $\gamma - \gamma$ coincidence method.

Using the MC simulation, the position of the Compton edge is identified by comparing the measured gamma-ray spectrum with the simulated DE spectrum. Figure 17 shows the measured gamma-ray spectrum as compared to the simulated DE spectrum [101].

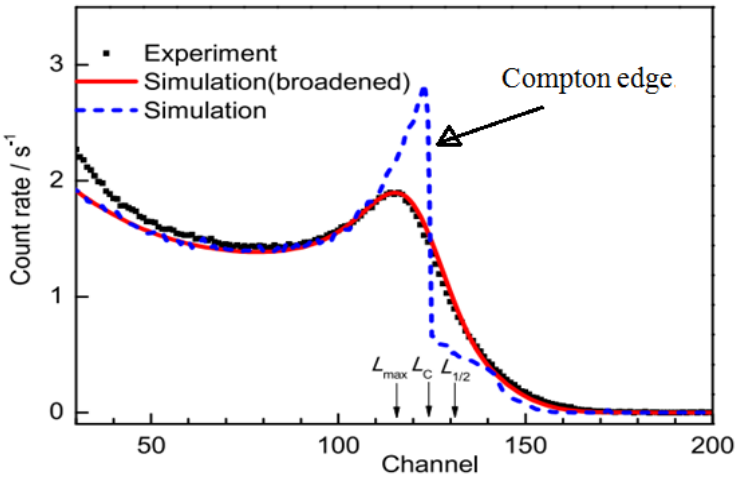

Figure 17: BC-537 liquid scintillator gamma-ray spectrum as compared to the simulated DE spectrum in order to find the Compton edge position, where L_C is the Compton edge position, L_{max} is the spectrum peak position, and $L_{1/2}$ is the half peak height position [101].

To use the $\gamma - \gamma$ coincidence method, gamma-ray sources with high energies and intensities are needed [101]. It was reported that two OLS detectors were used (BC-501A OLS detectors): the first was exposed to the gamma-ray source, while the second was exposed to both the gamma-ray source and the backscattered gamma rays [33]. Figure 18 shows the $\gamma - \gamma$ coincidence method scheme from a literature review [33].

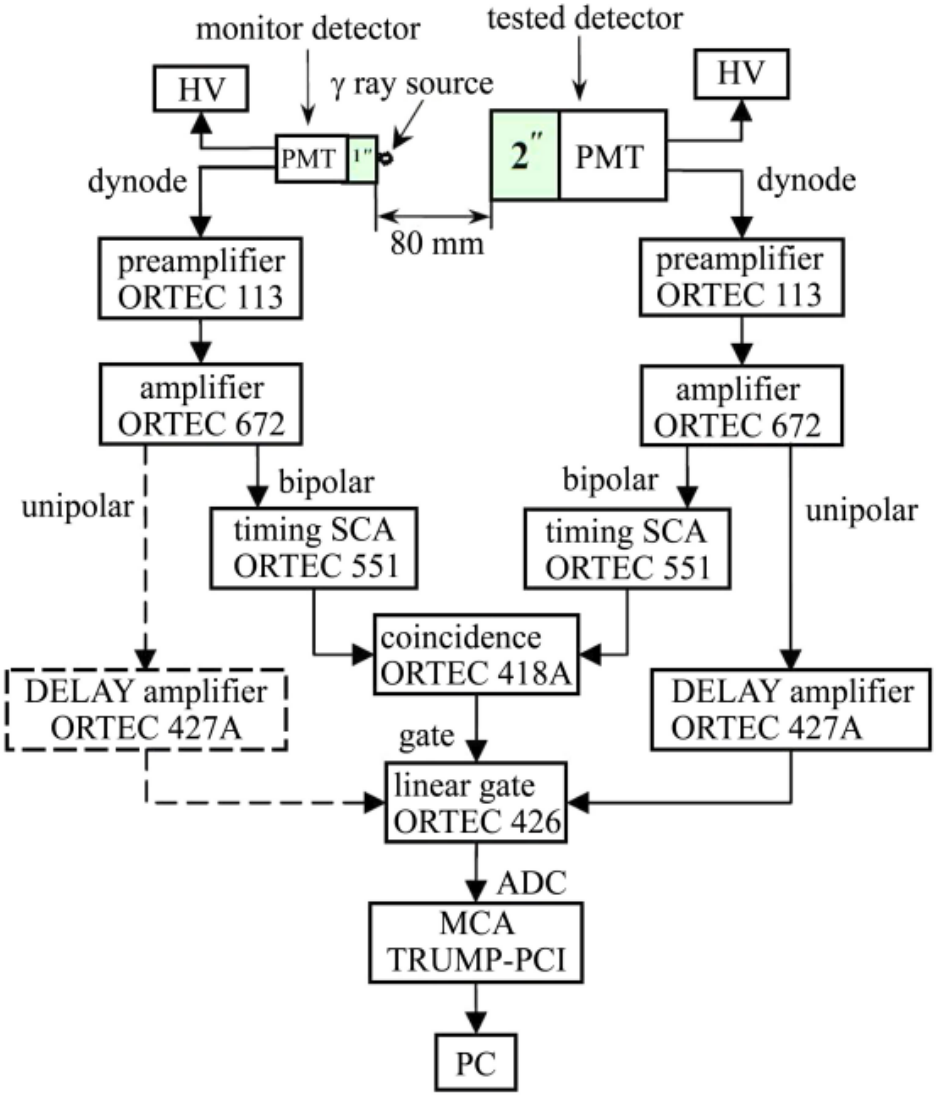

Figure 18: γ − γ coincidence method scheme [33].

The single channel analyser of the monitor detector was adjusted to measure over a narrow energy range, whereas the analyser for the detector being tested was adjusted to measure over a wide energy range. The monitor detector recorded the electrons produced by backscattered gamma rays, whereas the detector being tested recorded electrons with energies from Compton scattering. By applying the coincidence technique, the detector being tested was recording signals that coincided with the chosen signal from the monitor detector (i.e. backscattered gamma rays signals). Therefore, the Compton edge position was determined from the recorded coincident

spectrum [33]. Figure 19 shows the gamma-ray energy spectrum with and without coincident and the coincident gamma-ray spectrum [33].

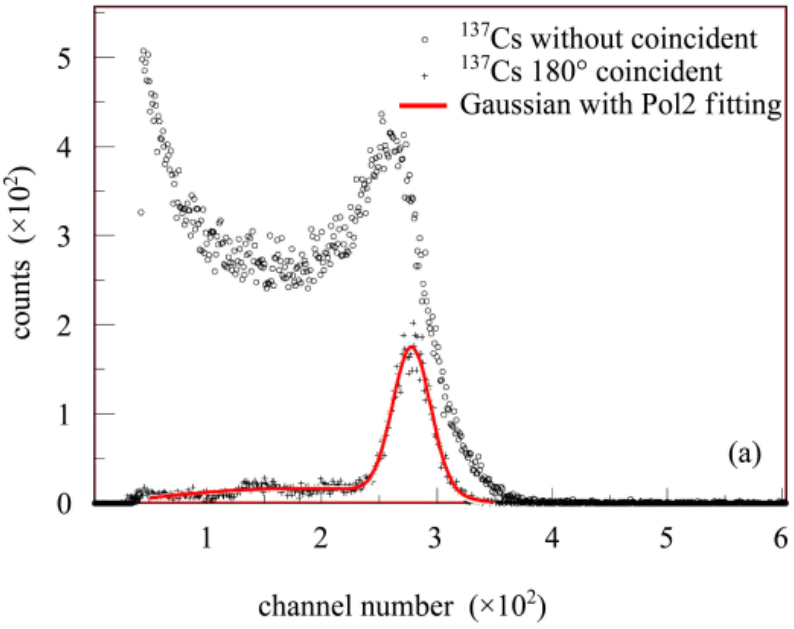

Figure 19: Gamma-ray energy spectrum and coincident spectrum. The Gaussian fitting of the coincident spectrum represents the detector energy resolution [33].

The difference in the Compton edge position and the spectrum peak position is relevant in terms of the OLS detector energy resolution (pulse height resolution) [139] [138]. This can be clearly recognised from Figure 16. The ratio of Compton edge counts to spectrum peak counts reflects the detector energy resolution. Theoretically, at a maximum ratio (where the ratio is 1.00), the Compton edge and spectrum peak positions are superimposed. Thus, the higher ratio means a sharper spectrum peak and, therefore, a higher detector energy resolution. For example, when using BC-501A OLS detectors, the ratio of Compton edge counts to spectrum peak counts was found to be 0.90±0.05 [33]. In another study, the ratio was considered to be 0.76±0.04 [101]. Thus, the first study introduced an OLS detector with a higher energy resolution than the second.

Using the MC simulation, identifying the Compton edge position to calibrate the detector energy range and evaluate the detector energy resolution was done for the final neutron detector design (i.e. the fourth prototype neutron detector). Whereas, for the first, second and third prototype neutron detector designs, the energy range calibration is not important. However, improvement in energy resolution in the first,

second and third prototype neutron detectors was traced using spectrum peak FWHM comparisons [140] [141]. In addition, the results were compared with the reference Cs^{137} spectrum. Figure 20 shows data extracted from the reference Cs^{137} spectrum and the FWHM of the spectrum peak Gaussian distribution, which is 60 channels.

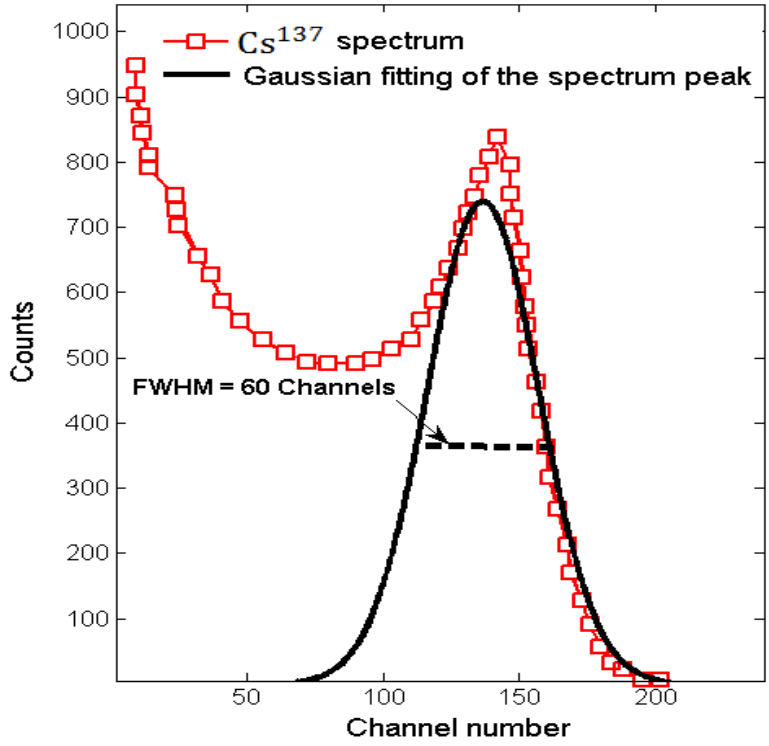

Figure 20: Data extracted from the reference Cs^{137} spectrum and the Gaussian fitting of the spectrum peak.

In addition, the extracted data of the Cs^{137} reference spectrum was plotted over the extracted data of the Cs^{137} spectrum using a BC-501A OLS detector with an energy resolution of 16% at Cs^{137} Compton edge energy [33]. Figure 21 shows the plots of the two extracted Cs^{137} spectra.

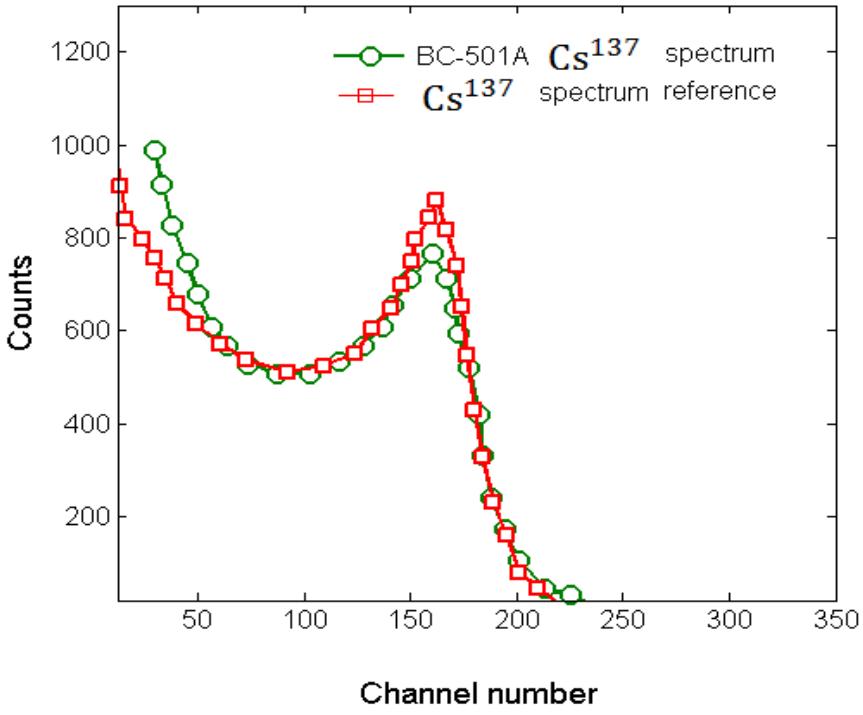

Figure 21: Extracted data of Cs^{137} from the reference spectrum and extracted data of the Cs^{137} spectrum obtained using a BC-501A OLS detector [33].

The plots reveal that the energy resolutions of the Cs^{137} reference spectrum and the BC-501A OLS detector are comparable, which is 16% at Cs^{137} Compton edge. Therefore, the 60-channel FWHM is equivalent to the energy resolution of approximately 16% at Cs^{137} Compton edge energy.

2.4.1 MCA, shaping amplifier and oscilloscope

The MCA was an ORTEC Aspec-927. The oscilloscope was a PicoScope 3000 Series with 1GS/s sampling, 200MHz bandwidth and 8-bit resolution. The shaping amplifier was a 921 made in Canberra.

The MCA was used to obtain Cs^{137} spectrum. This was done in order to compare the results from the MCA, the literature review and the oscilloscope.

The oscilloscope was movable, low weight and compact. It was ideal for in-field applications. It was used to record the output signals of the PMT.

The shaping amplifier modifies the scintillation pulse to be a semi-Gaussian shape (the PMT output is the exponential shape pulse) with regard to the shaping time constant used (the pulse width can be from 3μs to 70μs). This gives the required energy resolution in the spectroscopy [142]. Therefore, the shaping amplifier was used with the MCA.

2.4.2 Photomultiplier tubes

Firstly, The PMT used in the first, second and third prototype neutron detector designs was made by Thorn, with the serial number 9939B EMI [143]. The PMT glass window diameter was 5.1cm and was made of borosilicate glass. The PMT properties were equivalent to the properties of a standard PMT used with visible light emission scintillation materials, such as EJ-331 and BC-521 (gadolinium-loaded OLSs).

- Firstly, the PMT spectral response curve covers the wavelength of the visible light emitted by the gadolinium-loaded OLS, which is 424nm.
- Secondly, the PMT quantum efficiency, which is the number of electrons emitted from the PMT photocathode per the number of incident light photons, is 28%. Most PMTs' quantum efficiencies are between 20% and 30% [12].

Secondly, the PMT used in the design of the fourth prototype neutron detector was made by ET Enterprises, with the serial number 9305KB [144]. The PMT glass window diameter was 7.5cm and made of borosilicate glass. The PMT was placed inside an aluminium housing in order for it to be light-tight. The properties of the 9305KB and 9939B PMTs are shown in Table 16.

Table 16: Properties of the 9305KB and 9939B PMTs [144] [143].

Properties	9305KB PMT	9939B PMT
Weight	130g	150g
Active diameter	78mm	5.1mm
Maximum quantum efficiency	30%	28%
Applications	Scintillation spectroscopy	High-energy physics
Single electron rise time	3ns	–
Single electron FWHM	4ns	–
Multi-electron FWHM	15ns	4.5ns
Multi-electron rise time	7.5ns	3ns
Dark current at 20°C	$500s^{-1}$	$800s^{-1}$

The maximum quantum efficiencies of the 9305KB and 9939B PMTs at the EJ-331's emission light wavelength (424nm) are the same, which is 27.5%. Figure 22 shows the extracted data from the 9305KB and 9939B PMTs' quantum efficiency curves plotted on the extracted data from the emission light wavelength spectrum of the EJ-331 liquid scintillator [130] [144] [143].

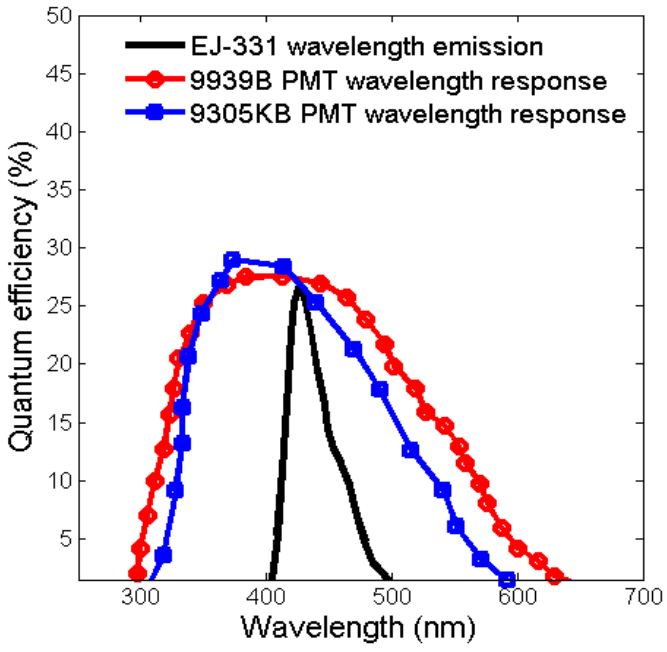

Figure 22: Extracted data from the 9305KB and 9939B PMTs' quantum efficiency curves plotted on the extracted data from the emission light wavelength spectrum of the EJ-331 [143] [144] [130].

2.6 Performance testing of the equipment

The objectives of these experiments were to make sure that the instruments were working correctly and were ready to be used in the following steps. The instruments used during the experiments were the MCA, coaxial cables, the shaping amplifier and the 9939B PMT.

Firstly, the MCA, the cables and the shaping amplifier were tested using a high-purity germanium (HPGe) detector. Cs^{137} was obtained and its shape was typical according to the literature review [64]. Figures 23 and 24 show the Cs^{137} spectrum obtained using the HPGe detector and the spectrum from the literature review (i.e. using an HPGe detector) [145].

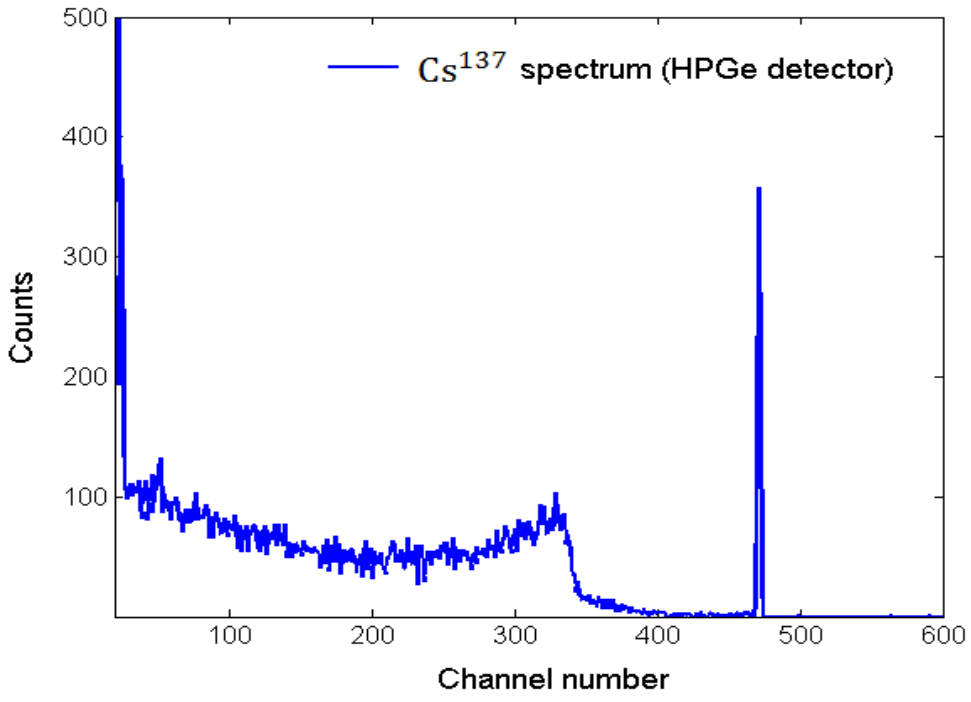

Figure 23: The Cs^{137} spectrum obtained using an HPGe detector.

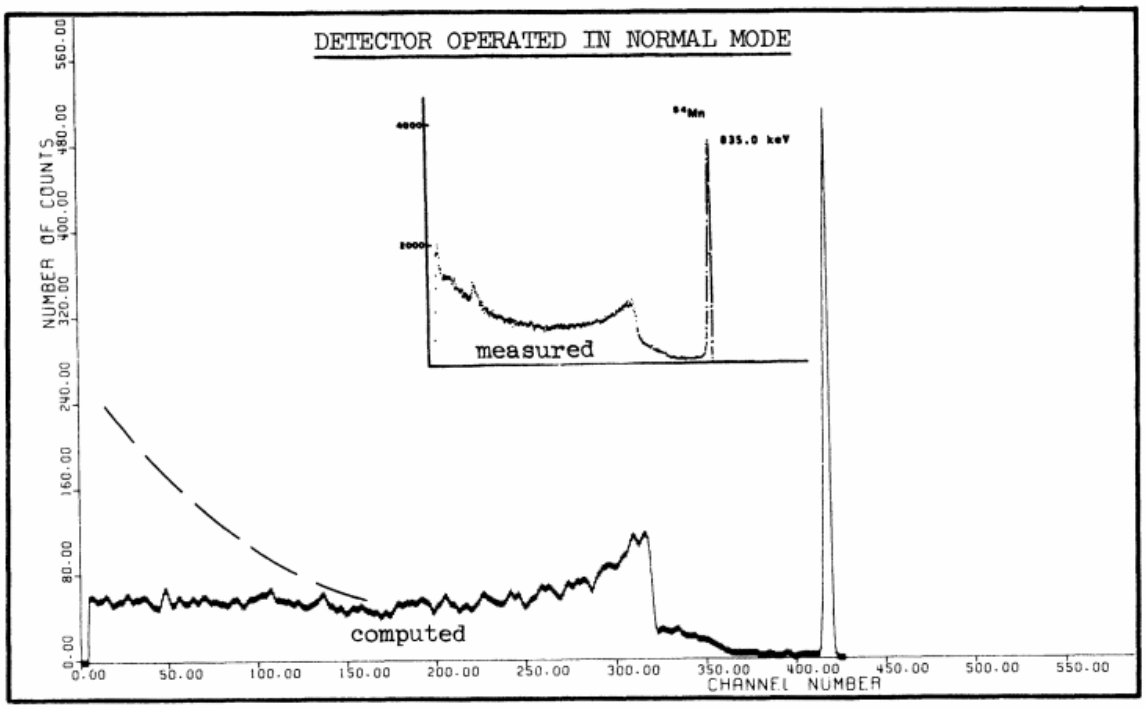

Figure 24: The Cs^{137} spectrum obtained using an HPGe detector from the literature review [145].

Secondly, the PMT was tested using a CsI crystal that was coupled directly to the PMT glass window. In order to remove the air gap between the CsI crystal and the PMT, light, transparent grease was used. The obtained Cs^{137} spectrum was typical to that of the literature review; the spectra are shown respectively in Figures 25 and 26 [65].

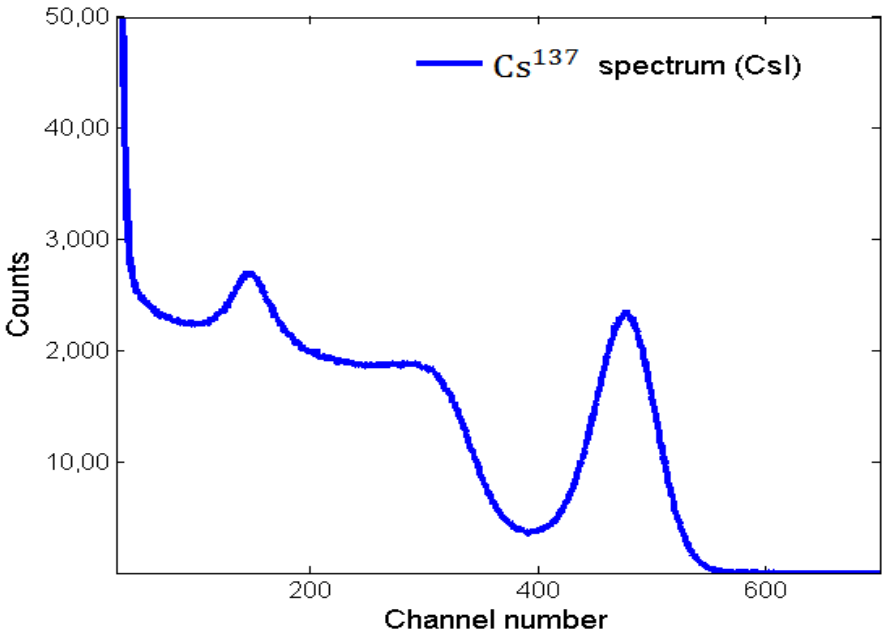

Figure 25: The obtained Cs^{137} spectrum using a CsI crystal and the PMT.

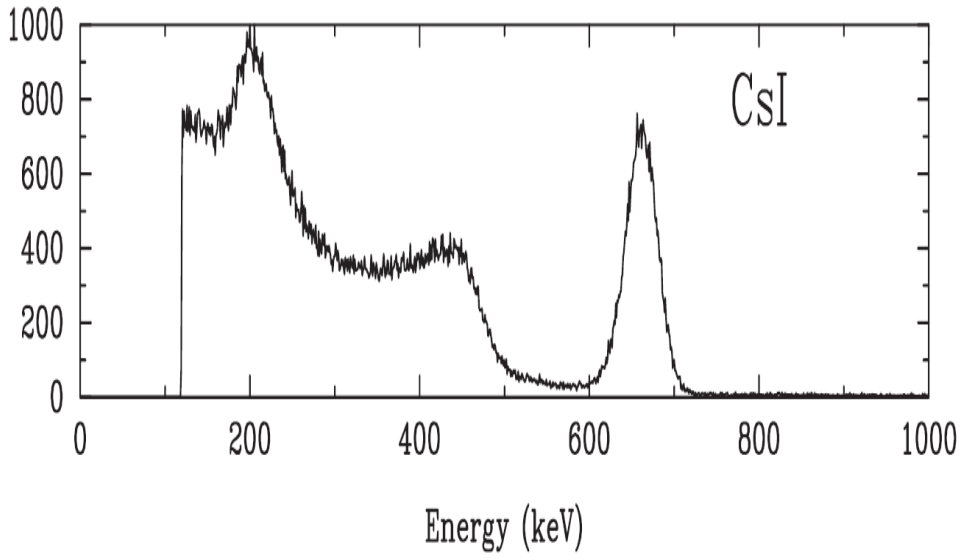

Figure 26: The Cs^{137} spectrum obtained using a CsI detector from the literature review [65].

Thus, it has been confirmed that the instruments were working correctly and were ready to be used during the experiments in the subsequent steps of the research.

2.7 Experimental setup of the first and second prototype neutron detectors

These experiments were conducted using the first and second prototype neutron detectors, the MCA, the shaping amplifier and the MAESTRO program for Windows on a laptop. Figure 27 shows the experimental setup scheme for the first and second prototype neutron detectors. The applied voltage was fixed at 1,600V and the radiation source (Cs^{137}) was attached directly to the bottom of the detector cell.

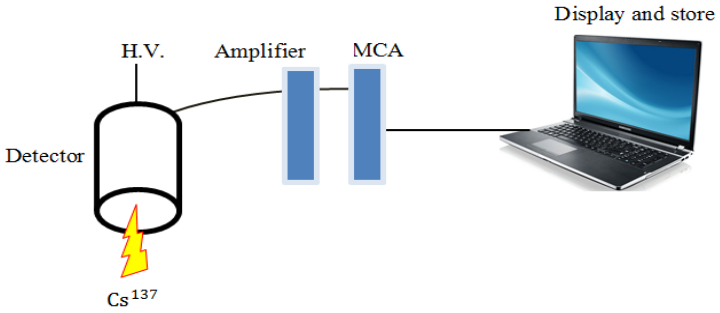

Figure 27: Experimental setup schemes for the first and second prototype neutron detectors.

2.8 First prototype neutron detector design

2.8.1 Objectives

The main objective of the first prototype neutron detector design was to find the response of the detection material (EJ-331) to the gamma-ray source (Cs^{137}). Testing the performance of the first neutron detector design included scintillation light collection and obtaining the energy spectrum of the Cs^{137} radiation source.

2.8.2 Design

The PMT was coupled directly to the liquid scintillator (EJ-331) to minimise the light loss that occurs in indirect coupling. The detector cell was cylindrical (9cm x 20cm), made of Teflon, and had an open side in order to insert and couple the PMT directly to the liquid scintillator.

Teflon has a high resistance to strong chemical solvent materials, such as OLSs. In addition, light reflectivity, which depends on the angle of the scattered light photons from the Teflon walls, was found to be between 47% and 66% [147]. Therefore, Teflon was considered suitable for use as an OLS container.

At this stage of the research, the detection material (EJ-331) was under examination to recognise its response to the gamma-ray source. The size of the Teflon cell was the largest cell size among the four prototype neutron detector designs. The large size was chosen to increase the detection efficiency as much as was achievable. Detection efficiency is directly proportional to detection material volume [148]. The gamma-ray detection efficiency of the first prototype neutron detector was approximately 55%, which was calculated at Cs^{137} energy (662keV) from the following equation [12]:

$$\varepsilon_{\mathbf{gamma}} = \mathbf{1\text{-}e^{-\mu x}}$$

Here, ε_{gamma} is the gamma-ray detection efficiency, x is the EJ-331 thickness, and μ is the gamma linear attenuation coefficient.

However, self-light-absorption should be considered with a large scintillator volume. The scintillation light that lost per scintillator length can be calculated from the following equation [149]:

$$\frac{\mathbf{s'}}{\mathbf{s^0}} = \mathbf{e^{-x/\Lambda}}$$

Here, s^0 is the primary generated scintillation light amount, s' is the scintillation light amount that reaches x length of the scintillator, and Λ is the light attenuation length at a certain light wavelength (nm).

Regarding the first prototype neutron detector, the light attenuation at a 424nm wavelength (i.e. EJ-331 scintillation light wavelength) was approximately 7.8m [150]. Therefore, the maximum light absorption (as the scintillation emission occurred at 10cm away from the PMT glass window) was 1.27%, which is insignificant.

The detector (the cell and the PMT) was placed inside a black, cylindrical pipe to ensure it was light-tight and was then connected to the shaping amplifier and the MCA. Figure 28 shows a diagram of the first prototype neutron detector design.

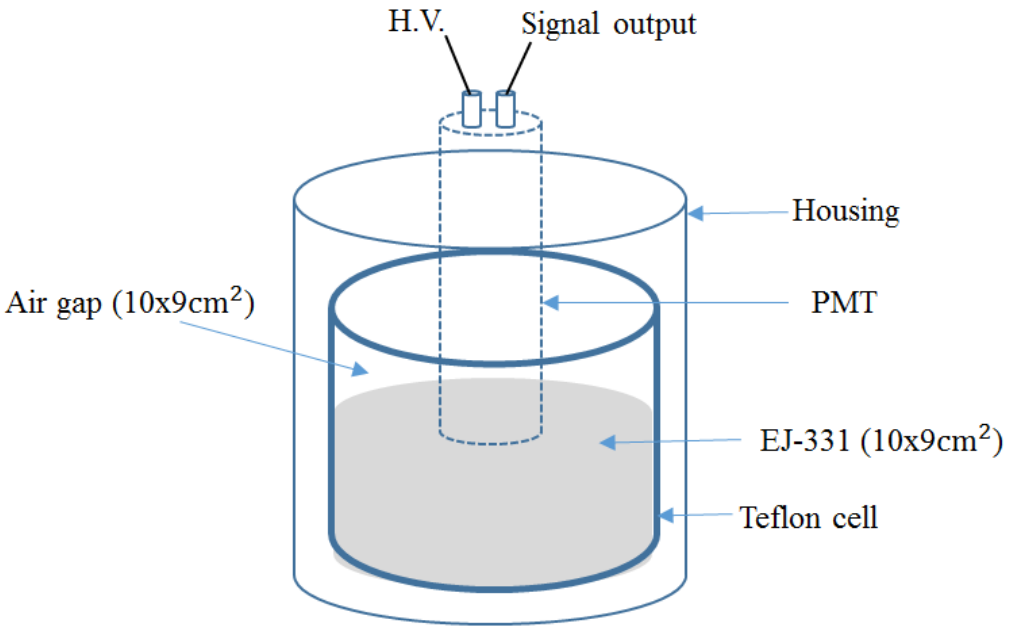

Figure 28: The first prototype neutron detector design.

2.8.3 Results and discussion

The first prototype neutron detector was exposed to the Cs^{137} radiation source and the energy spectrum was displayed and stored on a laptop using the MAESTRO program for Windows. Figure 29 shows the Cs^{137} energy spectrum obtained from the first prototype neutron detector design.

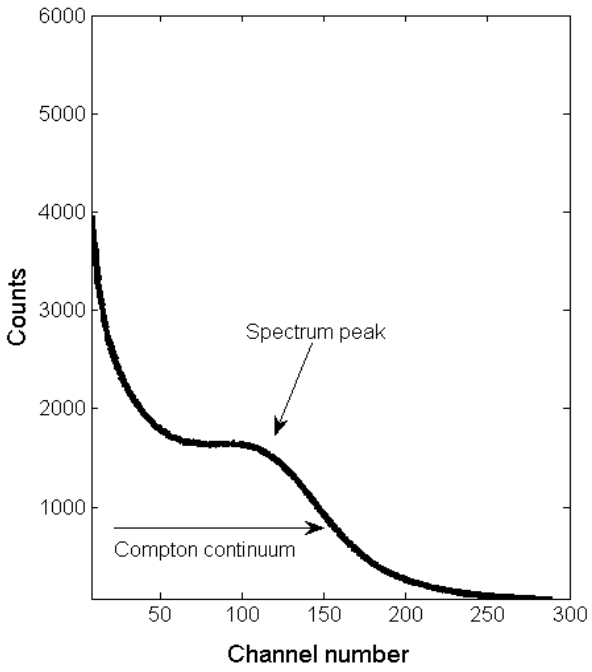

Figure 29: The Cs^{137} energy spectrum obtained from the first neutron detector design.

The obtained Cs^{137} spectrum was found to be different from the reference Cs^{137} spectrum. The obtained spectrum was found to have a broadened peak due to the loss of scintillation light (low detector energy resolution). Figure 30 shows the problem of the scintillation light loss that occurred in the first prototype neutron detector design.

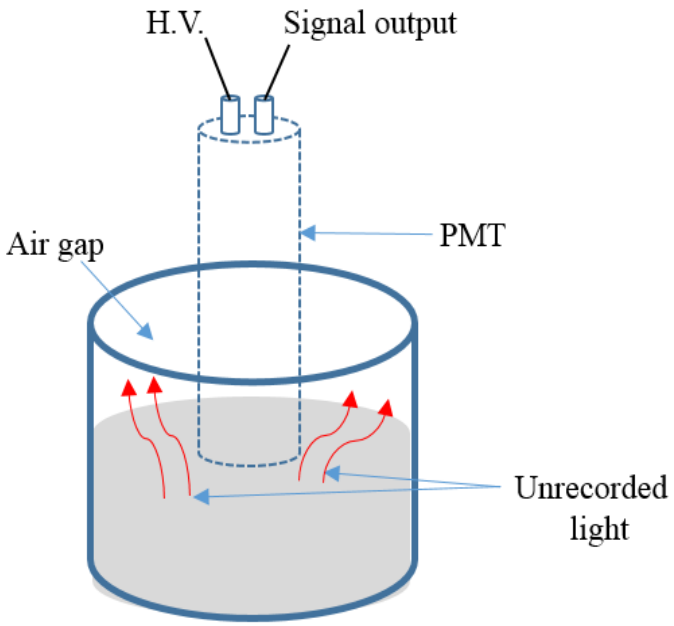

Figure 30: The diameter of the cell in the first neutron detector design was not matched with the PMT's diameter. This caused the loss of scintillation light.

The detector cell's diameter (9cm) was much larger than the PMT's diameter (5cm). This led to the loss of some of the scintillation light, which did not reflect onto the PMT glass window. In addition, scintillation light was lost due to the difference in refractive index between the air and the EJ-331 liquid scintillator. Therefore, the detector energy resolution was degraded and the Cs^{137} spectrum peak appeared to be broadening. Thus, at this stage, matching the cell and PMT diameters was considered an important detector design feature.

2.9 Second prototype neutron detector design

2.9.1 Objectives

The main objective of the second neutron detector design was to improve the detector energy resolution (i.e. scintillation light collection). The energy resolution is significantly related to the scintillation light collection and signal processing system (i.e. the detector cell design and the PMT properties) [151] [12]. Therefore, the energy resolution reflects the performance of the OLS detector system. The typical OLS detector's Compton edge energy resolution (FWHM/peak centroid) was found to be 16–20% at Cs^{137} Compton edge energy. However, the improvement in energy resolution when progressing through the first, second and third prototype neutron detector designs will be evaluated using the FWHM of the spectrum peaks [140] [141]. The improvement in energy resolution will be compared to the FWHM of the Cs^{137} reference spectrum, which was 60 channels.

2.9.2 Design

The detector cell was 5.3cm x 5cm, made of light, transparent glass, and had an open side in order to insert and couple the PMT directly to the liquid scintillator. Moreover, the inside cell walls were covered with aluminium foil, which was chosen to act as a light reflector. The detector was placed inside a black, cylindrical pipe to ensure it was light-tight and was then connected to the shaping amplifier and the MCA. Figure 31 shows the second prototype neutron detector design.

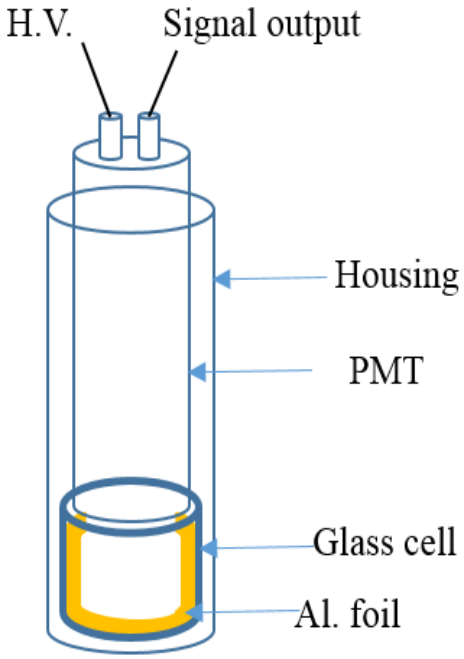

Figure 31: The second neutron detector design.

2.9.3 Results and discussion

The second prototype neutron detector was exposed to the Cs^{137} radiation source and the energy spectrum was displayed and stored on a laptop using the MAESTRO program for Windows. Figure 32 shows the Cs^{137} energy spectrum obtained from the second prototype neutron detector design.

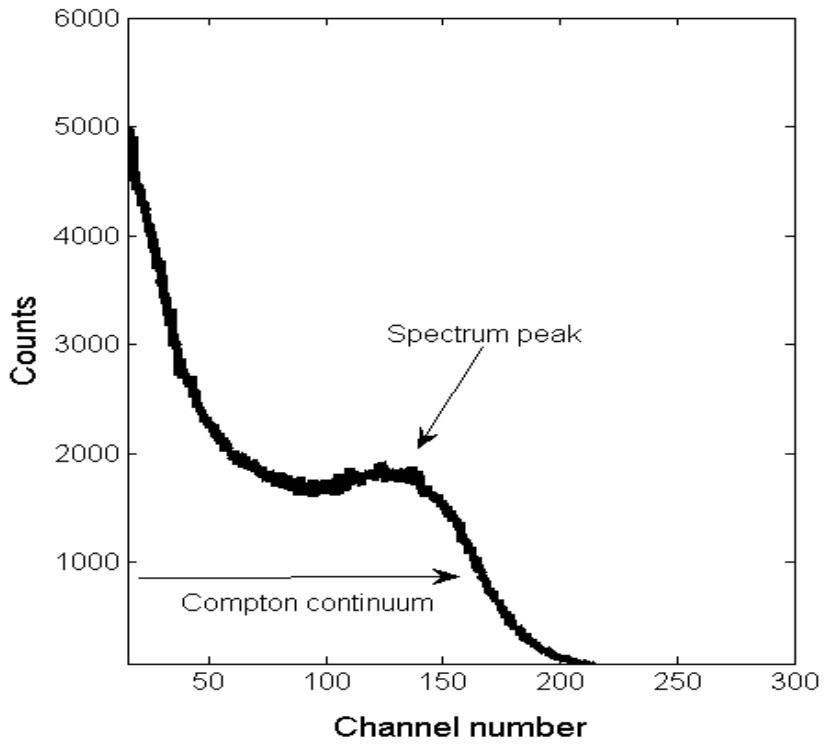

Figure 32: Cs^{137} energy spectrum obtained from the second neutron detector design.

In the second neutron detector design, loss of the scintillation light was avoided by using a cell with a 5.3cm diameter, which matched the PMT's diameter (5.2cm). The inner wall of the cell was covered with aluminium foil to act as a light reflector. Figure 33 shows the improvement achieved through using the second prototype neutron detector design as opposed to using the first detector design.

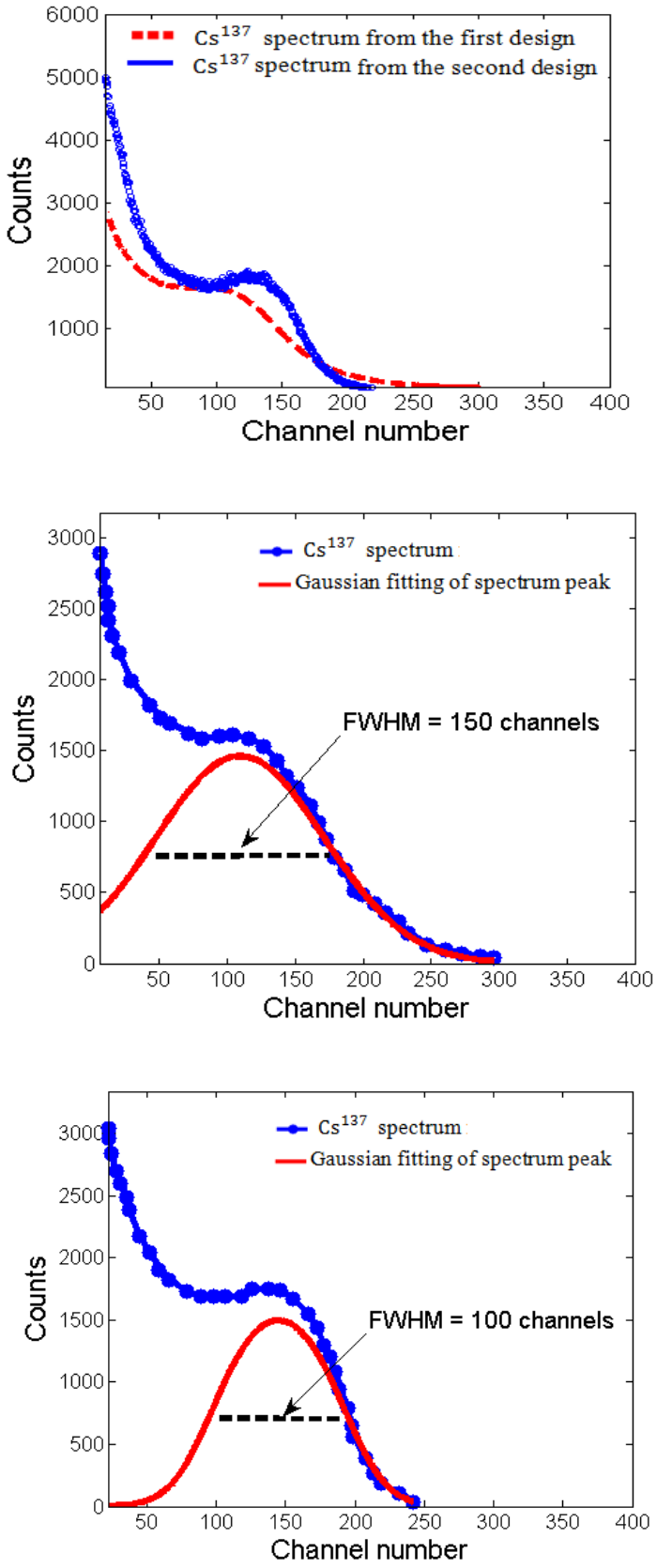

Figure 33: A comparison of the first and second prototype neutron detector designs: the Cs^{137} spectrum obtained using the first and second designs (upper plot); the energy resolution of the first neutron detector design (middle plot); and the energy resolution of the second neutron detector design (lower plot).

The improvement in energy resolution in the second neutron detector design was 50% as compared to the first neutron detector design. However, the improvement of the detector energy resolution was not adequate, as the FWHM of the spectrum peak was 100 channels, while the Cs^{137} reference spectrum was 60 channels.

In the second design, the main problem was the light reflector, which was aluminium foil. The aluminium foil was not completely smooth, because it was manually mounted onto the cell's inner walls. Therefore, a significant amount of scintillation light was not reflected onto the PMT glass window and this degraded the detector energy resolution. At this stage, two design considerations were recognised to be significant:

- The scintillation light reflector.
- The matching of the PMT and cell diameters.

2.10 Third prototype neutron detector design

2.10.1 Objectives

1 Finding a suitable scintillation light reflector.
2 Obtaining the Cs^{137} energy spectrum using an MCA.
3 Obtaining the Cs^{137} energy spectrum using an oscilloscope.

The first objective was to improve the detector energy resolution to make it comparable to the Cs^{137} reference spectrum's FWHM.

The second objective was to obtain the Cs^{137} spectrum using an MCA and to compare it with the reference Cs^{137} spectrum to confirm the improvement achieved in the third prototype neutron detector design.

The third objective was to make sure that the spectrum could be obtained using an oscilloscope. This was to confirm that the two procedures (using an MCA and using an oscilloscope) would give the same results. If so, using an oscilloscope to obtain the secondary neutron spectrum during the proton irradiation in the proton therapy room at Clatterbridge Hospital would be confirmed as having been done correctly.

2.10.2 Design

The diameters of the PMT and the detector cell were 5.2cm and 5.3cm respectively. The detector cell was cylindrical, 5.3cm x 5cm, and made of white plastic with an open side to insert and couple the PMT directly to the liquid scintillator. The white inner wall of the cell was considered to be a light reflector and it was tested as being dissolve resistant when used in the OLS. The light reflector performance in this design was expected to be much better than the first and the second prototype neutron detector designs.

The detector cell and the PMT were placed inside a black, cylindrical pipe to ensure that it was light-tight. Figure 34 shows the third prototype neutron detector design.

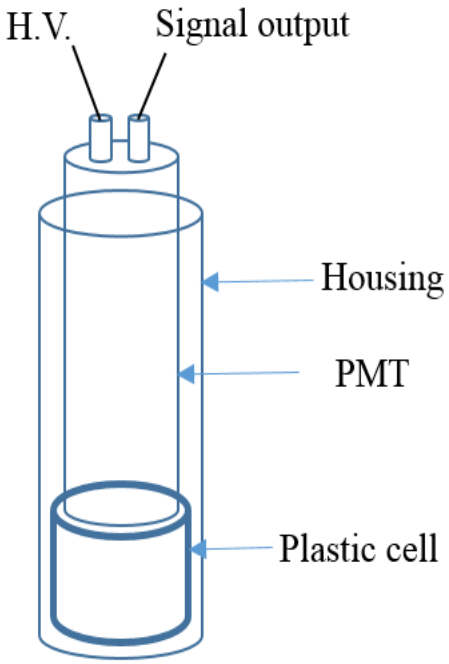

Figure 34: The third neutron detector design.

2.10.3 Experimental setup of the third prototype neutron detector

The experiments were conducted using two setups. In the first setup, the prototype neutron detector was connected to the MCA through a shaping amplifier. The MCA

output was displayed and stored using the MAESTRO program for Windows on a laptop. In the second setup, the detector was directly connected to the oscilloscope and the oscilloscope output was recorded and displayed using PicoScope software for Windows on a laptop. Thus, Cs^{137} spectrum was obtained in two different procedures.

Figure 35 shows the experimental setup schemes of the third prototype neutron detector. In all the setups, the applied voltage was fixed at 1,600V and the radiation source was attached directly to the bottom of the detector cell.

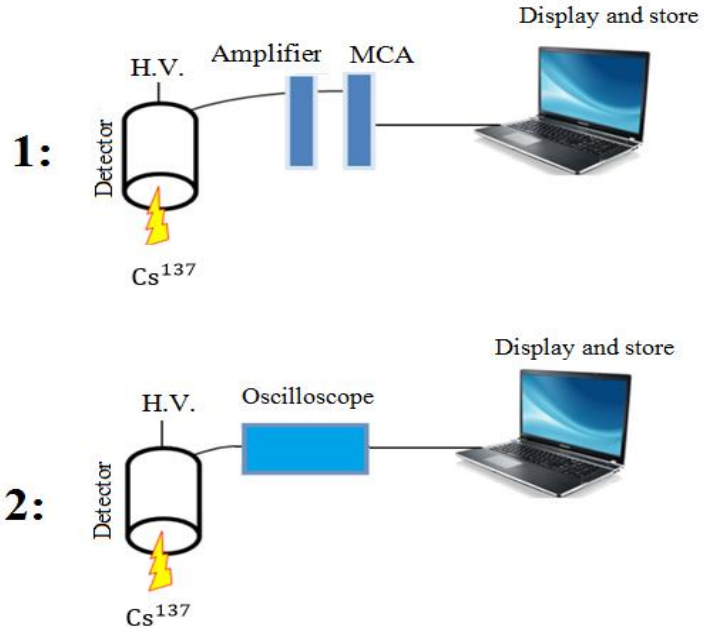

Figure 35: The experimental setup schemes of the third prototype neutron detector.

2.10.4 Results and discussion

- **The first setup**

In the first setup, the prototype neutron detector was exposed to the $\boldsymbol{Cs^{137}}$ radiation source. The energy spectrum was displayed and stored using the MAESTRO program for Windows on a laptop.

Results

Figure 36 shows the Cs^{137} energy spectrum obtained in the first setup from the third prototype neutron detector design.

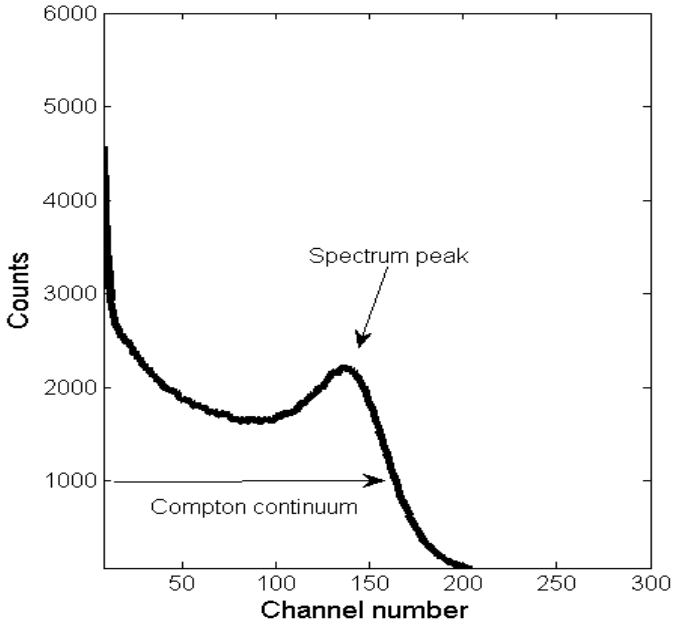

Figure 36: Cs^{137} energy spectrum obtained in the first setup from the third neutron detector design.

The improvement of the Cs^{137} spectrum shape was visibly recognised when obtained using the third detector design. The detector energy resolution was significantly improved as compared to the first and second prototype neutron detector designs. This will be confirmed by comparing the spectrum obtained to the reference Cs^{137} spectrum.

- **The second setup**

In the second setup, the prototype neutron detector was exposed to the Cs^{137} radiation source. After this, the signals (i.e. the output of the PMT) were displayed and stored using PicoScope software on a laptop. Using the MATLAB program, Cs^{137} signal amplitudes were measured and the energy spectrum was obtained from the pulse amplitudes histogram.

Result

Firstly, the Cs^{137} spectrum was obtained from the second setup using the oscilloscope and was then compared with the spectrum obtained using the MCA. Figure 37 shows the Cs^{137} spectrum obtained using the oscilloscope compared with that obtained using the MCA.

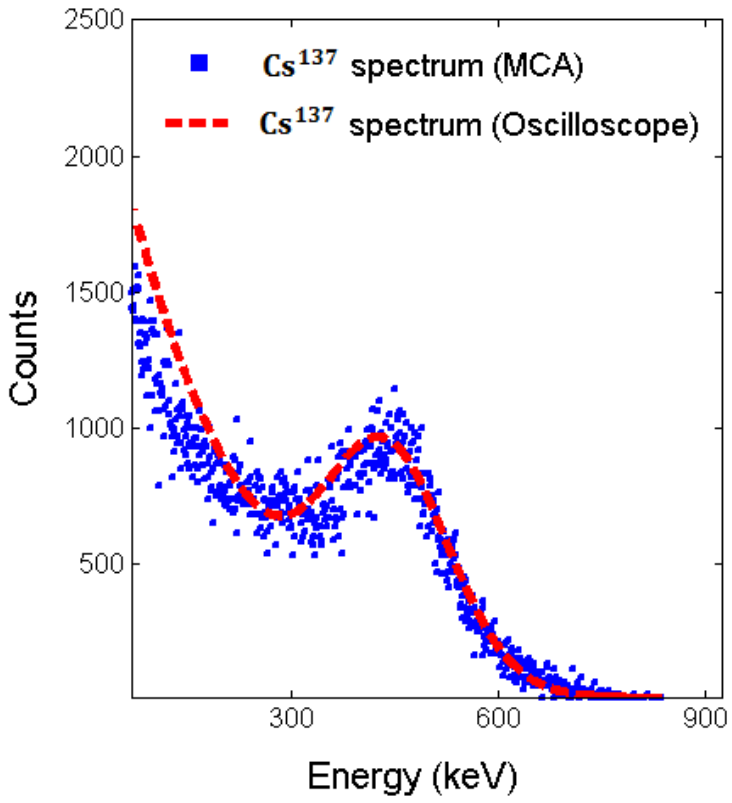

Figure 37: Cs^{137} spectrum obtained using the oscilloscope as compared to the Cs^{137} spectrum obtained using the MCA.

Figure 37 confirms that the two procedures (using the MCA and using the oscilloscope) give the same results. Therefore, an oscilloscope can be used to obtain the secondary neutron spectrum during the proton irradiation in the proton therapy room at Clatterbridge Hospital. The main purpose of using an oscilloscope is to analyse the collected signals and to apply a suitable PSD method.

- **Comparison of the three Cs^{137} spectra**

The Cs^{137} spectrum obtained from the first, second and third prototype neutron detector designs are shown in Figure 38. In addition, the first, second and third prototype neutron detector energy resolutions are shown in Figure 39.

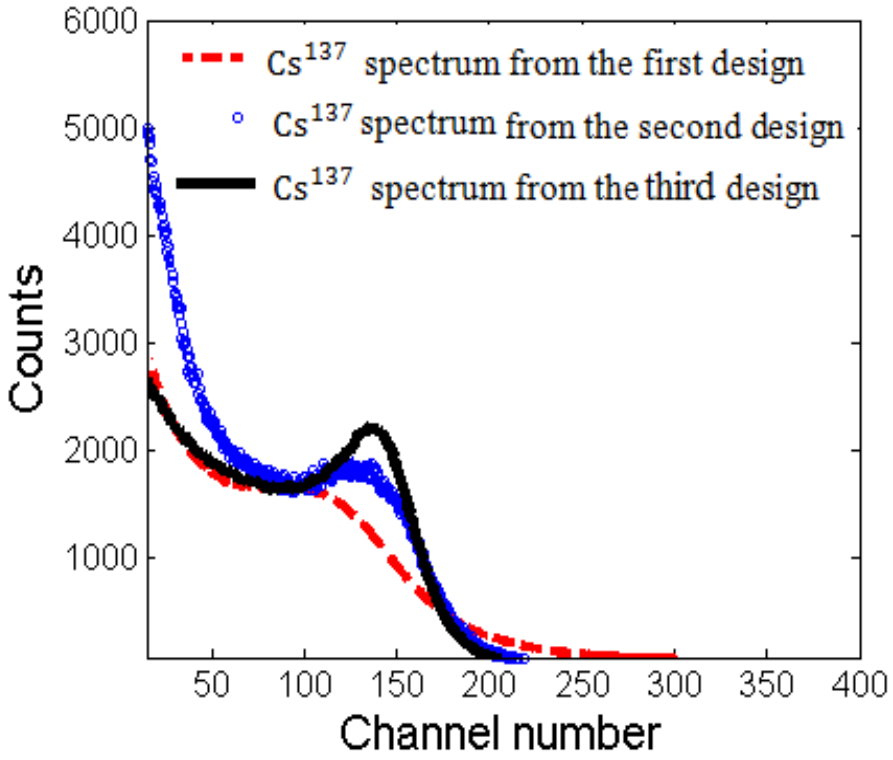

Figure 38: The Cs^{137} spectrum obtained from the first, second and third prototype neutron detector designs.

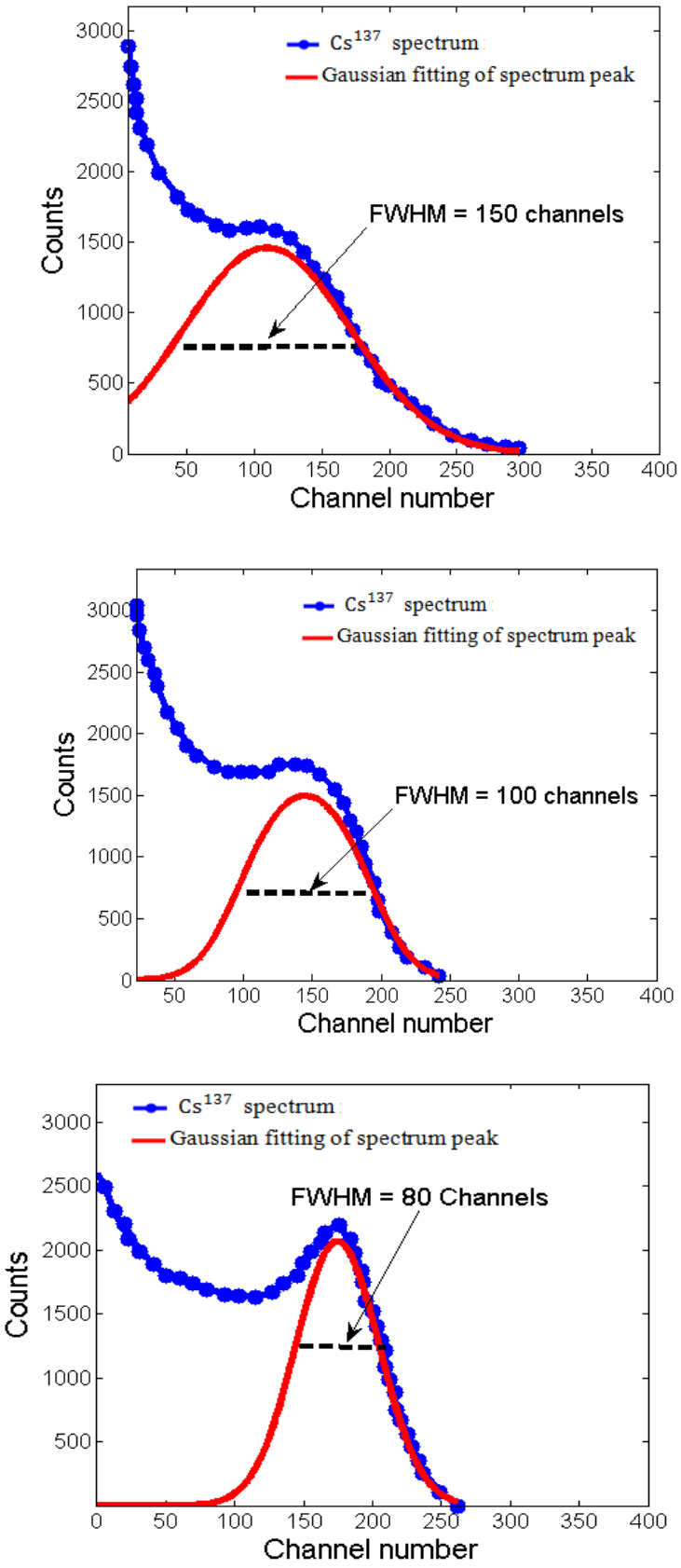

Figure 39: The first (upper plot), second (middle plot) and third (lower plot) prototype neutron detector energy resolutions.

The energy resolution (FWHM of the spectrum peak) of the second design was improved by 50% as compared to the first design. The improvement was approximately double in the third detector design, which was 80 channels, as compared to the first detector energy resolution.

- **Comparison between the results of the third detector and the reference spectrum**

Figure 40 shows the obtained Cs^{137} spectrum plotted over the extracted data from the reference Cs^{137} spectrum.

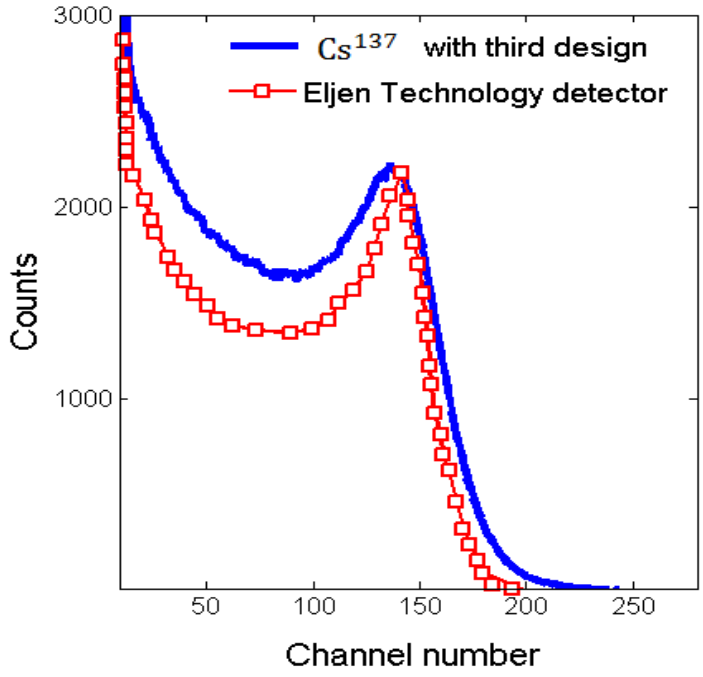

Figure 40: The Cs^{137} spectrum plotted over the extracted data from the reference Cs^{137} spectrum (i.e. the Eljen Technology detector).

Figure 40 shows that the obtained Cs^{137} spectrum has a broadened peak as compared to the Cs^{137} reference spectrum. The energy resolutions of the obtained Cs^{137} spectrum, using the third prototype neutron detector, and the Cs^{137} reference spectrum were 80 and 60 channels respectively. Thus, the energy resolution was 25% inferior compared to the Cs^{137} reference spectrum.

The broadened spectrum peak of the obtained Cs^{137} spectrum was due to the leakage of scintillation light through the white plastic cell walls, which were not 100% opaque. This was avoided in the fourth prototype neutron detector design.

2.11 Summary

The properties of the gadolinium-loaded OLS made it superior in terms of neutron detection for a wide range of neutron energy. It was therefore used in designing the prototype neutron detectors. The neutron detector design for such detection material and application was strongly affected by certain features that should be taken into consideration, such the geometry of the liquid scintillator container and the type of light reflector.

Compton scattering is the dominant interaction, where photoelectric absorption and pair production are insignificant with low atomic number materials such as an OLS. The energy calibration of the OLS detectors using gamma-ray energies is done using the Compton edges of the gamma-ray spectrum. Practically, the Compton edge position of the gamma-ray spectrum is recognised using two methods. The first is the MC simulation and the second is the $\gamma - \gamma$ coincidence method.

The OLS detector energy resolution is evaluated using the FWHM of the Compton edges and the spectrum peak Gaussian distribution. The typical OLS detector's Compton edge energy resolution (FWHM/peak centroid) was found to be 16–20% at the Cs^{137} Compton edge energy.

At this stage, three prototype neutron detectors had been designed. The detection material was selected to be a gadolinium-loaded OLS (EJ-331).
In the first, second and third designs of the prototype neutron detector, only the cell of the detection material was changed (Teflon 9cm x 20cm, glass 5.3cm x 5cm, and white plastic 5.3cm x 5cm), while the instruments (the MCA, shaping amplifier, cables, PMT and oscilloscope) remained the same.

The comparison of the obtained Cs^{137} spectrum to the Cs^{137} reference spectrum was to evaluate the improvement achieved among the first, second and third prototype

neutron detector designs and to confirm that the detectors were working appropriately. In addition, a comparison was made between using an MCA and using an oscilloscope to confirm that the two procedures would give the same results. This is to confirm that using the oscilloscope would be appropriate for measurement taking during the proton irradiation in the proton therapy room at Clatterbridge Hospital.

In the first prototype neutron detector design, the Cs^{137} spectrum was found to have a broadened spectrum peak due to the loss of scintillation light. The detector cell diameter (9cm) was much larger than the PMT diameter (5cm). In addition, scintillation light was lost due to the difference in refractive index between the air and the EJ-331 liquid scintillator. This degraded the energy resolution.

In the second prototype neutron detector design, the loss of scintillation light was avoided by using a cell with a 5.3cm diameter that matched the PMT diameter of 5.2cm. However, the improvement in the energy resolution was not adequate due to the light reflector, which was aluminium foil that had been mounted onto the cell wall manually.

In the third prototype neutron detector design, the detector cell was cylindrical (5.3cm x 5cm) and made of white plastic. The white inner wall of the cell was considered to be a light reflector. The detector energy resolution significantly improved as compared to the first and second prototype neutron detector designs.

The energy resolution of the second design was improved by 50% as compared to the first design. The improvement was approximately double in the third detector design, which was inferior by 25% to the Cs^{137} reference spectrum.

2.12 Conclusion

The first, second and third prototype neutron detectors were judged to have not met the physical and clinical criteria of a neutron detector to be used in a proton therapy room. The improvement for the energy resolution did not achieve the optimum, which is approximately 16% at Cs^{137} Compton edge energy.

Therefore, the target improvement for the energy resolution of the fourth prototype neutron detector will be 25% higher than the resolution achieved using the third prototype neutron detector. In addition, MC simulations will be used as an additional criterion to validate the fourth prototype detector design before the detector's construction.

2.13 Fourth prototype neutron detector design validation using an MC simulation program

Geant4 is an MC simulation toolkit that was written in the C++ programing language. It simulates and tracks the travel of particles through different materials. The toolkit includes a variety of physics, geometry, generators and user action models. In order to simplify Geant4, a few MC simulation toolkits were developed—for example, GAMOS, GATE and TOPAS [152] [153]. In addition to the simplicity of using GAMOS—where user action commands were used to describe, for example, physics, geometry and detector properties—three major medical applications were included [154] [155]:

1. Nuclear medicine.
2. Compton camera.
3. Radiotherapy.

Monte Carlo simulation programs (i.e. Geant4.9.5.p02 and GAMOS.4.0.0) were installed and run on Ubuntu 64-bit operating system (i.e. Linux operating system) in VMware Player for windows. Using the MC simulation program, GAMOS.4.0.0, and Geant4 codes, the fourth prototype neutron detector was validated with regard to the following aspects:

1. Detection material.
2. Container volume and light reflector.
3. Scintillation light and PMT.
4. DE and scintillation spectra.

2.13.1 MC simulations of DE spectrum

Geant4 was only used to simulate the fourth prototype neutron detector geometry, whereas GAMOS.4.0.0 was used to apply the required physics models, to simulate the radiation generators, to track secondary radiation particles, and to obtain energy histograms. An OLS was considered to be the optimum neutron detection material. Thus, three commercially available OLS detectors were compared. The three different types of OLS detectors (based on detection materials) were pure, boron-loaded and

gadolinium-loaded. These three materials were selected because they were regularly used for neutron detection. Table 17 shows the properties of the three simulated detection materials, which were a pure OLS (EJ-309), a gadolinium-loaded OLS (EJ-331) and a boron-loaded OLS (EJ-339) [156] [130] [157].

Table 17: Three OLS detectors simulated using GAMOS.4.0.0[156] [130] [157]**.**

Properties	EJ-309	EJ-331	EJ-339
Loaded	–	Gd 0.5%, w/w	B 0.95%, w/w
Density (g/cc)	0.959	0.90	0.92
Light output (photons/MeV)	11,500/MeV	10,400/MeV	10,000/MeV
Refractive index	1.57	1.50	1.415
H:C ratio	1.25	1.32	1.73
Wavelength of maximum emission	424nm	424nm	425nm
Bulk light attenuation length	>1m	>4m	–

The following GAMOS.4.0.0 physics lists were used:

- GmEMPhysics, which is an electromagnetic radiation physics list.
- GmEMExtendedPhysics, which is an electromagnetic radiation extended physics list.
- QGSP_BIC_HP, which is a neutron physics list.
- Opticalphoton, which is an optical photons physics list.

After this, the radiation generators (neutron and gamma-ray sources) were chosen to be Cs^{137} and $Am-Be$, and the detection material was chosen to be EJ-331, EJ-339 and EJ-309 respectively. At this stage, the detector's sensitive volume was selected to be the detection material (10cm diameter x 10cm height, cylindrical shape). GAMOS data analysis was used to select the data output file format (i.e. CSV, text or root file) and to obtain energy histograms. Figures 41 and 42 show the simulated DE spectrum of Cs^{137} (i.e. from gamma rays) and $Am-Be$ (i.e. from neutrons) obtained from the three scintillator MC simulations.

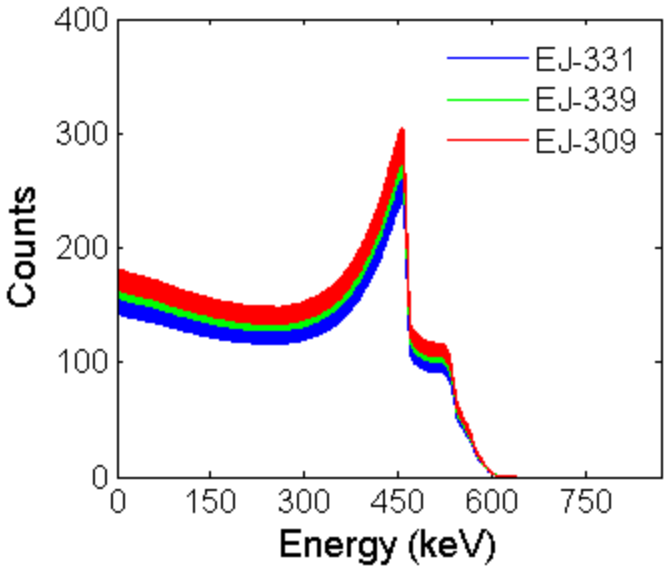

Figure 41: Simulated Cs^{137} gamma-ray DE spectrum from the three scintillator MC simulations.

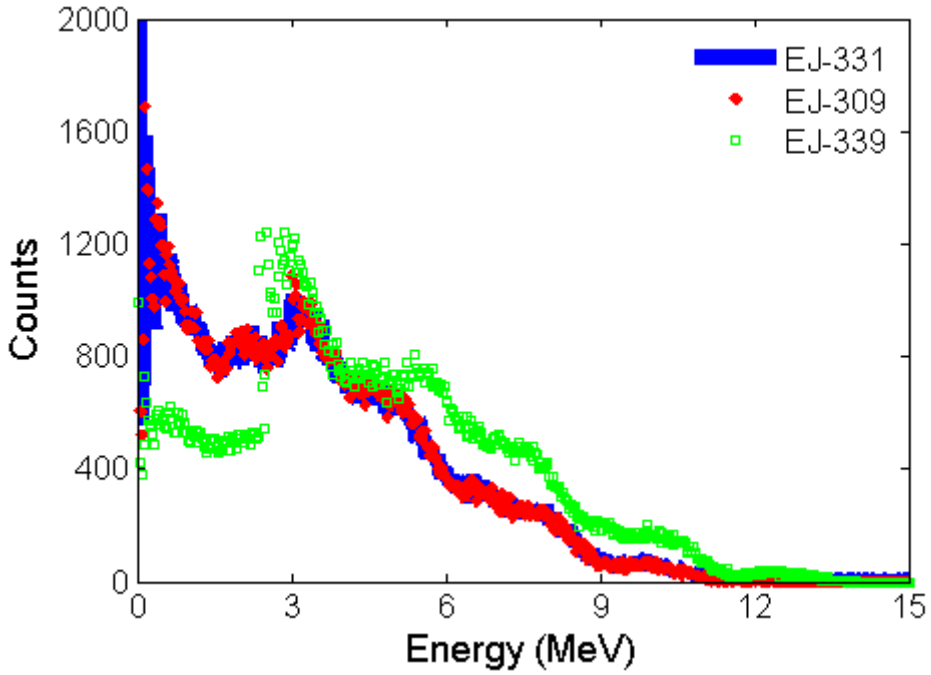

Figure 42: Simulated Am– Be neutron DE spectrum from the three scintillator MC simulations.

The plots of the simulated Cs^{137} DE spectra show that the three detection materials (EJ-331, EJ-339 and EJ-309) have the same response to the gamma-ray source.

However, the difference in the DEs of the three materials is due to the difference in their respective densities. On the other hand, the simulated Am–Be neutron DE spectrum of EJ-331 and EJ-309 show a difference of approximately <6% due to the difference between their H:C ratios. However, the fast neutron DE in EJ-339 appears to be higher than in EJ-331 and EJ-309 at high neutron energies due to EJ-339's H:C ratio, which is approximately 20% higher than the ratios of EJ-331 and EJ-309.

2.13.2 MC simulations of scintillation spectrum

The detection material properties (i.e. scintillation efficiency, refractive index and scintillation absorption length) and the detector container's specifications (i.e. shape, dimensions and light reflector) were added in the neutron detector geometry file. Furthermore, the scintillation process was activated using the opticalphoton physics list. Figure 43 shows the geometry image of the simulated neutron detector, the radiation generator and the scintillation light.

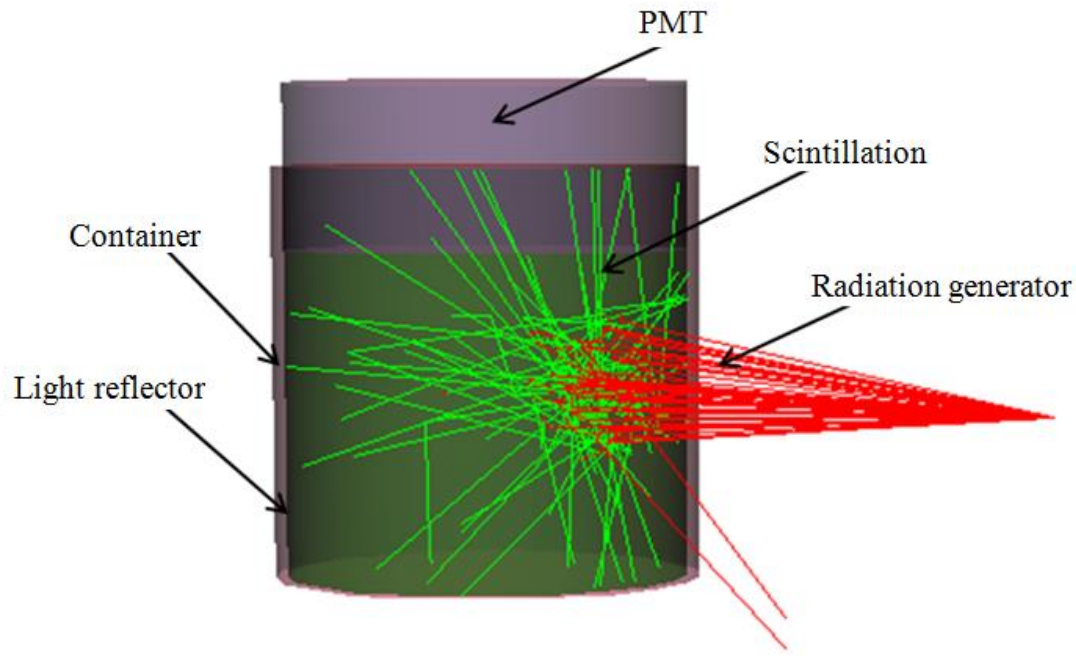

Figure 43: The geometry image of the simulated neutron detector, radiation generator and the scintillation light.

The container was cylindrical in shape (10cm diameter x 10cm height), with a glass window (95% light transparency and 1.5 refractive index) that was to be coupled to the PMT. The container was made of aluminium with a wall thickness of 3mm. The PMT was simulated to be cylindrical in shape with the same diameter as the scintillator. The PMT was glass and was attached to the side of the container. The coupling material (i.e. light guide) and the elimination of dissolved oxygen (i.e. nitrogen bubbling) were not considered. However, light loss regarding the use of the light guide (i.e. Perspex) and the dissolved oxygen effect (i.e. conducting nitrogen bubbling) were considered to be 8% and 2% respectively [158] [107]. Then, the detector was exposed to Cs^{137} and $Am-Be$ simulated sources respectively. The scintillation light photons, incident on the PMT, were scored and energy histograms were obtained. Figures 44 and 45 show the scintillation spectra of Cs^{137} and $Am-Be$ as obtained from the three scintillator MC simulations.

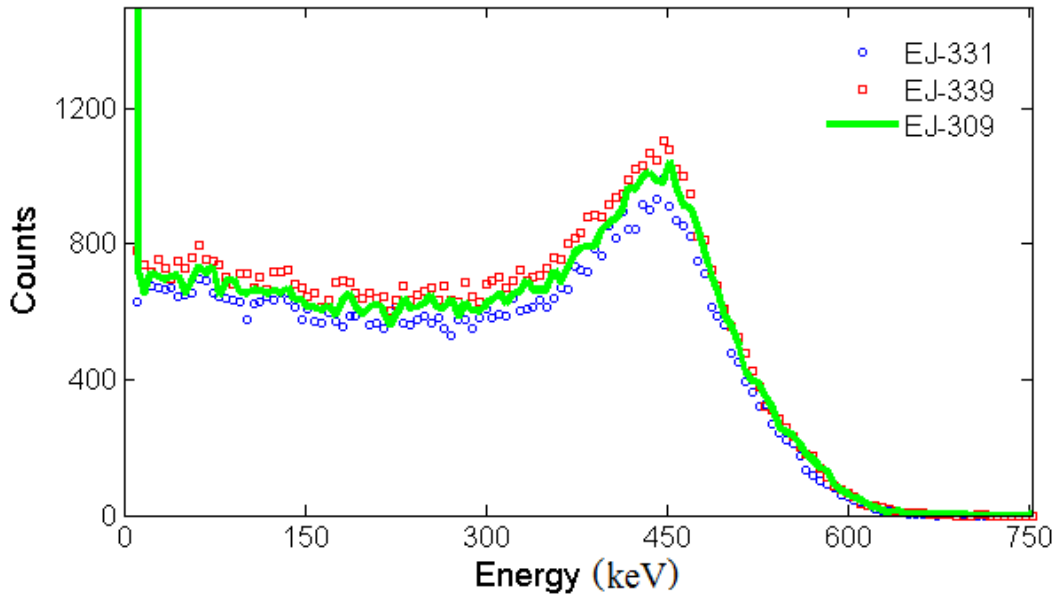

Figure 44: Simulated Cs^{137} gamma-ray scintillation energy spectrum from the three scintillator MC simulations.

According to the plot, the simulated Cs^{137} gamma-ray scintillation spectra show that the three detection materials (EJ-331, EJ-339 and EJ-309) have a similar response to the gamma-ray source. There is an approximately ±5% count difference in the scintillation efficiencies of the three materials.

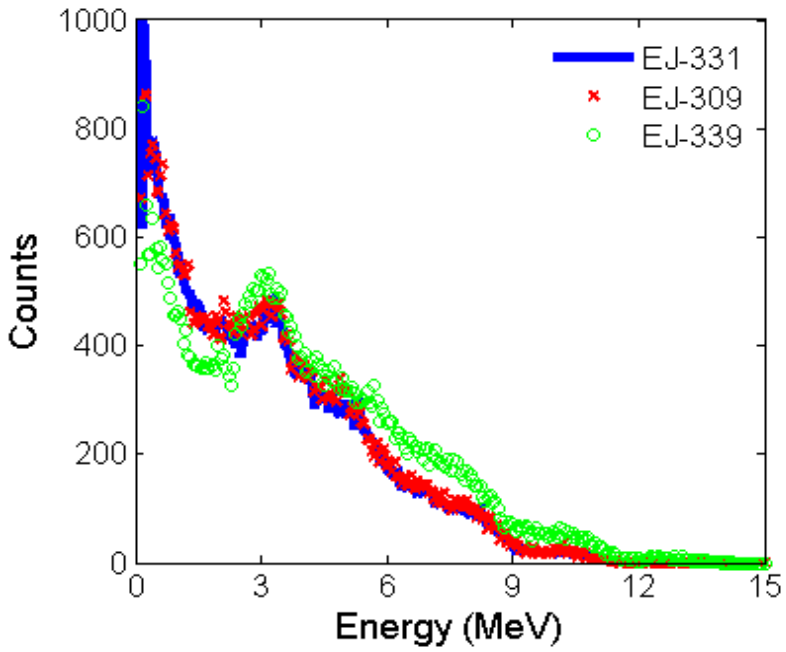

Figure 45: Simulated Am– Be neutron scintillation energy spectrum from the three scintillator MC simulations.

According to the plot, the simulated Am– Be neutron scintillation spectrum achieved with the EJ-331 and EJ-309 detection materials are similar. Whereas, EJ-339 is relatively better at detecting high-range neutron energy.

2.13.3 MC simulations of thermal neutron scintillation spectrum

The simulated neutron detector was exposed to 0.025eV thermal neutrons. Then, the thermal neutron scintillation spectra from EJ-331 and EJ-339 were obtained and are shown in Figure 46.

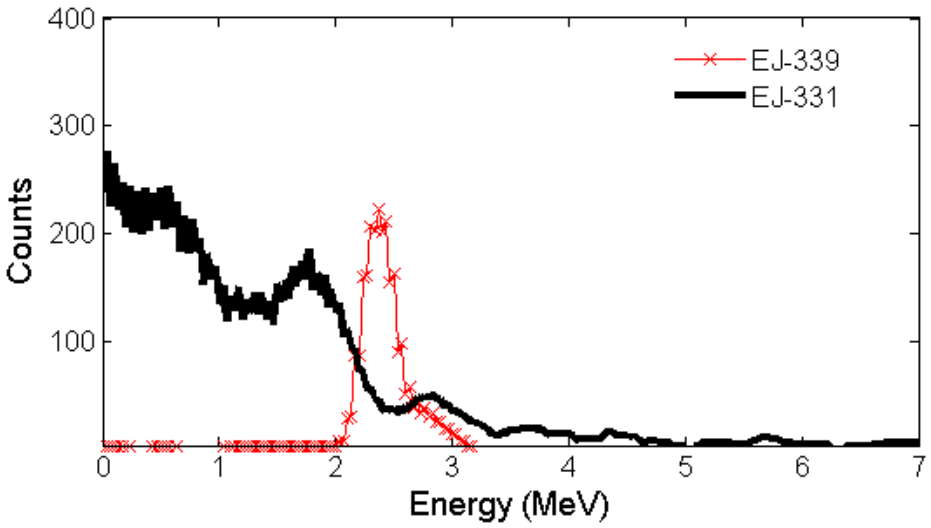

Figure 46: Thermal neutron spectra from EJ-331 and EJ-339 detection materials.

The plot shows that EJ-331 produced a continuous gamma-ray spectrum, which is related to the gamma rays released from the gadolinium and hydrogen thermal neutron capture reactions. The spectrum contains some gamma-ray Compton edges. The highest Compton edge count is around 2.15MeV (mainly from the de-excitation of excited $^{158}_{64}$Gd, which produces 3.288 gamma rays with an average energy of 2.394MeV). On the other hand, EJ-339's thermal neutron capture scintillation spectrum has two overlapping peaks, which are related to the alpha particles released from the boron thermal neutron capture reaction. The two peaks' energy distributions were around 2.4MeV.

Thermal neutron detection was found to be good with both EJ-331 and EJ-339. Nevertheless, in field measurements, applying PSD is required to separate fast and thermal neutron events from a high gamma-ray background.

Geant4 has the ability to simulate neutron and gamma-ray PSD [89]. In Geant4, the scintillation yield ratio (fast components/slow components), which forms the pulse shape of gamma-ray and neutron events, is written regarding the type of radiation particles (i.e. neutrons and gamma rays) and the well-known properties of the detection material. For example, EJ-331 produces scintillation light with different

scintillation yield ratios when it is exposed to gamma rays or neutrons. Therefore, PSD can be simulated to recognise the difference in these two radiation types.

However, more significantly, the MC simulation can be utilised to calculate the improvement in PSD performance with detector designs and experimental setups—for example, using different detector sizes, light guides and reflectors, and using a lead shield or fast neutron moderator [89]. Experimentally, the PSD performances of the three detection materials with regard to separating fast neutrons from gamma rays were reported to be good with EJ-331, EJ-339 and EJ-309 [156] [130] [157].

2.13.4 Energy calibration and detector resolution

The energy calibration of the organic scintillator neutron detectors can be done using the Compton edge energies of gamma-ray sources. The results from the MC simulations showed different shapes with regard to the DE and the scintillation spectra from the organic scintillator detectors. Figure 47 shows the MC simulations of the Cs^{137}scintillation and the DE spectra.

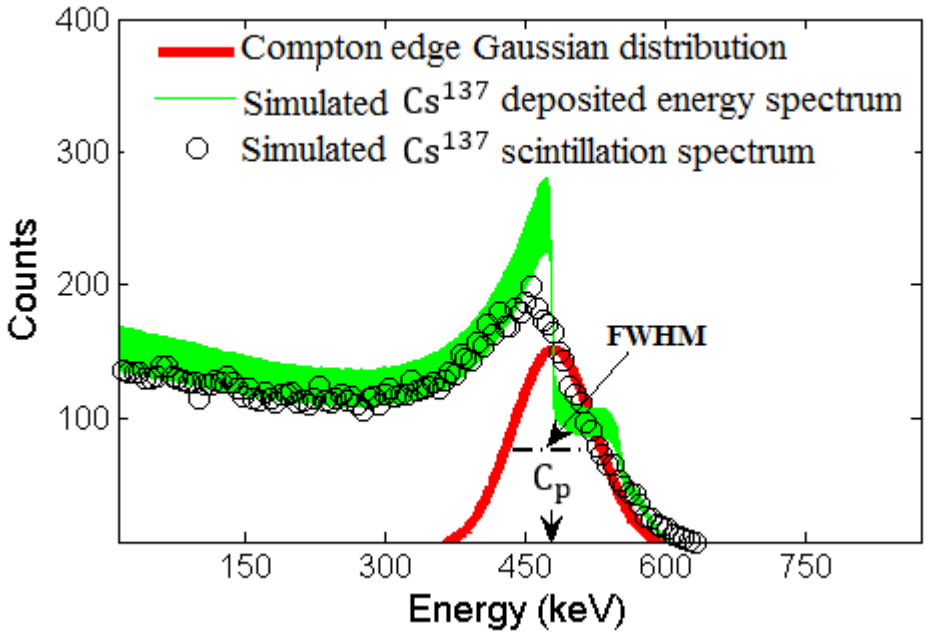

Figure 47: Simulated Cs^{137} scintillation spectrum plotted over simulated Cs^{137} DE spectrum to indicate the Compton edge position and the detector energy resolution.

The plot shows the Cs^{137} gamma-ray DE spectrum with the precise Compton edge position. It should be noted that the Cs^{137} Compton edge position cannot be observed on the scintillation spectrum. However, the Compton edge of the scintillation spectrum can be recognised by plotting the MC simulation of the DE spectrum over the scintillation spectrum, which can be measured.

Moreover, the energy resolution of the organic scintillator detectors can be obtained from the FWHM of the Compton edge Gaussian distribution over its peak position (i.e. energy, channel or volt). Thus, according to the MC simulation data, the simulated neutron detector energy resolution (C_p/FWHM) is 17% at the Cs^{137} Compton edge energy (i.e. 477keV). The Gaussian fitting of the Compton edge distribution was done using the MATLAB program.

2.13.5 Summary

Geant4 was used to simulate the fourth prototype neutron detector geometry, whereas GAMOS.4.0.0 was used to apply the required physics models, to simulate the radiation generators, to track secondary radiation, and to obtain energy histograms. An OLS was considered to be the optimum neutron detection material. Thus, three commercially available OLS detectors were compared. The three different types of OLS detectors were pure, boron-loaded and gadolinium-loaded. These three materials were selected because they have been regularly used in neutron detection. Comparisons were conducted between the DE spectra and the scintillation spectra of the Cs^{137} and $Am-Be$ radiation sources. In addition, the scintillation spectrum from the gadolinium and the boron thermal neutron capture was simulated.

The simulated Cs^{137}scintillation spectrum revealed that the three detection materials have similar response to the gamma-ray source. The simulated $Am-Be$ scintillation spectrum showed that the EJ-331 and EJ-309 were very similar, whereas the EJ-339 appeared to have higher detection efficiency at higher neutron energies due to its high H:C ratio.

2.14 The fourth prototype neutron detector construction

2.14.1 Design

The detector cell was a cylindrical aluminium container (10cm x 10cm) with a glass window (3mm Pyrex glass) to transmit the scintillation light to the PMT window. In addition, two valves were made on the container's sides for nitrogen bubbling. The container's inner walls were painted using titanium dioxide white paint (EJ-520) made by Eljen Technology [159]. The EJ-520 was tested and it was confirmed that it would not dissolve in strong chemical solvents. The container was filled with EJ-331, and the EJ-520's clear white colour did not change in the many observations conducted over several weeks.

The 9305KB PMT and the container's glass window were coupled using a cylindrical Perspex slab (3cm length x 7cm diameter). Optical grease (Cargille Optical Gel, code 0608) was used to eradicate the air gaps between the coupled materials. The Cargille 0608 has 99% light transparency, with a 1mm thickness and a 1.47 refractive index at 424nm light wavelength [160]. Figure 48 shows a diagram of the fourth prototype neutron detector design.

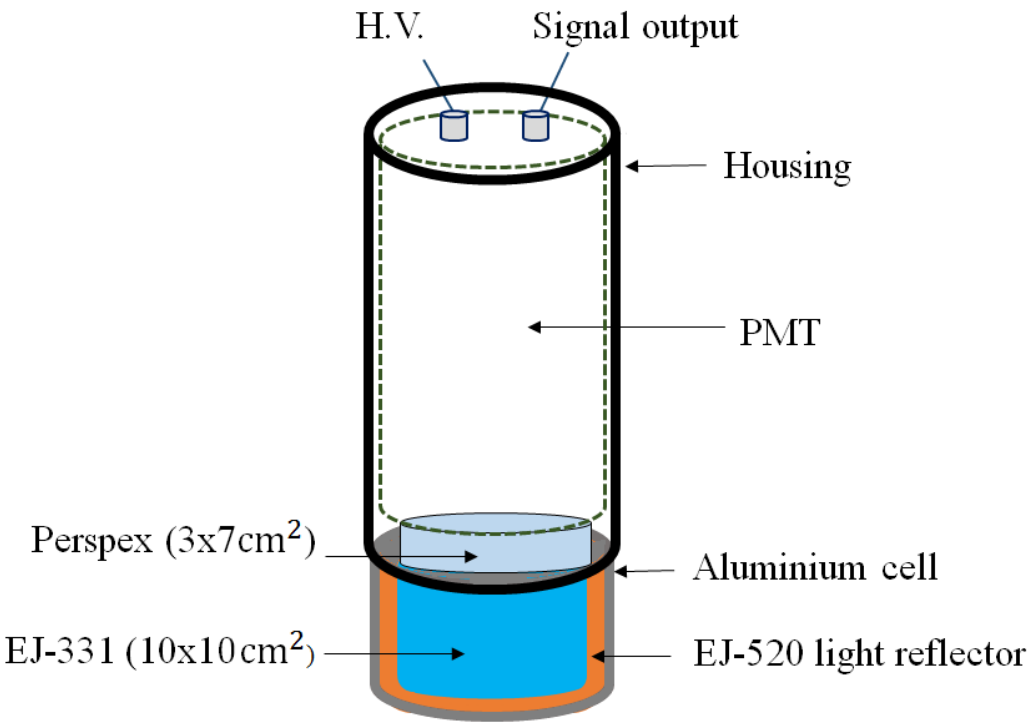

Figure 48: Diagram of the fourth prototype neutron detector design.

2.14.2 Nitrogen bubbling

Dissolved oxygen can be removed from OLS detectors using three methods: ultrasonic degassing [161], vacuum distillation, and inert gas (such as nitrogen and argon [162]) bubbling. Among the three techniques, a low-cost and easy procedure for oxygen elimination is inert gas bubbling. Therefore, an inert gas (nitrogen) was used to eliminate the dissolved oxygen in the EJ-331. Figure 49 shows the detector container under the fume hood filled with EJ-331 and connected to the nitrogen cylinder through the container's side valve.

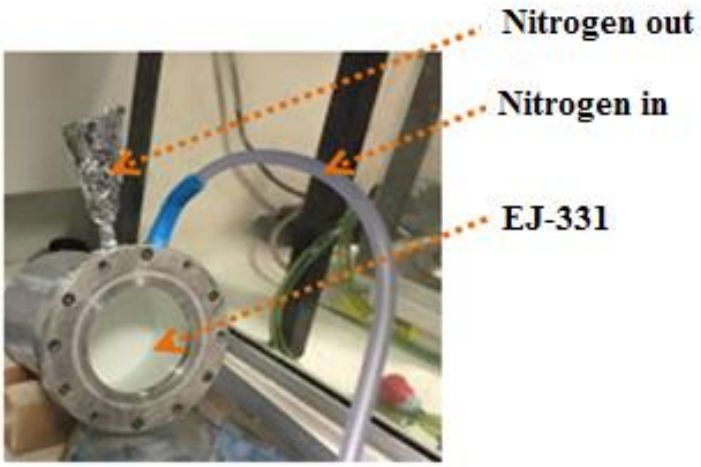

Figure 49: Detector container under the fume hood filled with EJ-331 and connected to the nitrogen cylinder through the container's side valve.

The container's valve and the nitrogen gas cylinder were connected under the fume hood using a plastic pipe, and the EJ-331 liquid scintillator (785cm^3) was purged with a 150ml/min nitrogen flow rate for 1.5 hours. It was reported that the light yield of an OLS with a volume of 49cm^3 would reach 98% and then saturate after purging the liquid with nitrogen gas at a flow rate of 40ml/min for 15 minutes and 30 minutes respectively [107].

2.14.3 The fourth prototype neutron detection efficiency

The detector efficiency is the number of recorded radiation particles over the number of incident radiation particles. The neutron detection efficiency was calculated according to the neutron energy range, which was between 1MeV and 56MeV. The recoil proton detection and total fast neutron detection efficiencies can be calculated with the following equation [12]:

$$\mathbf{En}_{\mathbf{total}} = \mathbf{1 - e^{-(H(atoms*\sigma)+C(atoms*\sigma)*x)}}$$

$$\mathbf{En}_{\mathbf{recoil}} = \frac{\mathbf{H(atoms*\sigma)}}{\mathbf{H(atoms*\sigma)+C(atoms*\sigma)}} \mathbf{(1 - e^{-(H(atoms*\sigma)+C(atoms*\sigma)*x)})}$$

Here, En_{total} is the total fast neutron detection efficiency and En_{recoil} is the recoil proton detection efficiency. $H(atoms * \sigma)$ is the product of the number of hydrogen atoms multiplied by the hydrogen fast neutron microscopic cross section, while $C(atoms * \sigma)$ is the product of the number of carbon atoms multiplied by the carbon fast neutron microscopic cross section [163] [164] [165]; x is the detection material's thickness (i.e. EJ-331 thickness).

The calculated total neutron detection efficiency of the fourth prototype curve is shown in Figure 50.

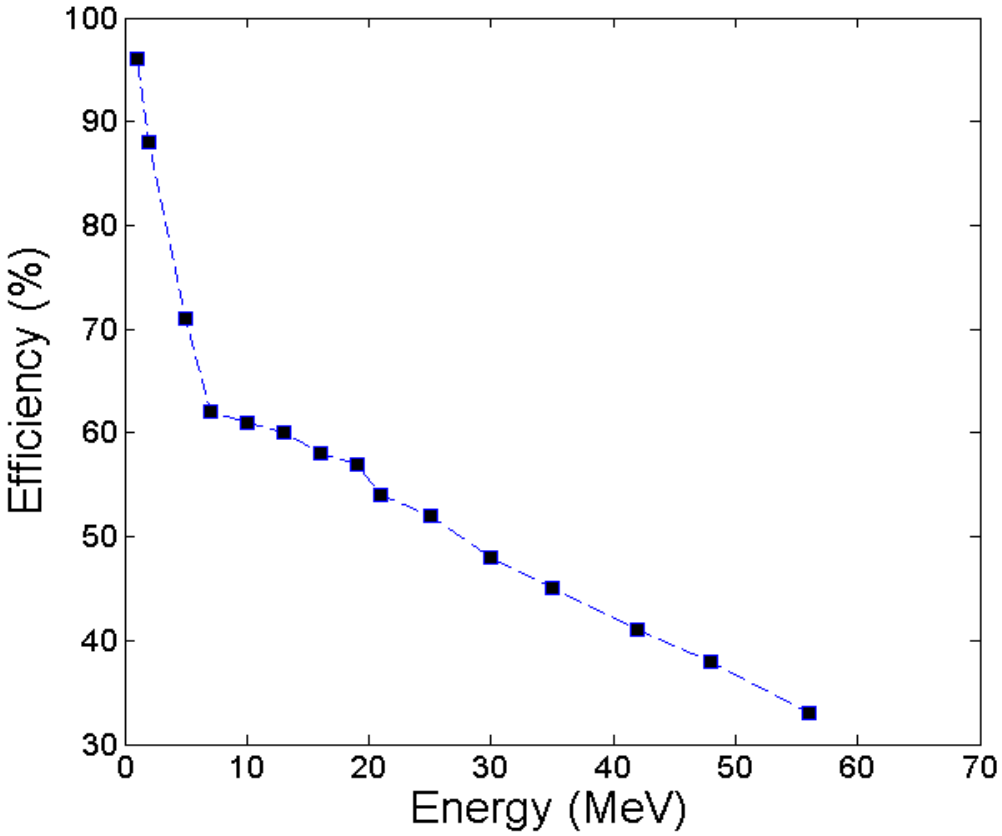

Figure 50: Calculated total neutron detection efficiency of the fourth prototype neutron detector.

According to Figure 50, the neutron detection efficiency with the neutron energy of a 1MeV was >90%. Then, the detection efficiency dropped rapidly with the neutron energy being 62% at 7MeV to 8MeV. The detection efficiency dropped gradually between 8MeV to 20MeV to be 57% at 20MeV. This is a result of increasing the

neutron total cross section of the carbon at high neutron energies [166] [106]. After this, the efficiency dropped as neutron energy was increased to be 34% at 56MeV. Thus, the fourth prototype neutron detector has good neutron detection efficiency and is able to detect secondary neutrons over a wide energy range during the proton irradiation at Clatterbridge Hospital.

2.14.4 Experimental setups

The experiments using the fourth prototype neutron detector were conducted using two setups. In the first setup, the detector was connected to the MCA through the shaping amplifier. The MCA output was displayed and stored using MAESTRO software for Windows on a laptop. In the second setup, the detector was connected to the oscilloscope, and the oscilloscope output was recorded and displayed using PicoScope software for Windows on a laptop.

The objectives of the first setup were to confirm that the detector was working properly, to compare the result with results from the literature review, and to find the detector's energy resolution.

The objective of the second setup was to calibrate the detector energy range (volt to MeVee). MeVee (electron equivalent energy) is a term used to compare the light produced from interactions of different radiation types (e.g. proton and alpha) to the light produced from electrons [12]. For example, the scintillation light produced from protons is significantly less than the scintillation light produced from electrons, both with the same energy [167].

Figure 51 shows the experimental setup schemes. In the two setups, the applied voltage was fixed at 1,250V and the radiation source was directly attached to the outer lower side of the detector cell.

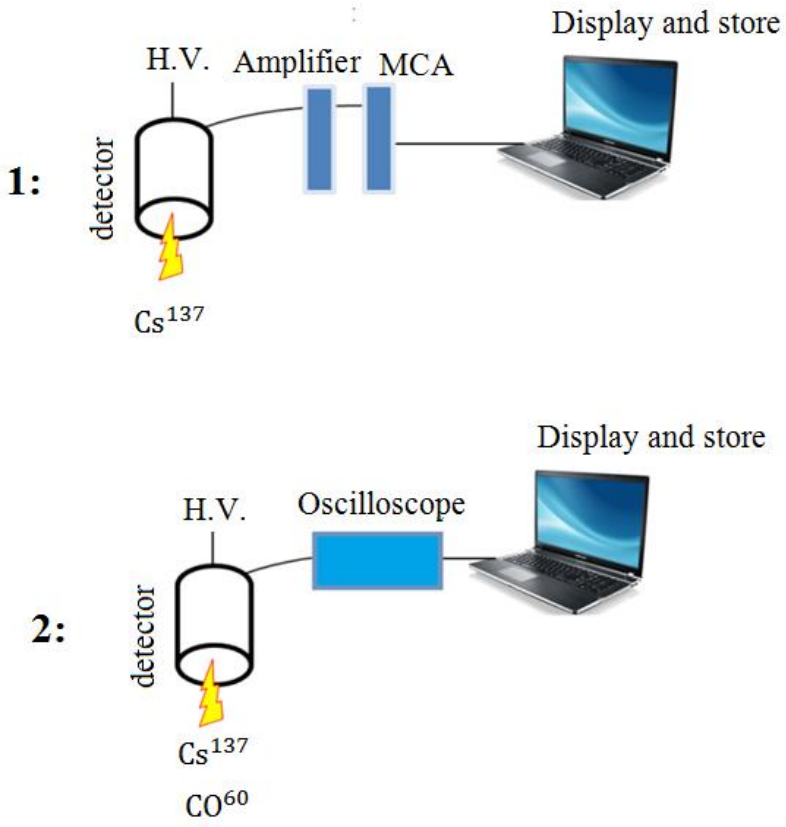

Figure 51: Experimental setup schemes.

2.14.5 Results and discussions

- **Gamma-ray spectroscopy**

The detector was exposed to the Cs^{137} gamma-ray source and the spectrum was plotted and compared to the reference Cs^{137} spectrum. Figure 52 shows the obtained spectrum compared with the reference Cs^{137} spectrum.

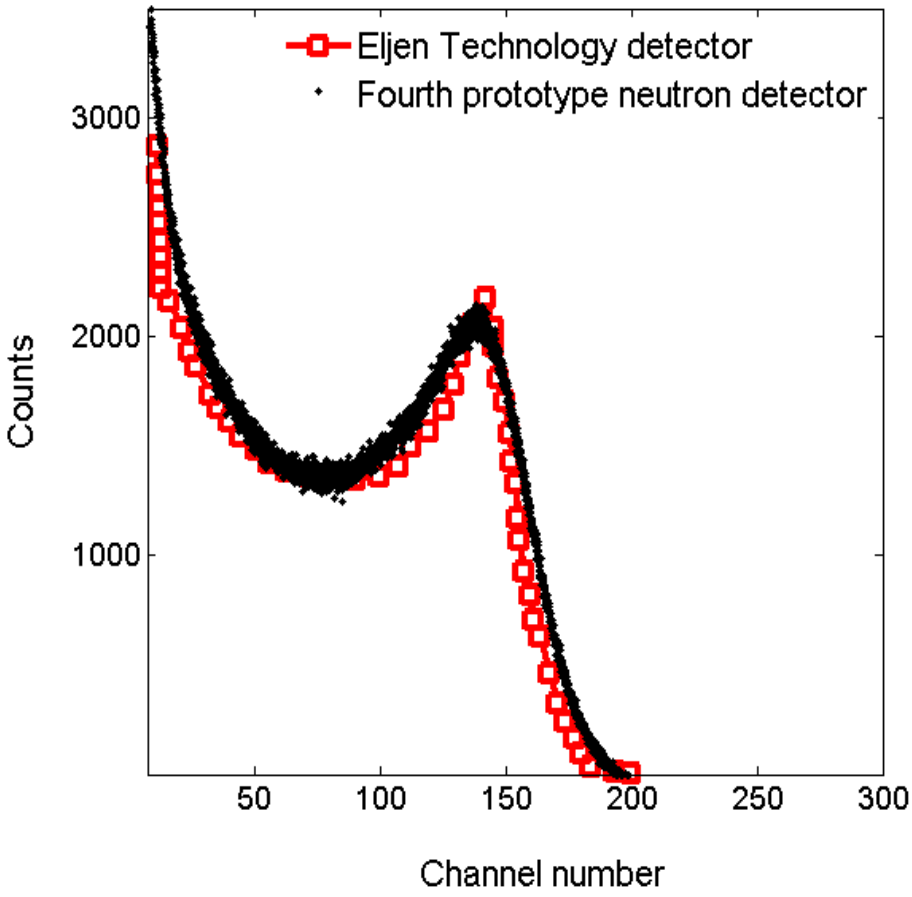

Figure 52: The obtained Cs^{137} spectrum from the fourth prototype neutron detector plotted over the extracted data from the reference Cs^{137} spectrum (i.e. from Eljen Technology detector).

The improvement of the Cs^{137} spectrum result when using the fourth prototype neutron detector was evident compared to the first, second and third prototype neutron detectors. Thus, the obtained spectrum shape was comparable to the reference Cs^{137} spectrum.

Figure 53 shows the obtained Cs^{137} spectrum plotted over the Cs^{137} spectrum obtained from the third prototype neutron detector.

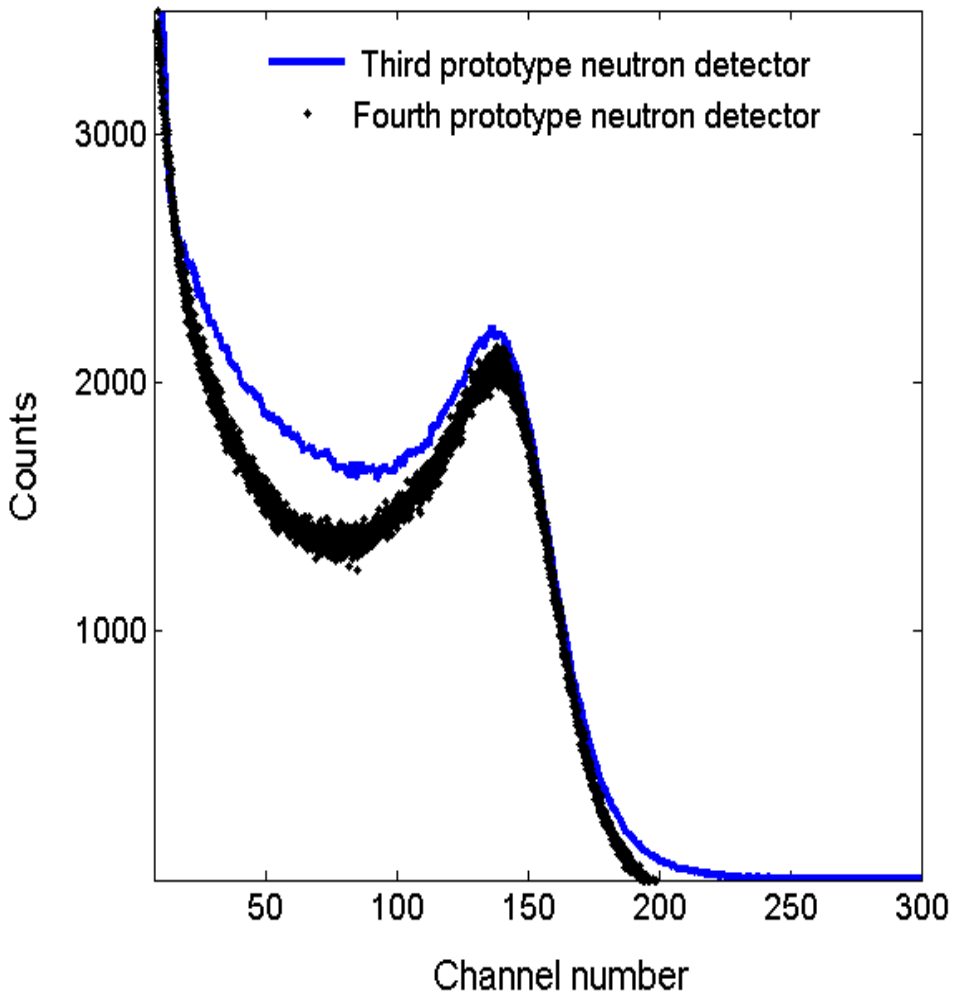

Figure 53: The obtained Cs^{137} spectrum from the fourth prototype neutron detector plotted over the Cs^{137} spectrum obtained from the third prototype neutron detector.

In addition, the Cs^{137}spectrum obtained from the fourth prototype neutron detector was compared to the Cs^{137} spectrum obtained using an MC simulation. In order to compare the simulated and measured Cs^{137} spectrum, the simulated Cs^{137} spectrum was normalised to be the same in length and counts as the measured Cs^{137} spectrum. This was done using a MATLAB program. Thus, the two results were in agreement and this is shown in Figure 54.

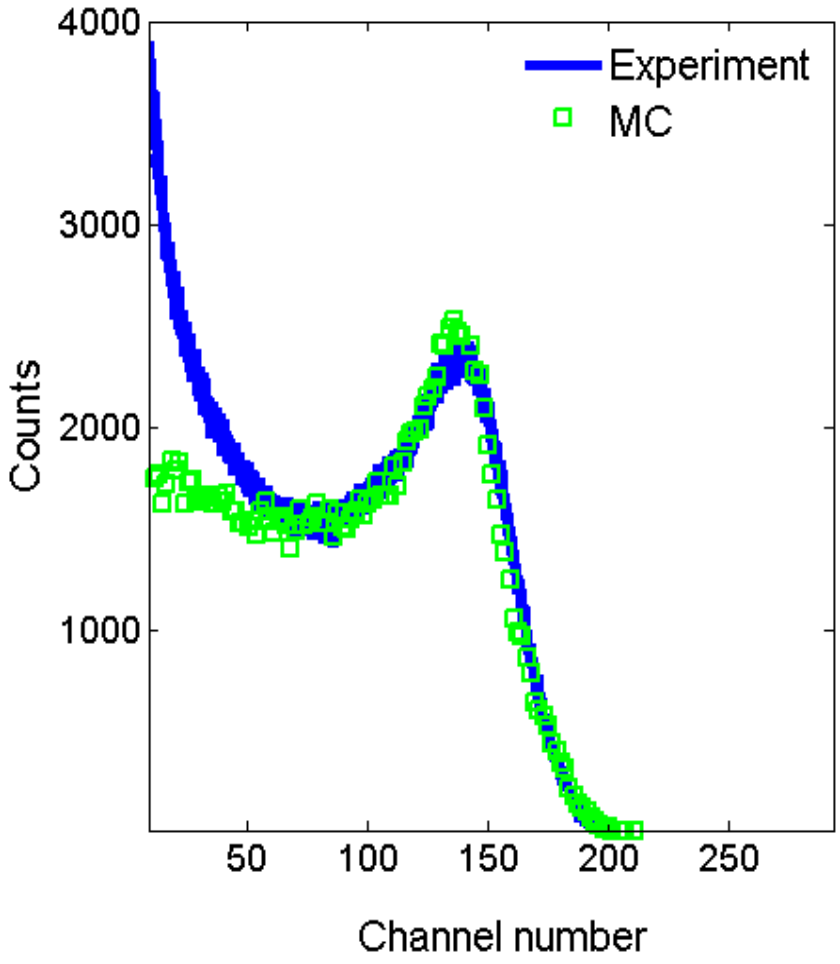

Figure 54: The experimental Cs^{137} scintillation spectrum as compared to the MC simulation of the Cs^{137} scintillation spectrum.

2.14.6 Detector energy range calibration

Using the second experimental setup, the energy calibration of the fourth prototype neutron detector was conducted. The detector was exposed to two gamma-ray sources: Cs^{137} and Co^{60}. By comparing the MC simulation of the DE spectrum to the measured scintillation energy spectrum, the Compton edges of the two sources were recognised. Figure 55 shows the Cs^{137} and Co^{60} scintillation energy spectra plotted over Cs^{137} and Co^{60}simulated DE spectra.

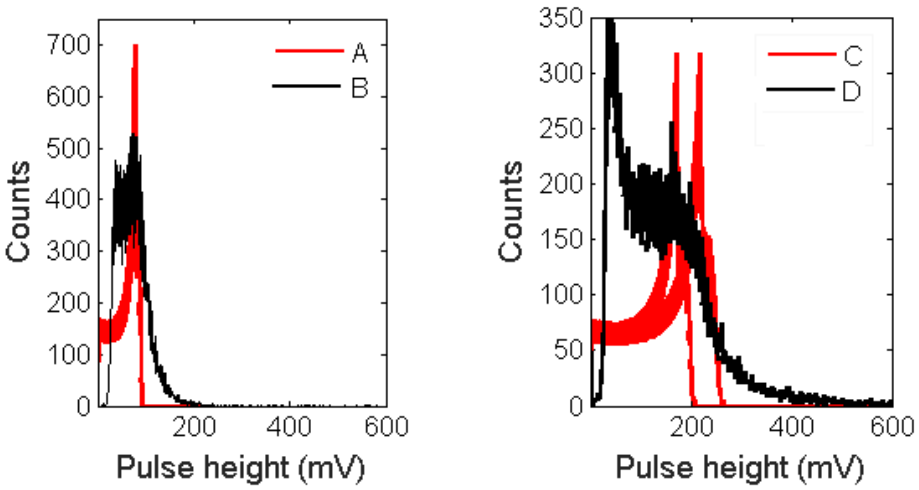

Figure 55: Cs^{137} (left) and Co^{60} (right) scintillation energy spectra (B and D) plotted over Cs^{137} and Co^{60}simulated DE spectra (A and C) to calibrate the detector energy range.

The energy calibration curve of the detector is shown in Figure 56. The calibration factor is the factor used to convert voltage to MeVee. This is equal to the Compton edge position in millivolt (mV) over the Compton edge energy in MeVee. Thus, the obtained calibration factor was 0.233±0.009 (volt to MeVee).

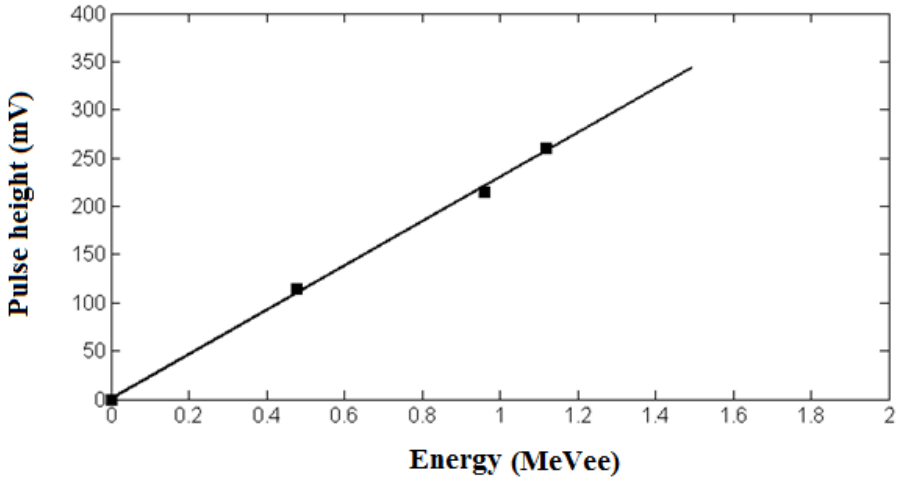

Figure 56: Energy calibration curve ±4% of the fourth prototype neutron detector.

2.14.7 Detector energy resolution

Based on the measured and the simulated DE Cs^{137}spectrum, the detector energy resolution was identified. The detector energy resolution was measured as the FWHM of the Compton edge Gaussian distribution over the position of the Compton edge. Figure 57 shows the procedure followed to obtain the fourth prototype neutron detector energy resolution.

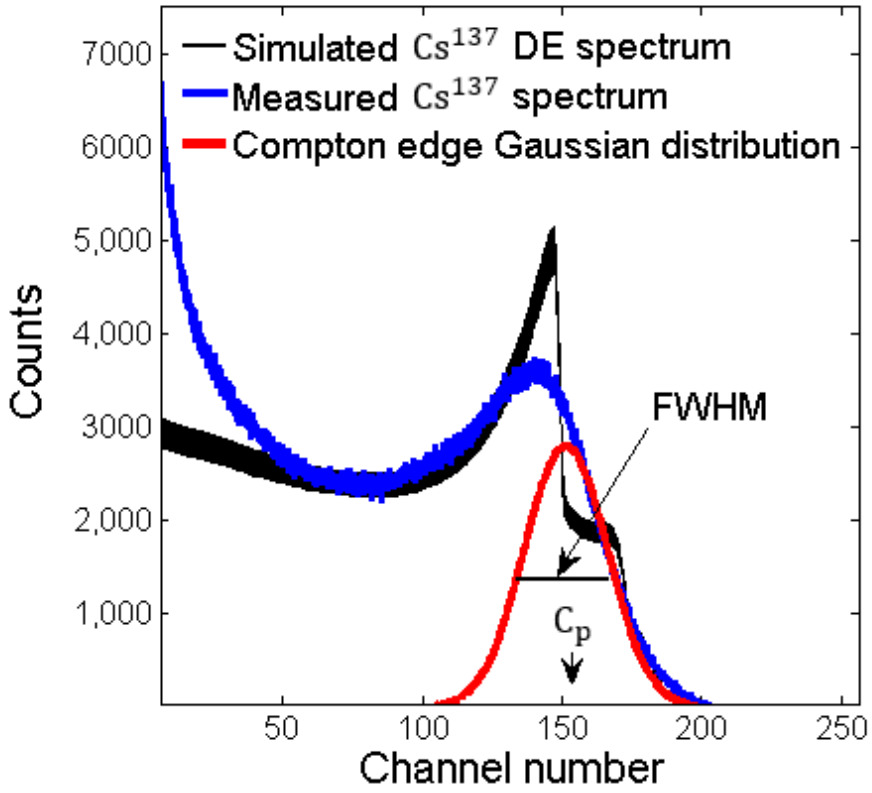

Figure 57: MC simulation and measured data used to obtain the energy resolution (C_P/FWHM) and the Compton edge position (C_P).

The measured detector energy resolution was the same as the simulated detector energy resolution, which was 17% at the Cs^{137} Compton edge position.

2.14.8 Summary

A gadolinium-loaded OLS (EJ-331) was considered to be a convenient detection material. The detector cell was 10cm x 10cm and was a cylindrical aluminium container. The container's inner walls were painted using titanium dioxide white paint (EJ-520). The 9305KB PMT and the container glass window were coupled using a cylindrical Perspex slab that was 3cm long x 7cm diameter. Optical grease (Cargille 0608) was used to eradicate the air gaps between the coupled materials. The Cs^{137} spectrum shape obtained using the fourth prototype neutron detector was comparable to the reference Cs^{137} spectrum shape. In addition, the detector had good neutron detection efficiency and was able to detect secondary neutrons over a wide energy range during the proton irradiation at Clatterbridge Hospital. Furthermore, the measured detector energy resolution was the same as the simulated detector energy resolution, which was 17% at the Cs^{137} Compton edge position. In addition, the energy calibration curve was obtained and the calibration factor was 0.233±0.009 (volt to MeVee).

2.15 Conclusions and discussions

The first, second and third prototype neutron detectors showed that light collection is a critical specification of OLS detectors. In addition, the calibration of the OLS detector energy range using gamma-ray sources required recognition of the Compton edge position. The FWHMs of the Compton edge or the spectrum peak Gaussian distribution were used to evaluate the OLS detector's energy resolution.

Though the energy resolution of the third prototype neutron detector was inferior by 25% as compared to the Cs^{137} reference spectrum, it was equivalent to some results from the literature review. For example, it was comparable to the Cs^{137} spectrum obtained using the EJ-309 liquid scintillator detector [168]. Figure 58 shows a comparison between the Cs^{137} spectrum obtained using the third prototype neutron detector and the extracted data from the Cs^{137} spectrum obtained using the EJ-309 liquid scintillator detector [168].

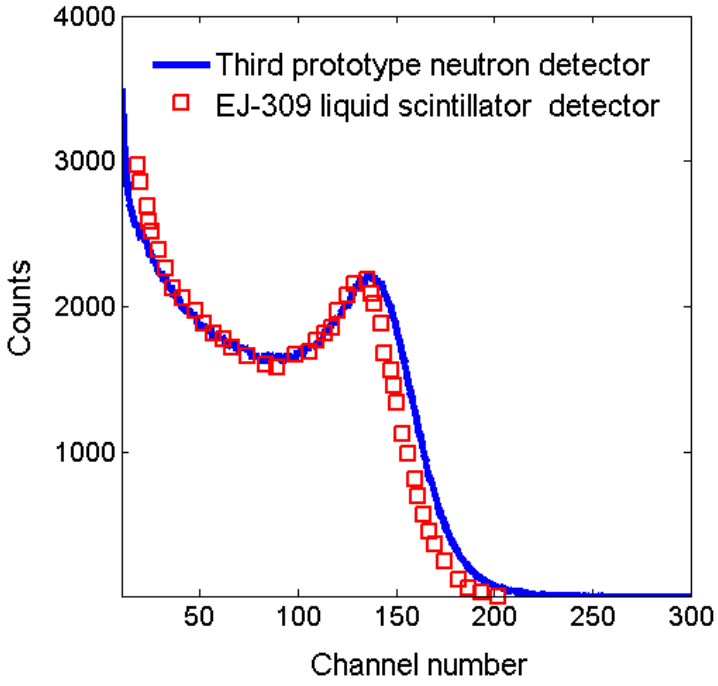

Figure 58: A comparison between the Cs^{137} spectrum obtained using the third prototype neutron detector and the extracted data from the Cs^{137} spectrum obtained using the EJ-309 liquid scintillator detector [168]**.**

However, the first, second and third prototype neutron detectors were judged to have not met the physical and clinical criteria of a neutron detector to be used in a proton therapy room.

The fourth prototype neutron detector energy resolution was considered to be an optimum energy resolution. In addition, the detection efficiency was found to be good enough to detect the neutron energy range from thermal to 60MeV of low intensity during proton irradiation. Furthermore, the PSD performances of the EJ-331 detection material with regard to separating fast neutrons from gamma rays were reported to be good. However, the PSD performance of the fourth prototype neutron detector will be examined in the next chapter.

Thus, the fourth prototype neutron detector meets the physical and clinical criteria and would be efficient in detecting different radiation types in a proton therapy room, particularly in the proton therapy room at Clatterbridge Hospital. In addition, it could be used in other mixed neutron and gamma radiation fields.

Chapter 3. Pulse shape discrimination with an organic liquid scintillator detector

3.1 Introduction

The mixed secondary radiation field during proton therapy (neutrons, gamma rays and other radiation particles [85] [122]) necessitates the use of methods to discriminate between the different radiation types. This chapter describes the use of PSD. PSD is applied using the following different methods:

- Charge comparison PSD method

The charge comparison PSD method has been widely used [169]. This method is applied by comparing the integration of a pulse charge at two different times during the scintillation pulse lifetime. The integration can be done through the summation of the pulse charge under the pulse curve at any two time periods of interest. Often, the time periods of interest are the pulse total charge and the pulse tail charge time periods. Thereby, the charge comparison PSD method is obtained by finding the ratio of the two time periods of interest —for example, the tail-to-total PSD method [103].

- Rise time PSD method

The rise time PSD method is applied by measuring the time taken for the scintillation pulse to reach a specific portion of the pulse peak [170]. Therefore, the time taken for the HLET particles (i.e. protons) will be more than the time taken for the low linear energy transfer (LLET) particles (i.e. electrons) [171]. This PSD method has been widely used [169]. The rise time PSD method can be applied in several ways, such as the zero crossover [172], time over threshold [173] and the trailing edge pulse timing [174] PSD methods.

- Charge to amplitude comparison PSD method

The charge to amplitude comparison method is obtained in a similar way to the charge comparison PSD method. The difference here is the comparison between the pulse charge and the pulse amplitude, while, in the charge comparison PSD method, the comparison is done between two charge integrals. Thereby, the charge-to-amplitude comparison method is obtained by finding the ratio of the pulse charge to the pulse amplitude—such as the charge-to-current ratio PSD method [174].

3.2 The scintillation process of an organic liquid scintillator

A scintillation emission in an organic scintillator is produced as a result of the changes in the energy level states of the organic molecules (hydrocarbons), regardless of the molecules' physical state (solid, liquid or gas) [175]. Organic molecules with a π-electron, such as ethylene (C_2H_4) and acetylene (C_2H_2), emit visible light when they are exposed to radiation [176]. Figure 59 shows the energy level states of organic molecules with π-electron configurations as presented by Birks [176].

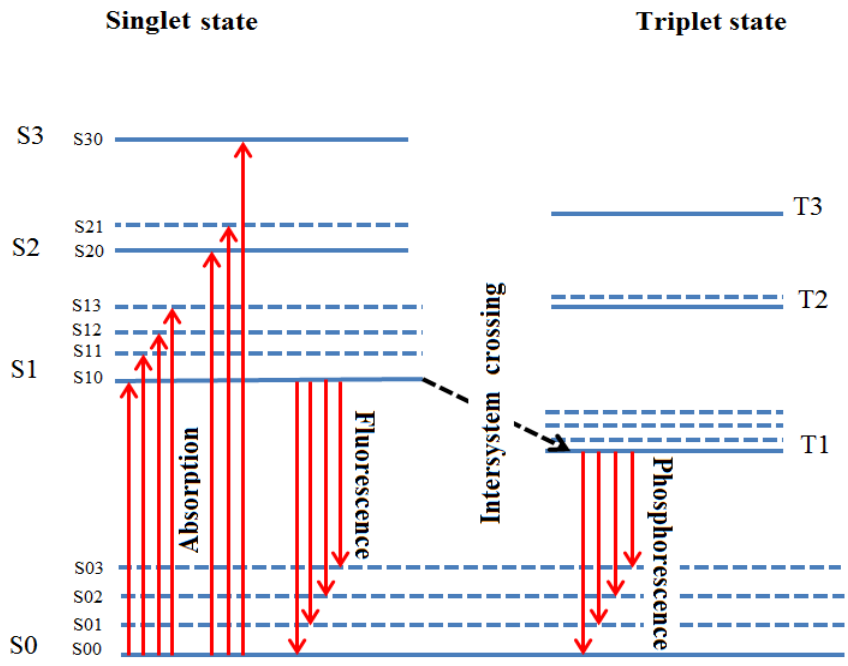

Figure 59: Energy level states of organic molecules with π-electron configurations as presented by Birks [176].

Energy level states of π-electron organic molecules are singlet (S_0, S_1…) and triplet (T_1, T_2…). In addition, each singlet energy level contains vibrational levels ($S_{00,}$ S_{01}…) with energy spaces of 0.15eV. At room temperature (20–26°C), organic molecules are in the lowest (ground) energy level state (S_{00}) [12]. Typically, the energy needed for π-electron organic molecules' excitation from ground energy level (S_0) to the first excited energy level (S_1) is 3eV to 4eV.

The scintillation process of the organic molecules is divided into three categories: prompt fluorescence, delayed fluorescence and phosphorescence.

Firstly, prompt fluorescence (fast components) occurs through the excitation of the organic molecules (i.e. it is exposed to radiation particles) from ground singlet energy level (S_0) to higher energy level (S_2, S_3 ...). The molecules' de-excitation occurs from the higher energy level to S_1 through radiationless IC in picoseconds [177], followed by de-excitation from S_1 to the ground energy level (S_0), with visible light emission in only a few nanoseconds [12].

Secondly, delayed fluorescence (slow components) occurs when a singlet S_1 (spin 0) excited energy level transforms to a triplet T_1 (spin 1) excited energy level through a process called intersystem crossing [178]. Then, the organic molecule returns (i.e. thermally) to the singlet state and de-excites from S_1 to ground energy level (S_0) through visible light emission [179]. This process takes significantly more time than the prompt fluorescence process (i.e. a few hundred nanoseconds) [12].

Fast component and slow component emissions are created from the interaction of both gamma rays and neutrons with the organic scintillator [180]. However, the emission ratio (slow components/fast components) of the organic scintillator is changeable regarding the type of radiation (neutron or gamma ray) [181] [182]. The emission ratio regarding neutron interaction is significantly higher than the ratio related to gamma-ray interaction. The probability of a slow component emission compared to a fast component emission is significantly higher with HLET particles, such as neutrons (i.e. recoil protons) and alphas.

Thereby, in comparison with a gamma-ray pulse shape (i.e. electron pulse shape), a neutron pulse shape (i.e. recoil proton pulse shape) has a longer tail that is formed by the high-ratio emission of the slow components. Figure 60 shows the electron and

recoil proton scintillation pulses obtained using the fourth prototype neutron detector and an Am–Be neutron–gamma source.

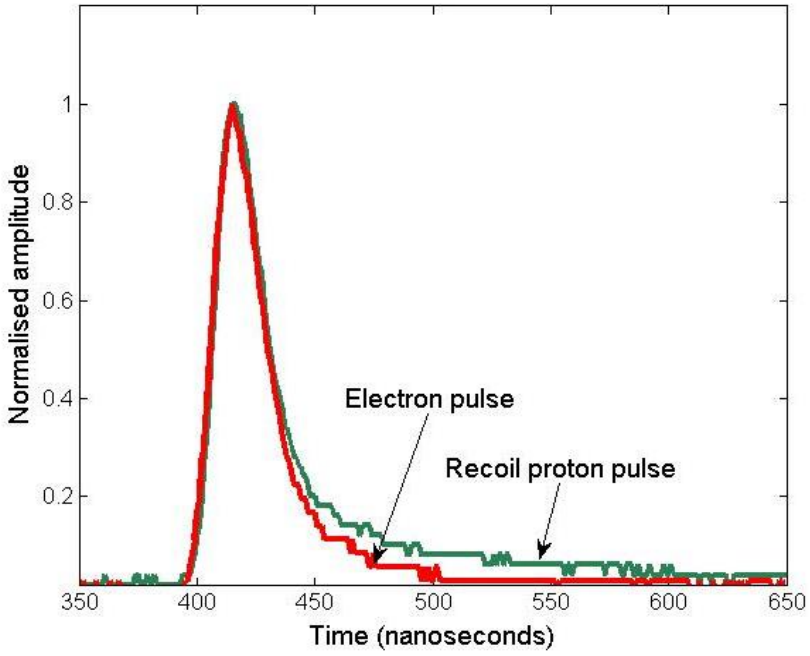

Figure 60: Electron and recoil proton scintillation pulses obtained using the fourth prototype neutron detector and an Am–Be neutron–gamma source.

Thirdly, phosphorescence occurs when an organic molecule de-excites from excited triplet level (T_1) to ground singlet level (S_0) without returning back to singlet excited level (S_1). This process is unlikely to happen [183] as it occurs in seconds, which is excessively longer than fluorescence time, and it has a longer scintillation light wavelength therefore, it may not be useful in some applications, such as radiation detection and spectroscopy.

3.3 Absolute light yield of organic scintillators

The absolute light yield (i.e. scintillation efficiency) is the gross scintillation light photons produced by a scintillator over the radiation DE (i.e. light-photons/MeV) [184]. The light yield of the organic scintillators is determined by the type and the energy of incoming radiation particles [185]. In addition, the quenching effect should be considered.

HLET particles, such as protons and alphas, produce low-light photons compared to LLET particles, such as electrons. For example, the light photons yield from the interactions of a 40MeV proton is equal to the light yield from the interactions of a 31.1MeV electron [167]. The low light yield of HLET particles is a result of the quenching effect, which has less of an effect at higher energies. Regarding the HLET particles, the main reduction of the light yield was found in the amount of fast components [176] [186].

Although the DE is directly proportional to the light photons yield, the relationship was found to be nonlinear [184]. The nonlinearity with gamma rays was observed for an energy range lower than 100keV [187]. On the other hand, the nonlinearity of the HLET particles was significantly greater than LLET particles at a wide energy range. The nonlinearity is related to the variation of the quenching effect with the radiation energy [188]. HLET particles significantly have a higher quenching effect (especially at low energy)—more than that of LLET particles [186]. In addition, the quenching agents in the scintillators, such as dissolved oxygen, impurities and quenching centres (scintillator damages), decrease the intensity of the light photons [162] [189].

To conclude, the light yield from the same DE of HLET particles and LLET particles is different. LLET particles' light yield is significantly higher than HLET particles' light yield. The reduction of the HLET particles' light yield is mainly from fast component intensity.

3.4 PSD Figure of merit

The PSD figure of merit (FoM) is defined as the separation between two radiation type peaks (e.g. electron-proton and electron-alpha separation) over the sum of the FWHM of the two radiation type distributions [190]. On a practical level, the FoM can be measured easily from the PSD method's data histogram [191]:

$$\mathbf{FoM = L/(N+G)}$$

Where L is the separation between the two peaks, N is the FWHM of the first radiation type distribution and G is FWHM of the second radiation type distribution. Figure 61

shows a diagram of the PSD FoM calculation, which evaluates the separation efficiency between two radiation particle distributions.

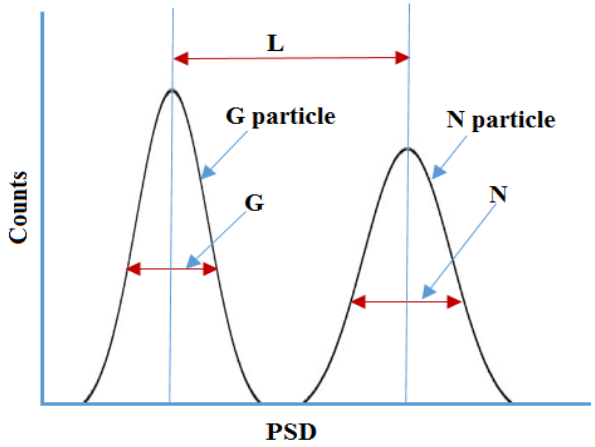

Figure 61: Diagram of FoM calculation, which evaluates separation efficiency between two radiation particle distributions (G and N).

FoM is being used to evaluate the performance of the PSD method. Thus, a higher FoM value means higher efficiency of the PSD achieved [192]. The calculation of the FoM value over a large energy range reflects the PSD performance of the detector (detection material and devices), while the calculation over a particular or short energy range can show the detection material properties [193].

The PSD performance is significantly affected by the detection material properties, the radiation energy range, and the devices used (e.g. the oscilloscope's properties) [194] [195].

Theoretically, the PSD performance is 100% for a FoM≥1.5. Therefore, the achieved rejection ratio of background or unwanted radiation particles will be approximately 100%. However, in practical terms, the PSD efficiency could be less than 100%—for example, due to pile-up events [194]. The rejection ratio related to the FoM values was calculated and is shown in Table 18 [193].

Table 18: Rejection ratio related to FoM values [193]**.**

FoM	Rejection ratio of x from y
0.5	2:1
0.75	12.5:1
1.0	750:1
≥1.5	∞

The table shows the rejection ratio of particle x from particle y; for example, at 0.75 FoM value, the rejection ratio is 12.5:1. This means that 1/12.5 of x particle counts cannot be recognised as x or y particles (e.g. overlap of x and y particles). Figure 62 shows the pulse tail charge versus the pulse total charge of neutron and gamma-ray events with an overlap area. The overlap area is the area where the type of radiation particles (i.e. neutron or gamma ray) cannot be recognised. This data was obtained during this research.

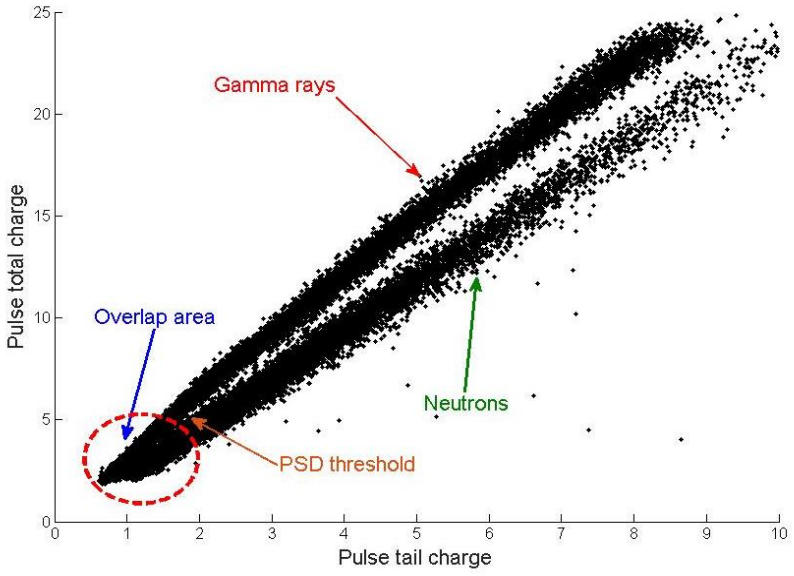

Figure 62: Pulse tail charge versus pulse total charge of neutron and gamma-ray events with overlap area.

The overlap clearly appears under the PSD threshold. On the other hand, the rejection of gamma-ray particles is approximately 100% in the area above the PSD threshold. Thereby, above the PSD threshold, the PSD efficiency is approximately 100%.

3.5 Experimental setup and materials

The experiment was conducted at the National Physical Laboratory (NPL)/Neutron Metrology group. The neutron detector was the fourth prototype detector, and its properties were mentioned in detail in Chapter 2, 'Prototype neutron detector designs'.

The neutron detector was connected to an oscilloscope by a signal cable with 50Ω impedance. The oscilloscope was a PicoScope 3000 Series with 1GS/s sampling, 200MHz bandwidth and 8-bit resolution. The oscilloscope was adjusted to a voltage range of 1V and a trigger of 100mV. The scintillation pulses were viewed and stored using a laptop computer. The detector was located 1.5m away from the Am–Be neutron–gamma source of 2.04×10^7 neutron/second emission rate. The measurements were taken for three hours and the total number of collected signals was in the form of 100 files, with each file containing 3,000 signals. Figure 63 shows the experimental setup.

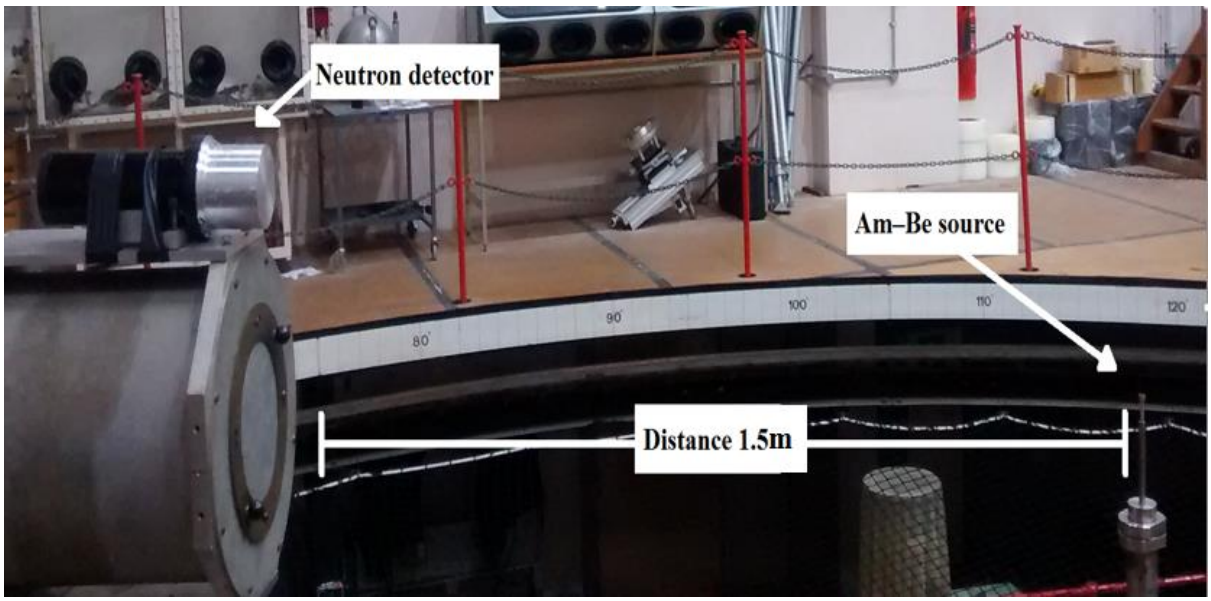

Figure 63: The fourth prototype neutron detector was exposed to an Am–Be neutron–gamma source at the NPL, UK.

3.6 Results and discussions

3.6.1 Pulse rise and fall times

The output files from the oscilloscope were the pulse amplitudes (Y-axis) and their times (X-axis). Using the MATLAB program, the pulse rise and fall times were measured to determine the ability to apply a convenient radiation discrimination method using these specifications (i.e. pulse time and amplitude). All pulse amplitudes were normalised to allow pulse times comparison. At the rising edge of the pulse, the pulse rise time was considered to be the time taken for the pulse to rise from 10% to 90% of the maximum pulse amplitude. In addition, at the falling edge of the pulse, the pulse fall time was considered to be the time taken for the pulse to fall from 90% to 10% of the maximum pulse amplitude. Figure 64 shows the parameters used to compare the pulse time profiles.

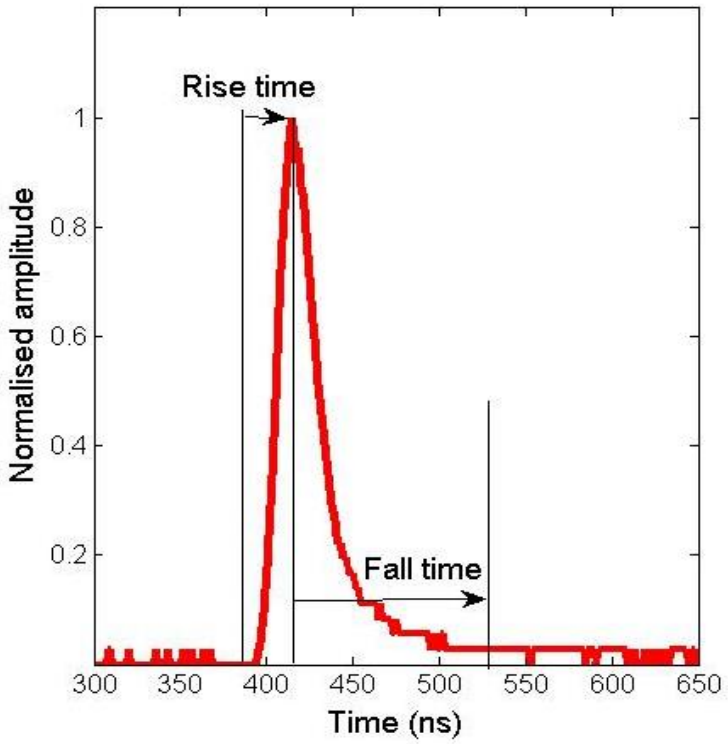

Figure 64: Pulse time profile parameters used for comparisons.

Firstly, the pulse rise time was measured for 30,000 scintillation pulses. The pulse rise time distribution was found to be around 15ns for the 30,000 scintillation pulses. Figure 65 shows the pulse rise time distribution of the 30,000 scintillation pulses.

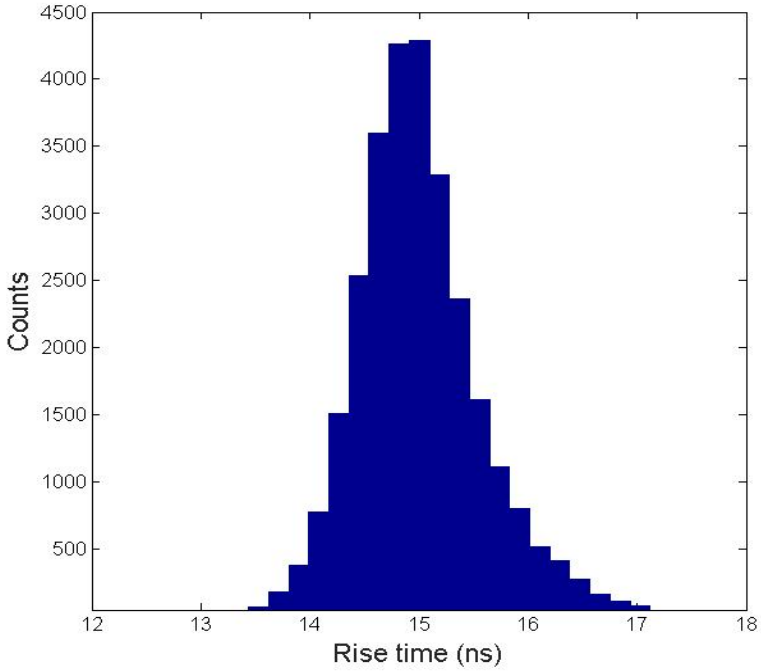

Figure 65: Rise time distribution of the 30,000 scintillation pulses.

From Figure 65, we can see that the difference in the pulses' rise time of neutron and gamma rays is insignificant, and applying PSD method using pulse rise time could not be achieved.

On the other hand, the pulse fall time was also measured for the 30,000 pulses. The pulse fall time distribution was found to be around two peak distributions. The first and second peak distributions were around 45ns and 55ns respectively. The two distributions were considered to be neutron and gamma-ray events. Figure 66 shows the pulse fall time distribution of the 30,000 scintillation pulses.

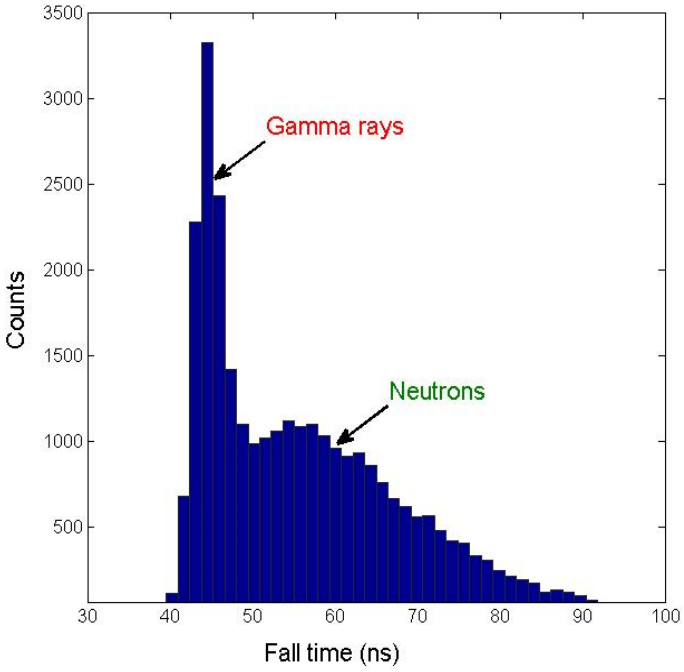

Figure 66: Fall time distribution of the 30,000 scintillation pulses.

Figure 66 shows that the difference in the pulses' fall time of neutrons and gamma rays is significant and it was therefore utilised to obtain PSD methods.

3.6.2 PSD methods

Four PSD methods were examined in order to choose the PSD method with the best performance. The PSD method with the best performance will be applied to the data, which will be collected in the proton therapy room at the Clatterbridge Hospital. The motivation is to identify neutron and gamma-ray spectra during proton irradiation.

- **Charges ratio PSD method**

The frequent use of charge comparison PSD methods has been due to its high efficiency and ease [196]. Usually, charge comparison PSD methods have been obtained through the same technique, which is comparing the pulse charge integration over two time periods during the pulse lifetime. The only difference is which two time periods are chosen. For example, the optimum charge comparison was considered to

be between the total charge (from the start of the scintillation pulse to 50ns) and the charge from 21ns to 50ns from the scintillation pulse peak [172].

In a similar way, the charges ratio PSD method was obtained. The calculation was done using the MATLAB program. A MATLAB script was written to integrate (summate) the pulse charge over any chosen time period during the pulse lifetime. The total pulse charge was considered to be the charge integration from the beginning of the pulse to 5% of the pulse's amplitude at the falling edge. In addition, the pulse tail charge was considered to be the charge integration at a period over the falling edge (i.e. from 90% to 5% [90 5] or from 80% to 5% [80 5], etc.). Figure 67 shows an example of neutron and gamma-ray pulse integration over two time periods.

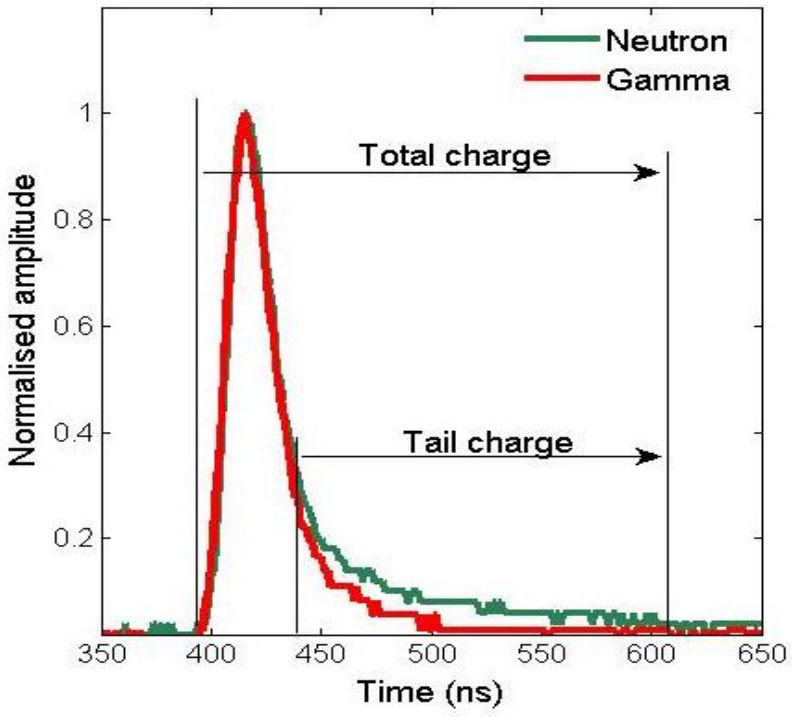

Figure 67: Example of neutron and gamma-ray pulse integrations over two time periods.

The plot demonstrates that a neutron pulse has a slow fall time compared to a gamma-ray pulse. This makes the neutron tail charge significantly more than the gamma-ray tail charge, with the same pulse amplitude. Figure 68 shows the tail charge versus the total charge of neutron and gamma-ray events obtained using the fourth prototype neutron detector and an Am–Be neutron–gamma source.

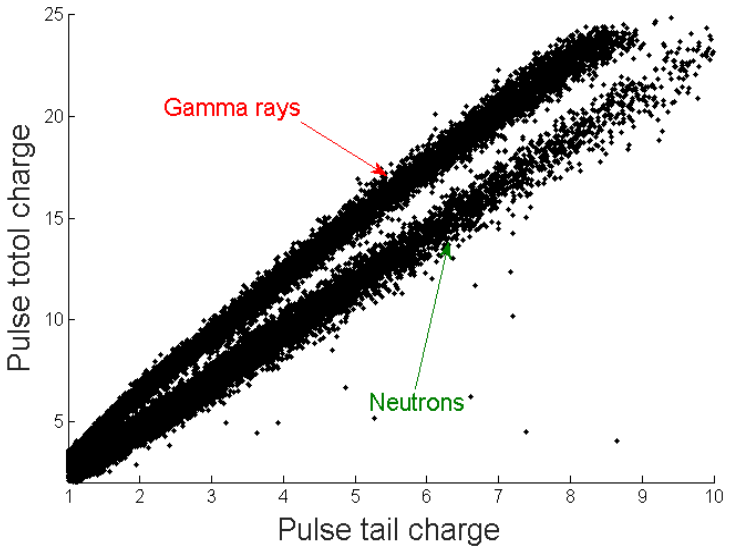

Figure 68: Tail charge versus total charge of neutron and gamma-ray events obtained using the fourth prototype neutron detector and an Am–Be neutron–gamma source.

In order to obtain the charges ratio PSD, the ratio of the pulse tail charge to the pulse total charge was calculated and optimised. The optimum charges comparison ratio was considered to be the maximum neutron–gamma separation and the lowest PSD threshold (i.e. the start of neutron–gamma separation). The optimum ratio was found between the integration of the total pulse charge and the integration of the pulse tail charge over the time period of pulse amplitude to fall from 60% to 5% [60 5]. Thereby, the charges ratio PSD method was obtained by dividing the pulse tail charges [60 5] over the total pulse charges. Figure 69 shows the MATLAB scatter plot of the charges ratio PSD method histogram versus the pulse amplitude scale (i.e. pulse height).

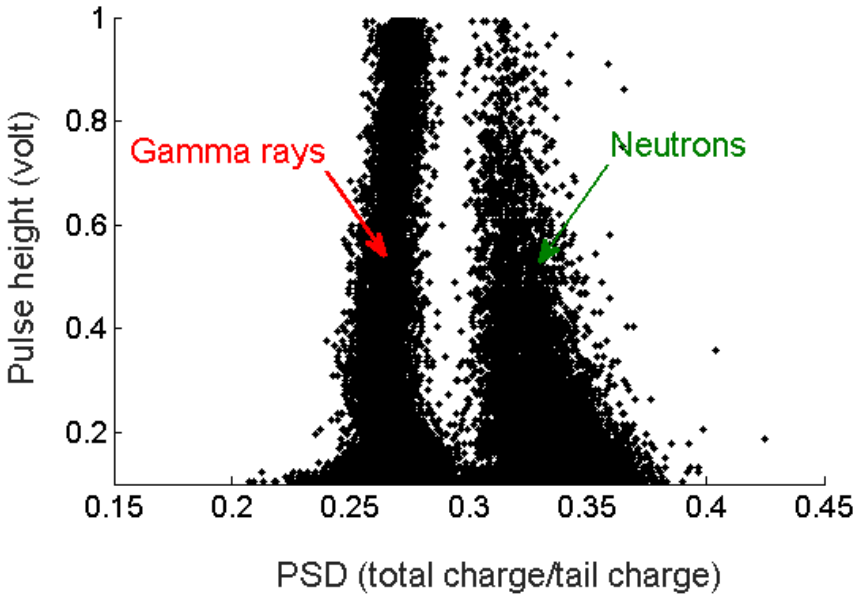

Figure 69: MATLAB scatter plot of the charges ratio PSD method.

- **Charge to amplitude ratio PSD method**

This technique involves the same approach as the charge comparison PSD method. The difference is that it compares the pulse charge and the pulse amplitude. The measurements of the pulse amplitudes and pulse charges integration were taken using the MATLAB program. The optimum charge to amplitude ratio was found between the integration pulse tail charge over the time period of pulse amplitude to fall from 60% to 5% [60 5] and the pulse amplitude. Figure 70 shows the MATLAB scatter plot of the pulse amplitude versus the pulse tail charge [60 5] of neutron and gamma-ray events, obtained using the fourth prototype neutron detector and an Am–Be neutron–gamma source.

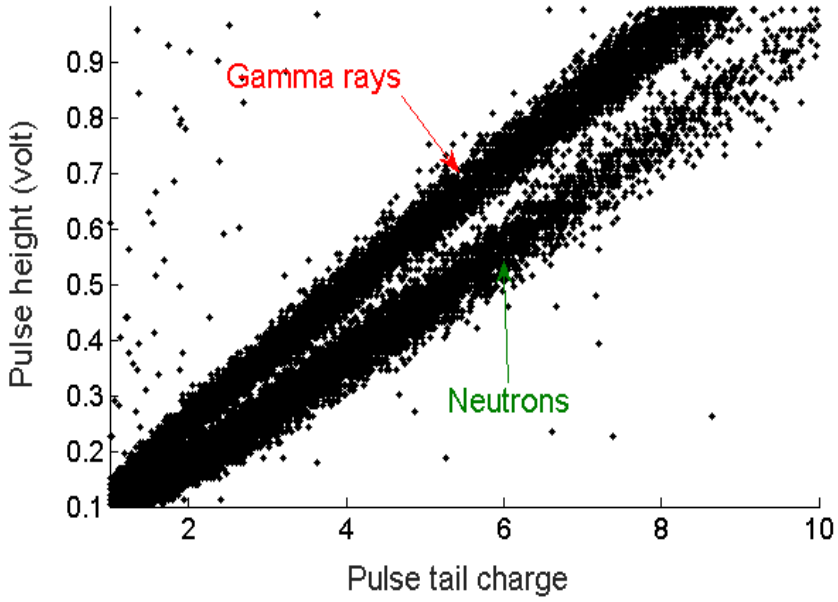

Figure 70: MATLAB scatter plot of the pulse amplitude versus the pulse tail charge of neutron and gamma-ray events, obtained using the fourth prototype neutron detector and an Am–Be neutron–gamma source.

The plot shows that the ratio of the pulse tail charge to the pulse amplitude for neutron and gamma-ray events are significantly different. Thereby, the charge to amplitude ratio PSD method was obtained by dividing the pulse tail charges [60 5] by the pulse amplitudes. Figure 71 shows a MATLAB scatter plot of the charge to amplitude ratio PSD method histogram versus the pulse amplitude scale (volt).

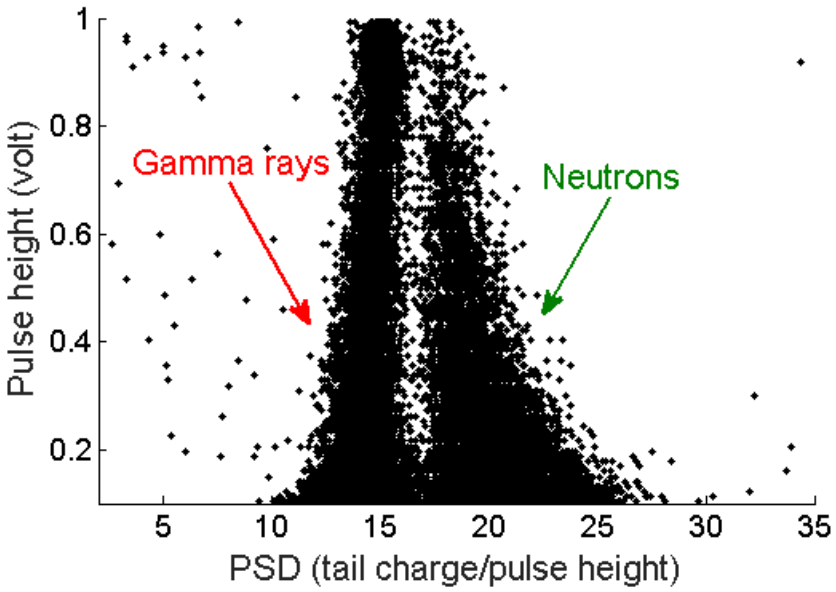

Figure 71: MATLAB plot of charge to amplitude ratio PSD method (histogram).

- **Amplitude-fall time PSD method**

In this PSD technique, the pulse fall time was determined as a function of the falling amplitude—for example, the pulse fall time at 10% of the pulse amplitude (at the pulse falling edge). Figure 72 shows the time difference between neutron and gamma-ray events at a fixed falling pulse amplitude.

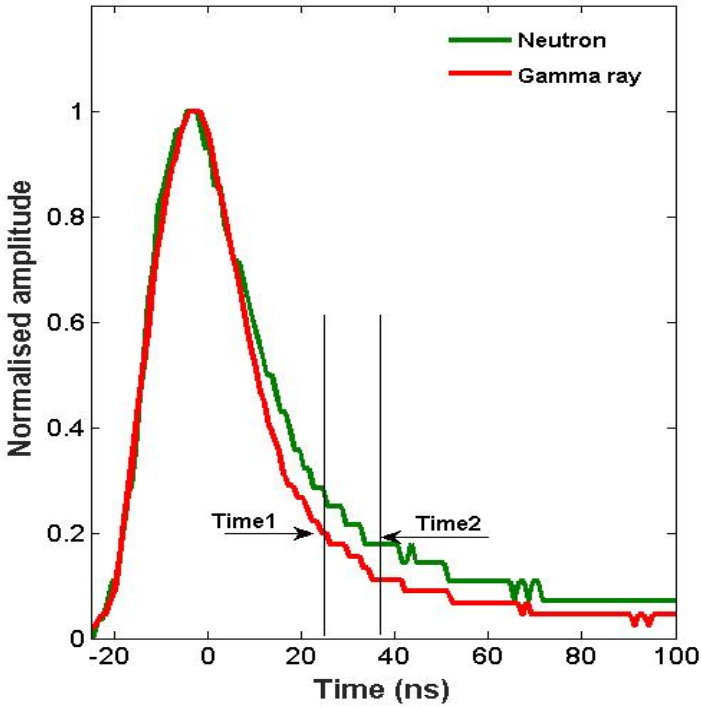

Figure 72: Fall time comparison between neutron and gamma-ray pulses at a fixed falling pulse amplitude.

The plot reveals that the pulse fall time at certain amplitude during the pulse falling edge is clearly different for gamma-ray and neutron events. The neutron pulse takes more time to reach a certain amplitude (i.e. 10% of the maximum pulse amplitude), which is more than a gamma-ray pulse.

Thus, the fall time difference between neutron and gamma-ray events was utilised to distinguish between these radiation types. Using the MATLAB program, normalisation and curve fitting was applied to the recorded pulses. The time taken for the pulse amplitudes to fall from 90% to 10% was considered to be the PSD method. Thus, the amplitude-fall time PSD method was obtained and is shown in Figure 73.

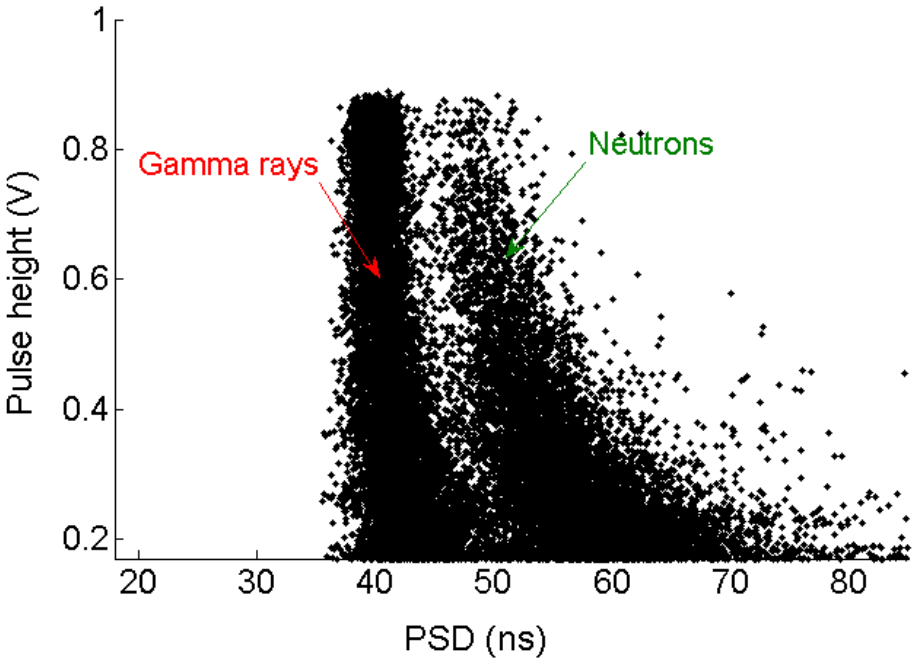

Figure 73: Amplitude-fall time PSD method.

- **Fall time-amplitude PSD method**

In this PSD technique, the pulse amplitude was determined as a function of the pulse fall time—for example, the pulse amplitude at 30ns from the pulse peak (at the pulse falling edge). Figure 74 shows the amplitude difference between neutron and gamma-ray events at 30ns from the pulse peak.

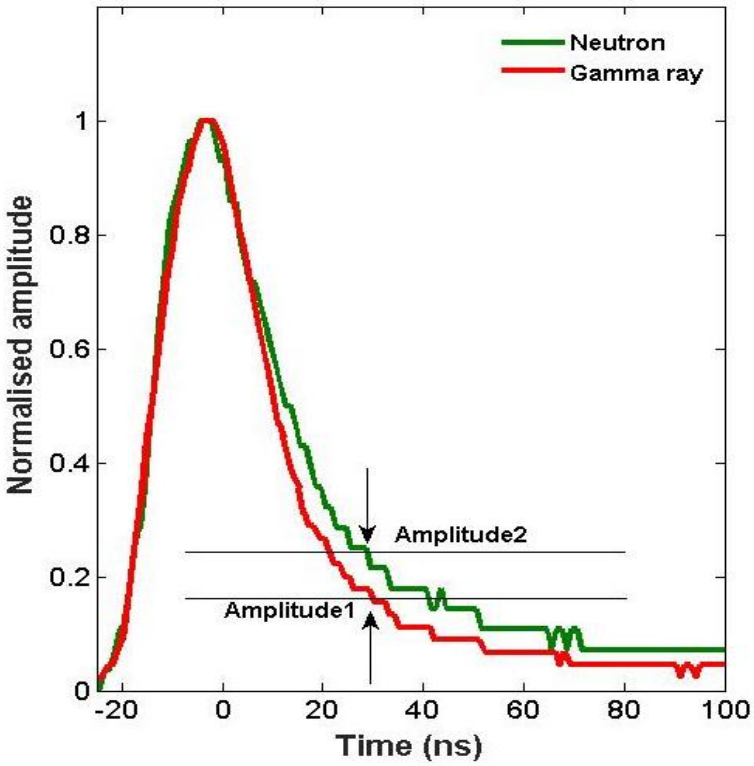

Figure 74: Amplitude comparison between neutron and gamma-ray events at fixed fall times.

The plot shows a significant difference between gamma-ray and neutron events. The neutron pulse has a higher pulse amplitude at certain fall time (e.g. 30ns). The amplitude difference between neutron and gamma-ray events was utilised to distinguish between these radiation types.

Using the MATLAB program, normalisation and curve fitting was applied to the recorded pulses. In addition, the pulses' amplitudes at 30ns were measured and were considered to be the PSD method. Thus, the fall time-amplitude PSD method was obtained and is shown in Figure 75.

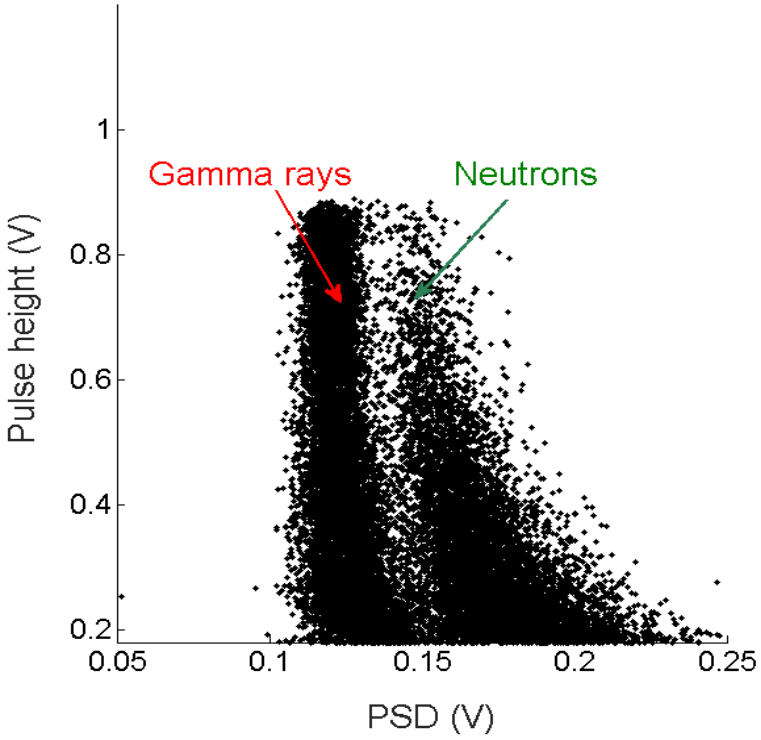

Figure 75: Fall time-amplitude PSD method.

3.6.3 PSD method performances

The performances of the PSD methods were evaluated by finding the FoM and the PSD threshold values. The best PSD performance involves high FoM and low threshold values. The high FoM provides high separation between the two radiation types (i.e. neutron and gamma-ray), whereas the low PSD threshold provides the ability to recognise the radiation of low energies (e.g. neutron energies below 0.5MeV).

Firstly, the FoM and threshold of the charges ratio PSD method were found to be 1.05 and 0.45MeVee respectively. Figure 76 shows the charges ratio PSD method histogram (two Gaussians), as well as the FoM and the PSD threshold values.

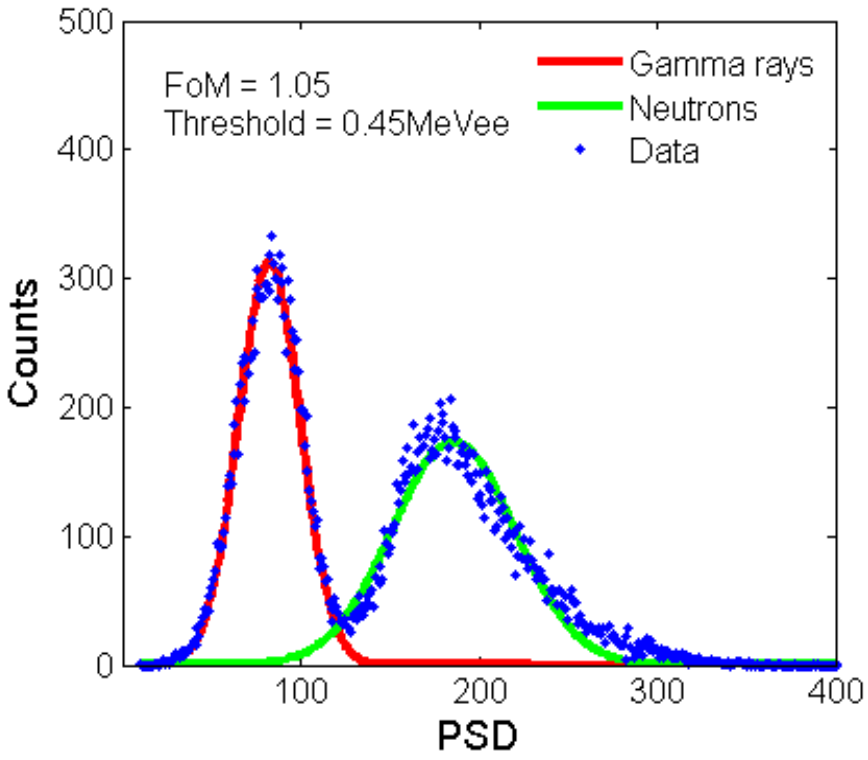

Figure 76: Charges ratio PSD method histogram (two Gaussians) showing FoM and PSD threshold values.

Secondly, the FoM and the PSD threshold of the charge to amplitude ratio PSD were found to be 0.86 and 0.45MeVee respectively. Figure 77 shows the charge to amplitude ratio PSD method histogram (two Gaussians), as well as the FoM and PSD threshold values.

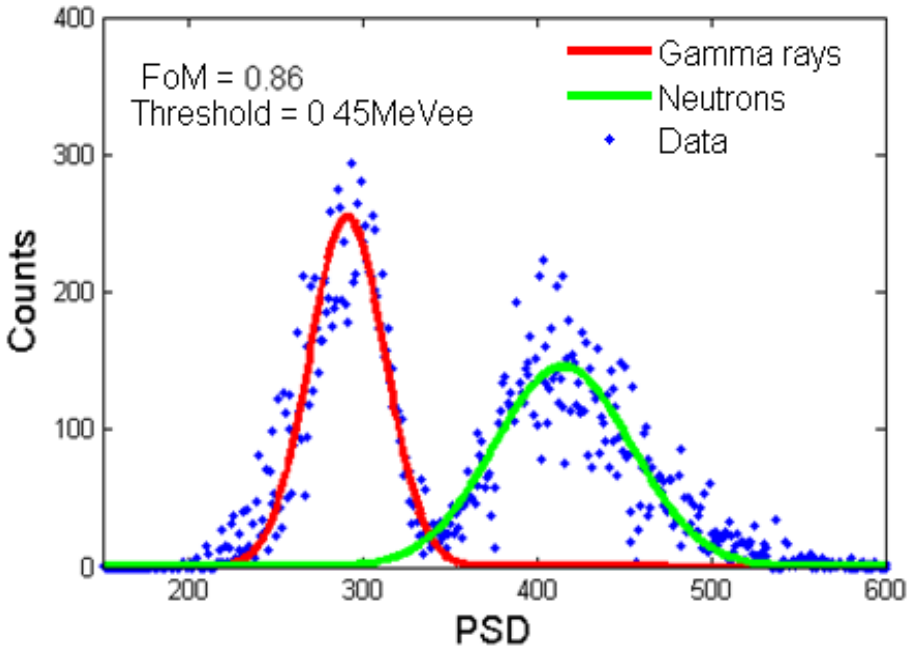

Figure 77: Charge to amplitude ratio PSD method histogram (two Gaussians) showing FoM and PSD threshold values.

Thirdly, the FoM and PSD thresholds of the amplitude-fall time PSD method were found to be 0.6 and 0.8MeVee respectively. Figure 78 shows the amplitude-fall time PSD method histogram (two Gaussians), as well as the FoM and PSD threshold values.

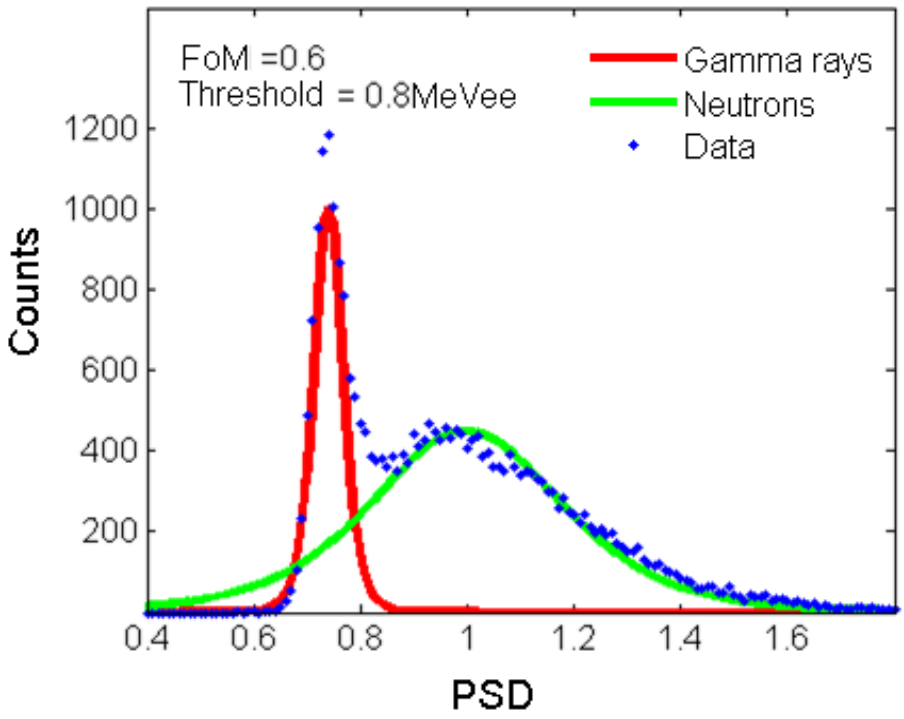

Figure 78: Amplitude-fall time PSD method histogram (two Gaussians) showing FoM and PSD threshold values.

Fourthly, the FoM and threshold of the fall time-amplitude PSD method were found to be 0.6 and 0.75MeVee respectively. Figure 79 shows the fall time-amplitude PSD method histogram (two Gaussians), as well as the FoM and PSD threshold values.

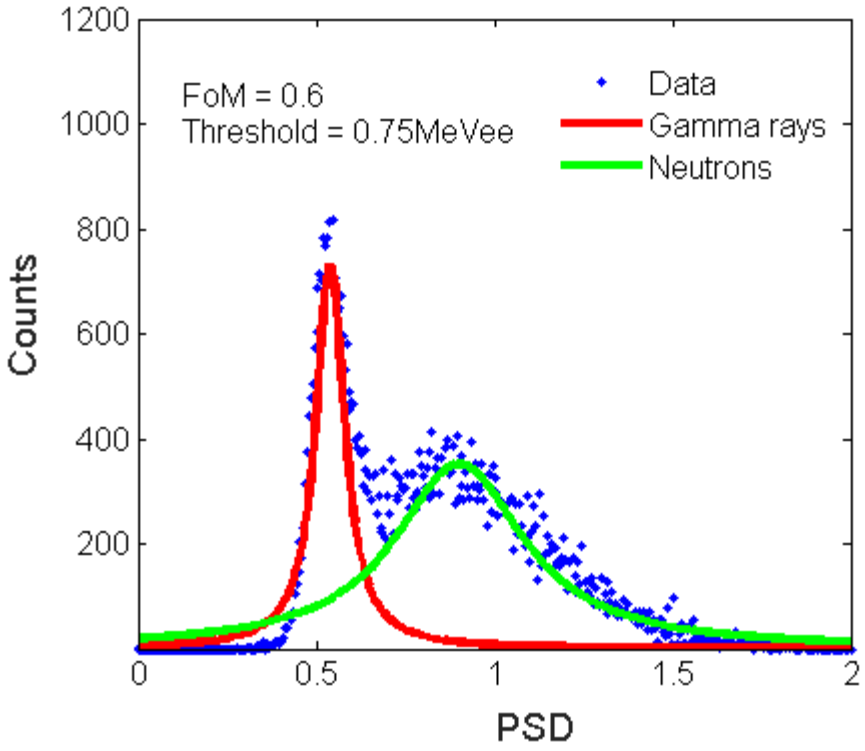

Figure 79: Fall time-amplitude PSD method histogram (two Gaussians) showing FoM and PSD threshold values.

3.7 Application of PSD technique to measured data

The charges ratio PSD method was applied to the recorded scintillation pulses obtained from exposing the fourth prototype neutron detector to an Am–Be neutron–gamma source. The radiation events below the PSD threshold (<0.45MeVee) were rejected. Then, the Am–Be total, neutron and gamma-ray energy spectra were obtained. In addition, the Am–Be neutron energy spectrum was compared to the MC simulation result. The Am–Be neutron energy spectrum was calibrated with regard to the MC simulation result. A good agreement was found between the MC simulation and the measured Am–Be neutron energy spectrum. Figure 80 shows the measured total, neutron and gamma-ray spectra and a comparison between the measured and MC simulation of the Am–Be neutron spectrum.

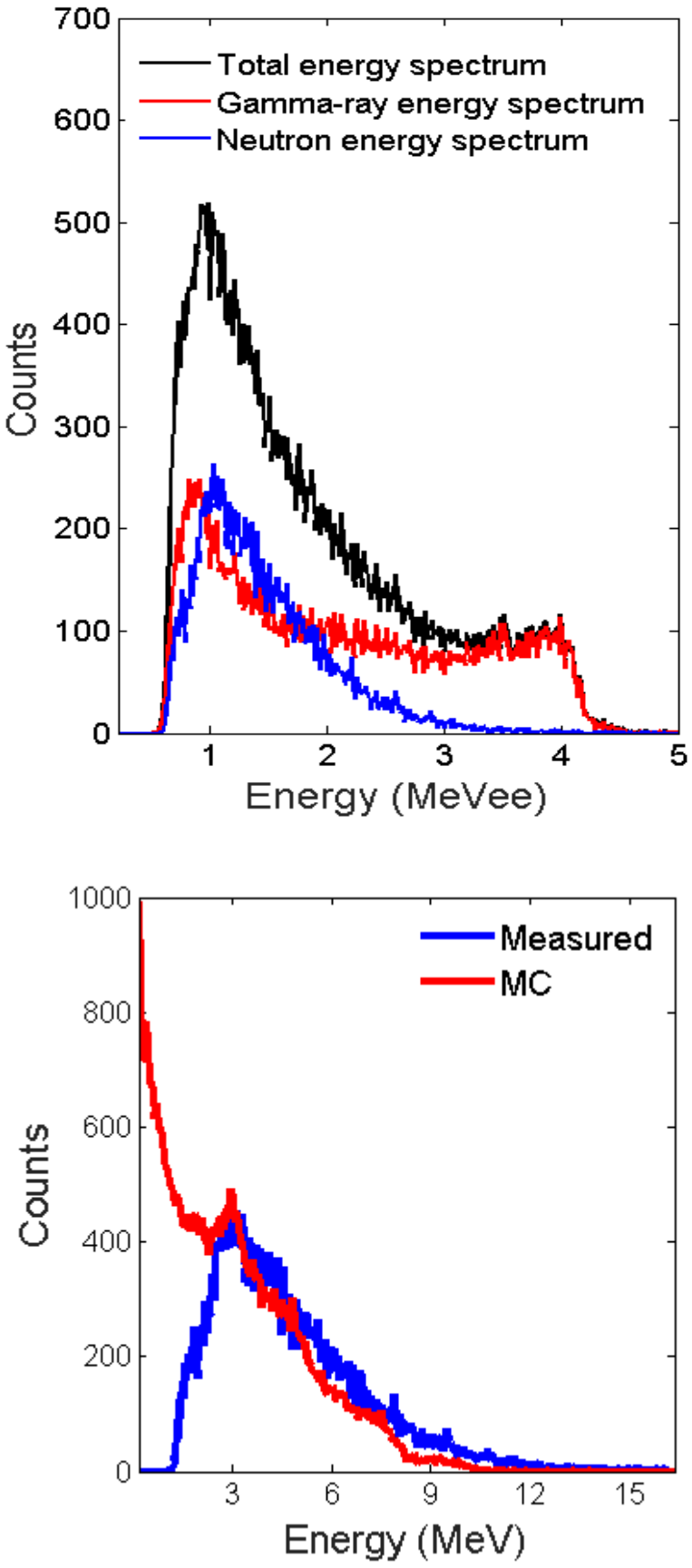

Figure 80: Measured total, neutron and gamma-ray Am–Be energy spectra (upper plot) and comparison between the measured and MC simulation of the Am–Be neutron spectrum (lower plot).

3.8 Discussions and comparisons

Regarding the PSD methods' performances, the best PSD method performance was found in the charges ratio PSD method. The charge to amplitude ratio PSD performance was inferior compared to the charges ratio PSD method. Nevertheless, it was superior compared to the amplitude-fall time PSD and the time-amplitude PSD methods. The time-amplitude PSD and the amplitude-fall time ratio PSD methods were found to be comparable.

The charges ratio PSD method was obtained in a similar way to the common charge comparison PSD methods. The difference was in the optimisation of the charges ratio (tail charge/total charge). It was noticed that the optimisation of the charges ratio has a significant effect on its performance. The optimum charge comparison was found between the integration of the total pulse charge and the integration of the pulse tail charge over the time period of pulse amplitude to fall from 60% to 5% [60 5].

Few researchers have reported a charge to amplitude comparison PSD—for example, the charge-to-current ratio PSD method. Usually, charge to amplitude comparison PSD methods are obtained using the same technique, which is comparing the pulse charge integration over a specific time period during the pulse lifetime to the pulse amplitude. The charge to amplitude ratio PSD method was similarly obtained. The difference was the optimum charge to amplitude comparison. The optimum comparison was between the pulse tail charge [60 5] and the pulse amplitude, whereas the charge-to-current ratio PSD method was obtained by comparing the total pulse charge to the pulse amplitude.

The amplitude-fall time PSD method was obtained in a similar way to the zero crossing, the time over threshold, and the trailing edge pulse timing PSD methods. Its difference from the zero crossing PSD method was that the output of the PMT was not modified. In addition, its difference from the time over threshold and trailing edge pulse timing PSD methods was that the pulse fall time (i.e. pulse rise time was excluded) at a certain amplitude was considered to be the PSD method, instead of the pulse lifetime (i.e. pulse rise time was included) over a certain amplitude.

The fall time-amplitude PSD method was novel in utilising the relation between the pulse fall time and its relevant amplitude. The pulse amplitude at a certain pulse fall time (e.g. 30ns) was considered to be the PSD method.

Table 19 shows the comparison between the performances of the obtained PSD methods and PSD methods from the literature review. The table is arranged from the highest to the lowest FoM.

Table 19: Comparison between the performances of the obtained PSD methods and PSD methods from the literature review.

Reference	PSD method	Energy range	Detector type	FoM	Threshold (MeVee)
[172]	Charge comparison method	Cf	Liquid scintillator (EJ-301)	1.1	0.3
In this work	Charges ratio	Am–Be	Liquid scintillator (EJ-331)	1.05	0.45
[174]	Charge-to-current ratio	Am–Be	Liquid scintillator (NE-213)	0.88	0.25
In this work	Charge to amplitude ratio	Am–Be	Liquid scintillator (EJ-331)	0.86	0.45
[174]	Trailing edge pulse timing	Am–Be	Liquid scintillator (NE-213)	0.6	0.25
In this work	Fall time-amplitude	Am–Be	Liquid scintillator (EJ-331)	0.6	0.75
In this work	Amplitude-fall time	Am–Be	Liquid scintillator (EJ-331)	0.6	0.8

The table shows that the performance of the charges ratio PSD method was good enough (i.e. to separate neutron and gamma-ray events) and its performance was comparable to the performance of the charge comparison PSD method. However, the differences in the values of the FoM and PSD thresholds were due to the used oscilloscope's limitations. In addition, the oscilloscope trigger was adjusted at 100mV, which is equal to 0.43MeVee.

3.9 Conclusion

An evaluation of the PSD methods was done using the FoMs and PSD thresholds. In this work, the highest PSD method performance was found in the charges ratio PSD method. However, a PSD method's performance is significantly affected by the oscilloscope used and its properties (resolution and sampling rate). Using an oscilloscope with a higher sampling rate and resolution will improve a PSD method's

performance; for example, the FoM was increased by 17.6% with an increasing sampling rate from 100MS/s to 1GS/s [197].

Amplitude-fall time and fall time-amplitude PSD methods need precise pulse details to be identified, such as a certain fall time and amplitude during the pulse lifetime. The precise pulse details were affected strongly by the low resolution of the oscilloscope used.

Regarding the high performance of the charges ratio PSD method, it was recommended to be applied to the data (i.e. neutrons and gamma rays) that was collected in the proton therapy room at Clatterbridge Hospital.

Chapter 4. MC simulations and measurements during proton irradiation at Clatterbridge Hospital

4.1 Introduction and overview

The source of secondary radiation (mainly neutrons and gamma rays) during proton therapy is the interaction of primary protons with high atomic number materials that are in the proton therapy beam line. Therefore, healthy tissue is exposed to an unwanted additional radiation dose. The additional dose has been assessed in many published papers, which were mentioned in the 'Introduction chapter' under the subtitle 'Neutron dose assessment during proton therapy'. However, it is still unknown whether the effect is significant or negligible.

The two main subjects covered in this chapter are the MC simulations and measurements during proton irradiation in the proton therapy room at Clatterbridge Hospital.

The MC simulation results were obtained using a simulated fourth prototype neutron detector and a voxelised water phantom within a simulated proton irradiation at Clatterbridge Hospital. In contrast, the measured results were obtained using the fourth prototype neutron detector without the water phantom and with a fixed location during the proton irradiation at Clatterbridge Hospital.

The Clatterbridge Hospital proton therapy beam line was simulated using Geant4 and GAMOS.4.0.0 MC simulation codes. In addition, a simulated voxelised water phantom and a neutron detector were included in the simulated proton irradiation environment.

The aim of the MC simulations was to find the relative integral neutron dose and its distribution in a voxelised water phantom during the proton irradiation at Clatterbridge Hospital. In addition, the MC simulation was done to simulate the setup of the measurement, which was taken during the proton irradiation at Clatterbridge Hospital.

Hence, the scintillation energy spectra (neutron and gamma ray) and their DEs were obtained.

The aim of taking measurement in the proton therapy room at Clatterbridge Hospital was to validate the MC simulation results of the neutron scintillation spectrum and its relative DE (or its absorbed dose). Hence, the MC simulation of relative DE distributions from the neutrons and the gamma rays in the voxelised water phantom were validated.

The measurement was taken using the fourth prototype neutron detector and the charges ratio PSD method to separate neutrons and gamma rays. Thus, neutron and gamma-ray scintillation spectra were obtained. In addition, the neutron and gamma-ray relative DEs were measured.

A good agreement was found between the MC simulation and the measured results of scintillation neutron spectrum and its relative absorbed dose, which were 2.63μGy/Gy and 2.08±0.42μGy/Gy respectively.

Thus, the main research question, which was whether the neutron dose during proton therapy is significant or negligible, was answered. Although the neutron dose was small compared to the prescribed proton therapy dose, it is not negligible.

In addition, Measurements were taken while wax and lead shields were used. The use of wax and lead shields considerably reduced the amount of gamma rays and neutrons reaching the detector. This was done to propose the use of a neutron shield to reduce neutron dose during proton therapy at Clatterbridge Hospital.

4.2 MC simulations during proton irradiation in the proton therapy room at Clatterbridge Hospital

4.2.1 Aim and objectives

The aim was to conduct an MC simulation of the relative neutron dose distribution (neutron equivalent dose/prescribed proton therapy dose) during the proton irradiation at Clatterbridge Hospital.

The objectives were the following:

- MC simulation of the proton therapy beam line at Clatterbridge Hospital.
- MC simulation of the DE distribution and the relative DE from gamma rays during the proton irradiation at Clatterbridge Hospital.
- MC simulation of the relative DEs from thermal and internal neutrons during the proton irradiation at Clatterbridge Hospital.
- MC simulation of the measurement setup, which was taken in the proton therapy room at Clatterbridge Hospital.

In the simulation model and the measurements, the proton beam was configured to produce a full energy Bragg peak. The estimated statistical errors associated with the simulated dose was ±0.91%, with one million proton particles from which radiation dose was estimated (i.e. DE).

4.2.2 MC simulation of the proton therapy beam line

The proton therapy beam line, the voxelised water phantom and the fourth prototype neutron detector were simulated using Geant4 and GAMOS.4.0.0 MC simulation codes.

Geant4 was used to simulate the following geometries:

- The proton therapy beam line.
- The voxelised water phantom.
- The fourth prototype neutron detector.

GAMOS.4.0.0 was used for the following:

- Simulating physics models.
- Simulating the proton generator.
- Tracking secondary radiation particles.
- Scoring DE distributions and obtaining energy histograms

With reference to C. Baker et al., A. Kacperek and D. E. Bonnett et al. [41] [198] [199] , the proton therapy beam line at Clatterbridge Hospital was simulated using Geant4 and GAMOS.4.0.0MC simulation codes. The component specifications of the proton therapy beam line are shown in Table 20.

Table 20: The component specifications of the proton therapy beam line at Clatterbridge Hospital, UK.

Component	Specifications
1. Available dose rate	From 1Gy/min to 40Gy/min
2. Proton beam	Gaussian-shape 62MeV with 0.1 standard deviation
3. Pre-collimator	10mm height x 3mm radius (brass)
4. First scattering foil	0.025mm tungsten (W-73)
5. Stopper	6mm height x 2.85mm radius (brass)
6. Second scattering foil	0.025mm tungsten (W-73)
7. Kapton window	0.05mm thickness
8. Modulator	0.84mm thickness PMMA (32 steps)
9. Range shifter	PMMA
10. Monitor chamber	0.02mm mylar, 0.04mm aluminium
11. Second collimator	10mm height x 20mm radius (brass tube)
12. Nozzle	70mm height x 17mm radius (brass tube)

Table 20 shows the beam line components for the proton therapy at Clatterbridge Hospital, arranged from the proton beam generator to the target (i.e. the phantom). The distance from the pre-collimator to the end of the second collimator (i.e. the final collimator) was 2.026m. Figure 81 shows a diagram of the simulated proton therapy beam line geometry.

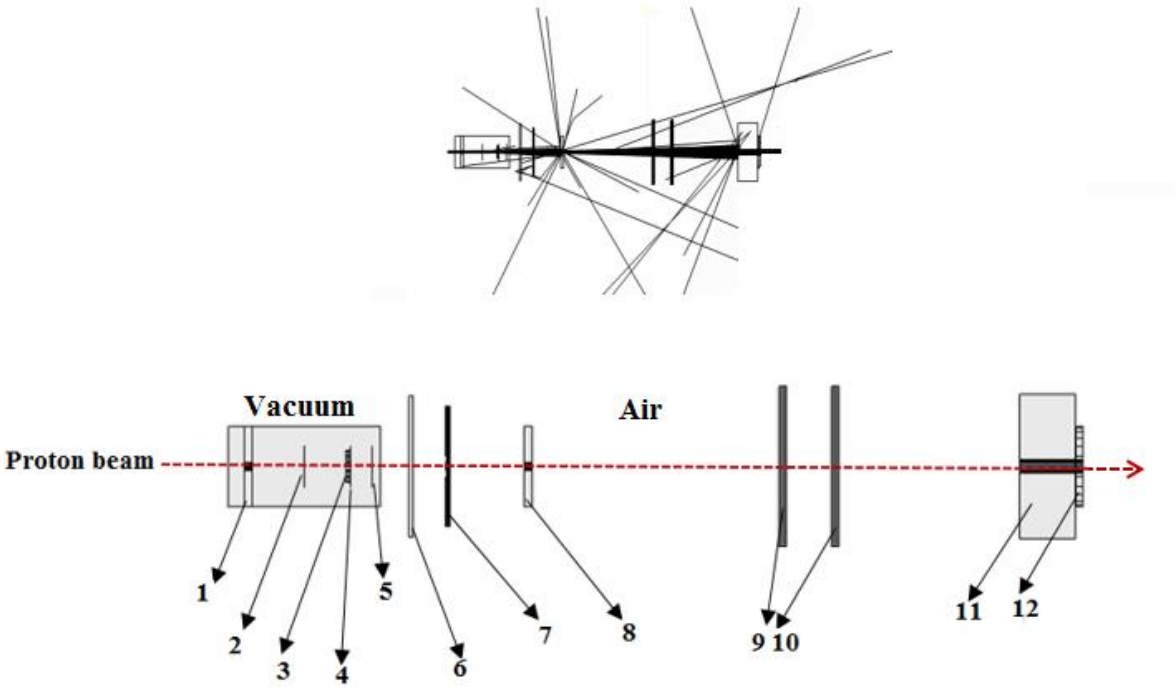

Figure 81: First and second scatterers (2 and 4), central stopper (3), collimators (1, 8 and 12), Kapton window (5), range shifter (6), modulator wheel (7), dose monitors (9 and 10), and nozzle (11). The upper image was taken when the MC simulation program was running.

The diagram shows that the proton beam travels through the first and second scatterers (2 and 4), central stopper (3), collimators (1, 8 and 12), Kapton window (5), range shifter (6), modulator wheel (7), dose monitors (9 and 10), and nozzle (11).

The QGSP_BIC_HP GAMOS physics lists were used to simulate the interactions of the primary protons and the secondary radiation (i.e. neutrons and gamma rays). The QGSP_BIC_HP physics lists were used to describe the production of the secondary particles due to the neutron and proton interactions with matter. QGSP_BIC_HP physics lists contain the following physics constructors [200]:

- G4DecayPhysics.
- G4EmStandardPhysics.
- G4EmExtraPhysics.
- G4IonPhysics.
- G4StoppingPhysics.
- G4HadronElasticPhysics.

The primary proton generator was simulated as the proton source, with a Gaussian-shape distribution and a standard deviation (SD) of 0.1% [41].

GAMOS user actions were used to track the different radiation particles, and GAMOS data analysis was used to obtain energy histograms (i.e. the energy spectrum). In addition, GAMOS scoring was used to obtain the DE distributions.

4.2.3 DE scoring

In addition to the proton therapy beam line MC simulation, the fourth prototype neutron detector and voxelised water phantom were simulated using Geant4 and GAMOS.4.0.0 MC simulation codes, and were included in the proton therapy room. Figure 82 shows a diagram of the proton therapy beam line geometry and the voxelised water phantom.

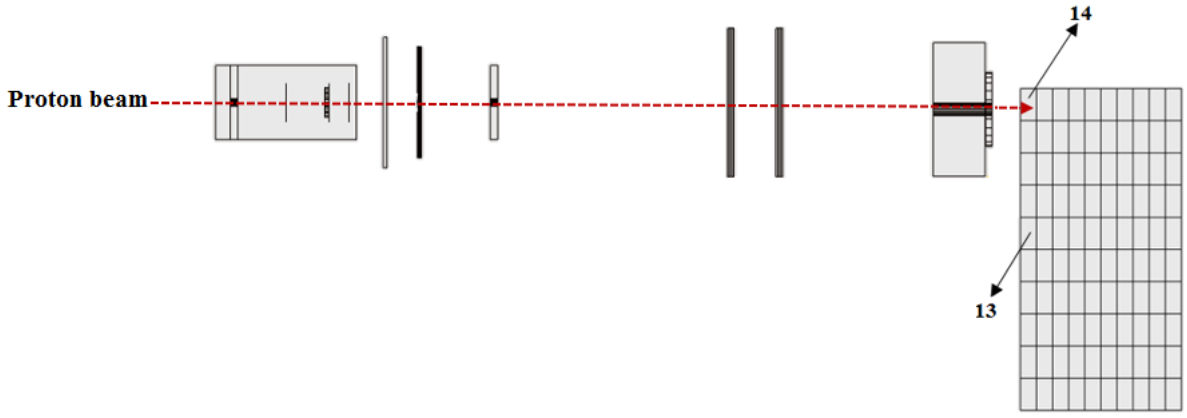

Figure 82: Diagram of the proton therapy beam line geometry and the voxelised water phantom (13), where 14 is the target voxel of the (0, 9, 4) copy number.

The simulated voxelised water phantom dimensions were 50cm (x), 100cm (y) and 50cm (z), and the voxels' dimensions were 5cm (x), 10cm (y) and 5cm (z). In total, there were 1,000 voxels (i.e. 10 (x), 10 (y), 10 (z)). The size of the voxelised water phantom was chosen to be approximately equivalent to the size of an adult patient's body (head, neck, chest and abdomen). The voxelised water phantom was simulated and included in the proton therapy room to find the relative DE distributions from neutrons and gamma rays and their relative integral DEs. In addition, the simulated

voxelised water phantom was used to find the relative integral DEs from internal, thermal and thermalised neutrons.

The MC simulation of the fourth prototype neutron detector during the proton irradiation at Clatterbridge Hospital was done to compare the simulated neutron and gamma-ray spectra with the measured neutron and gamma-ray spectra. The neutron detector was the same as the one that was simulated, designed and used during the measurements at the NPL. Figure 83 shows a diagram of the proton therapy beam line geometry and the detector position.

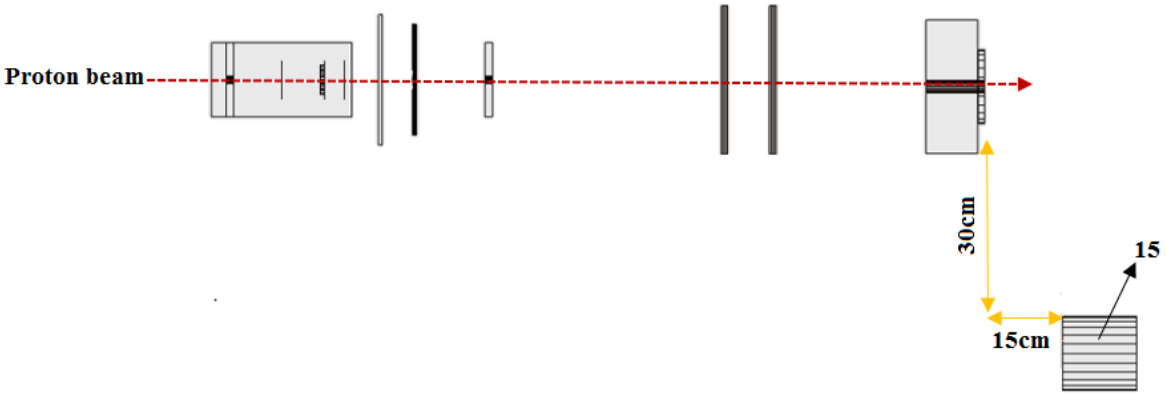

Figure 83: Diagram of the proton therapy beam line geometry and the detector (15). The detector location is 15cm in front of and 30cm below the second collimator of the proton therapy beam line.

Firstly, using the MC simulation geometry shown in Figure 82, the DE of the different radiation particles on the voxelised water phantom was scored. The voxelised water phantom was located 1cm in front of the second collimator of the proton therapy beam line. The copy number (x, y, z) of the target voxel was (0, 9, 4), which was the front-top-middle voxel. At each MC simulation, 10^6 proton particles were run.

The MC simulation results of the DE were the following:

1. The relative DE distribution of the total neutrons (external and internal) was obtained and displayed in a 2D plot. This was done by scoring the DE from all neutrons, external and internal, from a thermal to fast energy range at each voxel of the voxelised water phantom.

2. The relative DE distribution of gamma rays was obtained and displayed in a 2D plot. This was done by scoring the DE from gamma rays incident on the voxelised water phantom at each voxel.

In addition, the following quantities were obtained to be compared with the relative integral DE of total neutrons:

1. The relative integral DE of internal neutrons was obtained by scoring the DE from the internal neutrons generated within the voxelised water phantom from a thermal to fast energy range.

2. The relative integral DE of thermal neutrons was obtained by scoring the DE from the thermal neutrons incident on the voxelised water phantom with energy below 1eV (thermal to slow neutron energy range).

3. The relative integral DE of thermalised neutrons was obtained by scoring the DE from the thermalised fast neutrons, which were the external and internal neutrons that had been thermalised within the voxelised water phantom.

Secondly, using the MC simulation geometry shown in Figure 83, the scintillation spectra of neutrons and gamma rays were obtained from the simulated fourth prototype neutron detector. In addition, the relative DEs of the scintillation spectra were calculated.

4.2.4 Results

The following describes some of the MC simulation results that this study aimed to obtain:

1. The relative DE distribution is the DE distribution, in a 2D plot, of neutrons or gamma rays in the voxelised water phantom. It was obtained by dividing the DE from the neutron or gamma ray at each voxel by the summation of the proton DE (e.g. prescribed proton therapy dose).
2. The relative integral DE is the integral DE from different radiation particles (e.g. internal neutrons, thermal neutrons or gamma rays) in the voxelised water

phantom. It was obtained by dividing the summation of the DE from different radiation particles by the summation of the proton DE.

- **Relative DE distributions**

The relative DE distributions from neutrons and gamma rays are displayed in the 2D plots (X-Y) in Figure 84. The X-Y 2D plot was a vertical slice taken from the voxelised water phantom at the level of the target voxel.

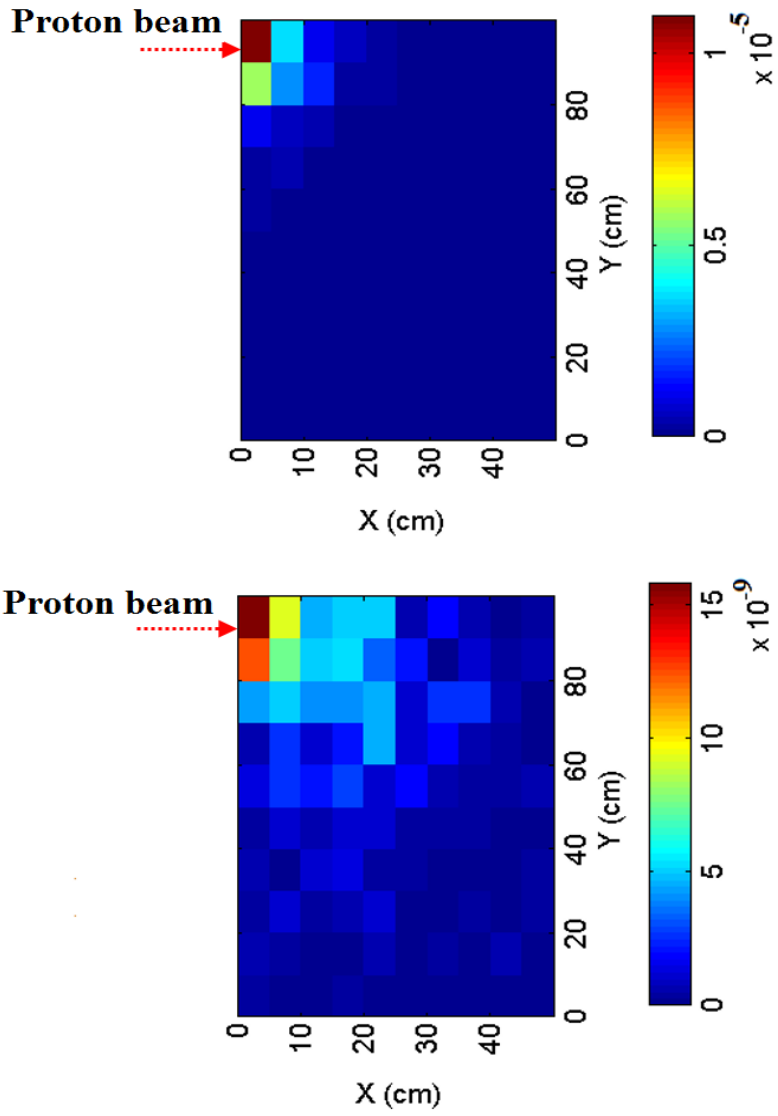

Figure 84: 2D plot of the relative DE distributions (X-Y) from neutrons (upper plot) and gamma rays (lower plot) at the level of the target voxel.

The X-Y plots in Figure 84 show that the relative neutron DE distribution is mainly in and around the primary proton target voxel. Although the highest neutron DE was at the target voxel (5 x 10 x 5cm^3), there was significant neutron DE at a distance of approximately 20 x 20 x 20cm^3 around the target voxel. The highest neutron DE at the target voxel was considered to be due to the contribution of the internal neutron DE. In contrast, the gamma-ray DE was widely distributed within the voxelised water phantom (i.e. compared to the neutron DE distribution).

In addition, the following radiation quantities were obtained:

1 The relative integral DE of total neutrons.
2 The relative integral DE of gamma rays.
3 The relative integral DE of internal neutrons.
4 The relative integral DE of thermal neutrons.
5 The relative integral DE of thermalised neutrons.

Table 21 shows the relative integral DEs obtained from different radiation particles in the voxelised water phantom during the proton irradiation at Clatterbridge Hospital.

Table 21: MC simulation result of the relative DEs obtained from different radiation particles during the proton irradiation at Clatterbridge Hospital.

Type of secondary radiation	Relative DE %	Radiation weighting factor [8]
Total neutrons (thermal to fast)	14.8 x 10^{-3}	From 5–20
Internal neutrons (thermal to fast)	0.61 x 10^{-3}	From 5–20
Thermal neutrons	0.0121 x 10^{-3}	5
Thermalised neutrons	0.35 x 10^{-3}	5
Gamma rays	8 x 10^{-3}	1

Table 21 shows the contribution of internal neutron DE and total thermal neutron DE (i.e. thermal and thermalised) to the total neutron DE were 4.1% and 2.4% respectively. Thus, fast external neutrons are the main source of neutron dose during proton irradiation at Clatterbridge Hospital.

The ratio of gamma-ray DE over the total neutron DE was 0.54. Nevertheless, the weighted neutron dose (equivalent dose) is several times higher than the weighted

gamma-ray dose. The weighted neutron dose is the calculated neutron absorbed dose (Gy) to equivalent dose (Sv) by using a neutron quality factor or weighting factor [199] [2] [67].

The MC simulation results show the neutron dose as having an SD of ±0.91%. Therefore, integral neutron DE (or absorbed dose) can be obtained by multiplying the prescribed proton therapy dose by (14.8±0.135) x10^{-5}. In addition, the integral neutron equivalent dose can be obtained from the following relation:

Integral neutron equivalent dose (Sv) = (14.8±0.135) × 10^{-5} × prescribed proton dose (Gy) × neutron weighting factor

- **MC simulation result of the scintillation spectra and the relative absorbed doses from the simulated fourth prototype neutron detector**

Using MC simulation, neutron and gamma-ray scintillation spectra were obtained during the proton irradiation at Clatterbridge Hospital. The MC simulation results of the neutron and gamma-ray scintillation spectra are shown in Figure 85.

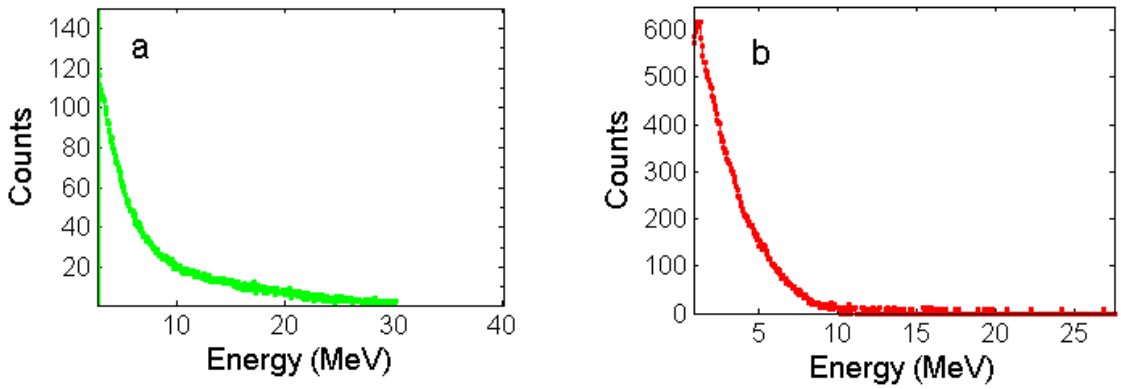

Figure 85: Neutron (a) and gamma-ray (b) scintillation spectra during the proton irradiation at Clatterbridge Hospital.

Figure 85 shows the scintillation neutron spectrum (a) with an exponential decay shape extending from thermal to 32MeV. The neutron nuclear data presented in International Commission on Radiation Units and Measurements (ICRU) Report 63 confirmed that neutrons from proton interaction with elements (such as, copper, tungsten and lead) are decreasing as dramatically as the produced neutrons with high energy [201]. For

example, the number produced of neutrons with an energy of thermal–3MeV, from 60MeV protons incident on tungsten, is 37 times more than produced neutrons with an energy of 27–31MeV [201]. Thus, the neutron spectrum appears to have an exponential decay shape.

Figure 85 shows that the scintillation gamma-ray spectrum (b) was extended to 10MeV. However, gamma-ray counts were approximately five times higher than the neutron counts at the lower neutron energies (<10MeV).

The relative neutron and gamma-ray DEs (or absorbed doses), obtained by dividing the integration of the scintillation spectra by the proton DE, were found to be 2.63 x 10^{-6}% and 1.4 x 10^{-6}% respectively. These results will be compared to the measured results that were taken using the fourth prototype neutron detector during the proton irradiation at Clatterbridge Hospital.

4.2.5 Summary and discussion

The relative DE distributions in the voxelised water phantom of neutrons and gamma rays were obtained using an MC simulation, and were presented in 2D plots. The relative integral neutron DE was found to be higher than that of gamma-ray DE. In addition, most of the neutron DE was distributed in and around the target voxel. In contrast, the gamma-ray DE was widely distributed.

The relative integral neutron DE in the voxelised water phantom was (14.8±0.135) x 10^{-3}%, where the highest DE was in the target voxel. The neutron dose in the target voxel (i.e. the proton therapy target volume) was found to be 7.4% of the total neutron dose.

The contribution of the gamma-ray DE to the total DE was found to be 35% (8 x 10^{-3}%) and it was widely distributed within the voxelised water phantom. However, the gamma-ray weighting factor is several times lower than the neutron weighting factor. The contribution of internal neutron DE and thermal (i.e. thermal and thermalised) neutron DE to the total neutron DE were 4.1% and 2.4% respectively.

In addition, the MC simulations of the neutron and gamma-ray scintillation spectra were obtained during the proton irradiation at Clatterbridge Hospital. The scintillation neutron spectrum appeared to have an exponential decay shape and extended from thermal to 32MeV. However, as a result of the neutron production decreasing dramatically at the high energy range, the neutron count >27MeV was found to be insignificant. The scintillation gamma-ray spectrum was extended to 10MeV. Gamma-ray counts were approximately five times higher than the neutron counts at the lower neutron energies (<10MeV). In addition, the relative neutron and gamma-ray absorbed doses, obtained from their scintillation spectra, were found to be 2.63 x 10^{-6} and 1.4 x 10^{-6} respectively. These results will be compared to the measured results that were taken using the fourth prototype neutron detector during the proton irradiation at Clatterbridge Hospital.

4.3 Measurements during proton irradiation in the proton therapy room at Clatterbridge Hospital

4.3.1 Aim and objectives

The MC simulation and the measurement attempted to determine the neutron scintillation spectrum during the proton irradiation at Clatterbridge Hospital. In addition, the MC simulation attempted to determine the relative neutron DE distribution in a voxelised water phantom.

The aim of taking the measurement was to validate the MC simulation of the neutron scintillation spectrum and its relative DE (or its absorbed dose). Hence, the MC simulations of the relative DE distributions from the neutrons and gamma rays in the voxelised water phantom were validated.

The MC simulation and measured results of the neutron scintillation spectrum were obtained from the designed and the simulated fourth prototype neutron detector. Then, the relative neutron DE was determined by dividing the summation of the scintillation energy spectrum by the prescribed therapeutic proton dose.

The measurement geometry during the proton irradiation at Clatterbridge Hospital was adjusted so that it was the same to the MC simulation geometry. The fourth prototype neutron detector was located in the same position as that of the MC simulation, and the configurations of the proton therapy beam line were considered.

Furthermore, the following objectives were achieved:

1. Applying the charges ratio PSD method to the collected data.

The performance of the charges ratio PSD method in the NPL measurements was found to be superior compared to the other tested PSD methods. Therefore, the charges ratio PSD method was applied to the collected data to separate the collected neutron and gamma ray signals. In addition, an evaluation of the applied charges ratio PSD method was conducted by measuring the FoM and PSD threshold.

2. Estimating the relative thermal and gamma-ray DEs (or absorbed doses) in the fourth prototype neutron detector.

The measured DEs from thermal neutrons and gamma rays were obtained by subtracting the neutron DE from the total DE, as measured by the fourth prototype neutron detector.

Extra measurements were taken using the same detector location and the proton therapy beam line configurations. The detector was first shielded by 5cm-thick lead, and then 5cm-thick wax. These measurements were taken in order to show the effectiveness of using radiation shields to reduce the neutron and gamma-ray events (i.e. radiation doses from neutrons and gamma rays).

4.3.2 Materials and methods

- **Neutron detector**

The neutron detector was the fourth prototype neutron detector, which was the same as that used for the NPL measurements. The properties of the fourth prototype neutron detector were mentioned in detail in Chapter 2, 'Prototype neutron detector designs'.

- **Clatterbridge proton therapy beam line**

The location of Clatterbridge Hospital is Bebington in the UK. The Clatterbridge proton cyclotron is the Scanditronix MC-60 PF, which has been used to provide proton beams since 1983. The energy of the proton therapy particles is 60MeV, with 31mm maximum penetration in water [198]. The therapeutic proton energy is degraded from 62MeV as it passes through the beam line to 60MeV at the treated target. The proton therapy system at Clatterbridge Hospital is a double-scattering proton therapy system [202].

4.3.3 Measurement setup

Table 22 shows the proton beam configurations used for the measurements during the proton irradiation at Clatterbridge Hospital.

Table 22: Configurations of the Clatterbridge proton therapy beam line.

Proton therapy energy	60MeV (full energy Bragg peak)
Beam field size	20 x 20mm
Proton therapy dose rate	40Gy/min

The detector was connected to an oscilloscope via a signal cable with 50Ω impedance. The oscilloscope was a PicoScope 3000 Series with 1GS/s sampling, a 200MHz bandwidth and an 8-bit resolution. The scintillation pulses were viewed and stored on a laptop computer. The detector was located 15cm in front of and 30cm below the final collimator (i.e. the second collimator) of the proton therapy beam line. Figure 86 shows the Measurement setup in the proton therapy room at Clatterbridge Hospital.

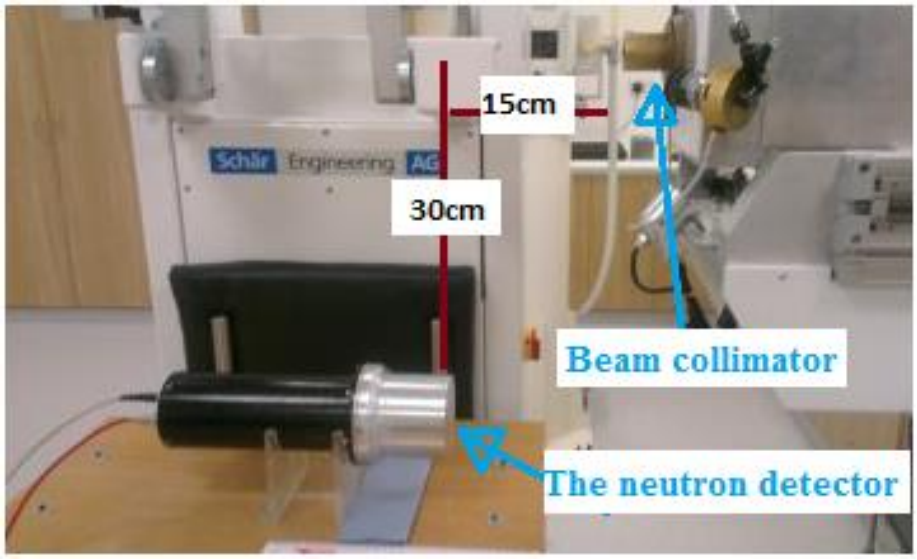

Figure 86: Measurement setup in the proton therapy room at Clatterbridge Hospital.

With regard to the MC simulation results, the estimated neutron energy range was from thermal to 32MeV; therefore, two voltage ranges of the oscilloscope were used. These two ranges were 500mV and 5V. In addition, the trigger of the oscilloscope was adjusted at 40mV and 200mV respectively. Therefore, the two ranges were equivalent to the energy ranges from 0.17MeVee to 2.1MeVee, and from 0.85MeVee to

21MeVee respectively regarding the volt-to-MeVee calibration factor, which was 0.233±0.009 (volt to MeVee).

The proton therapy machine was run and the fourth prototype neutron detector was exposed twice to the secondary radiation (out-of-field) for 10 minutes; signals were collected. For each voltage range, there were 20 files of collected signals (each file contains 6,000 signals). When taking these measurements, the setup was fixed and the data were collected.

In addition, extra measurements were taken. The measurement was conducted twice at the high voltage range in the same condition as before, but each time the detector was shielded with 5cm-thick lead and 5cm-thick wax respectively. For example, a 5cm thickness of lead is efficient for reducing the initial intensity of monoenergetic 4.5MeV gamma rays to 9%, while a 5cm thickness of wax is efficient for reducing the initial intensity of monoenergetic 4.5MeV neutrons to 39%, in terms of the following equations [8]:

$$\mathbf{G_1/G_0 = e^{-\mu x}}$$

$$\mathbf{N_1/N_0 = e^{-\Sigma x}}$$

Where G_0 is the initial gamma-ray intensity, G_1 is the final gamma-ray intensity. N_0 is the initial neutron intensity, and N_1 is the final neutron intensity. X is the shield thickness, and μ and Σ are the gamma-ray linear attenuation coefficient and neutron macroscopic cross section respectively [137] [203].

4.3.4 Results

- **Charges ratio PSD method**

The charges ratio PSD method was obtained in the same way to that obtained from the collected data during the NPL measurements, which was explained in the previous chapter. Figure 87 shows the MATLAB scatter plots of the charges ratio PSD method

obtained for the high and low voltage ranges during the proton irradiation at Clatterbridge Hospital.

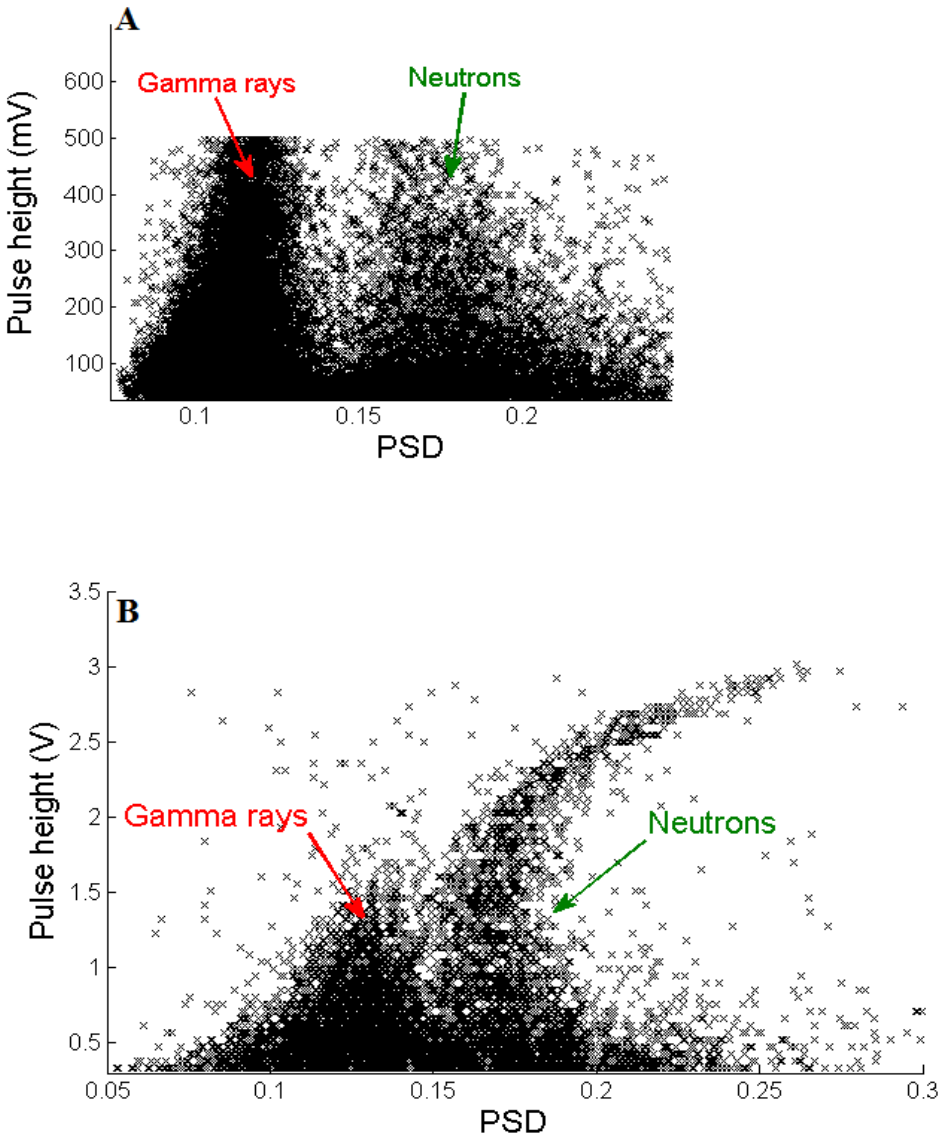

Figure 87: MATLAB scatter plots of the charges ratio PSD method obtained for the low (A) and high (B) voltage ranges.

The plots show acceptable separation between neutron and gamma-ray events. The performance of the PSD method was evaluated using the FoM and PSD threshold values.

- **FoMs**

The performance of the charges ratio PSD method was evaluated by finding the FoMs and the PSD threshold values. The FoMs of the charges ratio PSD method for the low voltage and the high voltage ranges were found to be 1.1 and 0.65 respectively. Therefore, the neutron-gamma separation was >90% and >70% for the low and high voltage ranges respectively [193]. Figures 88 and 90 show the charges ratio PSD method histograms obtained from the collected data at both the low and high voltage ranges during the proton irradiation at Clatterbridge Hospital.

Regarding the volt-to-MeVee calibration factor, the thresholds of the charges ratio PSD method at both the low and high voltage ranges were found to be 0.21MeVee and 1.8MeVee respectively.

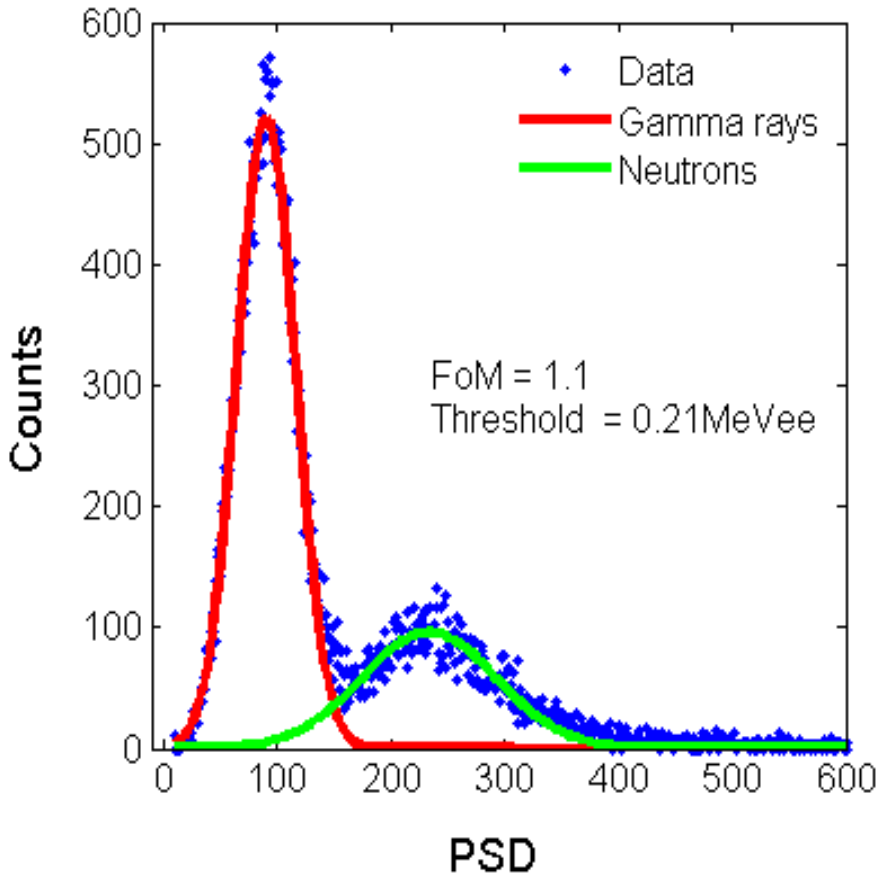

Figure 88: Charges ratio PSD method histograms (two Gaussians) obtained from the collected data at the low voltage range during the proton irradiation at Clatterbridge Hospital.

The performance of the charges ratio PSD method at the low range was good over 0.21MeVee. Therefore, below 0.21MeVee the recorded radiation signals cannot be identified as neutron or gamma-ray signals. Regarding the neutron energy calibration curve (i.e. from MeVee to MeV) shown in Figure 89, the lowest detected fast neutron energy was 1MeV. Thereby, the detected neutron energy range at the low voltage range was from 1MeV to 5.5MeV.

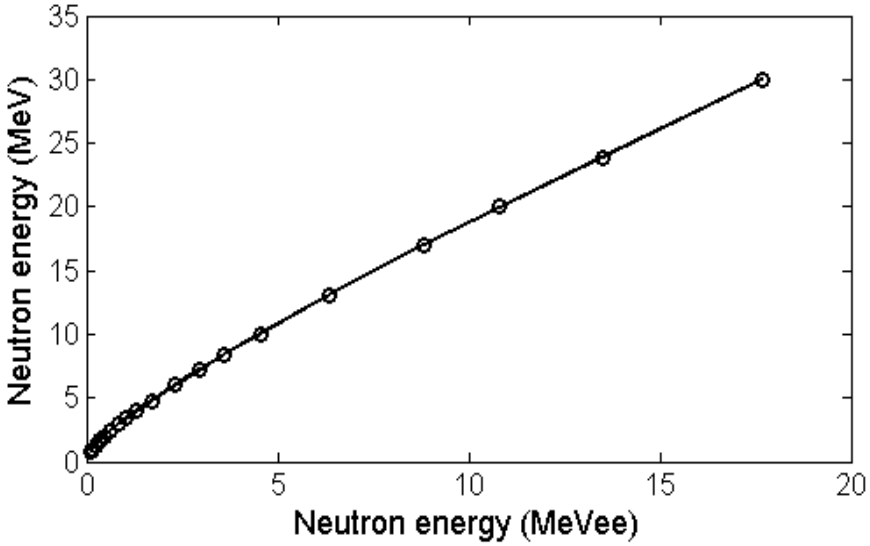

Figure 89: Neutron energy calibration curve based on the data from the literature review [83]**.**

The neutron energy calibration curve shown in Figure 89 was obtained based on the data from the literature review [83]. This data, which was used to calibrate the neutron energy range from MeVee to MeV, was obtained from an N-213 OLS detector's measured and MC simulated results.

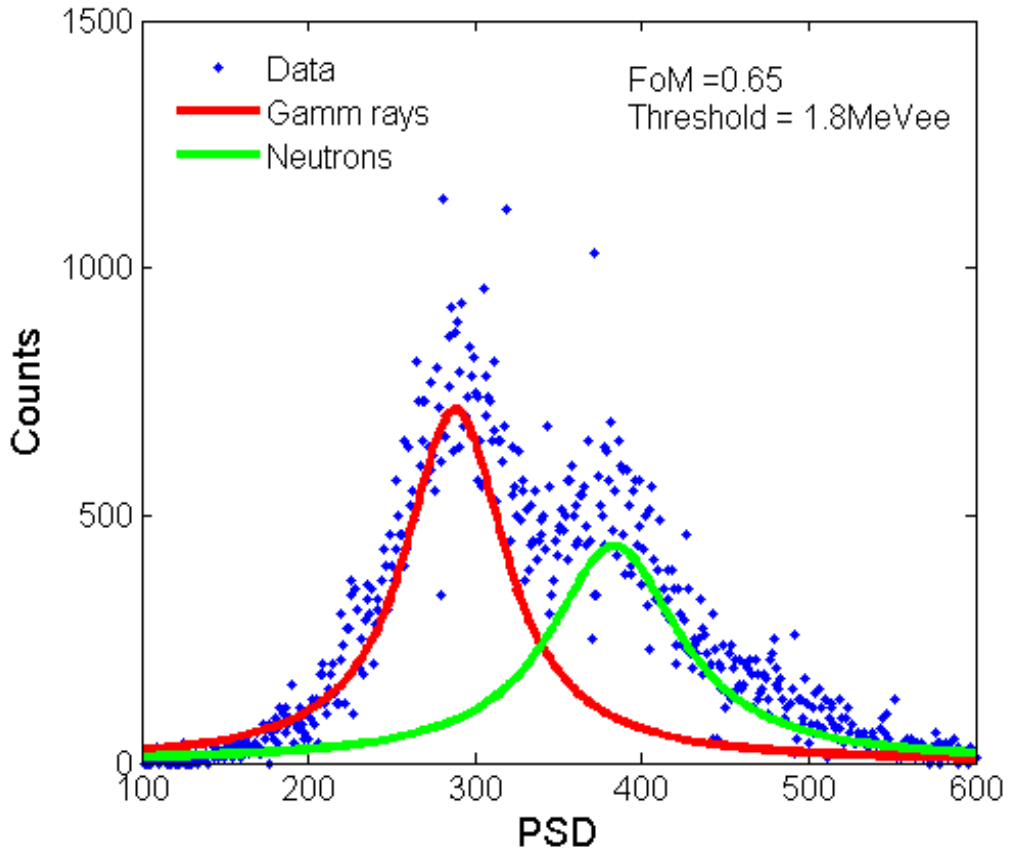

Figure 90: Charges ratio PSD method histograms (two Gaussians) obtained from the collected data at the high voltage range during the proton irradiation at Clatterbridge Hospital.

The performance of the charges ratio PSD method at the high voltage range was acceptable over 1.8MeVee. Therefore, below 1.8MeVee the recorded radiation signals cannot be identified as neutron or gamma-ray signals. Regarding the energy calibration curve shown in Figure 89, the lowest detected fast neutron energy was 4.2MeV. Thereby, the detected neutron energy range at the high voltage range was from 4.2MeV to 27MeV.

Thus, the FoM values of the charges ratio PSD method, which were 1.1 and 0.65 at the low and the high voltage ranges respectively, show that the separation of neutron and gamma-ray events is acceptable. Therefore, the detected neutron energy range was from 1MeV to 27MeV. The implication of the undetected neutron energies (<1MeV) will be evaluated by comparing the relative DEs from the measured and simulated neutron scintillation spectrum.

- **Measured neutron and gamma-ray scintillation spectra**

Using the charges ratio PSD method, neutrons and gamma rays were separated. The average neutron and gamma-ray counts were found to be 28% and 72% respectively. In contrast, the MC simulation result of the gamma-ray count was 80%. The difference resulted from using a 0.21MeVee oscilloscope trigger during the measurement, whereby 8% of the gamma-ray count was eliminated.

Thus, at the low and high voltage range measurements, neutron and gamma-ray spectra were obtained. Figure 91 shows the neutron and gamma-ray scintillation spectra obtained at the low voltage range using the fourth prototype neutron detector and the charges ratio PSD method during the proton irradiation at Clatterbridge Hospital.

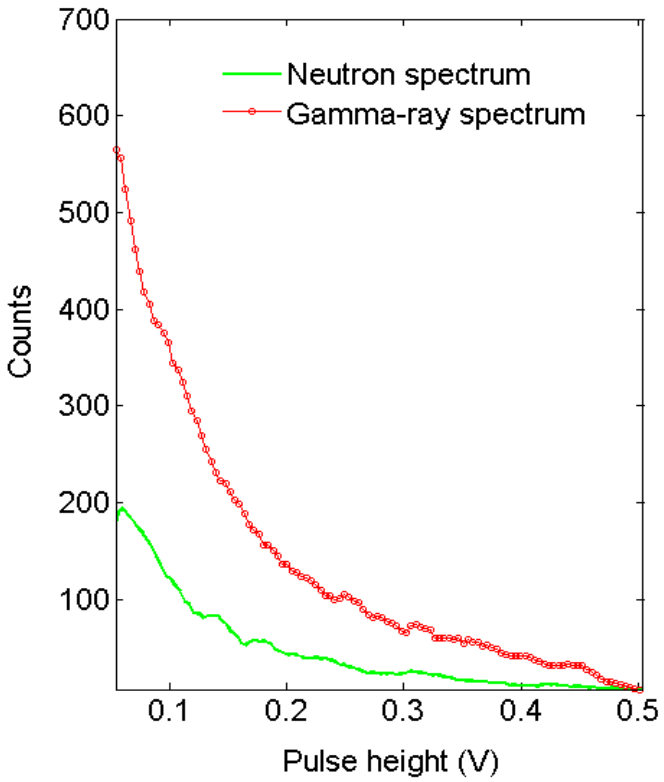

Figure 91: Neutron and gamma-ray scintillation spectra obtained at the low voltage range using the fourth prototype neutron detector and the charges ratio PSD method during the proton irradiation at Clatterbridge Hospital.

The voltage range of the neutron and gamma-ray spectra shown in Figure 91 was from 0.05V to 0.5V. However, the oscilloscope trigger was adjusted to be 0.04V where the PSD threshold was 0.05V. Therefore, the signals below the threshold were rejected. In addition, regarding the calibration factor (volt to MeVee), the energy range was from 0.21MeVee to 5.5MeVee.

Figure 92 shows the neutron and gamma-ray scintillation spectra obtained at the high voltage range using the fourth prototype neutron detector and the charges ratio PSD method during the proton irradiation at Clatterbridge Hospital.

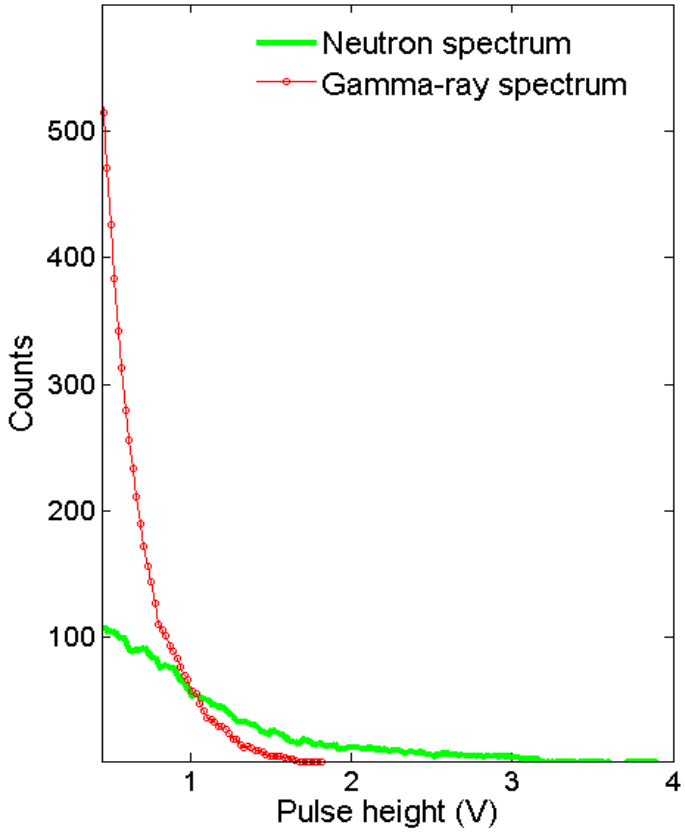

Figure 92: Neutron and gamma-ray scintillation spectra obtained at the high voltage range using the fourth prototype neutron detector and the charges ratio PSD method during the proton irradiation at Clatterbridge Hospital.

The voltage range of the neutron and gamma-ray spectra shown in Figure 92 was from 0.5V to 3.2V. However, the oscilloscope trigger was adjusted to be 0.2V where the PSD threshold was 0.42V. Therefore, the signals below the threshold were rejected. In addition, the voltage range between 0.42V and 0.5V was included in the neutron-

detected energies at the lower voltage range measurements. Therefore, the voltage range below 0.5V can be rejected. Thus, regarding the calibration factor (volt to MeVee), the energy range was from 5.5MeV to 27MeV.

In addition, at the high voltage range, extra measurements were taken with the detector at the same fixed location and with the same proton therapy beam line configurations. In these measurements, the fourth prototype neutron detector was shielded with the following:

1. 5cm-thick lead.
2. 5cm-thick wax.

This was done to show the effectiveness of the shields in order to reduce the neutron and gamma-ray events and to propose a neutron shield that would reduce a patient's neutron dose. Figures 93 and 94 show the measurement results.

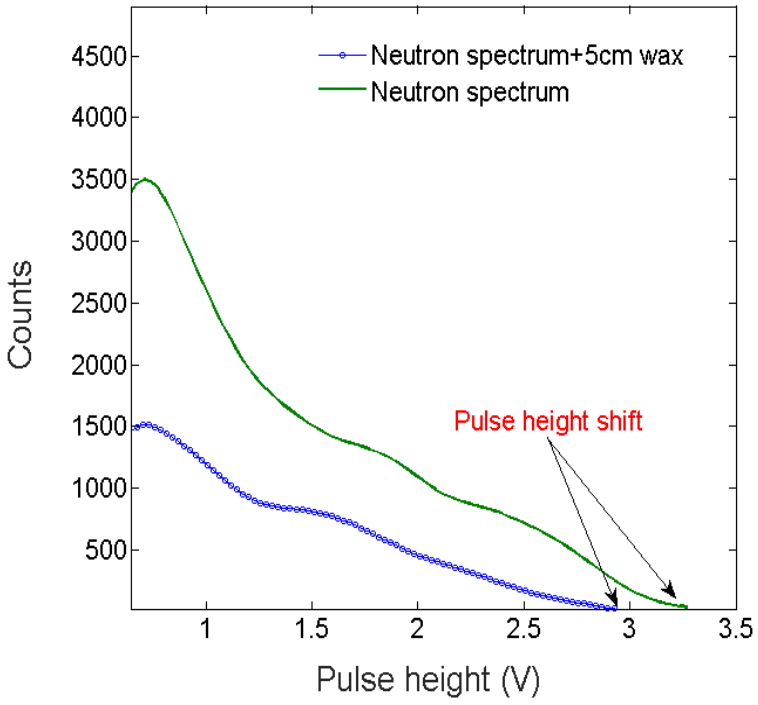

Figure 93: Neutron scintillation spectrum with and without the 5cm-thick wax shield.

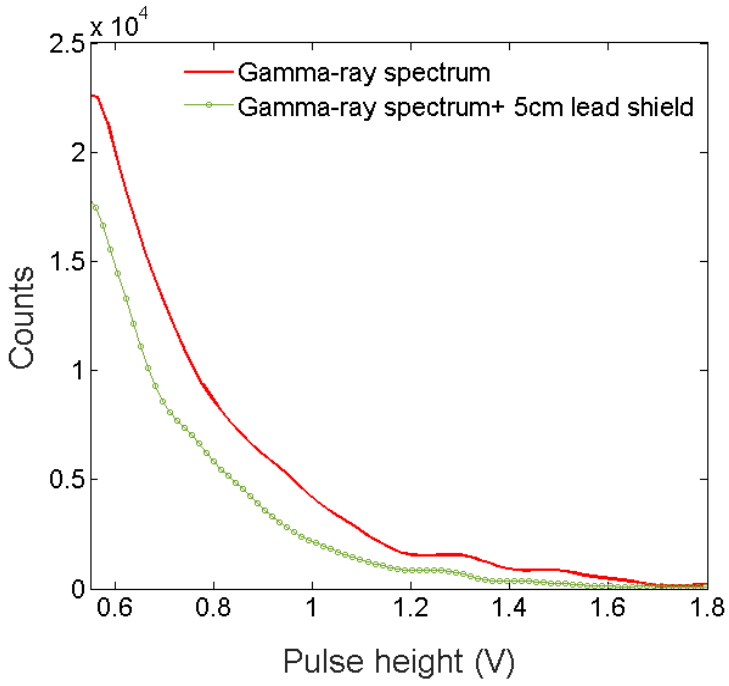

Figure 94: Gamma-ray scintillation spectrum with and without the 5cm-thick lead shield.

The plots confirm that gamma-ray and neutron events during the proton irradiation at Clatterbridge Hospital were reduced considerably when using neutron and gamma-ray shields (wax and lead respectively). Therefore, using a few centimetres' thickness of neutron shield would significantly reduce the neutron dose.

- **Comparison of the MC simulation and measurement results of scintillation spectra**

In order to compare the simulated and measured spectra, the simulated neutron and gamma-ray spectra were normalised to be the same in counts (Y-axis) as the measured spectra. This was done using a MATLAB program. In addition, the calibration curve (MeVee to MeV) shown in figure 89 was used to calibrate the energy range of the measured neutron spectrum (i.e. X-axis).

Figure 95 shows the comparison between both the measured and the simulated neutron and gamma-ray scintillation spectra.

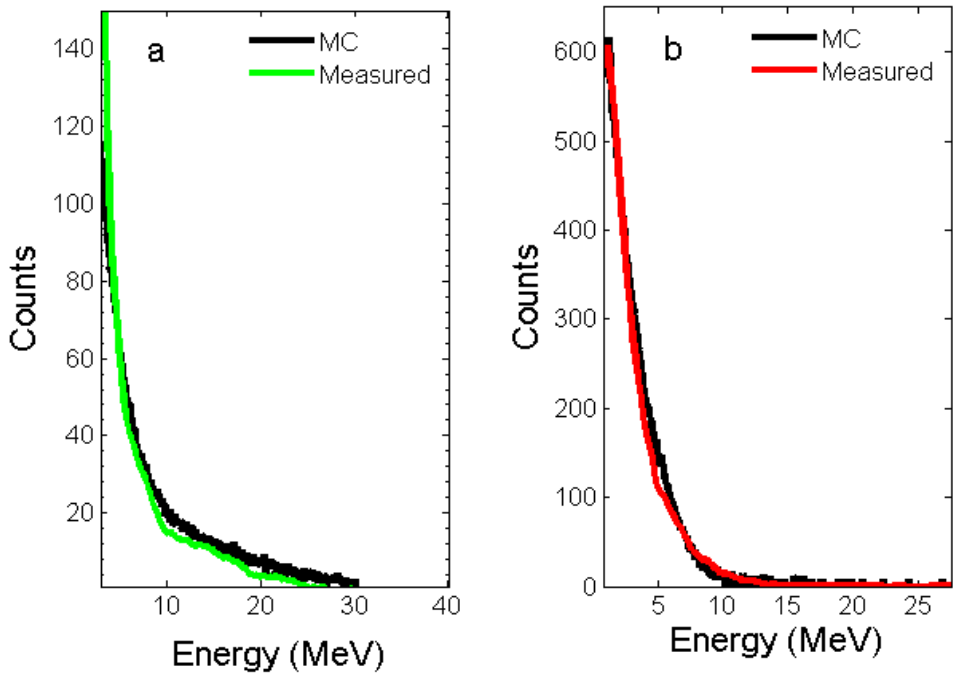

Figure 95: Measured and MC simulation results of the neutron (a) and the gamma-ray (b) spectra.

The measured and simulated scintillation gamma-ray and neutron spectra show good agreement. However, the MC scintillation neutron spectrum shows an insignificant count at the fast neutron energy range >27MeV (i.e. <1.5%). This can be explained by the neutron nuclear data presented in ICRU Report 63, which shows that the neutron count, from proton interaction with elements, dramatically decreases at the high energy range [201].

- **Relative absorbed dose estimation in the fourth prototype neutron detector**

1. **Estimation of relative neutron absorbed dose in the fourth prototype neutron detector**

The MC simulation and the measured results of the neutron absorbed dose were obtained by dividing the summation of the scintillation energy spectrum (i.e. DE to absorbed dose) by the primary proton absorbed dose.

The MC simulation result of the relative neutron absorbed dose was 2.63μGy/Gy. In addition, the MC simulation shows that the neutron count rate was 5.7 x 10^3

scintillation signal/Gy. The limitations of the oscilloscope and laptop were due to the speed of recording signals. Experimentally, the maximum recorded signal count rate was 6,000 signals/Gy, whereas the estimated count rate (neutrons and gamma rays incident on the detector) was >20,000 signals/Gy.

The measured neutron count rate (i.e. by applying the PSD method) was 1.7 x 10^3 signals/Gy. While the MC simulation result showed that the estimated neutron count rate (i.e. neutron incident on the detector) was 3.4 times more than the measured. Accordingly, the measured neutron count rate was corrected with regard to the MC simulation result.

In addition, table 23 shows the calibration factors used to calibrate the measured neutron absorbed dose.

Table 23: Calibration factors used to estimate the neutron DE during the proton irradiation at Clatterbridge Hospital.

Calibration factors	Value
Volt to MeVee conversion	Volt × 0.233±0.009 (obtained from Figure 56)
MeVee to MeV conversion	From the calibration curve in Figure 89
DE (MeV) to absorbed dose (Gy)	MeV × 1.6 x 10^{-13} [11]

Thus, the relative absorbed dose obtained from the measured scintillation neutron energy spectrum was 2.08±0.42µGy/Gy. Hence, the agreement between the measured and the MC simulation results of the relative neutron absorbed doses was within 80±20. However, the difference was due to the calibration and correction factors' uncertainties. In addition, the lower measured neutron energy was 1MeV regarding the threshold of the charge ratio PSD method. Thereby, the MC simulation results of the relative DE distributions from neutrons and gamma rays in the voxelised water phantom were validated.

2. Estimation of relative thermal neutron and gamma-ray absorbed doses in the fourth prototype neutron detector

In addition to the high gamma-ray background during the proton irradiation at Clatterbridge Hospital, the EJ-331 (the detection material used) produced conversion electrons and gamma rays as a result of thermal neutron capture reactions. Moreover, the threshold of the applied charges ratio PSD Method was 0.21MeVee where the significant energy range of the conversion electrons was lower than 0.21MeVee. In addition, the conversion electrons and gamma rays have the same scintillation pulse shape.

Thereby, utilising conversion electron signals (energy and shape) to recognise thermal neutrons was found to be impossible. However, the measured thermal neutron and gamma-ray absorbed doses can be estimated by subtracting the measured neutron absorbed dose (2.08±0.42μGy/Gy) from the total absorbed dose recorded by the fourth prototype neutron detector.

Thus, the measured thermal neutron and external gamma-ray absorbed dose was 1.12±0.25μGy/Gy. In addition, the MC simulation estimation of the thermal neutron absorbed dose during the proton irradiation was 5% of the total gamma-ray absorbed dose. Figure 96 shows the total gamma-ray spectrum compared to the gamma-ray spectrum released from the EJ-331 thermal neutron capture reactions.

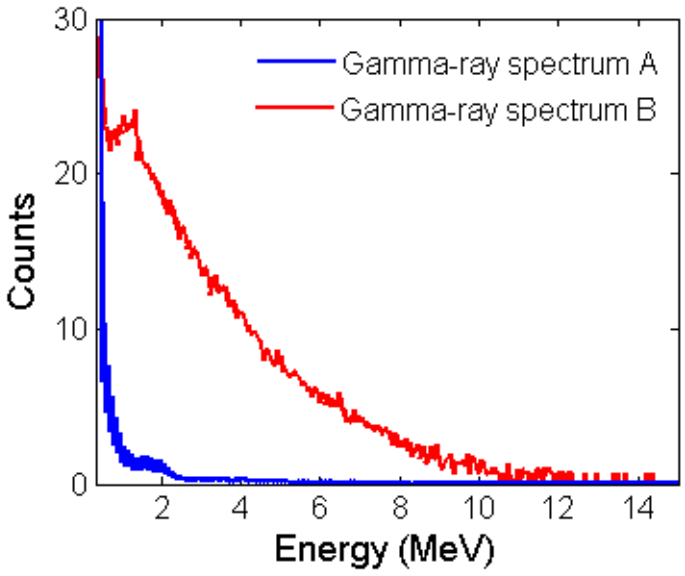

Figure 96: Gamma-ray spectrum released from the gadolinium thermal neutron capture reactions (A) compared to the total gamma-ray spectrum (B) (i.e. from the external gamma rays and the gamma rays released from the thermal neutron capture).

Therefore, the estimated measured thermal neutron absorbed dose and the gamma-ray absorbed dose were 0.06±0.012μGy/Gy and 1.07±0.22μGy/Gy respectively.

4.3.5 Summary

Measurements were taken during the proton irradiation at Clatterbridge Hospital in order to validate the MC simulation of the neutron scintillation spectrum and its relative absorbed dose. Hence, the MC simulation of the relative DE distributions from the neutrons and gamma rays in the voxelised water phantom was validated.

Measurement was taken using the fourth prototype neutron detector. Neutron and gamma-ray spectra and the relative absorbed doses were obtained. Even though the MC simulation of the scintillation neutron spectrum shows an insignificant neutron count >27MeV, there was a good agreement between the MC simulation result and the obtained energy neutron spectrum up to 27MeV. In addition, the MC simulation and measured results of the gamma-ray spectrum show a good agreement, with a same energy range.

The agreement between the measured and the simulated relative neutron absorbed dose was found to be within 80%, at 2.08±0.42μGy/Gy and 2.63μGy/Gy respectively.

4.4 Discussions and comparisons

The relative integral neutron absorbed dose within the voxelised water phantom was 0.148±0.00135mGy/Gy. The neutron absorbed dose was converted to an equivalent dose by using the neutron weighting factor as shown in the following equation:

Neutron equivalent dose (Sv) = neutron weighting factor x neutron absorbed dose (Gy) [204]

Using the neutron weighting factor of 10 [199] [2] [67], the relative integral neutron equivalent dose within the voxelised water phantom was found to be 1.48±0.0135mSv/Gy. In addition, the contribution from the relative integral internal neutron equivalent dose was 0.061mSv/Gy. Therefore, the contribution of internal neutrons to the total neutron dose was found to be 4.1%.

Moreover, the relative integral thermal neutron and the relative integral gamma-ray absorbed doses in the voxelised water phantom were 0.0036mGy/Gy and 0.08mGy/Gy respectively. In addition, the relative integral thermal neutron and gamma-ray absorbed doses were converted to equivalent doses by using a thermal neutron weighting factor of 5 and a gamma-ray weighting factor of 1 [8]. Therefore, the relative integral thermal neutron and gamma-ray equivalent doses were 0.018mSv/Gy and 0.08mSv/Gy respectively.

Thus, the contribution of gamma rays to the relative integral secondary radiation equivalent dose was 5.1%. In addition, the contribution of thermal neutrons to the relative integral neutron equivalent dose was 1.2%. The contribution of thermal neutrons and gamma rays was reported to be less than 10% of the total secondary radiation dose [95]. Therefore, fast external neutrons are the main source (89.6%) of the additional unwanted dose during proton irradiation at Clatterbridge Hospital.

The relative integral neutron equivalent dose was compared to many published papers' results; for example, the MC simulation result was found to be within 95% to 98% agreement with the result of the Harvard Cyclotron Laboratory, and with the result of the Proton Medical Research Center at Tsukuba University respectively [205] [206]. Table 24 shows the obtained MC result of the relative integral neutron equivalent dose

(mSv/Gy), compared to the MC simulation and the measured results from the literature review.

Table 24: MC simulation result of the relative integral neutron equivalent dose (mSv/Gy) during the proton irradiation at Clatterbridge Hospital compared to the MC simulation and measured results from the literature review.

Institute	Method	Parameters	Beam target	Neutron dose
Proton therapy at Clatterbridge Hospital (this work)	MC simulation (Geant4)	62MeV and 2cm field size (patient location)	Water phantom box (50 x x 100 x 50cm^3)	1.48
Harvard Cyclotron Laboratory [205]	• MC simulation (MCNP) • Measured (Bonner spheres)	152MeV and 5cm field size (patient location)	Lucite phantom cylinder (26cm dia. x 24cm length)	• 1.4 • 2.2
Proton Medical Research Center at Tsukuba University [206]	Measured (WENDI-II)	250MeV and 5cm field size and 90^0 50cm from beam axis	Water phantom box (22 x x 24 x 39cm^3)	1.45
Proton therapy at Loma Linda University Cancer Center [64]	Measured (silicon on insulator)	Typical prostate proton therapy • 90^0 and 2.5cm from beam axis • 0^0 and 0.6cm from beam axis	• Anthropomorphic phantom • Polystyrene plate phantom	• 3.9 • 1.6
MD Anderson Proton Therapy Center [84]	Measured (extended range Bonner sphere)	250MeV proton 90^0 100cm	No target	1.6
Proton Medical Research Center [69]	Measured (proportional counter, REM500)	200MeV 0^0 along the beam axis to 80cm	Water phantom	2
University of Florida Health Proton Therapy Institute (IBA eye-line) [81]	Measured (neutron bubble detector)	105MeV and 2cm field size (patient location)	Head phantom	0.197

Table 24 shows that some assessments of the neutron equivalent dose during proton irradiation were between 1mSv/Gy and 4mSv/Gy. In addition, the neutron equivalent dose was reported to be around this value in other published papers [67] [207].

However, regarding the measured result (i.e. 0.197mS/Gy) at the University of Florida Health Proton Therapy Institute, the beam line (IBA eye-line) schematic showed that there was a 42cm-thick polyethylene neutron shield around the brass collimator.

Nevertheless, the neutron equivalent dose depended strongly on the proton therapy facility, measurement methods and materials (i.e. simulated or measured), and the measurement conditions (i.e. the distance from the proton therapy beam axis and the degree of incident neutrons). Thereby, some published papers show the neutron equivalent dose as being significantly more and others significantly less than those shown in Table 24. For example, the relative neutron equivalent dose was assessed for unmodulated proton therapy at a different beam configuration [208]. The relative neutron equivalent dose was found to be 19mSv/Gy with 250MeV proton energy, a closed aperture and a large field size, whereas it was found to be 0.3mSv/Gy with 100MeV proton energy, a closed aperture and a small field size.

Thus, the integral neutron equivalent dose, during proton irradiation (i.e. proton therapy) at Clatterbridge Hospital, can be obtained from the following relation:

Integral neutron equivalent dose (Sv) = (14.8±0.135) × 10^{-5} × prescribed proton dose (Gy) × neutron weighting factor

The integral neutron equivalent dose from the prescribed proton therapy dose of 53.1Gy [209] during the proton irradiation at Clatterbridge Hospital was found to be 78.6mSv. Moreover, the localised neutron equivalent doses in a patient's head, neck, chest and abdomen (i.e. in a voxelised water phantom using an MC simulation) were obtained and are dem**o**nstrated in Figure 97. This was done by the summation of neutron equivalent doses in the voxels of the water phantom localised in the regions of the patient's head, neck, chest and abdomen respectively.

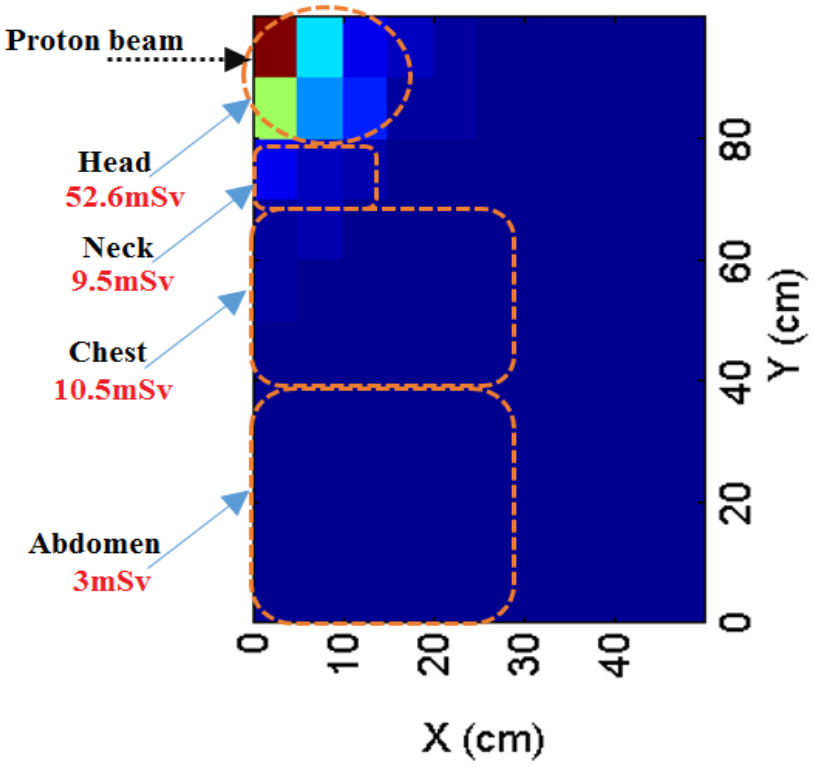

Figure 97: MC simulation results of the localised neutron equivalent dose at the head, neck, chest and abdomen (i.e. positions in the voxelised water phantom) from the prescribed proton therapy dose of 53.1Gy [209]**.**

In addition, the integral gamma-ray equivalent dose from the prescribed proton therapy dose of 53.1Gy was found to be 4.25mSv, which was widely distributed in the voxelised water phantom compared to the neutron equivalent dose. Thereby, it was found to be insignificant and can be neglected.

The neuron dose in the proton therapy target (i.e. target voxel) was small compared to the out-of-target neutron dose. It was found to be 5.8mSv (i.e. 7.4% of the total neutron dose). The neutron dose in the patient's head was 60% of the total neutron dose. Therefore, using a few centimetres of shielding (i.e. 5cm around the final collimator) would reduce the neutron dose by more than 50%.

However, the estimated risk of secondary cancers from the neutron dose during proton therapy at Clatterbridge Hospital is small. For, example, using BEIR VII report, the highest PCCs (the probability of cancers causation) for male patients were found to be 7.8% and 0.45% for leukaemia and thyroid cancers respectively. In addition the highest PCCs for female patient were found to be 7.8%, 0.95% and 0.45% for

leukaemia, thyroid and breast cancers respectively. Thus, the main concern related to the secondary neutron dose during proton therapy at Clatterbridge Hospital is the probability related to the occurrence of leukaemia (7.8%), whereas the risks related to other secondary cancers could be insignificant (<1%).

To conclude, fast external neutrons are the main concern in terms of the additional unwanted secondary radiation dose during proton therapy at Clatterbridge Hospital. Although the neutron dose was small compared to the prescribed proton therapy dose, it is not negligible and the dose distribution can be used as the basis of the risk estimation from radiation induced secondary cancers.

Chapter 5. Summary, discussions and conclusions

The significance of proton therapy treatment is the high proton energy deposition at the target volume. Neutrons are generated from interactions of high-energy protons with the treatment head and the patient's body (treated target).

During the scattering proton therapy delivery, in order to deliver a useful, uniform, flat proton beam to the target volume, the initial narrow pencil proton beam needs to be converted to a wide, flat and uniform proton beam profile, which is the beam spreading process. This is done by using high atomic number materials (scatterers). In addition, the proton beam needs to be modulated to cover the whole target volume (modulating). During proton beam spreading and the modulating, the proton particles interact with the beam treatment head materials located in the proton beam path. Secondary neutrons are generated from these interactions (external neutron source). In addition, the interaction of proton particles with the target volume is another source of secondary neutrons (internal neutron source).

The neutron production during the spot-scanning delivery technique was reported to be significantly low compared to the scattering delivery technique, because of the absence of the proton beam shaping devices such as scatterers, collimators and compensators in the spot-scanning proton therapy system. Therefore, the dominant neutron source is the internal neutrons generated inside the treated target. During spot scanning, the neutrons are generated in the target volume from thermal to the maximum proton energy. In contrast, compensators and collimators are used in the wobbling proton therapy system. Therefore, the neutron production from the wobbling proton therapy system could be higher compared with the spot-scanning proton therapy system.

Regarding the high radiation weighting factor of neutrons, a minor neutron dose could be significant. During scattering proton therapy, the neutron dose could be ten to several ten times more than that of spot-scanning proton therapy. However, the dose distribution (dose location) is the basis of the risk estimation from radiation induced secondary cancers.

In addition, estimation of the secondary cancers risk involves converting the neutron dose (Sv) to risk.

The neutron dose to healthy tissue near the treated target could be the same for both spot-scanning and scattering proton therapy. It was reported that the neutron dose at a few centimetres from the target during spot-scanning proton therapy could be comparable to the dose from scattering proton therapy. This is because, near the treated target, the dominant of the neutron source is the internal neutrons generated inside the target.

MC simulations were used widely to estimate the neutron dose during the proton therapy. The reasons were found to be the following:

- The difficulty of neutron detection in a high gamma-ray background.
- The difficulty and complexity of constructing more realistic human-body phantoms.
- Most of the measured neutron doses were obtained in terms of the distance from the central proton therapy beam. The MC simulation gives a better idea of the neutron dose distribution over body organs, which is the basis of the risk estimation for radiation developing secondary cancers.

Therefore, MC simulations were used to find the neutron and gamma-ray dose distributions during the proton irradiation at Clatterbridge Hospital.

MC simulations of the proton therapy beam line at Clatterbridge Hospital, the DE distributions, the measurement setup, and the data analysis were done using Geant4 and GAMOS.4.0.0 MC simulation codes. Geant4 was used to simulate the geometries. GAMOS.4.0.0 was used to apply the required physics models in order to simulate the proton therapy generator, track the secondary radiation particles, and score the DE and scintillation light.

The DE distributions from neutrons and gamma rays in a 50 x 100 x 50cm^3 voxelised water phantom (1,000 voxels) were scored. The neutron DE was found to be higher than the gamma-ray DE. In addition, most of the neutron DE was distributed around and within the target voxel. In contrast, the gamma-ray DE was widely distributed.

The relative integral neutron DE to the primary proton DE in the voxelised water phantom was (14.8±0.135) x 10^{-3}%. The contribution of the gamma-ray DE to the total DE was found to be 35% (8 x 10^{-3}%). However, the gamma-ray weighting factor is several times lower than the neutron weighting factor. The contribution of the internal neutron DE to the total neutron DE was found to be 4.1%. Furthermore, the contribution of the thermal and thermalised neutron DE was found to be 2.4%.

Thus, the MC simulation results showed that fast external neutrons are the main source (89.6%) of the additional unwanted dose during proton irradiation at Clatterbridge Hospital.

The validation of the MC simulation results was done using the designed fourth prototype neutron detector. This was done through five stages, which were the following:

1. Designing four prototype neutron detectors.
2. Validation the fourth prototype neutron detector using MC simulation.
3. Testing the fourth prototype neutron detector in a mixed radiation field and evaluating the performances of four PSD methods to discriminate neutrons from gamma rays.
4. Taking measurements during the proton irradiation at Clatterbridge Hospital using the fourth prototype neutron detector. This was done to validate the MC simulation results of the neutron scintillation spectrum and its relative absorbed dose.

Firstly, in the first, second and the third prototype neutron detector designs, only the cell of the detection material was changed (Teflon 9cm x 20cm, glass 5.3cm x 5cm and white plastic 5.3cm x 5cm), while the instruments—oscilloscope, MCA, shaping amplifier, cables and PMT—remained the same. In addition, the EJ-331 (gadolinium-loaded liquid scintillator) was used as a detection material in the three designs. The main concern during the designing of the first, second and third prototype neutron detectors was the scintillation counting and the improvement of the detector energy resolution.

In the first prototype neutron detector design, the Cs^{137} spectrum was found to have a broadened spectrum peak due to the loss of scintillation light. The detector cell

diameter (9cm) was much larger than the PMT diameter (5cm). This led to the loss of scintillation light and therefore degraded the energy resolution. In addition, scintillation light was lost due to the difference in refractive index between the air and the EJ-331 liquid scintillator. This degraded the energy resolution.

In the second prototype neutron detector design, the loss of scintillation light was avoided by using a cell with a 5.3cm diameter that matched the PMT diameter of 5.2cm. However, the improvement in the energy resolution was not adequate due to the light reflector, which was aluminium foil that had been mounted on the cell wall manually.

In the third prototype neutron detector design, the detector cell was cylindrical (5.3cm x 5cm) and made of white plastic. The white inner wall of the cell was considered to be a light reflector. The detector energy resolution significantly improved as compared to the first and second prototype neutron detector designs.

The energy resolution of the second design was improved by 50% as compared to the first design. The improvement was approximately double in the third detector design, which was inferior by 25% to the Cs^{137} reference spectrum (i.e. the Cs^{137} spectrum provided by Eljen Technology). The target improvement for the energy resolution of the fourth prototype neutron detector design was 25% higher than the resolution achieved using the third prototype neutron detector.

Secondly, in order to validate the fourth prototype neutron detector design, an MC simulation was used as a guideline when constructing the detector. The simulated detector was an aluminium container that was cylindrical in shape (10cm diameter x 10cm height), with a glass window that was to be coupled to the PMT. The PMT was simulated to be cylindrical in shape with the same diameter as the scintillator; it was made of glass and was attached to the side of the container.

An OLS was considered to be the optimum neutron detection material. Thus, three commercially available OLS detection materials were compared. The three different types of OLS detectors (based on materials) were pure (EJ-309), boron-loaded (EJ-339) and gadolinium-loaded (EJ-331). These three materials were selected because they are regularly used in neutron detection.

Comparisons were conducted for the DE spectrum and the scintillation spectrum of the Cs^{137} and $Am-Be$ radiation sources. The MC simulation results of the Cs^{137} scintillation spectrum from the three detection materials (EJ-331, EJ-339 and EJ-309) had the same response to the gamma-ray source. However, there was approximately a ±5% count difference in the scintillation efficiencies of the three materials. The MC simulation results of the $Am-Be$ scintillation spectrum from the EJ-331 and EJ-309 were very similar, whereas the EJ-339 appeared to have a higher detection efficiency at higher neutron energies due to its high H:C ratio.

Thirdly, the fourth prototype neutron detector was constructed based on EJ-331 and a 9305KB PMT. The liquid container was cylindrical, measuring 10cm x 10cm in diameter and length, and the inside walls were painted with an adhesive light reflector (EJ-520). The detector was tested and calibrated. In order to increase the scintillation efficiency, inert gas (nitrogen) was used to eliminate dissolved oxygen in the EJ-331. A good agreement was found between the measured and the simulated Cs^{137} spectrum.

The energy calibration of the fourth prototype neutron detector was done by comparing the MC simulation of the DE spectrum to the measured scintillation energy spectrum to recognise the Compton edges of the gamma-ray sources that were used. In addition, the measured detector energy resolution was the same as the simulated energy resolution, which was 17% at the Cs^{137} Compton edge position (477keV), which is considered to be an optimum energy resolution for OLS detectors.

Fourthly, the detector was exposed to an Am–Be neutron–gamma source of 2.04×10^7 neutron/second emission rate at the NPL. Four PSD methods were obtained.

The charges ratio PSD method was obtained in a similar way to the common charge comparison PSD methods. The difference was in the optimisation of the charges ratio (tail charge/total charge). It was found that the optimisation of the charges ratio has a significant effect on the PSD performance. The optimum charge comparison was found between the integration of the total pulse charge and the integration of the pulse tail charge over the time period of pulse amplitude to fall from 60% to 5% [60 5].

Few researchers have reported a charge to amplitude comparison PSD—for example, the charge-to-current ratio PSD method. Usually, the charge to amplitude PSD

methods are obtained using the same technique, which is comparing the pulse charge integration over a specific time period during the pulse lifetime to the pulse amplitude. The charge to amplitude ratio PSD method was similarly obtained. The difference was the optimum charge to amplitude comparison. The optimum comparison was between the pulse tail charge [60 5] and the pulse amplitude. The charge-to-current ratio PSD method was obtained by comparing the total pulse charge to the pulse amplitude.

The amplitude-fall time PSD method was obtained in a similar way to the zero crossing, the time over threshold and the trailing edge pulse timing PSD methods. Its difference from the zero crossing PSD method was that the output of the PMT was not modified. In addition, its difference from the time over threshold and trailing edge pulse timing PSD methods was that the pulse fall time at a certain amplitude was considered to be the PSD method, instead of the pulse lifetime over a certain amplitude.

The fall time-amplitude PSD method was novel in utilising the relation between the pulse fall time and its relevant amplitude. The pulses' amplitudes at 30ns were considered to be the PSD method.

The PSD methods were evaluated using the FoM and are shown in Table 25.

Table 25: Evaluation of the four obtained PSD methods (FoM and threshold).

PSD method	FoM	Threshold (MeVee)
Charges ratio	1.05	0.45
Charge to amplitude ratio	0.86	0.45
Fall time-amplitude	0.6	0.75
Amplitude-fall time	0.6	0.8

The best PSD method performance was found in the charges ratio PSD method. However, a PSD method's performance is significantly affected by the oscilloscope used and its properties (resolution and sampling rate). Amplitude-fall time PSD and fall time-amplitude PSD methods need precise pulse details to be identified, such as a certain fall time and amplitude during the pulse lifetime. The precise pulse details were affected strongly by the low resolution of the oscilloscope used.

Thus, the designed fourth prototype neutron detector was judged to have met the physical and clinical criteria, and was considered to be efficient in detecting neutrons and gamma rays in the proton therapy room. In addition, it can be used in other mixed neutron and gamma radiation fields.

Fifthly, the measurement was taken during the proton irradiation at Clatterbridge Hospital in order to validate the MC simulation results. In particular, it was taken in order to validate the MC simulation of the neutron scintillation spectrum and its relative DE (or its absorbed dose). Hence, the MC simulation of the relative DE distributions from the neutrons and gamma rays in the voxelised water phantom were validated.

The measurement geometry was adjusted to be similar to that of the MC simulation geometry. Neutron and gamma-ray events were separated by applying the charges ratio PSD method. Neutron and gamma-ray spectra were obtained and the relative absorbed doses were calculated. A good agreement was found between the measured and simulated scintillation neutron energy spectrum and its relative absorbed dose, which were 2.08±0.42μGy/Gy and 2.63μGy/Gy respectively.

Therefore, the MC simulation of the relative DE distributions from the neutrons and gamma rays in the voxelised water phantom were validated. The integral relative DEs from the neutrons and gamma rays in the voxelised water phantom were (14.8±0.135) x 10^{-3}% and 8 x 10^{-3}% respectively. These results can be generalised for any proton therapy prescribed dose during the proton therapy at Clatterbridge Hospital.

To conclude, fast external neutrons are the main concern in terms of the additional unwanted secondary radiation dose during proton therapy at Clatterbridge Hospital. Although the relative neutron dose was small (i.e. 1.48±0.0135mSv/Gy) compared to the prescribed proton therapy dose, it is not negligible and the dose distribution can be used as the basis of the risk estimation from radiation induced secondary cancers.

Bibliography

[1] R. A. Hälg, J. Besserer, M. Boschung, S. Mayer, A. J. Lomax, and U. Schneider, "Measurements of the neutron dose equivalent for various radiation qualities, treatment machines and delivery techniques in radiation therapy.," *Phys. Med. Biol.*, vol. 59, no. 10, pp. 2457–68, May 2014.

[2] E. J. Hall, "Intensity-modulated radiation therapy, protons, and the risk of second cancers.," *Int. J. Radiat. Oncol. Biol. Phys.*, vol. 65, no. 1, pp. 1–7, May 2006.

[3] U. Schneider and R. Hälg, "The Impact of Neutrons in Clinical Proton Therapy," *Front. Oncol.*, vol. 5, no. October, pp. 1–5, Oct. 2015.

[4] B. S. Athar and H. Paganetti, "Comparison of second cancer risk due to out-of-field doses from 6-MV IMRT and proton therapy based on 6 pediatric patient treatment plans.," *Radiother. Oncol.*, vol. 98, no. 1, pp. 87–92, Jan. 2011.

[5] W. D. Newhauser, J. D. Fontenot, A. Mahajan, D. Kornguth, M. Stovall, Y. Zheng, P. J. Taddei, D. Mirkovic, R. Mohan, J. D. Cox, and S. Woo, "The risk of developing a second cancer after receiving craniospinal proton irradiation.," *Phys. Med. Biol.*, vol. 54, no. 8, pp. 2277–91, Apr. 2009.

[6] B. S. Athar and H. Paganetti, "Neutron equivalent doses and associated lifetime cancer incidence risks for head & neck and spinal proton therapy.," *Phys. Med. Biol.*, vol. 54, no. 16, pp. 4907–26, Aug. 2009.

[7] C. Zacharatou Jarlskog and H. Paganetti, "Risk of developing second cancer from neutron dose in proton therapy as function of field characteristics, organ, and patient age.," *Int. J. Radiat. Oncol. Biol. Phys.*, vol. 72, no. 1, pp. 228–35, Sep. 2008.

[8] Herman Cember and Thomas E.Johnson, "Introduction to Health Physics," 4th ed., The McGraw-Hill Companies, Inc., 2009, pp. 13, 52, 164, 186–205, 263–269, 301–332, 348, 373.

[9] J. Fontenot, P. Taddei, Y. Zheng, and D. Mirkovic, "Equivalent dose and effective dose from stray radiation during passively scattered proton," *Energy*, vol. 1677, 2008.

[10] P. J. Taddei, D. Mirkovic, J. D. Fontenot, A. Giebeler, Y. Zheng, D. Kornguth, R. Mohan, and W. D. Newhauser, "Stray radiation dose and second cancer risk for a pediatric patient receiving craniospinal irradiation with proton beams.," *Phys. Med. Biol.*, vol. 54, no. 8, pp. 2259–75, Apr. 2009.

[11] D. J. Brenner and E. J. Hall, "Secondary neutrons in clinical proton radiotherapy: a charged issue.," *Radiother. Oncol.*, vol. 86, no. 2, pp. 165–70, Feb. 2008.

[12] G. F. Knoll, "Radiation Detection and Measuremen," 4th ed., John Wile & Sons, Inc., 2010, pp. 30–62,115–119, 223–278, 352, 519–523 and 562–582.

[13] R. R. Wilson, "Radiological use of fast protons.," *Radiology*, vol. 47, no. 5, pp. 487–91, Nov. 1946.

[14] W. D. Newhauser and R. Zhang, "The physics of proton therapy.," *Phys. Med.*

Biol., vol. 60, no. 8, pp. R155–209, Apr. 2015.

[15] A. M. Koehler, "Flattening of proton dose distributions for large-field radiotherapy," *Med. Phys.*, vol. 4, no. 4, p. 297, 1977.

[16] H. Paganetti, *Proton Therapy Physics*, 1st ed. Taylor & francis Group, LLC, 2012.

[17] C. S. Vargas, O. Van Hoey, G. Mathot, F. Stichelbaut, G. Manessi, N. Dinar, E. Aza, C. Cassell, M. Silari, F. Vanhavere, B. Triomphe, and I. B. A. S. A, "Secondary neutron doses in a proton therapy centre," pp. 1–6, 2015.

[18] M. Mizumoto, Y. Oshiro, D. Takizawa, T. Fukushima, H. Fukushima, T. Yamamoto, A. Muroi, T. Okumura, K. Tsuboi, and H. Sakurai, "Proton beam therapy for pediatric ependymoma.," *Pediatr. Int.*, vol. 57, no. 4, pp. 567–71, Aug. 2015.

[19] "Neutron scattering lengths and cross sections," *Xcom*, 2013. [Online]. Available: https://www.ncnr.nist.gov/resources/n-lengths/.

[20] A. G. Çelik, "Investigation on characteristic properties of potassium borate and sodium borate blended perlite bricks," *J. Clean. Prod.*, vol. 102, pp. 88–95, Sep. 2015.

[21] J. Byrne, "A review of "Neutrons, nuclei, and matter: An exploration of the physics of slow neutrons.," *Neutron News*, vol. 6, no. 3, pp. 23–23, Jan. 1995.

[22] V. B. Brudanin, V. I. Bregadze, N. A. Gundorin, D. V Filossofov, O. I. Kochetov, I. B. Nemtchenok, A. A. Smolnikov, and S. I. Vasiliev, "ELEMENT-LOADED ORGANIC SCINTILLATORS FOR NEUTRON AND NEUTRINO PHYSICS," no. 6, 2001.

[23] C. H. Johnson, "Proton-Recoil Neutron Spectrometer," *Rev. Sci. Instrum.*, vol. 27, no. 7, p. 468, 1956.

[24] P. Kandlakunta, L. R. Cao, and P. Mulligan, "Measurement of internal conversion electrons from Gd neutron capture," *Nucl. Instruments Methods Phys. Res. Sect. A Accel. Spectrometers, Detect. Assoc. Equip.*, vol. 705, pp. 36–41, Mar. 2013.

[25] F. . Brooks and H. Klein, "Neutron spectrometry—historical review and present status," *Nucl. Instruments Methods Phys. Res. Sect. A Accel. Spectrometers, Detect. Assoc. Equip.*, vol. 476, no. 1–2, pp. 1–11, Jan. 2002.

[26] R. Batchelor, W. B. Gilboy, J. B. Parker, and J. H. Towle, "The response of organic scintillators to fast neutrons," *Nucl. Instruments Methods*, vol. 13, no. 3, pp. 70–82, Aug. 1961.

[27] T. B. Ryves, "A proton recoil telescope for 12–20 MeV neutrons," *Nucl. Instruments Methods*, vol. 135, no. 3, pp. 455–458, Jun. 1976.

[28] D. J. Thomas and a. V. Alevra, "Bonner sphere spectrometers - A critical review," *Nucl. Instruments Methods Phys. Res. Sect. A Accel. Spectrometers, Detect. Assoc. Equip.*, vol. 476, no. 1–2, pp. 12–20, 2002.

[29] F. Foulon, P. Bergonzo, V. N. Amosov, Y. Kaschuck, V. Frunze, D. Tromson, and a. Brambilla, "Characterisation of CVD diamond detectors used for fast neutron flux monitoring," *Nucl. Instruments Methods Phys. Res. Sect. A Accel. Spectrometers, Detect. Assoc. Equip.*, vol. 476, no. 1–2, pp. 495–499, 2002.

[30] L. Kuijpers, R. Herzing, P. Cloth, and K. Jiilich, “On The Determination Of Fast Neutron Spectra With Activation Techniques ; Its Application In A Fusion Reactor Blanket Model,” *Nucl. Instruments Methods*, vol. 144, pp. 215–224, 1977.

[31] E. Dietz, M. Matzke, W. Sosaat, G. Urbach, and M. Weyrauch, “Neutron response of an 3He proportional counter,” *Nucl. Instruments Methods Phys. Res. Sect. A Accel. Spectrometers, Detect. Assoc. Equip.*, vol. 332, no. 3, pp. 521–528, 1993.

[32] K. Banerjee, T. K. Ghosh, S. Kundu, T. K. Rana, C. Bhattacharya, J. K. Meena, G. Mukherjee, P. Mali, D. Gupta, S. Mukhopadhyay, D. Pandit, S. R. Banerjee, S. Bhattacharya, T. Bandyopadhyay, and S. Chatterjee, “Variation of neutron detection characteristics with dimension of BC501A neutron detector,” *Nucl. Instruments Methods Phys. Res. Sect. A Accel. Spectrometers, Detect. Assoc. Equip.*, vol. 608, no. 3, pp. 440–446, 2009.

[33] Y. Jie, L. Rong, L. Cheng, J. Li, L. Xin-Xin, and Z. Tong-Hua, “Energy calibration of a BC501A liquid scintillator using a γ-γ coincidence technique,” *Chinese Phys. C*, vol. 34, no. 7, pp. 993–997, 2010.

[34] N. Nakao, T. Nakamura, M. Baba, Y. Uwamino, N. Nakanishi, H. Nakashima, and S. Tanaka, “Measurements of response function of organic liquid scintillator for neutron energy range up to 135 MeV,” *Nucl. Instruments Methods Phys. Res. Sect. A Accel. Spectrometers, Detect. Assoc. Equip.*, vol. 362, no. 2–3, pp. 454–465, Aug. 1995.

[35] R. Batchelor, R. Aves, and T. H. R. Skyrme, “Helium-3 filled proportional counter for neutron spectroscopy,” *Rev. Sci. Instrum.*, vol. 26, no. 11, pp. 1037–1047, 1955.

[36] ICRP, “ICRP publication 103,” *Ann. ICRP*, vol. 37, Apr. 2007.

[37] J. Valentin, R. Cox, and A. M. Kellerer, “Relative biological effectiveness (RBE), quality factor (Q), and radiation weighting factor (wR),” *Annals of the ICRP*, vol. 33, no. 4. pp. 1–117, 2003.

[38] G. KRAFT, “Tumor therapy with heavy charged particles,” *Prog. Part. Nucl. Phys.*, vol. 45, pp. S473–S544, 2000.

[39] H. M. K. Thomas F. De Laney, *Proton and Charged Particle Radiotherapy*. Wolters Kluwer Lippincott Williams and Wilkins, 2008.

[40] E. Grusellt, A. Monteliust, A. Brahmeg, G. Riknerl, and K. Russell, “A general solution to charged particle beam flattening using an optimized dual-scattering-foil technique , with application to proton therapy beams,” vol. 2201.

[41] C. Baker, D. Shipley, H. Palmans, and A. Kacperek, “Monte carlo modelling of a clinical proton beam-line for the treatment of ocular tumours,” *Nucl. Instruments Methods Phys. Res. Sect. A Accel. Spectrometers, Detect. Assoc. Equip.*, vol. 562, no. 2, pp. 1005–1008, 2006.

[42] J. D. Fontenot, “Design tools for proton therapy nozzles based on the double-scattering foil technique,” *Radiat. Prot. Dosimetry*, vol. 116, no. 1–4, pp. 211–215, Dec. 2005.

[43] S. B. Jia, F. Romano, G. A. P. Cirrone, G. Cuttone, M. H. Hadizadeh, A. A. Mowlavi, and L. Raffaele, “Designing a range modulator wheel to spread-out

the Bragg peak for a passive proton therapy facility," *Nucl. Instruments Methods Phys. Res. Sect. A Accel. Spectrometers, Detect. Assoc. Equip.*, vol. 806, pp. 101–108, Jan. 2016.

[44] H. Paganetti and T. Bortfeld, *Proton Beam Radiotherapy - The State of the Art 1*, no. October. 2005.

[45] A. R. Smith, "Proton therapy.," *Phys. Med. Biol.*, vol. 51, no. 13, pp. R491–504, Jul. 2006.

[46] W. T. Chu, B. A. Ludewigt, and T. R. Renner, "Instrumentation for treatment of cancer using proton and light-ion beams," *Rev. Sci. Instrum.*, vol. 64, no. 8, p. 2055, 1993.

[47] H. Liu and J. Y. Chang, "Proton therapy in clinical practice," *Chin. J. Cancer*, vol. 30, no. 5, pp. 315–326, 2011.

[48] M. S. Wagner, "Automated range compensation for proton therapy," *Med. Phys.*, vol. 9, no. 5, p. 749, 1982.

[49] D. Lesyna, "Facility Overview for a Proton Beam Treatment Center," vol. 6, no. 4, 2015.

[50] A. Pérez-Andújar, W. D. Newhauser, and P. M. Deluca, "Neutron production from beam-modifying devices in a modern double scattering proton therapy beam delivery system.," *Phys. Med. Biol.*, vol. 54, no. 4, pp. 993–1008, Feb. 2009.

[51] ".decimal® Products - Protons," 2012. [Online]. Available: http://www.dotdecimal.com/resources/products/protons.

[52] U. Schneider, S. Agosteo, E. Pedroni, and J. Besserer, "Secondary neutron dose during proton therapy using spot scanning.," *Int. J. Radiat. Oncol. Biol. Phys.*, vol. 53, no. 1, pp. 244–51, May 2002.

[53] X. R. Zhu, Y. Li, D. Mackin, H. Li, F. Poenisch, A. K. Lee, A. Mahajan, S. J. Frank, M. T. Gillin, N. Sahoo, and X. Zhang, "Towards effective and efficient patient-specific quality assurance for spot scanning proton therapy.," *Cancers (Basel).*, vol. 7, no. 2, pp. 631–47, Jan. 2015.

[54] T. R. Renner, "Wobbler facility for biomedical experiments," *Med. Phys.*, vol. 14, no. 5, p. 825, 1987.

[55] Y. Kase, H. Yamashita, M. Sakama, M. Mizota, Y. Maeda, Y. Tameshige, and S. Murayama, "Semi-analytical model for output factor calculations in proton beam therapy with consideration for the collimator aperture edge.," *Phys. Med. Biol.*, vol. 60, no. 15, pp. 5833–52, Aug. 2015.

[56] J. B. Farr, A. E. Mascia, W.-C. Hsi, C. E. Allgower, F. Jesseph, A. N. Schreuder, M. Wolanski, D. F. Nichiporov, and V. Anferov, "Clinical characterization of a proton beam continuous uniform scanning system with dose layer stacking," *Med. Phys.*, vol. 35, no. 11, p. 4945, 2008.

[57] P. J. Taddei, J. D. Fontenot, Y. Zheng, D. Mirkovic, A. K. Lee, U. Titt, and W. D. Newhauser, "Reducing stray radiation dose to patients receiving passively scattered proton radiotherapy for prostate cancer.," *Phys. Med. Biol.*, vol. 53, no. 8, pp. 2131–47, Apr. 2008.

[58] J. C. Polf and W. D. Newhauser, "Calculations of neutron dose equivalent exposures from range-modulated proton therapy beams.," *Phys. Med. Biol.*, vol.

50, no. 16, pp. 3859–73, Aug. 2005.

[59] B. S. Athar, B. Bednarz, J. Seco, C. Hancox, and H. Paganetti, "Comparison of out-of-field photon doses in 6 MV IMRT and neutron doses in proton therapy for adult and pediatric patients.," *Phys. Med. Biol.*, vol. 55, no. 10, pp. 2879–91, May 2010.

[60] G. Mesoloras, G. A. Sandison, R. D. Stewart, J. B. Farr, and W. C. Hsi, "Neutron scattered dose equivalent to a fetus from proton radiotherapy of the mother," *Methods*, pp. 2479–2490, 2006.

[61] D. J. Brenner, C. D. Elliston, E. J. Hall, and H. Paganetti, "Reduction of the secondary neutron dose in passively scattered proton radiotherapy, using an optimized pre-collimator/collimator.," *Phys. Med. Biol.*, vol. 54, no. 20, pp. 6065–78, Oct. 2009.

[62] X. Wang, N. Sahoo, R. X. Zhu, J. R. Zullo, and M. T. Gillin, "Measurement of neutron dose equivalent and its dependence on beam configuration for a passive scattering proton delivery system.," *Int. J. Radiat. Oncol. Biol. Phys.*, vol. 76, no. 5, pp. 1563–70, Apr. 2010.

[63] H. Paganetti, H. Jiang, S. Lee, and H. M. Kooy, "Accurate Monte Carlo simulations for nozzle design , commissioning and quality assurance for a proton radiation therapy facility," *Therapy*, pp. 2107–2118, 2004.

[64] A. Wroe, A. Rosenfeld, and R. Schulte, "Out-of-field dose equivalents delivered by proton therapy of prostate cancer," *Med. Phys.*, vol. 34, no. 9, p. 3449, 2007.

[65] J. Farah, V. Mares, M. Romero-Expósito, S. Trinkl, C. Domingo, V. Dufek, M. Klodowska, J. Kubancak, Ž. Knežević, M. Liszka, M. Majer, S. Miljanić, O. Ploc, K. Schinner, L. Stolarczyk, F. Trompier, M. Wielunski, P. Olko, and R. M. Harrison, "Measurement of stray radiation within a scanning proton therapy facility: EURADOS WG9 intercomparison exercise of active dosimetry systems.," *Med. Phys.*, vol. 42, no. 5, pp. 2572–84, May 2015.

[66] J. S. Kim, J. S. Shin, D. Kim, E. Shin, K. Chung, and S. Cho, "Feasibility Study of Neutron Dose for Real Time Image Guided Proton Therapy : A Monte Carlo Study."

[67] X. Yan, U. Titt, A. . Koehler, and W. . Newhauser, "Measurement of neutron dose equivalent to proton therapy patients outside of the proton radiation field," *Nucl. Instruments Methods Phys. Res. Sect. A Accel. Spectrometers, Detect. Assoc. Equip.*, vol. 476, no. 1–2, pp. 429–434, Jan. 2002.

[68] J. H. N. A. Centre and F. S. Africa, "Secondary dose exposures during 200 MeV proton therapy," p. 28059023, 1997.

[69] R. Tayama, Y. Fujita, M. Tadokoro, H. Fujimaki, T. Sakae, and T. Terunuma, "Measurement of neutron dose distribution for a passive scattering nozzle at the Proton Medical Research Center (PMRC)," *Nucl. Instruments Methods Phys. Res. Sect. A Accel. Spectrometers, Detect. Assoc. Equip.*, vol. 564, no. 1, pp. 532–536, Aug. 2006.

[70] Y. Zheng, W. Newhauser, J. Fontenot, P. Taddei, and R. Mohan, "Monte Carlo study of neutron dose equivalent during passive scattering proton therapy.," *Phys. Med. Biol.*, vol. 52, no. 15, pp. 4481–4496, 2007.

[71] S. Kim, B. J. Min, M. Yoon, J. Kim, D. H. Shin, S. B. Lee, S. Y. Park, S. Cho, and D. H. Kim, "Secondary radiation doses of intensity-modulated radiotherapy and proton beam therapy in patients with lung and liver cancer.," *Radiother. Oncol.*, vol. 98, no. 3, pp. 335–9, Mar. 2011.

[72] C. Zacharatou Jarlskog, C. Lee, W. E. Bolch, X. G. Xu, and H. Paganetti, "Assessment of organ-specific neutron equivalent doses in proton therapy using computational whole-body age-dependent voxel phantoms.," *Phys. Med. Biol.*, vol. 53, no. 3, pp. 693–717, Feb. 2008.

[73] M. Yoon, S. H. Ahn, J. Kim, D. H. Shin, S. Y. Park, S. B. Lee, K. H. Shin, and K. H. Cho, "Radiation-induced cancers from modern radiotherapy techniques: intensity-modulated radiotherapy versus proton therapy.," *Int. J. Radiat. Oncol. Biol. Phys.*, vol. 77, no. 5, pp. 1477–85, Aug. 2010.

[74] B. Clasie, A. Wroe, H. Kooy, N. Depauw, J. Flanz, and H. Paganetti, "Assessment of out-of-field absorbed dose and equivalent dose in proton fields," *Methods*, no. January, pp. 311–321, 2010.

[75] U. Schneider, A. Lomax, P. Pemler, J. Besserer, D. Ross, N. Lombriser, and B. Kaser-hotz, "The Impact of IMRT and Proton Radiotherapy on Secondary Cancer Incidence," *Cancer*, no. 11, pp. 647–652, 2006.

[76] B. Mukherjee, J. Lambert, R. Hentschel, and J. Farr, "Explicit estimation of out-of-field neutron and gamma dose equivalents during proton therapy using thermoluminescence-dosimeters," *Radiat. Meas.*, vol. 46, no. 12, pp. 1952–1955, Dec. 2011.

[77] J. D. Fontenot, A. K. Lee, and W. D. Newhauser, "Risk of secondary malignant neoplasms from proton therapy and intensity-modulated x-ray therapy for early-stage prostate cancer.," *Int. J. Radiat. Oncol. Biol. Phys.*, vol. 74, no. 2, pp. 616–22, Jun. 2009.

[78] I. Kristensen, K. Nilsson, and P. Nilsson, "Comparative Proton and Photon Treatment Planning in Pediatric Patients with Various Diagnoses," *Int. J. Part. Ther.*, vol. 2, no. 2, pp. 367–375, Sep. 2015.

[79] S. J. Dowdell, B. Clasie, N. Depauw, P. Metcalfe, A. B. Rosenfeld, H. M. Kooy, J. B. Flanz, and H. Paganetti, "Monte Carlo study of the potential reduction in out-of-field dose using a patient-specific aperture in pencil beam scanning proton therapy.," *Phys. Med. Biol.*, vol. 57, no. 10, pp. 2829–42, May 2012.

[80] D. Azimi-Garakani and C. Wernli, "Response and background study of various PADC materials," *Int. J. Radiat. Appl. Instrumentation. Part D. Nucl. Tracks Radiat. Meas.*, vol. 19, no. 1–4, pp. 445–448, Jan. 1991.

[81] R. L. Slopsema, M. Mamalui, T. Zhao, D. Yeung, R. Malyapa, and Z. Li, "Dosimetric properties of a proton beamline dedicated to the treatment of ocular disease Dosimetric properties of a proton beamline dedicated to the treatment," *Med. Phys.*, vol. 41, no. 1, p. 011707, 2014.

[82] J. B. Czirr, D. B. Merrill, D. Buehler, T. K. McKnight, J. L. Carroll, T. Abbott, and E. Wilcox, "Capture-gated neutron spectrometry," *Nucl. Instruments Methods Phys. Res. Sect. A Accel. Spectrometers, Detect. Assoc. Equip.*, vol. 476, no. 1–2, pp. 309–312, 2002.

[83] V. V. Verbinski, W. R. Burrus, T. A. Love, W. Zobel, N. W. Hill, and R. Textor, "Calibration of an organic scintillator for neutron spectrometry," *Nucl.*

Instruments Methods, vol. 65, no. 1, pp. 8–25, 1968.

[84] R. M. Howell and E. A. Burgett, "Secondary neutron spectrum from 250-MeV passively scattered proton therapy: Measurement with an extended-range Bonner sphere system," *Med. Phys.*, vol. 41, no. 9, p. 092104, 2014.

[85] C.-H. Min, C. H. Kim, M.-Y. Youn, and J.-W. Kim, "Prompt gamma measurements for locating the dose falloff region in the proton therapy," *Appl. Phys. Lett.*, vol. 89, no. 18, p. 183517, 2006.

[86] D. Cester, G. Nebbia, L. Stevanato, F. Pino, and G. Viesti, "Experimental tests of the new plastic scintillator with pulse shape discrimination capabilities EJ-299-33," *Nucl. Instruments Methods Phys. Res. Sect. A Accel. Spectrometers, Detect. Assoc. Equip.*, vol. 735, pp. 202–206, Jan. 2014.

[87] C. D. Bass, E. J. Beise, H. Breuer, C. R. Heimbach, T. J. Langford, and J. S. Nico, "Characterization of a 6Li-loaded liquid organic scintillator for fast neutron spectrometry and thermal neutron detection," *Appl. Radiat. Isot.*, vol. 77, pp. 130–138, 2013.

[88] J. Poitou and C. Signarbieux, "A Monte-Carlo simulation of the capture and detection of neutrons with large liquid scintillators," *Nucl. Instruments Methods*, vol. 114, no. 1, pp. 113–119, Jan. 1974.

[89] Z. S. Hartwig and P. Gumplinger, "Simulating response functions and pulse shape discrimination for organic scintillation detectors with Geant4," *Nucl. Instruments Methods Phys. Res. Sect. A Accel. Spectrometers, Detect. Assoc. Equip.*, vol. 737, pp. 155–162, Feb. 2014.

[90] G. E. Granroth and S. E. Hahn, "Monte Carlo simulation of the resolution volume for the SEQUOIA spectrometer," *EPJ Web Conf.*, vol. 83, p. 03006, 2015.

[91] Y. Wang, Y. Zhang, N. Wu, B. Wu, Y. Liu, X. Cao, and Q. Wang, "Monte carlo simulation of in situ gamma-spectra recorded by NaI (Tl) detector in the marine environment," *J. Ocean Univ. China*, vol. 14, no. 3, pp. 471–474, 2015.

[92] A. B. Rosenfeld and P. D. Bradley, "Semiconductor Microdosimetry in Mixed Radiation and Photon Fields: Present and Future," *Radiat. Prot. Dosim.* , vol. 85 , no. 1–4 , pp. 385–388, Sep. 1999.

[93] J. Birks, "Scintillation efficiency of anthracene crystals," *Proc. Phys. Soc. Sect. A*, vol. 63, no. 11, pp. 1294–1295, Nov. 1950.

[94] Y. Chen, Y. Lin, H. Chen, and H. Tsai, "SU-E-T-594: Out-Of-Field Neutron and Gamma Dose Estimated Using TLD-600/700 Pairs in the Wobbling Proton Therapy System.," *Med. Phys.*, vol. 42, no. 6, p. 3472, Jun. 2015.

[95] A. J. Wroe, "Evaluation and Mitigation of Secondary Dose Delivered to Electronic Systems in Proton Therapy," *Technol. Cancer Res. Treat.*, pp. 1–9, Jan. 2015.

[96] H. Search, C. Journals, A. Contact, M. Iopscience, and I. P. Address, "Nuclear interactions in proton therapy : dose and relative biological effect distributions originating," *Online*, vol. 747, 2002.

[97] N. N. D. Center, "Evaluated Nuclear Data File (ENDF)," 2011. [Online]. Available: http://www.nndc.bnl.gov/exfor/endf00.jsp.

[98] H. Scholermann and H. Klein, "OPTIMIZING THE ENERGY RESOLUTION

OF SCINTILLATION COUNTERS," vol. 169, pp. 0–6, 1979.

[99] M. Moszyński, "Inorganic scintillation detectors in γ-ray spectrometry," *Nucl. Instruments Methods Phys. Res. Sect. A Accel. Spectrometers, Detect. Assoc. Equip.*, vol. 505, no. 1–2, pp. 101–110, 2003.

[100] H. Klein and S. Neumann, "Neutron and photon spectrometry with liquid scintillation detectors in mixed fields," *Nucl. Instruments Methods Phys. Res. Sect. A Accel. Spectrometers, Detect. Assoc. Equip.*, vol. 476, no. 1–2, pp. 132–142, Jan. 2002.

[101] J. Qin, C. Lai, B. Ye, R. Liu, X. Zhang, and L. Jiang, "Characterizations of BC501A and BC537 liquid scintillator detectors," *Appl. Radiat. Isot.*, vol. 104, pp. 15–24, 2015.

[102] F. Masetti, "Optical study of a large-scale liquid-scintillator," vol. 68, no. 1996, 2000.

[103] G. Ranucci, A. Goretti, and P. Lombardi, "Pulse-shape discrimination of liquid scintillators," vol. 412, no. February, pp. 374–386, 1998.

[104] "SAINT-GOBAIN," *Scintilltion Products*, 2001. [Online]. Available: http://www.crystals.saint-gobain.com/uploadedFiles/SG-Crystals/Documents/Operation_Handling/Safety and Handling Liquid Scintillators.pdf.

[105] J. M. Pates, G. T. Cook, A. B. MacKenzie, and C. J. Passo, "The implications of beta energy and quenching for alpha/beta liquid scintillation spectrometry calibration.," *Analyst*, vol. 123, pp. 2201–2207, 1998.

[106] H. Klein and F. D. Brooks, "Scintillation detectors for fast neutrons," *FNDA2006 - Int. Work. Fast Neutron Detect. Appl. Univ. Cape Town, Cape Town, South Africa, April 3-6, 2006*, 2006.

[107] X. Hua-Lin, "Oxygen quenching in LAB based liquid scintillator and nitrogen bubbling model," vol. 571, 2009.

[108] L. Stolarczyk, P. Olko, T. Cywicka-Jakiel, M. Ptaszkiewicz, J. Swakoń, B. Dulny, T. Horwacik, B. Obryk, and M. P. R. Waligórski, "Assessment of undesirable dose to eye-melanoma patients after proton radiotherapy," *Radiat. Meas.*, vol. 45, no. 10, pp. 1441–1444, Dec. 2010.

[109] J. Pietras and S. Smith, "Photomultiplier tubes and detector packaging for hostile environments," *Nucl. Sci. IEEE Trans.*, vol. 35, no. 1, pp. 863–866, 1988.

[110] J. T. M. de Haas and P. Dorenbos, "Methods for Accurate Measurement of the Response of Photomultiplier Tubes and Intensity of Light Pulses," *IEEE Trans. Nucl. Sci.*, vol. 58, no. 3, pp. 1290–1296, Jun. 2011.

[111] C. Z. Jarlskog, C. Lee, and W. E. Bolch, "Assessment of organ-specific neutron equivalent doses in proton therapy using computational whole-body age-dependent voxel phantoms," vol. 693, 2008.

[112] Y. Zheng, W. Newhauser, J. Fontenot, P. Taddei, and R. Mohan, "Monte Carlo study of neutron dose equivalent during passive scattering proton therapy.," *Phys. Med. Biol.*, vol. 52, no. 15, pp. 4481–96, Aug. 2007.

[113] D. Shin, M. Yoon, J. Kwak, J. Shin, S. B. Lee, S. Y. Park, S. Park, D. Y. Kim, and K. H. Cho, "Secondary neutron doses for several beam configurations for

proton therapy.," *Int. J. Radiat. Oncol. Biol. Phys.*, vol. 74, no. 1, pp. 260–5, May 2009.

[114] R. C. Sangster and J. W. Irvine, "Study of Organic Scintillators," *J. Chem. Phys.*, vol. 24, no. 4, p. 670, 1956.

[115] J. A. Lockwood, C. Chen, L. A. Friling, D. Swartz, R. N. St. Onge, A. Galonsky, and R. R. Doering, "Response functions of organic scintillators to high energy neutrons," *Nucl. Instruments Methods*, vol. 138, no. 2, pp. 353–362, 1976.

[116] G. Dietze, "Energy calibration of NE-213 scintillation counters by γ-rays," *IEEE Trans. Nucl. Sci.*, vol. 26, no. 1, pp. 398–402, Feb. 1979.

[117] N. A. Lurie, L. Harris, and J. C. Young, "Calculation of gamma-ray response matrix for 5 cm NE-213 organic liquid scintillation detector," *Nucl. Instruments Methods*, Nov. 1975.

[118] F. D. Brooks, "A scintillation counter with neutron and gamma-ray discriminators," *Nucl. Instruments Methods*, vol. 4, no. 3, pp. 151–163, 1959.

[119] M. Anghinolfi, G. Ricco, P. Corvisiero, and F. Masulli, "The response function of organic scintillators to fast neutrons," *Nucl. Instruments Methods*, vol. 165, no. 2, pp. 217–224, 1979.

[120] B. Hamermesh, G. R. Ringo, and S. Wexler, "The Thermal Neutron Capture Cross Section of Hydrogen," *Phys. Rev.*, vol. 90, no. 4, pp. 603–606, May 1953.

[121] M. Drosg, D. M. Drake, and P. Lisowski, "The contribution of carbon interactions to the neutron counting efficiency of organic scintillators," *Nucl. Instruments Methods*, vol. 176, no. 3, pp. 477–480, Oct. 1980.

[122] J. E. Al Smeets, "Prompt Gamma Imaging with a slit camera for real-time range control in proton therapy," *Phys. Med. Biol.*, vol. 57, pp. 3371–3405, 2012.

[123] B. R. Kim, S. C. Kim, K. K. Joo, C. D. Shin, S. H. So, and I. S. Yeo, "Development of (Gd, 6Li)-loaded organic liquid scintillators for reactor neutrino detection," *J. Korean Phys. Soc.*, vol. 66, no. 5, pp. 768–773, 2015.

[124] B. R. Kim, B. Y. Han, E. J. Jeon, K. K. Joo, J. Kang, N. Khan, H. J. Kim, H. Kim, J. Y. Kim, K. Siyeon, S. C. Kim, Y. Kim, Y. J. Ko, J. Lee, J. Lee, J. Y. Lee, K. J. Ma, H. Park, H. K. Park, K. S. Park, and K. M. Seo, "Pulse shape discrimination capability of metal-loaded organic liquid scintillators for a short-baseline reactor neutrino experiment," vol. 055302.

[125] D. L. Smith, R. G. Polk, and T. G. Miller, "Measurement of the response of several organic scintillators to electrons, protons and deuterons," *Nucl. Instruments Methods*, vol. 64, no. 2, pp. 157–166, 1968.

[126] L. R. Greenwood, N. R. Chellew, and G. a Zarwell, "6Li-loaded liquid scintillators with pulse shape discrimination," *Rev. Sci. Instrum.*, vol. 50, no. 4, p. 472, 1979.

[127] A. Foglio-Para, N. A. Gottardi, and M. M. Bettoni, "Thermal neutrons Gd-detector," *Nucl. Instruments Methods*, vol. 65, no. 1, pp. 110–112, Oct. 1968.

[128] G. Abdullaeva, G. Djuraeva, A. Kim, Y. Koblik, G. Kulabdullaev, T. Rakhmonov, and S. Saytjanov, "Evaluation of absorbed dose in Gadolinium neutron capture therapy," *Open Phys.*, vol. 13, no. 1, pp. 183–187, 2015.

[129] P. . Lightfoot, V. . Kudryavtsev, N. J. . Spooner, I. Liubarsky, R. Luscher, and

N. J. . Smith, “Development of a gadolinium-loaded liquid scintillator for solar neutrino detection and neutron measurements,” *Nucl. Instruments Methods Phys. Res. Sect. A Accel. Spectrometers, Detect. Assoc. Equip.*, vol. 522, no. 3, pp. 439–446, Apr. 2004.

[130] E. Technology, “Gadolinium Loaded Liquid Scintillators,” *Aug, 2004*. [Online]. Available: http://www.eljentechnology.com/images/stories/Data_Sheets/Loaded_Scintillators/EJ331-335 data sheet.pdf.

[131] G. H. V. Bertrand, M. Hamel, S. Normand, and F. Sguerra, “Pulse shape discrimination between (fast or thermal) neutrons and gamma rays with plastic scintillators: State of the art,” *Nucl. Instruments Methods Phys. Res. Sect. A Accel. Spectrometers, Detect. Assoc. Equip.*, vol. 776, pp. 114–128, 2015.

[132] Z. W. Bell, G. M. Brown, C. H. Ho, and F. V Sloop, “Y-12 National Security Complex ; b Oak Ridge National Laboratory Organic scintillators for neutron detection,” *Security*, vol. 4784, pp. 150–163, 2002.

[133] Saint-gobain, “Gadolinium Loaded Liquid Scintillators,” 2005. [Online]. Available: http://www.crystals.saint-gobain.com/uploadedFiles/SG-Crystals/Documents/SGC BC521 Data Sheet.pdf.

[134] E. Technology, “EJ-301 Liquid Scintillator.” [Online]. Available: http://www.eljentechnology.com/index.php/products/liquid-scintillators/71-ej-301.

[135] P. R. J. Burch, “Gamma Ray Spectra in Large Organic Scintillators,” *Proc. Phys. Soc.*, vol. 77, no. 6, pp. 1125–1132, 2002.

[136] National Institute of Standards and Technology, “XCOM,” 2009. [Online]. Available: http://physics.nist.gov/PhysRefData/Xcom/html/xcom1.html.

[137] “X-Ray Mass Attenuation Coefficients,” *Xcom*, 2016. [Online]. Available: http://physics.nist.gov/PhysRefData/XrayMassCoef/tab3.html.

[138] N. . Hawkes, J. . Adams, D. . Bond, S. Croft, O. . Jarvis, and N. Watkins, “Measurements of the proton light output function of the organic liquid scintillator NE213 in several detectors,” *Nucl. Instruments Methods Phys. Res. Sect. A Accel. Spectrometers, Detect. Assoc. Equip.*, vol. 476, no. 1–2, pp. 190–194, Jan. 2002.

[139] V. K. Bharadwaj, M. P. Cain, D. O. Caldwell, B. H. Denby, A. M. Eisner, U. P. Joshi, A. Lu, R. J. Morrison, D. R. Pfost, D. J. Summers, S. J. Yellin, D. E. Pellett, and T. Nash, “An inexpensive large area shower detector with high spatial and energy resolution,” *Nucl. Instruments Methods*, vol. 155, no. 3, pp. 411–419, Oct. 1978.

[140] L. Lombigit, N. Yussup, M. M. Ibrahim, N. A. A. Rahman, and M. Rawi M. Z., “Characterization of liquid scintillation detector (BC-501A) and digital pulse shape discrimination (DPSD) system,” no. July 2015, p. 030007, 2015.

[141] J. Iwanowska, L. Swiderski, M. Moszynski, T. Szczesniak, P. Sibczynski, N. Z. Galunov, and N. L. Karavaeva, “Neutron/gamma discrimination properties of composite scintillation detectors,” *J. Instrum.*, vol. 6, no. 07, pp. P07007–P07007, Jul. 2011.

[142] C. L. Page, “Introduction to Amplifiers,” 2012. [Online]. Available:

www.ortec-online.com/download/amplifier-introduction.pdf.

[143] ET Enterprises Limited, “51 mm (2") photomultiplier 9939B series data sheet,” 2010. [Online]. Available: https://my.et-enterprises.com/pdf/9939B.pdf.

[144] ET Enterprises Limited, “78 mm (3") photomultiplier 9305KB series data sheet,” 2012. [Online]. Available: https://my.et-enterprises.com/pdf/9305KB.pdf.

[145] D. M. Walker and J. M. Palms, “Mone-Carlo Analysis of the Ge(Li) Detector used in the Sum-Coincidence,” no. Li, pp. 296–305.

[146] T. Nakamoto, Y. Fukazawa, T. Ohsugi, T. Kamae, and J. Kataoka, “BGO readout with photodiodes as a soft gamma-ray detector at,” *Nucl. Instruments Methods Phys. Res. Sect. A Accel. Spectrometers, Detect. Assoc. Equip.*, vol. 536, no. 1–2, pp. 136–145, Jan. 2005.

[147] C. Silva, J. Pinto Da Cunha, a. Pereira, V. Chepel, M. I. Lopes, V. Solovov, and F. Neves, “Reflectance of polytetrafluoroethylene for xenon scintillation light,” *J. Appl. Phys.*, vol. 107, no. 6, 2010.

[148] M. Dalla Palma, S. M. Carturan, M. Degerlier, T. Marchi, M. Cinausero, F. Gramegna, and a. Quaranta, “Non-toxic liquid scintillators with high light output based on phenyl-substituted siloxanes,” *Opt. Mater. (Amst).*, vol. 42, pp. 111–117, 2015.

[149] H.-L. Xiao, X.-B. Li, D. Zheng, J. Cao, L.-J. Wen, and N.-Y. Wang, “Study of absorption and re-emission processes in a ternary liquid scintillation system,” *Chinese Phys. C*, vol. 34, no. 11, pp. 1724–1728, 2010.

[150] G. Alimonti, C. Arpesella, M. Balata, G. Bellini, J. Benziger, S. Bonetti, B. Caccianiga, L. Cadonati, F. . Calaprice, G. Cecchet, M. Chen, N. Darnton, A. de Bari, M. Deutsch, F. Elisei, F. von Feilitzsch, C. Galbiati, F. Gatti, M. . Giammarchi, D. Giugni, T. Goldbrunner, A. Golubchikov, A. Goretti, T. Hagner, F. . Hartmann, R. von Hentig, G. Heusser, A. Ianni, M. Johnson, M. Laubenstein, P. Lombardi, S. Magni, S. Malvezzi, J. Maneira, I. Manno, G. Manuzio, F. Masetti, U. Mazzucato, E. Meroni, M. Neff, L. Oberauer, A. Perotti, R. . Raghavan, G. Ranucci, E. Resconi, C. Salvo, R. Scardaoni, S. Schönert, O. Smirnov, R. Tartaglia, G. Testera, R. . Vogelaar, S. Vitale, and O. Zaimidoroga, “Light propagation in a large volume liquid scintillator,” *Nucl. Instruments Methods Phys. Res. Sect. A Accel. Spectrometers, Detect. Assoc. Equip.*, vol. 440, no. 2, pp. 360–371, Feb. 2000.

[151] W. M. J., *Alpha Counting and Spectrometry Using Liquid Scintillation Methods*. Technical Information Center Office of Scientific and Technical Information United States Department of Energy, 1986.

[152] G. Santin, D. Strul, D. Lazaro, L. Simon, M. Krieguer, M. V. Martins, V. Breton, and C. Morel, “GATE: A Geant4-Based Simulation Platform for PET and SPECT Integrating Movement and Time Management,” *IEEE Trans. Nucl. Sci.*, vol. 50, no. 5 II, pp. 1516–1521, 2003.

[153] J. Perl, J. Shin, J. Schümann, B. Faddegon, and H. Paganetti, “TOPAS: An innovative proton Monte Carlo platform for research and clinical applications,” *Med. Phys.*, vol. 39, no. 11, p. 6818, 2012.

[154] P. Arce, J. I. Lagares, L. Harkness, L. Desorgher, G. de Lorenzo, Y. Abreu, and Z. Wang, “GAMOS: An easy and flexible way to use GEANT4,” *2011 IEEE*

Nucl. Sci. Symp. Conf. Rec., pp. 2230–2237, Oct. 2011.

[155] P. Arce, J. Ignacio Lagares, L. Harkness, D. Pérez-Astudillo, M. Cañadas, P. Rato, M. De Prado, Y. Abreu, G. De Lorenzo, M. Kolstein, and A. Díaz, "Gamos: A framework to do Geant4 simulations in different physics fields with an user-friendly interface," *Nucl. Instruments Methods Phys. Res. Sect. A Accel. Spectrometers, Detect. Assoc. Equip.*, vol. 735, pp. 304–313, 2014.

[156] E. Technology, "EJ-309 Liquid Scintillators," 2004. [Online]. Available: http://www.eljentechnology.com/index.php/products/liquid-scintillators/73-ej-309.

[157] E. Technology, "EJ-339 Boron Loaded Liquid Scintillators," 2004. [Online]. Available: http://www.eljentechnology.com/index.php/products/loaded-scintillators/82-ej-339a.

[158] M. J. Roo-Ons, S. V. Shynu, M. J. Ammann, S. J. McCormack, and B. Norton, "Transparent patch antenna on a-Si thin-film glass solar module," *Electron. Lett.*, vol. 47, no. 2, p. 85, 2011.

[159] E. Technology, "EJ-520 bright white paint." [Online]. Available: http://www.eljentechnology.com/index.php/products/paints/87-ej-520.

[160] C. L. INC., "CARGILLE OPTICAL GEL CODE 0608." [Online]. Available: http://www.cargille.com/og0608.pdf.

[161] D. J. Chleck and C. A. Ziegler, "Ultrasonic degassing of liquid scintillators," *Rev. Sci. Instrum.*, vol. 28, no. 6, pp. 466–467, 1957.

[162] H. H. Seliger, C. A. Ziegler, and I. Jaffe, "Role of oxygen in the quenching of liquid scintillators," *Phys. Rev.*, vol. 101, no. 3, pp. 998–999, 1956.

[163] C. L. Bailey, W. E. Bennett, T. Bergstralth, R. G. Nuckolls, H. T. Richards, and J. H. Williams, "The Neutron-Proton and Neutron-Carbon Scattering Cross Sections for Fast Neutrons," *Phys. Rev.*, vol. 70, no. 9–10, pp. 583–589, Nov. 1946.

[164] P. H. Bowen, J. P. Scanlon, G. H. Stafford, J. J. Thresher, and P. E. Hodgson, "Neutron total cross-sections in the energy range 15 to 120 MeV," *Nucl. Phys.*, vol. 22, no. 4, pp. 640–662, Feb. 1961.

[165] "National Nuclear Data Center," *Evaluated Nuclear Data File (ENDF) Retrieval & Plotting*. [Online]. Available: http://www.nndc.bnl.gov/sigma/index.jsp?as=Elemental&lib=endfb7.1&nsub=10.

[166] W. Abfalterer, F. Bateman, F. Dietrich, R. Finlay, R. Haight, and G. Morgan, "Measurement of neutron total cross sections up to 560 MeV," *Phys. Rev. C*, vol. 63, no. 4, p. 044608, Mar. 2001.

[167] S. Mouatassim, G. J. Costa, G. Guillaume, B. Heusch, a Huck, and M. Moszy'nski, "The light yield response of NE213 organic scintillators to charged particles resulting from neutron interactions," *Nucl. Instruments Methods Phys. Res. Sect. A Accel. Spectrometers, Detect. Assoc. Equip.*, vol. 359, pp. 530–536, 1995.

[168] S. A. Pozzi, M. M. Bourne, and S. D. Clarke, "Pulse shape discrimination in the plastic scintillator EJ-299-33," *Nucl. Instruments Methods Phys. Res. Sect. A Accel. Spectrometers, Detect. Assoc. Equip.*, vol. 723, pp. 19–23, 2013.

[169] B. D. Mellow, M. D. Aspinall, R. O. Mackin, M. J. Joyce, and A. J. Peyton, "Digital discrimination of neutrons and g-rays in liquid scintillators using pulse gradient analysis," *Nucl. Instruments Methods Phys. Res.*, vol. 578, pp. 191–197, 2007.

[170] F. T. Kuchnir and F. J. Lynch, "Time Dependence of Scintillations and the Effect on Pulse-Shape Discrimination," *IEEE Trans. Nucl. Sci.*, vol. 15, no. 3, pp. 107–113, 1968.

[171] G. Ranucci, "An analytical approach to the evaluation of the pulse shape discrimination properties of scintillators," *Nucl. Instruments Methods Phys. Res. Sect. A Accel. Spectrometers, Detect. Assoc. Equip.*, vol. 354, no. 2–3, pp. 389–399, Jan. 1995.

[172] L. Yan-yan, "Study of digital pulse shape discrimination method for n- γ separation of EJ-301 liquid scintillation detector *," vol. 37, no. 1, pp. 1–6, 2013.

[173] S. D. Jastaniah and P. J. Sellin, "Digital techniques for n/γ pulse shape discrimination and capture-gated neutron spectroscopy using liquid scintillators," *Nucl. Instruments Methods Phys. Res. Sect. A Accel. Spectrometers, Detect. Assoc. Equip.*, vol. 517, pp. 202–210, 2004.

[174] T. Alharbi, "Simple algorithms for digital pulse-shape discrimination with liquid scintillation detectors," *Radiat. Phys. Chem.*, vol. 106, pp. 50–55, 2015.

[175] H. LEUTZ, "Scintillating fibres," *Nuclear Instruments and Methods in Physics Research Section B: Beam Interactions with Materials and Atoms*, vol. 364, no. 3. pp. 422–448, 1995.

[176] J B Birks, *The Theory and Practice of Scintillation Counting*, First edit. Pergamon Press Ltd, 1964.

[177] P. G. Sjölin, "The scintillation decay of some commercial organic scintillators," *Nucl. Instruments Methods*, vol. 37, pp. 45–50, Nov. 1965.

[178] T. A. King and R. Voltz, "The Time Dependence of Scintillation Intensity in Aromatic Materials," *Proceedings of the Royal Society A: Mathematical, Physical and Engineering Sciences*, vol. 289, no. 1418. pp. 424–439, 1966.

[179] B. Esposito, L. Bertalot, D. Marocco, M. Riva, Y. Kaschuck, S. Skopintsev, A. Zimbal, M. Reginatto, H. Schuhmacher, J. M. Adams, and A. Murari, "Neutron measurements on Joint European Torus using an NE213 scintillator with digital pulse shape discrimination," *Rev. Sci. Instrum.*, vol. 75, no. 2004, pp. 3550–3552, 2004.

[180] N. Zaitseva, B. L. Rupert, I. PaweŁczak, A. Glenn, H. P. Martinez, L. Carman, M. Faust, N. Cherepy, and S. Payne, "Plastic scintillators with efficient neutron/gamma pulse shape discrimination," *Nucl. Instruments Methods Phys. Res. Sect. A Accel. Spectrometers, Detect. Assoc. Equip.*, vol. 668, pp. 88–93, Mar. 2012.

[181] T. K. Alexander and F. S. Goulding, "An amplitude-insensitive system that distinguishes pulses of different shapes," *Nucl. Instruments Methods*, vol. 13, pp. 244–246, Aug. 1961.

[182] G. Blasse, "Scintillator materials," *Chem. Mater.*, vol. 6, no. 6, pp. 1465–1475, 1994.

[183] M. Baldo, M. Thompson, and S. Forrest, “High-efficiency fluorescent organic light-emitting devices using a phosphorescent sensitizer,” *Nature*, vol. 403, no. 6771, pp. 750–3, 2000.

[184] G. Bizarri, W. W. Moses, J. Singh, A. N. Vasil’Ev, and R. T. Williams, “An analytical model of nonproportional scintillator light yield in terms of recombination rates,” *J. Appl. Phys.*, vol. 105, no. 2009, 2009.

[185] J. B. Birks, “Scintillations from Organic Crystals: Specific Fluorescence and Relative Response to Different Radiations,” *Proc. Phys. Soc. Sect. A*, vol. 64, pp. 874–877, 2002.

[186] S. V. Budakovsky, N. Z. Galunov, J. K. Kim, Y. K. Kim, O. A. Tarasenko, and E. V. Martynenko, “New effective organic scintillators for fast neutron and short-range radiation detection,” *IEEE Nucl. Sci. Symp. Conf. Rec.*, vol. 2, no. 6, pp. 935–939, 2007.

[187] A. Nassalski, M. Moszynski, A. Syntfeld-Kazuch, L. Świderski, and T. Szczęśniak, “Non-proportionality of organic scintillators and BGO,” *IEEE Trans. Nucl. Sci.*, vol. 55, no. 3, pp. 1069–1072, 2008.

[188] F. A. Smith, *A Primer in Applied Radiation Physics*, First. World Scientific Publishing Co. Re. Ltd., 2000.

[189] D. L. Horrocks, “Interaction of fission fragments with organic scintillators,” *Rev. Sci. Instrum.*, vol. 34, no. 9, pp. 1035–1040, 1963.

[190] Y. Kaschuck and B. Esposito, “Neutron/γ-ray digital pulse shape discrimination with organic scintillators,” *Nucl. Instruments Methods Phys. Res. Sect. A Accel. Spectrometers, Detect. Assoc. Equip.*, vol. 551, no. 2–3, pp. 420–428, 2005.

[191] T. Yanagida, K. Watanabe, and Y. Fujimoto, “Comparative study of neutron and gamma-ray pulse shape discrimination of anthracene, stilbene, and p-terphenyl,” *Nucl. Instruments Methods Phys. Res. Sect. A Accel. Spectrometers, Detect. Assoc. Equip.*, vol. 784, pp. 111–114, 2015.

[192] K. Yang and P. R. Menge, “Pulse shape discrimination of Cs2LiYCl6:Ce3+ scintillator from −30°C to 180°C,” *Nucl. Instruments Methods Phys. Res. Sect. A Accel. Spectrometers, Detect. Assoc. Equip.*, vol. 784, pp. 74–79, 2015.

[193] R. A. Winyard, J. E. Lutkin, and G. W. McBeth, “Pulse shape discrimination in inorganic and organic scintillators. I,” *Nucl. Instruments Methods*, vol. 95, no. 1, pp. 141–153, Aug. 1971.

[194] R. A. Winyard and G. W. McBeth, “Pulse shape discrimination in inorganic and organic scintillators, II,” *Nucl. Instruments Methods*, vol. 98, no. 3, pp. 525–533, Feb. 1972.

[195] H. Singh and S. Singh, “Novel discrimination parameters for neutron-gamma discrimination with liquid scintillation detectors using wavelet transform,” *J. Instrum.*, vol. 10, no. 06, pp. P06014–P06014, 2015.

[196] J. K. Polack, M. Flaska, A. Enqvist, C. S. Sosa, C. C. Lawrence, and S. A. Pozzi, “An algorithm for charge-integration, pulse-shape discrimination and estimation of neutron/photon misclassification in organic scintillators,” *Nucl. Instruments Methods Phys. Res. Sect. A Accel. Spectrometers, Detect. Assoc. Equip.*, vol. 795, pp. 253–267, 2015.

[197] C. Liao and H. Yang, “Pulse shape discrimination using EJ-299-33 plastic

scintillator coupled with a Silicon Photomultiplier array," *Nucl. Instruments Methods Phys. Res. Sect. A Accel. Spectrometers, Detect. Assoc. Equip.*, pp. 1–8, 2015.

[198] A. Kacperek, "Protontherapy of eye tumours in the UK: a review of treatment at Clatterbridge.," *Appl. Radiat. Isot.*, vol. 67, no. 3, pp. 378–86, Mar. 2009.

[199] D. E. Bonnett, A. Kacperek, M. A. Sheen, R. Goodall, and T. E. Saxton, "The 62 MeV proton beam for the treatment of ocular melanoma at Clatterbridge," *Br. J. Radiol.*, vol. 66, no. 790, pp. 907–914, Oct. 1993.

[200] CERN, "Geant4 Reference Physics Lists," 2013. [Online]. Available: http://geant4.cern.ch/support/proc_mod_catalog/physics_lists/referencePL.shtml.

[201] ICRU, "Nuclear Data for Neutron and Proton Radiotherapy and for Radiation Protection (Report 63)." [Online]. Available: http://www.icru.org/home/reports/nuclear-data-for-neutron-and-proton-radiotherapy-and-for-radiation-protection-report-63.

[202] H. Blattmann, "Beam delivery systems for charged particles," *Radiat. Environ. Biophys.*, vol. 31, no. 3, pp. 219–231, Sep. 1992.

[203] B. Aygün, T. Korkut, A. Karabulut, O. Gencel, and A. Karabulut, "Production and Neutron Irradiation Tests on a New Epoxy/Molybdenum Composite," *Int. J. Polym. Anal. Charact.*, vol. 20, no. 4, pp. 323–329, 2015.

[204] K. G. Veinot, "Effective quality factors for neutrons based on the revised ICRP/ICRU recommendations," *Radiat. Prot. Dosimetry*, vol. 115, no. 1–4, pp. 536–541, Dec. 2005.

[205] J. C. Polf, W. D. Newhauser, and U. Titt, "Patient neutron dose equivalent exposures outside of the proton therapy treatment field.," *Radiat. Prot. Dosimetry*, vol. 115, no. 1–4, pp. 154–8, Jan. 2005.

[206] S. Yonai, N. Matsufuji, T. Kanai, Y. Matsui, K. Matsushita, H. Yamashita, M. Numano, T. Sakae, T. Terunuma, T. Nishio, R. Kohno, and T. Akagi, "Measurement of neutron ambient dose equivalent in passive carbon-ion and proton radiotherapies," *Med. Phys.*, vol. 35, no. 11, p. 4782, 2008.

[207] H. Jiang, B. Wang, X. G. Xu, H. D. Suit, and H. Paganetti, "Simulation of organ-specific patient effective dose due to secondary neutrons in proton radiation treatment.," *Phys. Med. Biol.*, vol. 50, no. 18, pp. 4337–53, Sep. 2005.

[208] Y. Zheng, J. Fontenot, P. Taddei, D. Mirkovic, and W. Newhauser, "Monte Carlo simulations of neutron spectral fluence, radiation weighting factor and ambient dose equivalent for a passively scattered proton therapy unit.," *Phys. Med. Biol.*, vol. 53, no. 1, pp. 187–201, Jan. 2008.

[209] B. Damato, A. Kacperek, M. Chopra, M. A. Sheen, I. R. Campbell, and R. D. Errington, "Proton beam radiotherapy of iris melanoma," *Int. J. Radiat. Oncol. Biol. Phys.*, vol. 63, no. 1, pp. 109–115, 2005.